# NUCLEAR INSTRUMENTS & METHODS

A JOURNAL ON ACCELERATORS, INSTRUMENTATION
AND TECHNIQUES IN NUCLEAR PHYSICS

EDITOR: K. SIEGBAHN - UPPSALA

VOLUME 9

OCTOBER 1960 — DECEMBER 1960

NORTH-HOLLAND PUBLISHING COMPANY — AMSTERDAM

PRINTED IN THE NETHERLANDS
DRUKKERIJ MEIJER N.V. WORMERVEER AND AMSTERDAM

NUCLEAR INSTRUMENTS AND METHODS

EDITORIAL BOARD:

J. B. ADAMS (CERN)
F. A. ALSINA (Buenos Aires)
E. AMALDI (Rome)
H. L. ANDERSON (Chicago)
K. T. BAINBRIDGE (Cambridge, Mass.)
P. R. BELL (Oak Ridge)
R. E. BELL (Montreal)
A. BERTHELOT (Saclay)
H. BRINKMAN (Groningen)
E. H. COOKE–YARBOROUGH (Harwell)
S. DE BENEDETTI (Pittsburgh)
M. DE HEMPTINNE (Louvain)
A. DE-SHALIT (Rehovoth)
M DEUTSCH (Cambridge, Mass.)
S. DU TOIT (Pretoria)
B. S. DŽELEPOV (Leningrad)
W. GENTNER (Heidelberg)
P. C. GUGELOT (Amsterdam)
H. HALBAN (Paris)
O. HAXEL (Heidelberg)
P. HUBER (Basel)
S. KIKUCHI (Tokyo)
J. KOCH (Copenhagen)
M. S. KOZODAEV (Moscow)
S. LIVINGSTON (Cambridge, Mass.)
E. M. MCMILLAN (Berkeley)
M. G. MEŠČERJAKOV (Moscow)
P. B. MOON (Birmingham)
M. L. OLIPHANT (Canberra)
W. PAUL (Bonn)
A. S. RAO (Bombay)
G. SALVINI (Rome)
P. SAVIĆ (Belgrade)
P. SCHERRER (Zürich)
CH. SCHMELZER (CERN)
R. TANGEN (Oslo)
D. TAYLOR (Northampton)
V. I. VEKSLER (Moscow)
G. VON DARDEL (CERN)
O. WERNHOLM (Stockholm)
R. R. WILSON (Cornell)
S. D. WINTER (Saclay)

OCTOBER 1960 VOLUME 9 (1960) No. 1

GREGG M. SINCLAIR LIBRARY
UNIVERSITY OF HAWAII
8-7-63

# NUCLEAR INSTRUMENTS & METHODS

A JOURNAL ON ACCELERATORS, INSTRUMENTATION AND TECHNIQUES IN NUCLEAR PHYSICS

EDITOR: K. SIEGBAHN - UPPSALA

CONTENTS

RICHARD L. BRAMBLETT, RONALD I. EWING and T. W. BONNER, A new type of neutron spectrometer . . . . . 1
M. BONITZ and E. J. BERLOVICH, Notes on a fast time analyzer for short lifetime measurements 13
L. WÅHLIN, Automatic mass number determination for isotope separators and mass spectrometers . . . . . 21
R. BALLINI et E. POMELAS, Mesures de temps dans le domaine de la nanoseconde: convertisseur de temps en amplitudes et circuits de coïncidences . . . . . 29
ROBERT F. SIPPEL and EVERETT D. GLOVER, Sedimentary rock analysis by charged particle bombardment . . . . . 37
W. I. B. SMITH, Improved focussing near the cyclotron source . . . . . 49
ARTHUR ROBERTS, A new type of Čerenkov detector for the accurate measurements of particle velocity and direction . . . . . 55

*(continued on p. 3 of cover)*

NORTH-HOLLAND PUBLISHING COMPANY — AMSTERDAM

# NUCLEAR INSTRUMENTS AND METHODS

*A journal on accelerators, instrumentation and techniques in nuclear physics*

EDITOR: K. SIEGBAHN, UPPSALA



EDITORIAL BOARD:

J. B. ADAMS (CERN)
F. A. ALSINA (Buenos Aires)
E. AMALDI (Rome)
H. L. ANDERSON (Chicago)
K. T. BAINBRIDGE (Cambridge, Mass.)
P. R. BELL (Oak Ridge)
R. E. BELL (Montreal)
A. BERTHELOT (Saclay)
H. BRINKMAN (Groningen)
E. H. COOKE-YARBOROUGH (Harwell)
S. DE BENEDETTI (Pittsburgh)
M. DE HEMPTINNE (Louvain)
A. DE-SHALIT (Rehovoth)
M. DEUTSCH (Cambridge, Mass.)
S. DU TOIT (Pretoria)
B. S. DŽELEPOV (Leningrad)
W. GENTNER (Heidelberg)
P. C. GUGELOT (Amsterdam)
H. HALBAN (Paris)
O. HAXEL (Heidelberg)
P. HUBER (Basel)
S. KIKUCHI (Tokyo)
J. KOCH (Copenhagen)
M. S. KOZODAEV (Moscow)
S. LIVINGSTON (Cambridge, Mass.)
E. M. MCMILLAN (Berkeley)
M. G. MEŠČERJAKOW (Moscow)
P. B. MOON (Birmingham)
M. L. OLIPHANT (Canberra)
W. PAUL (Bonn)
A. S. RAO (Bombay)
G. SALVANI (Rome)
P. SAVIĆ (Belgrade)
P. SCHERRER (Zürich)
CH. SCHMELZER (CERN)
R. TANGEN (Oslo)
D. TAYLOR (Northampton)
V. I. VEKSLER (Moscow)
G. VON DARDEL (CERN)
O. WERNHOLM (Stockholm)
R. R. WILSON (Cornell)
S. D. WINTER (Saclay)


INSTRUCTIONS FOR CONTRIBUTORS

Contributions may be sent to the Editor, Professor K. Siegbahn, Institute of Physics, University of Uppsala, Sweden, either directly or through the intermediation of one of the members of the Editorial Board. Contributions may be written in English, French or German but should always, except for very short papers, be supplied with a brief abstract in English. Figures should be in inked original drawings or glossy prints and they should be sufficiently large. Contributors should make sure that important details in drawings and photographs will show up clearly in the diminished copy used by the publisher.

Books for review should be sent to Professor Siegbahn.

Objective and descriptive material on endeavours and product developments from the industry for the section "Spotlight on Industry" should be sent directly to the publishers, North-Holland Publishing Company, P.O. Box 103, Amsterdam.


Nuclear Instruments and Methods is published monthly. The subscription price of a volume of 360 pages is $ 17.00 (130 s), postage free.

Subscriptions should be sent to the publishers, North-Holland Publishing Company, P.O. Box 103, Amsterdam, or to any subscription-agent.



No part of this issue may be reproduced in any form, by print, photoprint, microfilm or any other means without written permission from the publisher.

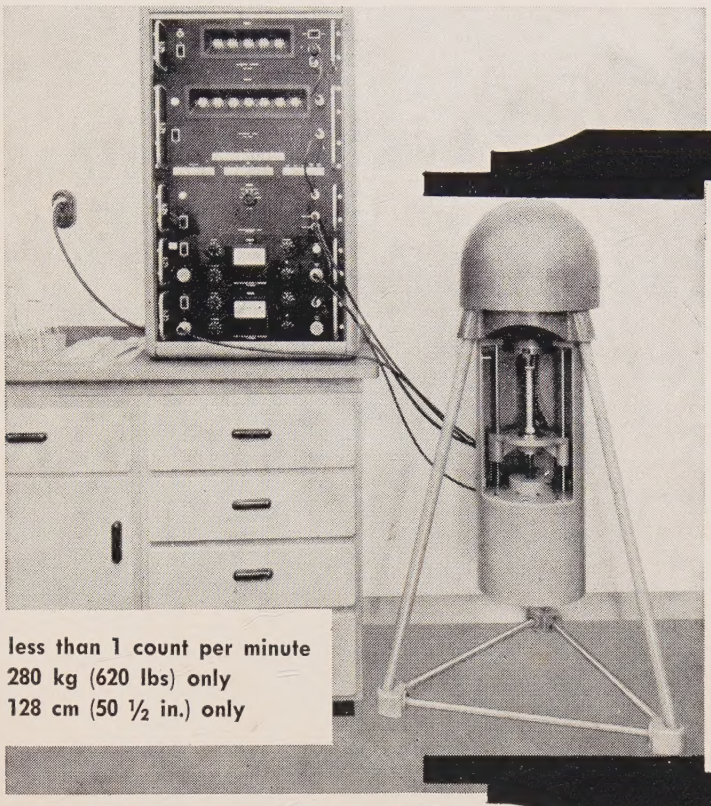

Background : less than 1 count per minute
Weight : 280 kg (620 lbs) only
Height : 128 cm (50 ½ in.) only

128 cm

# low-level beta counting

Low-level beta counting is brought to an elegant and simple solution by the novel Philips anti-coincidence assembly, type PW 4127, together with its associated electronic equipment.
The assembly comprises two radiation-sensitive elements only, viz. a low-level beta counting tube*), and a single guard tube which replaces the conventional array of dozens of guard tubes hitherto required for low-level work.
By virtue of this unique design tons of shielding material are eliminated; the electronic circuitry is considerably simplified, and hence overall reliability is greatly improved. Reproducibility is guaranteed by the fixed geometry of the sample with respect to the counting tube.
With a background of less than 1 count per minute, it is now possible to measure in a 300 mg sample a beta activity (e.g. $Sr^{90}$ or $Tl^{204}$) of $(5 \pm 0.5) \times 10^{-12}$ Curie in only one hour.

***) Two types available:**

type 18515 for measuring low-energy beta radiation, with a 1.5 mg/cm² mica window;

type 18516 for general low-level beta work, with a 10 mg/cm² Cr-Fe window.

PHILIPS

**PHILIPS**
*nuclear equipment*

N.V. PHILIPS' GLOEILAMPENFABRIEKEN - EINDHOVEN - HOLLAND

a new approach to time interval measurement

# 0.25 milli microsecond measurements

WITH THE

## Eldorado

MODEL TH-300

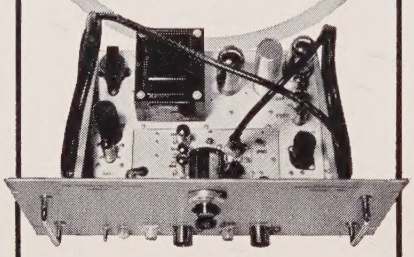

## TIME-TO-PULSE HEIGHT CONVERTER

### applications

* *Neutron time-of-flight measurements*
* *Half-life determinations of short lived isotopes*
* *Determination of short-time decay in isomeric states*
* *Fast coincidence studies*
* *Delay line calibration*
* *Energy determinations*
* *Transient time studies*

An analog-to-analog converter which transforms time to amplitude over the time range of 1 to 3000 milli microseconds, the TH-300 provides an output pulse whose amplitude is proportional to time. The output can be measured with a pulse height analyzer or scope.

KEY SPECIFICATIONS Three time ranges – 300, 1000, and 3000 milli microsecond full scale. Input, pulse start channel, amplitude of 2 – 100 v negative, duration of 0.01 – 0.10 microseconds; stop channel, amplitude 15 – 150 v negative, duration of 0.01 – 1.00 microseconds. Output, negative ramp, 8 v full scale. Domestic price $795. Immediate delivery.

For complete technical and sales information, call your nearest Eldorado Engineering Representative or write directly to Dept. 79

## Eldorado Electronics

*2821 Tenth Street*
*Phone THornwall 1-4613*
*Berkeley 10, California*

*nuclear physics*

FOR PULSED NEUTRON & TIME-OF-FLIGHT STUDIES • GAMMA AND COINCIDENCE PAIR SPECTROSCOPY

*health physics*

FOR WHOLE BODY COUNTERS • BIOLOGICAL ASSAYS • FALLOUT ANALYSES

*radiochemistry*

FOR QUALITATIVE AND QUANTITATIVE ANALYSES

*reactor engineering*

FOR REACTOR CONTROL DESIGN • FUEL ROD ANALYSIS

*mass spectroscopy*

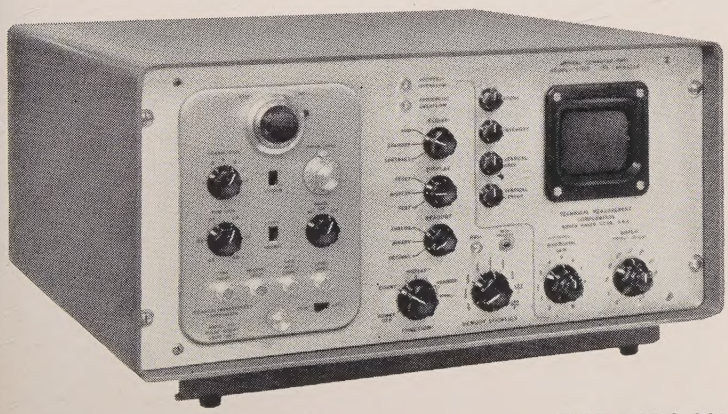

*and for other areas of research involving pulse or time measurements . . .*

**THE TMC MULTICHANNEL ANALYZER**

MODEL CN-110

First and finest of all transistorized multichannel analyzers, the CN-110 is now widely used throughout the U.S., Canada and Europe. Its interchangeable plug-in logic, 256-channel basic computer and associated data handling units are unconditionally guaranteed for two full years and backed by an unequalled service policy. Call or write for complete specifications.

TMC **TECHNICAL MEASUREMENT CORPORATION**

441 WASHINGTON AVE., NORTH HAVEN, CONN. • CE 9-2501

## ALL-ROUND, LOW PRICED MONITOR

Typically developed as a laboratory equipment the monitor 111-A1 combines quality and high performance with low cost.

- Completely transistorized
- Designed as portable type
- Very low count rate: 0 to 5 c.p.s. full scale
- Highest count rate: 0 to 5000 c.p.s. full scale
- Equalizing accumulators
- Automatically recharged from A.C. mains
- Priced $ 410 F.O.B. Antwerp

For further information on this and other applications in the field of "Electronics for Nucleonics" ask :

AN IT ASSOCIATE

**Bell Telephone Mfg Co**

"NUCLEAR ENERGY DIVISION"
33, Berkenrodelei
HOBOKEN-Antwerp
Belgium

NORTH-HOLLAND BOOKS

*Paul Ehrenfest*

COLLECTED SCIENTIFIC PAPERS

**XII + 632 pages**

**Guilders 45,00 (90s.)**

This volume makes widely scattered publications readily available. All Dutch articles appear here in English; the German publications are in the original language.

**Sole Agency for U.S.A.:**

**Interscience Publishers Inc. — New York**

**NORTH-HOLLAND PUBLISHING COMPANY - AMSTERDAM**

MODEL 412 MERCURY RELAY

## PRECISION SLIDING PULSER

**for Precise Calibration of Single & Multi-Channel Pulse Height Analyzers**

Determines Window Widths Using Principle of *Constant Angular Velocity*

**AUTOMATICALLY**
**10 × more accurately**
**40 × faster than conventional pulsers**

***Incorporates Both Manual Control and Precision Motor Drive***

**Simulates Pulses from Scintillation, Proportional or Geiger Counters**

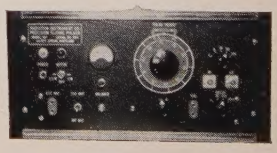

## MERCURY PULSER, Model 401

***Featuring Versatility and Precision***

**Specifically designed for the Nuclear Physics Laboratory**

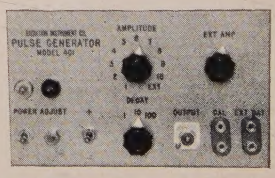


**Fast rise and exponential decay simulates scintillation, proportional or geiger counter pulses for test and calibration of amplifiers, pulse height analyzers, scalers, etc.**

**MODEL 412 . . . $ 450.00 — MODEL 401 . . . $ 125.00**

**RADIATION INSTRUMENT CO.**

**P. O. BOX 733, SILVER SPRING, MARYLAND, U.S.A.**

CDC's PROVEN PERFORMANCE

## 100-CHANNEL PULSE HEIGHT ANALYZER

# CHALK RIVER KICKSORTER

Manufactured by Computing Devices of Canada, Limited, from specifications prepared by Atomic Energy of Canada, Limited.

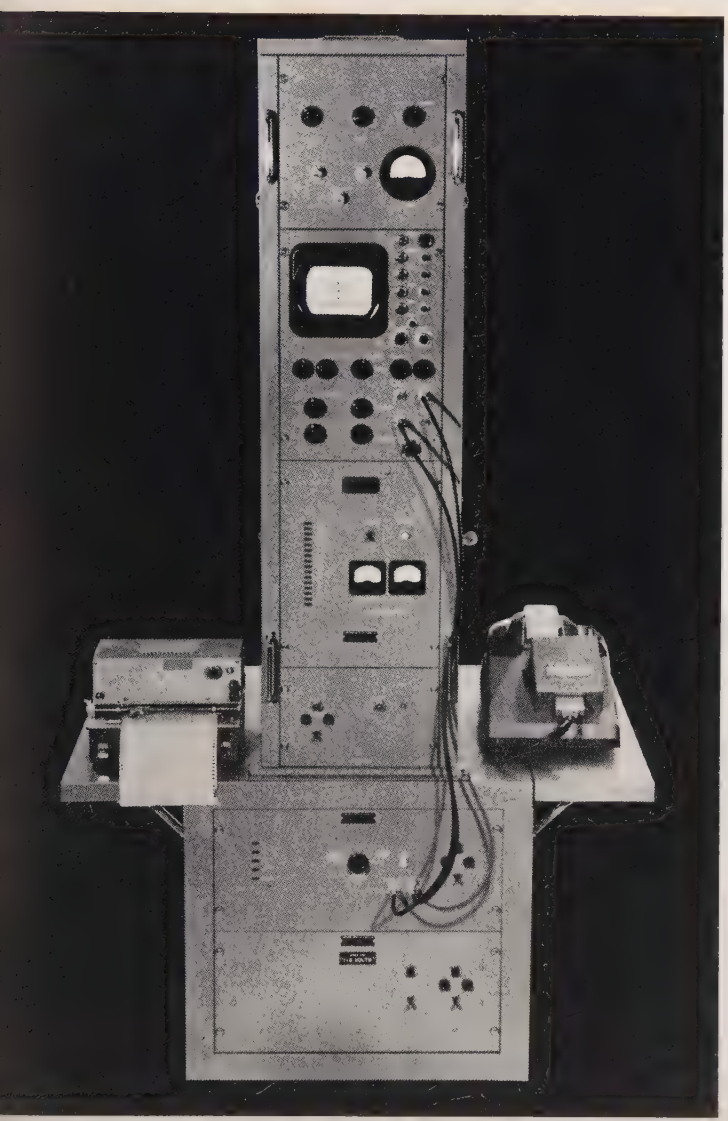

The convenience and speed of automatic printout can be obtained by adding a Decimal Scaler, a Print Control Unit, and an Electric Printer as accessories, shown with the Kicksorter. Provision is also made in the circuitry for the addition of a Pen Recorder for more accurate analog output.

## 88% TRANSISTORIZED

- Printed Circuitry
- Low Maintenance—High Reliability
- Low Power Consumption—120 Watts
- No Ventilation or Cooling Problems

## VERSATILE DATA PRESENTATION

- Oscilloscope Display
- Binary Manual count readout allows the count on any channel to be displayed in digital form.
- Magnetic Core Memory—65,535 counts can be stored per channel.
- Permanent Count Storage—sixteen magnetic cores for each of the 100 channels.
- Highly Versatile—can be modified to accommodate most applications which require additional features.

The Chalk River "Kicksorter" is designed to span random pulses of various amplitudes and shapes, sort them according to amplitude into 100 channels, and store a record of the counted pulses in a magnetic core memory. This computer, with its magnetic core memory and versatile data display system, makes it possible to observe the pulse amplitude spectrum as it accumulates or after it has accumulated.

In addition to its wide use in gamma spectroscopy, the "kicksorter" has many applications in medical research, neutron time-of-flight studies, radioactive fallout studies, shielding studies, oil well and uranium logging, neutron activation analyses, measuring of radioactivity in humans, and other areas.

The analyzer is designed so that information accumulated may be displayed or read out in various ways. Data may be observed on the oscilloscope, or information already accumulated in the memory core may be displayed on the screen, plotted on a strip chart recorder, or printed out in decimal form on an automatic printer.

*For additional information, wire or write to:*

**Bendix International**

DIVISION OF THE BENDIX CORPORATION
205 East 42nd Street
New York 17, N. Y., U.S.A.
Cable Address: "Bendixint"

Sales Representative for Great Britain
**NUCLEAR ENTERPRISES (G.B.) LTD.**
BANKHEAD MEDWAY, SIGHTHILL,
EDINBURGH 11, SCOTLAND

SALES AND SERVICE AVAILABLE THROUGHOUT THE WORLD

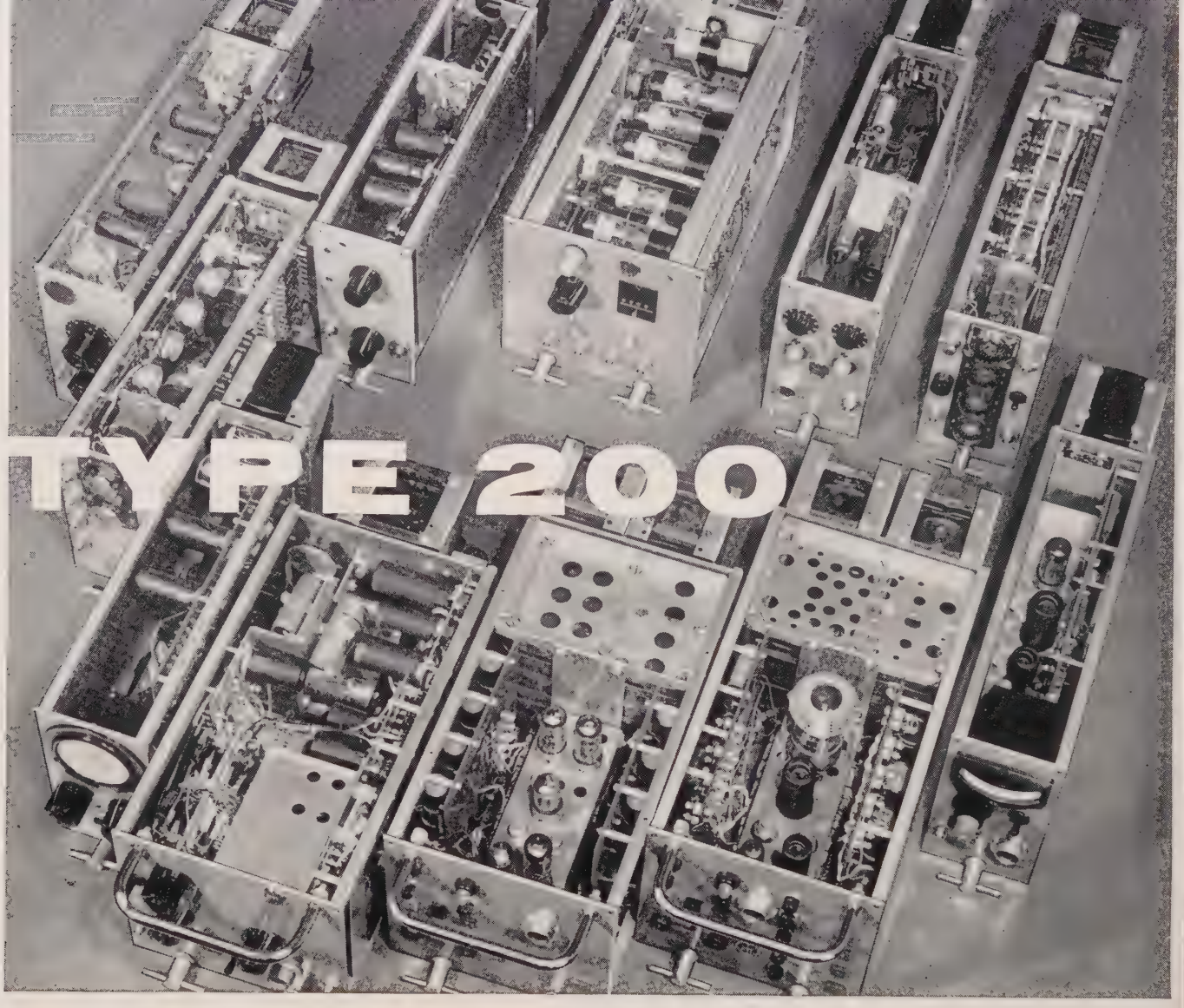


## UNITIZED NUCLEONIC RANGE

The plan behind this Type 200 equipment is to offer you a Unitized Range (already 24 units and still increasing) not only to cover every type of nucleonic counting, but one that can be added to at will, so that you get only what you want, when you want.

- **Suitable for all types of nucleonic detectors.**
- **Built to a stringent specification.**
- **Designed in conjunction with A.E.R.E. Harwell.**
- **Flexible in use—a unit for every purpose.**

*Enquiries should be addressed to:—*

**INSTRUMENT DIVISION**

*HIGH CHURCH STREET · NEW BASFORD · NOTTINGHAM*

ERICSSON

ERICSSON TELEPHONES LIMITED · HEAD OFFICE · 22 LINCOLN'S INN FIELDS LONDON W.C.2

maximum accessibility for servicing...
maximum flexibility of data presentation...

# AEI PULSE HEIGHT ANALYSER

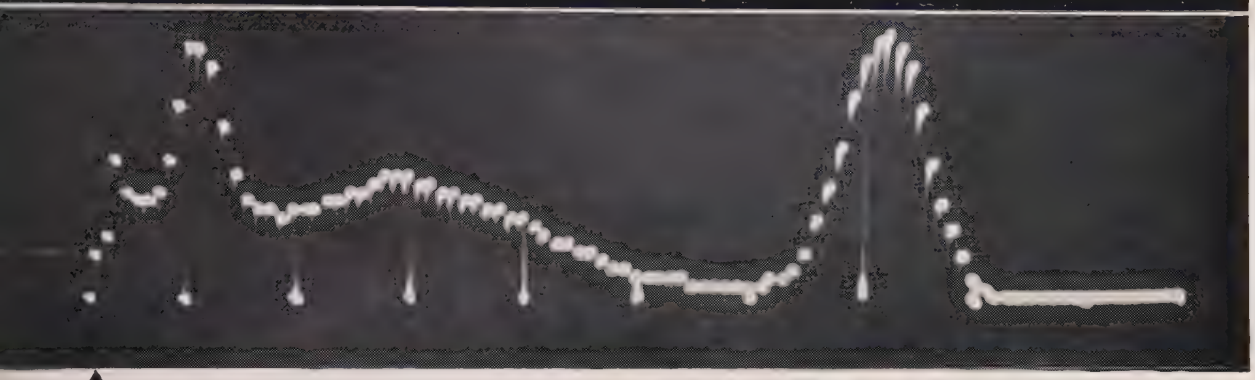

Typical presentation of analogue count on the CRT. This is the gamma spectrum of gold foil irradiated for 30 minutes at a neutron flux of $2 \times 10^8$ n/cm²/S. The curve and two significant peaks are due to $^{198}Au$.

* Unit construction for easy servicing
* Analogue presentation on cathode ray tube or chart recorder
* Decimal presentation on Dekatrons or 3″ paper tape
* Ferrite memory presents loss of count if mains fail
* Circuitry largely transistorised for reliability
* 100 Channels, capacity 65,535 pulses per channel
* Console or rack-mounted versions.

All units draw out on runners so that servicing and setting up can be accomplished without switching off power or removing inter-connecting cables.

A full technical specification of the P.H.A. is given in publications 2451-70 available from:

AEI

**Instrumentation Division**
**Associated Electrical Industries Limited**
P.O. Box 1 · Harlow · Essex · Tel: Harlow 25271
SC/108

*featuring ultra-high stability and precision switching*

## E.H.T. SUPPLIES NE 5302 & NE 5303

- VOLTAGE RANGES
  NE 5302: 500–1500 volts D.C.; max. output current 5mA.
  NE 5303: 1000–5000 volts D.C.; max. output current 3mA.
- SPECIAL PRECISION SWITCHING
  Both units feature use of switched precision resistors for coarse steps of voltage adjustment, and 0.1% ten-turn potentiometers for fine voltage control, thus ensuring accurate resetting of the output voltages to 0.1 volts.
- STABILITY AGAINST FULL LOAD
  For both units, 50 parts per million measured at full output voltage.
- STABILITY AGAINST LINE VARIATIONS OF ± 10% – For both units, ± 50 parts per million measured at full output voltage.
- NOISE AND RIPPLE LEVELS
  Less than 5 millivolts for any voltage setting.

Also available the following companion units: Non-overloading Linear Pulse Amplifier NE 5202; Pre-amplifier and Cathode Follower NE 5202 A; Single channel Pulse Height Selector NE 5102; Scanning Scintillation Spectrometer NE 8601; Ratemeter NE 5401. Complete assembly for C14 and H3 counting NE 8301.

ndh 1407

**Nuclear Enterprises (G.B.) Ltd**

BANKHEAD MEDWAY, SIGHTHILL, EDINBURGH 11, SCOTLAND. (TEL. CRA 5262)
Associate Company: Nuclear Enterprises Ltd., 1750 Pembina Highway, Winnipeg, Canada

## NORTH-HOLLAND BOOKS

*Analytical and Canonical Formalism in Physics*

*by*

**ANDRÉ MERCIER**

*Head of the Department of Theoretical Physics, University of Berne*

**6 × 9″ VIII + 222 pages Guilders 20.00 (40 s.)**

THE CONTENTS

i LAGRANGIAN FORMALISM
ii LAGRANGIAN DENSITY
iii CANONICAL FORMALISM
iv CANONICAL FORM OF ELECTRODYNAMICS
v HAMILTONIAN DENSITIES
vi TRANSFORMATIONS
vii CANONICAL FORMALISM WITH VANISHING JACOBIAN DETERMINANT

**Sole Agency for U.S.A.: Interscience Publishers Inc. – New York**

**NORTH-HOLLAND PUBLISHING COMPANY — AMSTERDAM**

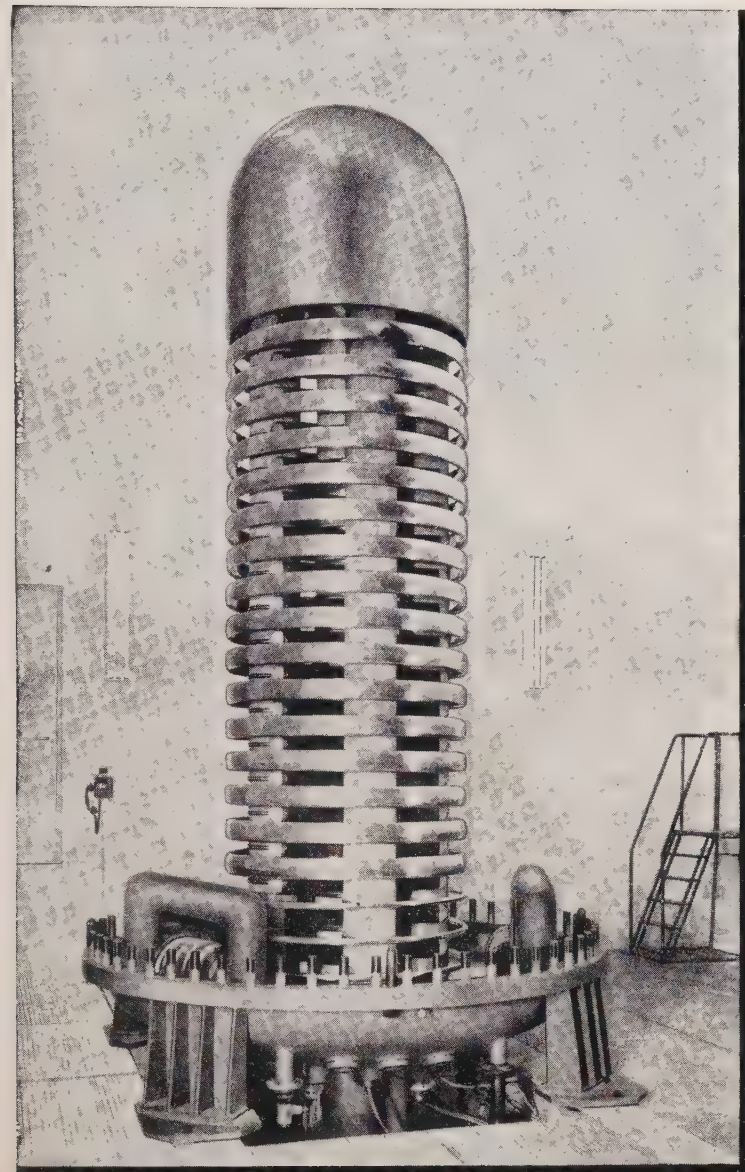

4 MV Particle Accelerator in the Physical Institute of the University of Basel (Switzerland)

# HAEFELY

**Particle Accelerators**
**up to 4 MV**
**with high beam intensity**

**for basic nuclear research**

**for industrial radiation processing**

Continuous irradiation of plastics

Sterilisation of drugs and preservation of foods

X-ray equipment for non-destructive product inspection

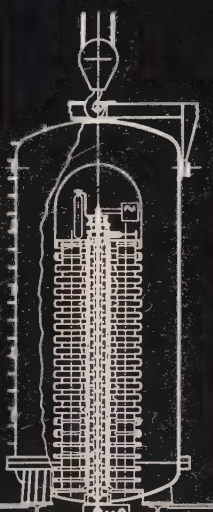

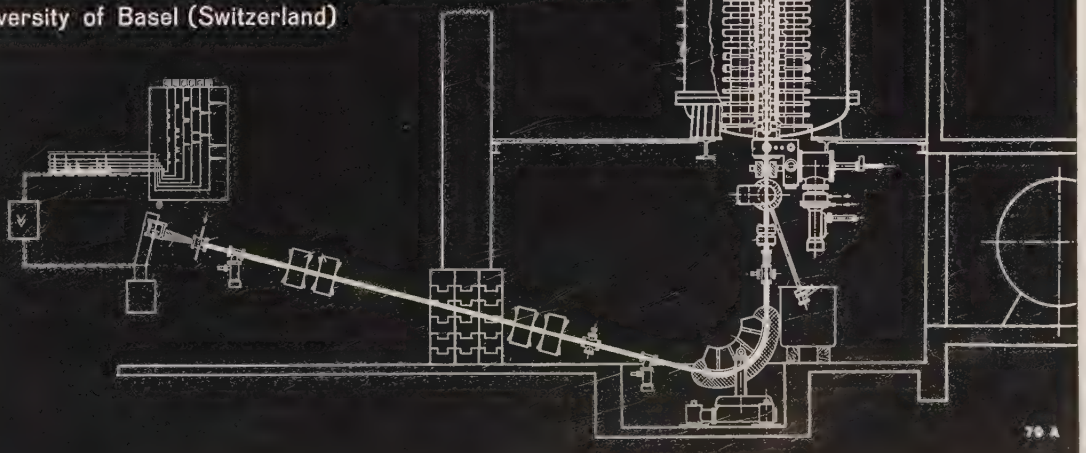

79 A

**EMILE HAEFELY & CO LTD BASEL-SWITZERLAND**

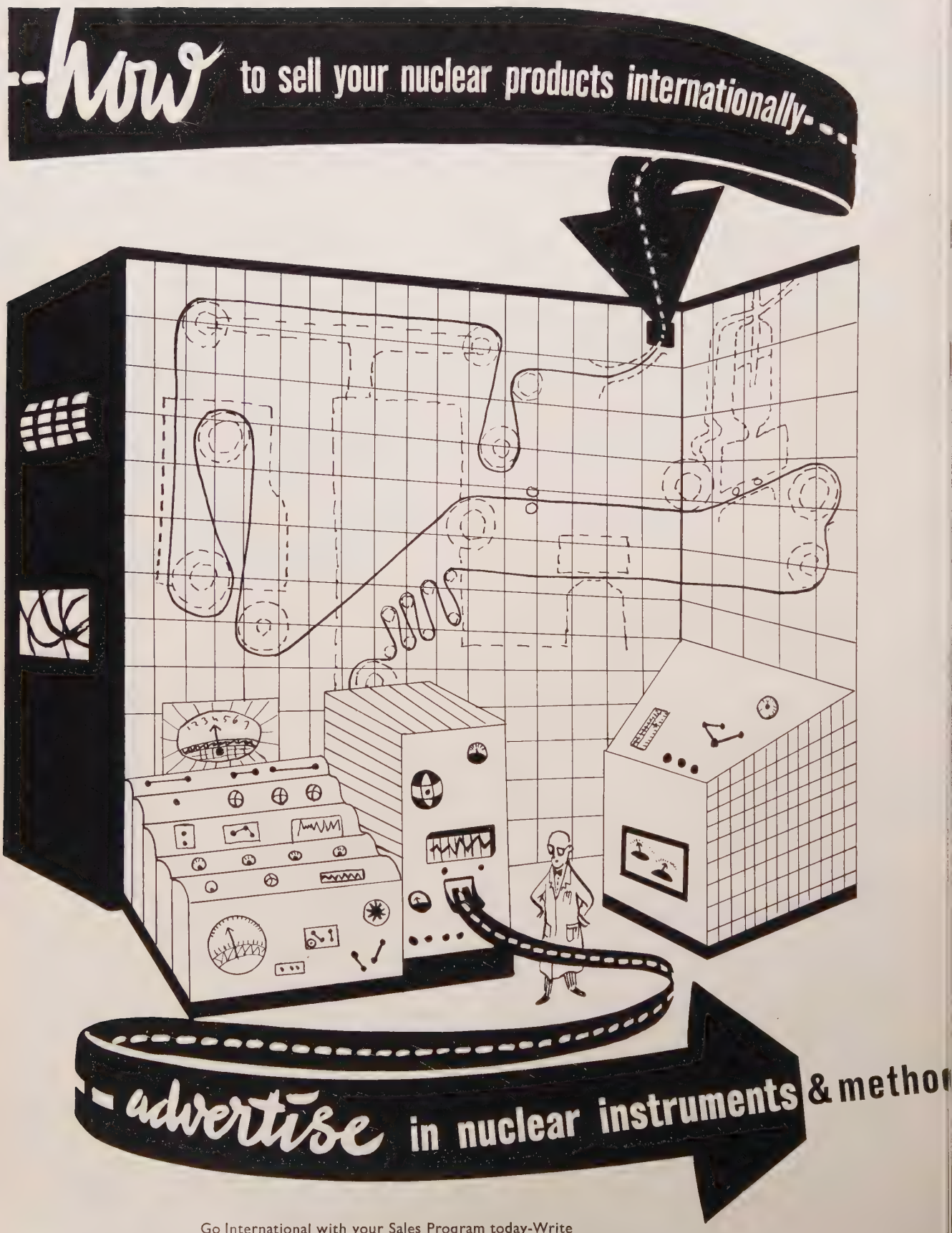


Go International with your Sales Program today-Write

**William F. Baars-Advertising Manager, North-Holland Publishing Company**

**P.O. Box 103, Amsterdam, The Netherlands**

**STANDARD FUNCTIONNAL UNITS . . .**

*FRENCH ATOMIC ENERGY COMMISSION SYSTEM*

# . . . master-key to nuclear instrumentation

*Standard functional units are assembled in cabinets in order to be used as complete assemblies : scales for counting, amplitude selectors, ratemeters, etc...*

REGISTER UNIT TYPE TND.1
Function :
counting (registering)
Dekatron divider

MER UNIT (SLOW RESPONSE)
PE TAL.2
ended
omatic
e-set
unting

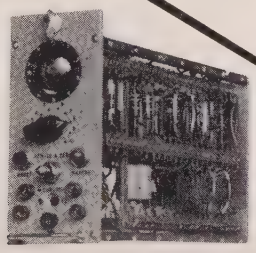

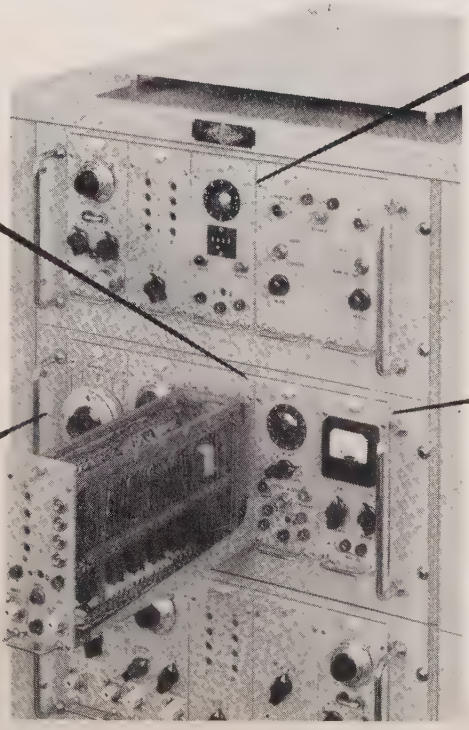

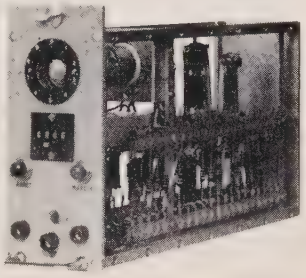

VERY HIGH TENSION UNIT

TEMETER TYPE TIS.1
plies a tension
a current
portionnal
the number
counts
eived

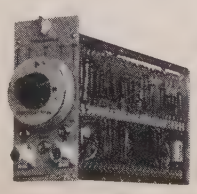

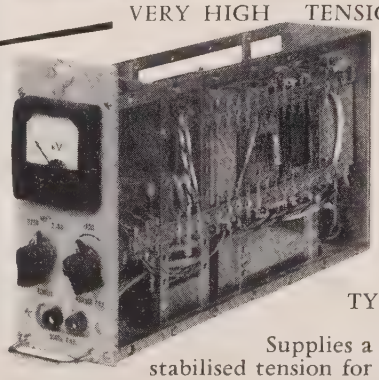

TYPE THT.4

Supplies a very high stabilised tension for detectors, pre-amplifiers

**L'ÉLECTRONIQUE APPLIQUÉE**

96/100, rue Maurice Arnoux • MONTROUGE • ALE 45-20, 83-20
25, rue du Docteur Finlay • PARIS 15e • TÉL. SÉGUR 14-75

# SETTING NEW STANDARDS
## at 99.98% of the speed of light.

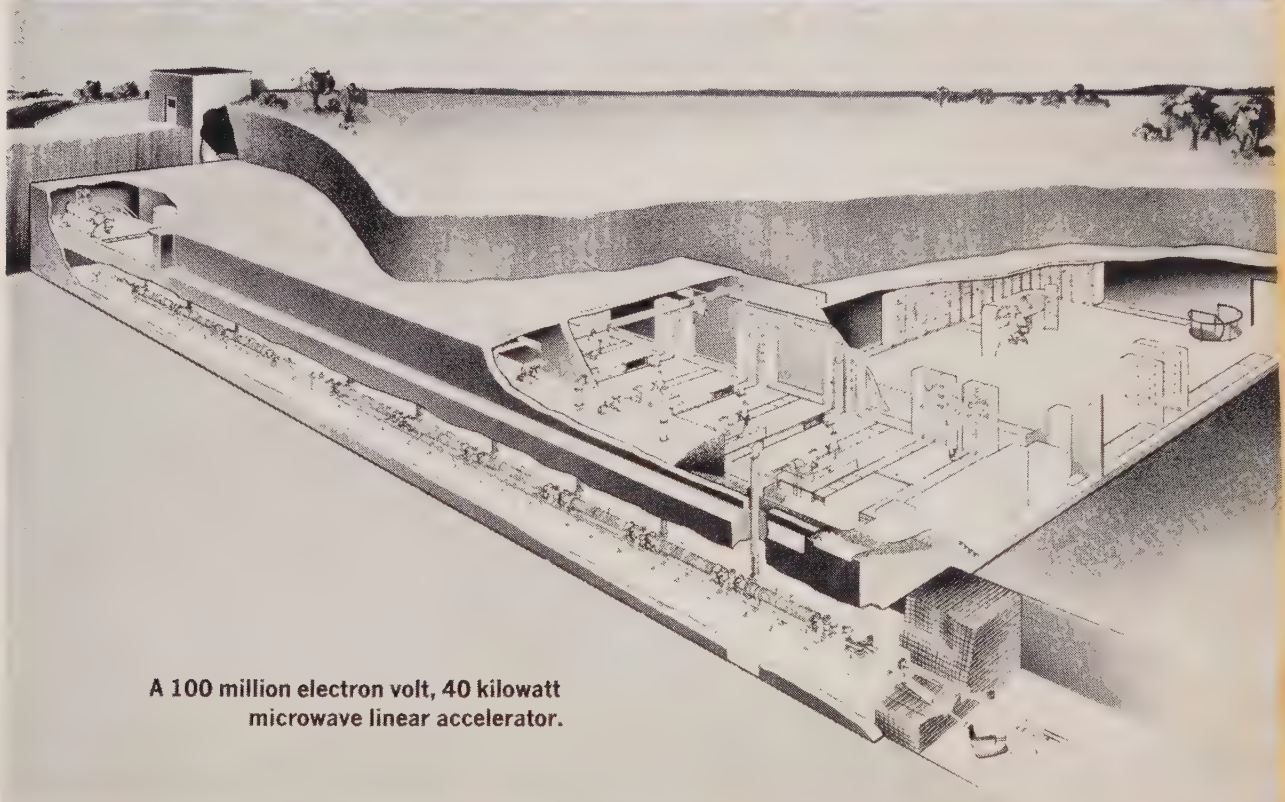

A 100 million electron volt, 40 kilowatt microwave linear accelerator.

One of the world's most powerful when completed, this high-energy electron accelerator will enable the U.S. National Bureau of Standards to carry out extensive programs in:

- ***Nuclear Physics Research***
- ***Radiation Effects***
- ***Dosimetry Standards***

. . . to meet the need for new data in the growing field of applied radiation.

The linear accelerator (Linac) is under construction at the manufacturing and test facility of Applied Radiation Corporation, Walnut Creek, California.

***Particle accelerators for science and industry***

High Voltage Servicing Company, Ltd.
London, England

High Voltage Engineering (Europa) N.V.
Amersfoort, The Netherlands

HVEC arco

**HIGH VOLTAGE ENGINEERING**
**CORPORATION**
BURLINGTON, MASSACHUSETTS • U. S. A.

APPLIED RADIATION CORPORATION HIGH VOLTAGE ENGINEERING (EUROPA) N.V.

NUCLEAR INSTRUMENTS AND METHODS 9 (1960) 1–12; NORTH-HOLLAND PUBLISHING CO.

# A NEW TYPE OF NEUTRON SPECTROMETER†

RICHARD L. BRAMBLETT, RONALD I. EWING and T. W. BONNER

*The Rice University, Houston Texas*

Received 4 July 1960

Neutrons are detected in a small $Li^6I(Eu)$ scintillator placed at the center of polyethylene moderating spheres with sizes ranging from 2 to 12 inches in diameter. The efficiency of this neutron counter has been experimentally determined using monoenergetic neutrons from thermal energies to 15 MeV. The counter has excellent energy sensitivity from 0.1 to 2 MeV and is particularly useful for determining the shapes of continuous neutron spectra. The pronounced difference in the efficiencies for the five sizes of spheres which have been calibrated provides a basis for accurate neutron energy determination. The good $\gamma$ ray discrimination of the counter allows it to be used with a radium-beryllium neutron source. Neutron spectra from a variety of sources have been determined with this counter. These include the two groups of neutrons from the $C^{14}(p,n)N^{14}$ reaction, the evaporation spectrum of the neutrons from the reaction $Rh^{103}(p,n)Pd^{103}$, the energy spectra of inelastically scattered neutrons, and the neutron spectrum from the scattering of fast neutrons by the floor and walls of a building.

## 1. Design of Counter

Of the many types of neutron counters that have been developed, some can be used as neutron spectrometers[1,2,3]) over a limited range of neutron energies and others[4,5]) have a nearly constant efficiency as a function of neutron energy for fast neutrons. The counter described here can give information about the energy of neutrons over a wide range of energies. The energy sensitivity remains good below 0.5 MeV, which is near the lower limit for most neutron spectrometers. This counter has good $\gamma$ ray discrimination, is simple in design and application, and has an efficiency of about 0.1%.

Neutrons are detected in a $Li^6I(Eu)$ scintillator after being moderated in polyethylene spheres of various sizes. Moderated neutrons are detected as scintillations resulting from the 4.787 MeV energy release in the $Li^6(n,\alpha)H^3$ reaction. The $Li^6I$ crystal was made by the Harshaw Chemical Company from a sample containing 96.1% $Li^6$. It is hermetically sealed in an aluminum container with a plate glass window. $Al_2O_3$ is used as reflector on the walls of the container. Fig. 1 shows the construction of the counter; the scintillation crystal is 4 mm in diameter and 4 mm thick and is optically coupled to a DuMont 6292 photomultiplier by a polystyrene light pipe $\frac{1}{2}$ inch in diameter and 6 inches long. The crystal and light pipe are enclosed in a rigidly mounted brass tube which supports the moderating sphere. The counter has been calibrated with polyethylene spherical moderators with nominal diameters of 2, 3, 5, 8, and 12 inches. Each sphere has a $\frac{5}{8}$ inch hole for insertion of the light pipe, and is positioned so that the $Li^6I$ crystal is at the center of the sphere.

The size and shape of the $Li^6I$ crystal was chosen to provide good $\gamma$ ray discrimination. About 80% of incident thermal neutrons are absorbed in 1.0 mm of $Li^6I$, so that thermal neutron detection is essentially a surface effect,

† Supported in part by the U.S. Atomic Energy Commission.

[1]) J. L. Fowler and J. E. Brolley, Jr., Revs. Mod. Phys. **28** (1956) 103.

[2]) C. H. Johnson and C. C. Trail, Rev. Sci. Instr. **27** (1956) 468.

[3]) L. Cranberg and J. S. Levin, Phys. Rev. **100** (1955) 434.

[4]) W. D. Allen and R. L. Henkel, Progress in Nuclear Energy, Ser. I, Vol. II (Pergamon Press, New York, 1958); W. D. Allen and A. T. Ferguson, Proc. Phys. Soc. A **70** (1957) 639; W. D. Allen, Chapter in Fast Neutron Physics, Part I, edited by J. B. Marion and J. L. Fowler (Interscience Publishers, Inc., New York, 1960).

[5]) A. O. Hansen and J. L. McKibben, Phys. Rev. **72** (1947) 673.

whereas the efficiency for detection of $\gamma$ radiation and fast neutrons is roughly proportional to the volume of the crystal. Consequently, a small (4 mm thick, and 4 mm in diameter) crystal, with large ratio of surface to volume, was used to minimize the proportion of counts not due to thermal neutrons. In addition to reducing the number of $\gamma$ ray pulses, the small size of the crystal limits the maximum pulse size due to $\gamma$ rays, and good $\gamma$ discrimination is obtained. Pulse height spectra obtained with Pu-Be and Ra-Be neutron sources are shown in fig. 2. The pulse height spectrum obtained with the Pu-Be source, which has about 0.6 $\gamma$ ray per neutron, shows only a well isolated neutron peak with a small low-energy tail. The Ra-Be source has about 30 000 $\gamma$ rays per neutron which cause the rapid rise below the neutron peak in the pulse height spectrum of Ra-Be. Note that the Ra-Be source was enclosed in 1 inch of lead which attenuates the lower energy $\gamma$ rays by a considerable amount. Since slow neutrons are predominately counted, the pulse height spectrum is independent of the energy of the incident neutrons. The pulse height spectrum is displayed on a multi-channel analyzer and only pulses greater than the discrimination level indicated by an arrow in fig. 2 are accepted. Proper adjustment of the bias on an integral discriminator would accomplish the same result.

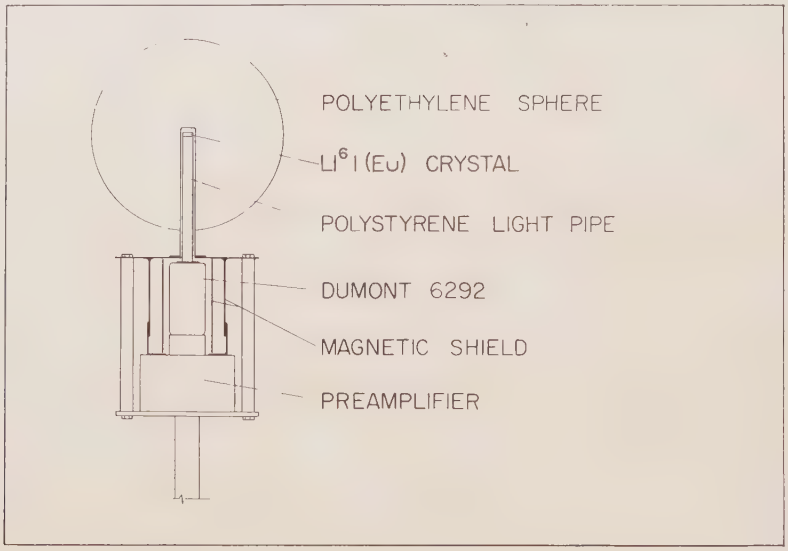


Fig. 1. Schematic drawing of neutron counter.

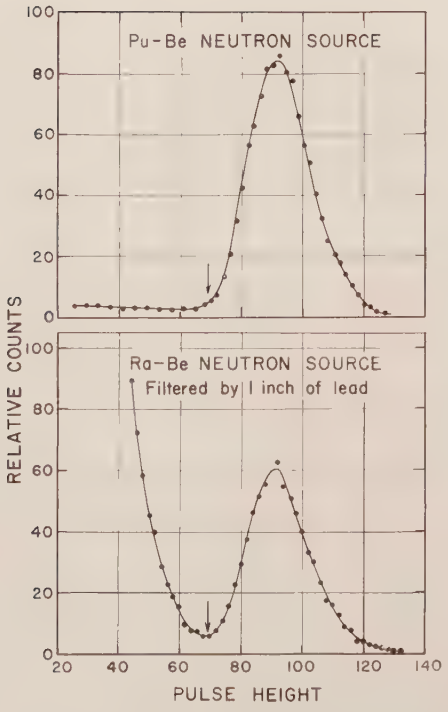


Fig. 2. Pulse spectra obtained with 8 inch counter showing the effect of a large number of $\gamma$ rays.

## 2. Calibration of Spectrometer

The counter was calibrated as a function of neutron energy from 0.050 to 15.1 MeV using monoenergetic neutrons from charged particle reactions. The center of the spherical counter was placed at either 20, 40, or 100 cm from the center of the neutron source. Five sizes of spheres were calibrated at each energy. A long counter[4,5]), placed 100 cm from the source at the same angle with the beam of charged particles as the spherical counter, was used to monitor the neutron flux. The spherical counter was removed during the long counter measurements.

The $Li^7(p,n)Be^7$ reaction was used to obtain neutrons in the energy range 0.050 MeV to 0.600 MeV, the $H^3(p,n)He^3$ reaction between 1.0 and 4.0 MeV, and $H^2(d,n)He^3$ reaction for 4.5 to 7.5 MeV neutrons. The $H^3(d,n)He^4$ reaction was used for a source of 15.1 MeV neutrons†. The lithium targets were Li metal evaporated on 0.020 inch tantalum blanks and had a thickness such that protons with an energy of 1.9 MeV lost approximately 0.010 MeV in the target. The $Li^7(p,n)$ threshold was used to calibrate the nuclear magnetic resonance magnetometer used to determine the energy of the bombarding particles. For neutrons of energy less than 0.16 MeV, the counters were moved to 60° with respect to the incident beam of protons.

Gas targets were used for the $H^3(p,n)He^3$ and $H^2(d,n)He^3$ reactions. A small gas target chamber to contain $H^3$ and $H^2$ gas was made from a thin walled platinum tube 1.6 cm long and 1 cm in diameter. Fifty curies of tritium gas were stored in an uranium metal trap[6]) which could be heated to about 500° C to evolve tritium gas into the target chamber to a pressure of 1 atmosphere. The energy loss of protons in the tritium gas ranged from 0.04 MeV at $E_p = 4.8$ MeV to 0.06 MeV at $E_p = 1.9$ MeV. The proton beam entered the target chamber through a 2.4 mg/cm² aluminum foil, in which the proton energy loss ranged between 0.15 MeV at $E_p = 4.8$ MeV and 0.26 MeV at $E_p = 1.9$ MeV. When using the $H^2(d,n)He^3$ reaction, the deuteron beam passed through a 2.4 mg/cm² nickel foil into the gas chamber. The energy loss of the deuterons in the foil and in the deuterium gas at a pressure of 1.5 atmospheres was respectively 0.20 and 0.07 MeV at $E_d = 4.04$ MeV, and 0.28 and 0.13 MeV at $E_d = 2.17$ MeV. When using the $H^2(d,n)He^3$ reaction, runs were taken with no gas in the target to determine the background due to other sources of neutrons.

The principle quantity of interest in the calibration of the spherical counter is the counting rate, as a function of neutron energy, from an isotropic point source of constant source strength. In order to obtain this quantity from the experimental data, small corrections must be applied to account for (1) the unequal illumination of different parts of the counter by the neutron source, (2) the background due to scattering of source neutrons in the walls of the room, and (3) the variation in the long counter efficiency. None of these corrections was larger than 16%. Since the neutron energy depends on its angle of emission, there is a spread in energy over the surface of the sphere; thus, the effective neutron energy depends on the sphere size and the distance from the source. The effective neutron energy differed by less than 1% from the energy at the center of the counter.

The illumination correction, due to the angular distribution of neutrons from the source, was obtained by integration of the source reaction cross section over the surface of the sphere. The angular distributions for the source reactions were taken from published data[1,7,8]). Ordinarily, the distance from the center of the counter to the source was 20 cm for the 2 and 3 inch counters and 40 cm for the 5, 8, and 12 inch counters. When using the $H^2(d,n)He^3$ neutron source, which has a strongly peaked angular distribution, data was obtained with the 8 and 12 inch counters at 100 cm in order to obtain more nearly uniform illumination. The corrections for

† The authors wish to thank Texas Nuclear Corporation for the use of their Van de Graaff accelerator and associated particle neutron monitor for the 15 MeV calibration data.

[6]) A. B. Lillie and J. P. Conner, Rev. Sci. Instr. **22** (1951) 210.

[7]) R. Taschek and A. Hemmendinger, Phys. Rev. **74** (1948) 373.

[8]) Gabbard, Davis and Bonner, Phys. Rev. **114** (1959) 201.

TABLE I
The four largest illumination corrections

| Source reaction | Neutron energy (MeV) | Counter diameter (inches) | Distance from source (cm) | Illumination ratio† | Illumination correction factor |
|---|---|---|---|---|---|
| $H^2(d,n)He^3$ | 4.5 | 12 | 100 | 1.11 | 1.06 |
| $H^2(d,n)He^3$ | 4.5 | 3 | 20 | 1.13 | 1.08 |
| $H^2(d,n)He^3$ | 7.5 | 12 | 100 | 1.22 | 1.10 |
| $H^2(d,n)He^3$ | 7.5 | 3 | 20 | 1.31 | 1.16 |

† Ratio of illumination at center of detector to that at the edge.

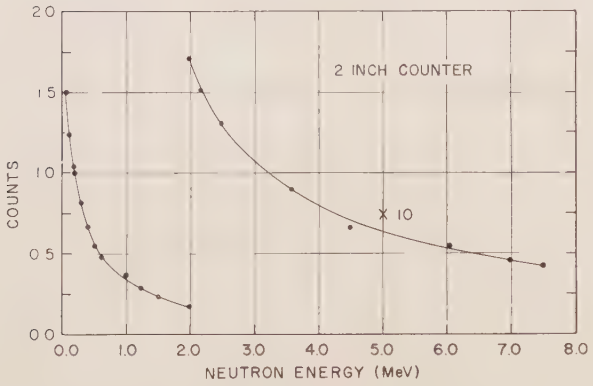


Fig. 3. Results with a 2 inch counter giving the counts per $10^6$ neutrons emitted from an isotropic point source 40 cm away.

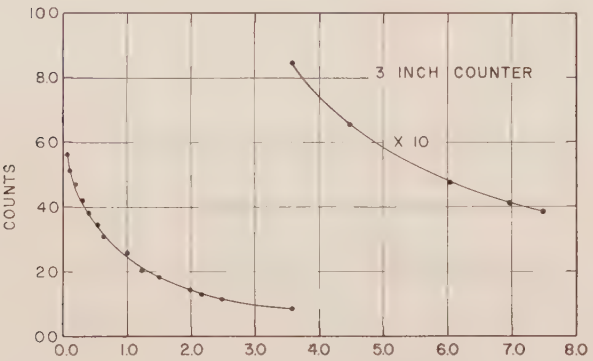


Fig. 4. Results with a 3 inch counter giving the counts per $10^6$ neutrons emitted from an isotropic point source 40 cm away.

the large counters at this distance were less than 10%. The corrected count rates at 40 cm were compared to the corrected count rates at 100 cm to check the accuracy of the illumination correction. It was found that, if the correction at 40 cm was less than 20%, the corrected count-rates agreed to 1%. Four of the largest illumination corrections are summarized in table 1. The ratio of the illumination at the center of the detector to that at the edge is given for each case.

The background due to scattering of source neutrons in the walls surrounding the target was investigated in detail. The closest scattering material was the floor, which was 12 feet from the target. The background was assumed to be constant within 100 cm from the target, and was determined by the variation of the counting rate as a function of distance from the target. The contribution of background neutrons was a negligible fraction of the total counts for the 5, 8, and 12 inch counters. The background ranged from 1.5% to 15% for the 2 inch counter, and from 0.7% to 6% for the 3 inch counter; the larger backgrounds were obtained at the higher neutron energies.

A long counter was used in conjunction with the known energy variation of the source reaction cross sections to determine the relative source strength of the calibration reactions. The relative long counter efficiency as a function of energy was taken from Allen *et al.*[4]). This relative long counter efficiency was experimentally compared with the variation in the $H^2(d,n)He^3$ cross section from 4.5 to 7.5 MeV. The relative efficiency and cross section agreed to $\pm 3\%$. The error in the relative long counter efficiency in the energy range from 0.1 MeV to 7 MeV is estimated to be $\pm 4\%$. The absolute long counter efficiency to $\pm 5\%$, was obtained using a calibrated Pu-Be source.

In addition to measurements of the sphere counting rates using neutrons from charged particle reactions, the count rates were measured

using thermal neutrons from the graphite column of the Rice Aerojet General 211 reactor. Data taken with the fast chopper at the Materials Testing Reactor† determined the shape of the counting rate curves of the 2 and 3 inch counters in the energy region around 300 eV. This data was very useful when estimating the low energy behavior of the counting rates.

The counting rate due to an isotropic source 40 cm from the center of the spherical counter is shown as a function of the energy of the incident neutrons in fig. 3 through 8. Above 50 keV, the counting rates of the 2 and 3 inch diameter counters decrease rapidly as the energy of the neutrons is increased. The counting rates of the larger counters first increase. reach a maximum, and then decrease. The reduced counting rate of the large spheres at low neutron energies is due to capture of thermalized neutrons in the hydrogen of the moderator. Low energy neutrons, requiring relatively few collisions to be thermalized, are thermalized near the surface of the spherical moderator. Consequently, in the larger spheres, the neutrons must traverse a longer path after thermalization, and they are more likely to be captured before reaching the $Li^6I$ crystal. The complicated structure in the curves shown in figs. 6, 7, and 8 for the 8 inch and 12 inch counters in the neutron energy range 3 to 4 MeV is due to resonances in the elastic scattering cross section of carbon. Similar structure has been observed for a long counter[4]).

An estimate of the counting rates between the experimentally determined values at 0.025 eV and 50 keV is given (dashed curve) in fig. 8. The counting rate of the 3 inch counter attains its maximum at about 300 eV neutron energy, but the absolute efficiency was not determined at this energy. The curve for the 2 inch counter attains its maximum somewhat above thermal energy; this follows from the fact that the bare $Li^6I$ crystal gives 30% more counts in an isotropic flux of thermal neutrons than with the 2 inch polyethylene sphere surrounding it.

† The authors wish to thank the Atomic Energy Division of Phillips Petroleum Company for the use of the fast chopper.

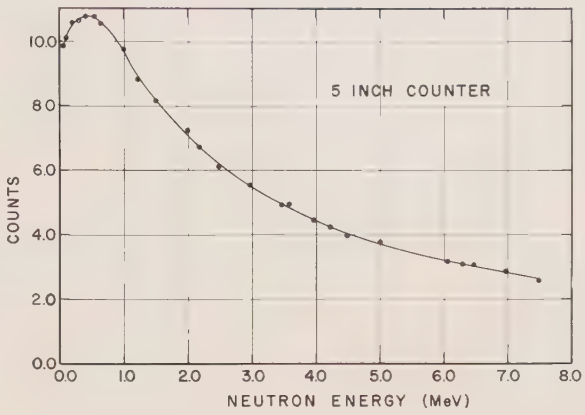


Fig. 5. Results with a 5 inch counter giving the counts per $10^6$ neutrons emitted from an isotropic point source 40 cm away.

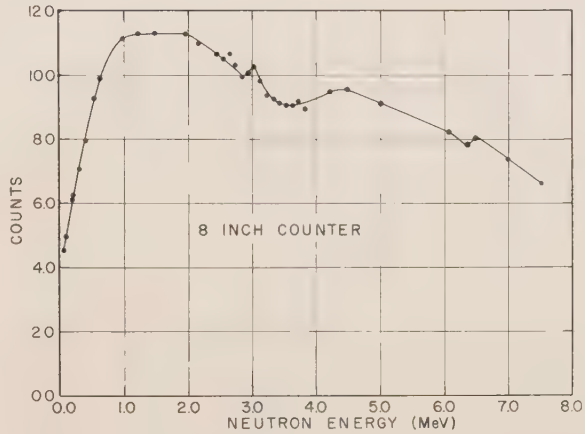


Fig. 6. Results with an 8 inch counter giving the counts per $10^6$ neutrons emitted from an isotropic point source 40 cm away.

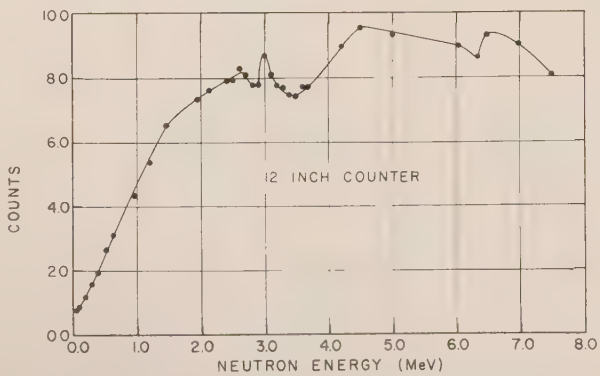


Fig. 7. Results with a 12 inch counter giving the counts per $10^6$ neutrons emitted from an isotropic point source 40 cm away.

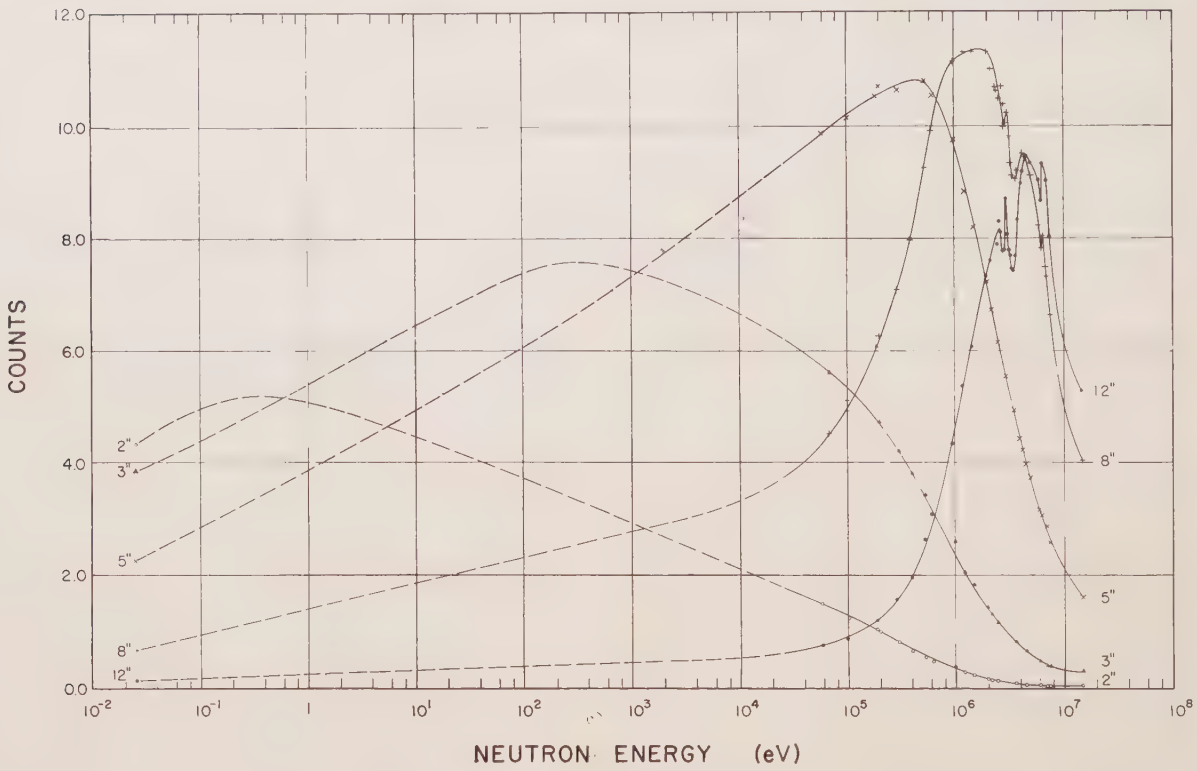


Fig. 8. Results with all counters giving the counts per $10^6$ neutrons emitted from an isotropic point source 40 cm away.

TABLE 2
Maxima of the counting rate curves

| Counter diameter (inches) | Position of maximum (eV) | Counts per $10^6$ neutrons† | Absolute efficiency†† in per cent |
|---|---|---|---|
| 2 | 0.3 | 5 | 0.5 |
| 3 | $3.0 \times 10^2$ | 8 | 0.3 |
| 5 | $4.5 \times 10^5$ | 10.8 | 0.172 |
| 8 | $1.7 \times 10^6$ | 11.3 | 0.069 |
| 12 | $5.0 \times 10^6$ | 9.4 | 0.025 |

† Counts per $10^6$ neutrons emitted from an isotropic source 40 cm away.

†† The percentage of the neutrons which strike the surface of the counter which result in a count.

Table 2 gives the maximum of the counting rate curve for each sphere and the position of the maximum. For comparison, the counting rate per $10^6$ neutrons emitted from a source 40 cm from the paraffin face of the long counter used at Rice is about 160. The $BF_3$ tube used in the Rice long counter is 1 inch in diameter, 34 cm long, and contains 96% $B^{10}F_3$ at 40 cm Hg pressure.

The errors in the counting rate curves between 0.050 and 7.5 MeV are of two types: absolute error due to uncertainty in the absolute calibration of the long counter ($\pm$ 5%), and relative errors, which include all other than absolute errors. On a relative basis, the principle source of uncertainty is the long counter efficiency as a function of energy ($\pm$ 4%). The statistical counting error was about 1% for all cases. Error in both the illumination and background corrections is estimated to be $\pm$ 1% for all except the 2 inch counter, for which the illumination correction error is negligible and the background correction error is estimated to be $\pm$ 2%. Consequently, the relative error of each curve is estimated to be less than $\pm$ 6%. At any incident neutron energy the ratios of the counting rates of the various counters was reproducible to $\pm$ 3%. The error of the data points at 0.025 eV and 15 MeV is estimated to be $\pm$ 10%.

The ratios of the counting rates of spherical

TABLE 3
Counter sensitivity

| Neutron energy (MeV) | Percent change in counter ratio corresponding to 1% increase in neutron energy | | | | | |
|---|---|---|---|---|---|---|
| | 12″ & 5″ counters | 12″ & 3″ counters | 12″ & 3″ counters | 8″ & 3″ counters | 8″ & 2″ counters | 5″ & 2″ counters |
| 0.10 | 0.29 | 0.46 | 0.56 | 0.36 | 0.46 | 0.27 |
| 0.50 | 0.88 | 1.23 | 1.56 | 0.84 | 1.16 | 0.67 |
| 1.00 | 1.26 | 1.58 | 1.79 | 0.71 | 0.93 | 0.53 |
| 2.00 | 1.01 | 1.30 | 1.58 | 0.79 | 1.06 | 0.57 |
| 5.00 | 0.53 | 0.68 | 0.83 | 0.42 | 0.57 | 0.30 |

counters of different size are sensitive functions of the neutron energy. The percentage change in the ratio of counts of several pairs of counters corresponding to a 1% change in neutron energy is shown in table 3. The counting ratio most sensitive to a change in neutron energy is that of the 12 inch to the 2 inch counter. The range of maximum sensitivity of the counting ratios for all the pairs of counters in table 3 is from 0.5 to 2 MeV.

TABLE 4
Counting rate for Pu-Be source
$(1.34 \pm 0.05) \times 10^6$ neutrons/sec.
Nearest scattering material 12 feet away

| Nominal counter diameter (inches) | Measured counter diameter† (inches) | Distance from counter to source (cm) | Counting rate (counts/sec) |
|---|---|---|---|
| bare | | 6.69 | 2.03 |
| 2 | 1.992 | 6.69 | 10.07 |
| 3 | 3.00 | 10.07 | 27.4 |
| 5 | 4.98 | 16.71 | 40.9 |
| 8 | 7.98 | 26.78 | 25.3 |
| 12 | 11.91†† | 40.00 | 9.15 |

† The density of the polyethylene used was 0.924 g/cm³.
†† The 12 inch counter was flattened on the bottom surface to facilitate mounting. The effective diameter given here compensates for the flattening.

For the convenience of those who might like to check the calibration of a similar set of counters, the counting rate of each counter at a specified distance from the center of a Pu-Be source is given in table 4. The distances were such that each sphere subtended the same solid angle from the source. The source strength was $(1.34 \pm 0.05) \times 10^6$ neutrons per second. The measured diameters of the polyethylene spheres are also given in table 4.

A quantity of incidental interest is the absorption of thermal neutrons by the spherical polyethylene moderators. The counting rate for thermal neutrons is given as a function of the diameter of the counter in fig. 9. About 30% of the incident thermal neutrons are absorbed before detection in the 2 inch diameter counter; whereas the 12 inch polyethylene sphere absorbs about 98% of the incident thermal neutrons.

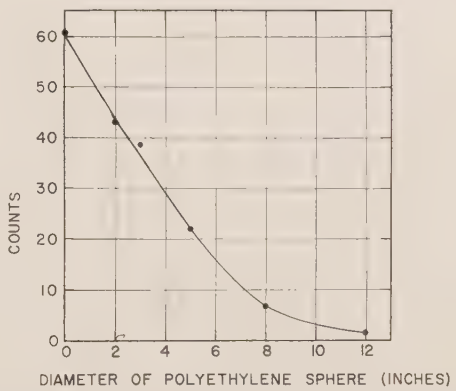


Fig. 9. Relative counting rates of the 2, 3, 5, 8, and 12 inch counters in a thermal neutron flux, showing absorption of the thermal neutrons.

Experiments to determine the energy distribution of neutrons from isotropic sources should be carried out with the source to detector distance as small as possible to reduce background

effects and increase the counting rate; but errors are introduced in applying the curves of fig. 3 through 8 if the solid angle subtended by the counter is too large. An experiment was performed using a Pu-Be source to determine the maximum solid angle that can be used without introducing error. The counting rate of the 12 inch counter was determined as a function of the distance to the source. It was found that the counting rate, after taking into account a background of 6% at 1 m, was proportional ($\pm$ 1%) to the total solid angle subtended by the 12 inch sphere, for distances greater than 40 cm. At a distance of 25 cm between the source and the center of the polyethylene sphere, the counting rate divided by the solid angle was 2.5% lower than at 40 cm, and at 20 cm the counting rate divided by the solid angle was 14% lower than at 40 cm. Hence, the 12 inch counter could be used at 30 cm without introducing an error greater than 1%. This distance corresponds to a half angle of 30°.

## 3. Application to Experiments

As a simple example of the use of the spherical counter, consider the case of two monoenergetic groups of neutrons of known energy but unknown intensities. For example, this situation occurs in neutron producing reactions where the emergent neutron can leave the residual nucleus in either its ground state or its first excited state. If the neutron groups have known energies, the relative intensities of the two groups can be determined from the counting rates in two different size counters. For example, if the two neutron energies are 0.5 and 4.0 MeV and the groups are of about equal intensity, then a 1% change in the ratio of the counting rates corresponds to a 1% change in the relative intensity.

The above method can be extended to determine the parameters of a continuous spectrum for which there is a theoretical or empirical form. If an assumed energy spectrum is multiplied by each of the counting rate curves of fig. 3 through 7 and the products are integrated over the energy range of interest, the result is a set of count rates for the particular spectrum that is assumed. If this procedure is carried out for several values of the parameters of the theoretical distribution, the parameters best fitting the observed counting ratios can be determined. A given spectrum fits the data if the calculated counting ratios fall within the experimental error for each independent sphere ratio. The best fitting spectrum is the one with the least root-mean-square deviation of the calculated ratios from the experimental ratios.

### 3.1. NEUTRONS RESULTING FROM PROTON BOMBARDMENT OF $C^{14}$

Neutrons produced in the reaction $C^{14}(p,n)N^{14}$ have been studied[9]) over the range of proton bombarding energies from 2.8 to 5.5 MeV using the polyethylene moderated neutron detector. Protons from the Rice 5.5 MeV van de Graaff accelerator were used to bombard a carbon target which was isotopically enriched to 25% $C^{14}$. The yield of monoenergetic neutrons was measured, using the 8 inch counter, from 2.8 MeV to the threshold for the second group of neutrons at 3.1 MeV. Between the neutron thresholds at 3.1 and 4.9 MeV, two monoenergetic groups of neutrons are energetically possible. The intensities of these two groups of neutrons were determined at 0° and 90° to the beam of protons from 3.4 to 4.9 MeV. For this purpose, the counting rate of the 8 inch counter at 20 cm from the target was obtained from 3.1 to 4.9 MeV. After removing the 8 inch counter, the 3 inch counter was positioned to subtend the same solid angle as the 8 inch at 20 cm, and the 3 inch counting rate was obtained. By using the same solid angle for each counter, effects due to rapid changes in the neutron angular distributions are eliminated. Analysis of the counting rates obtained using the known efficiencies of each counter shows that the ratio of the number of neutrons from the high energy group to the number of lower energy neutrons varies from 8.3 on the resonance at 3.40 MeV to 0.28 in a region where there were no resolved resonances.

[9]) Hanna, Bonner, Bramblett and St. Romain, to be published.

Above the threshold for the third group of neutrons, three counters were used to determine the intensities of the three groups of neutrons.

### 3.2. THE CONTINUOUS SPECTRUM OF NEUTRONS FROM $Rh^{103}(p,n)Pd^{103}$

The spectrum of neutrons resulting from bombardment of several intermediate weight nuclei with 5.30 MeV protons was investigated[10]). The counting rates of the 2, 3, 5, 8, and 12 inch diameter counters were obtained. Table 5 shows the

TABLE 5
Values of parameters required to fit experimental neutron spectrum from $Rh^{103}(p,n)$

| Counters used | Assumed spectrum | |
|---|---|---|
| | Evaporation $Ee^{-E/\tau}\tau$ (MeV) | Maxwellian $\sqrt{E}e^{-E/\theta}\,\theta$(MeV) |
| 12″ and 8″ | 0.582 | 0.792 |
| 12″ and 5″ | 0.592 | 0.844 |
| 12″ and 3″ | 0.581 | 0.856 |
| 12″ and 2″ | 0.591 | 0.912 |
| 8″ and 3″ | 0.577 | 0.908 |
| 8″ and 2″ | 0.593 | 0.983 |
| 5″ and 2″ | 0.587 | 1.042 |
| Average | 0.586 | 0.905 |

fit of the neutron spectrum from $Rh^{103}(p,n)Pd^{103}$ with two energy distributions having one unknown parameter: the evaporation spectrum, $E \exp(-E/\tau)$; and the Maxwellian distribution, $E^{\frac{1}{2}} \exp(-E/\theta)$. If the neutron spectrum is assumed to be of the evaporation form, the parameter, $\tau$, can be determined from the ratio of the counting rates of two counters. Since five sizes of counters were used, there are four independent determinations of $\tau$. If these independent determinations agree, the algebraic form assumed is correct. If they do not, another form must be chosen. The first column of table 5 shows the ratio under consideration, the second column gives the value of $\tau$ determined by the ratio. The average value of $\tau$ is 0.568 MeV and the largest deviation is 0.009 MeV, which is less than the estimated experimental error of about 0.014 MeV. It is concluded that the spectrum of neutrons from $Rh^{103}(p,n)$ fits the evaporation spectrum.

Another form that might fit the neutron spectrum is the Maxwellian distribution, with parameter $\theta$. The attempt to fit this spectrum is shown in the third column of table 5. This spectrum does not fit the experimental data. The values of $\theta$ determined by the ratios differ by as much as 0.14 MeV from the average of 0.90 MeV. The expected experimental error in this case is about 0.03 MeV. The ratios are listed in a meaningful order, starting with ratios of large counters at the top and ending with small counters at the bottom. When arranged in this order, a misfit to the neutron spectrum results in a trend in the values of the parameters indicated by the ratios. The trend for the Maxwellian form is apparent. Even though there are only four independent ratios, the use of more than four ratios in this manner makes the analysis easier. The evaporation and Maxwellian spectra are very similar distributions, and the differentiation between these two types by the spectrometer shows its inherent sensitivity.

### 3.3. ENERGY SPECTRA OF INELASTICALLY SCATTERED NEUTRONS

The energy spectra of neutrons inelastically scattered from Fe, Cd, Sn, Ta, and W have been investigated with the neutron spectrometer. Monoenergetic neutrons with energies of 1.00, 2.44, and 5.0 MeV were obtained with the Van de Graaff accelerator. These neutrons were scattered from samples which were placed at 0° to the bombarding beam. The dimensions of the scatterers were $1\frac{1}{2} \times 2\frac{3}{8} \times 2\frac{3}{8}$ inches. The neutron spectrometer was placed so that it counted neutrons which were scattered through an angle of 90° by the sample. The counter was shielded from the neutrons that came directly from the target. The number of counts due to neutrons scattered from the sample is equal to the difference of the counts with the scatterer in place and removed. Counts with the scatterer removed amounted to 35% to 60% of the number with a

[10]) Richard L. Bramblett and T. W. Bonner, Nuclear Physics **20** (1960) 395.

TABLE 6
Data on the energies of inelastically scattered neutrons

| Spherical counters | Energy of bombarding neutrons in MeV | | | | | | | | |
|---|---|---|---|---|---|---|---|---|---|
| | 1.00 | | | 2.44 | | | 5.0 | | |
| | 8/3 | 5/3 | 8/5 | 8/3 | 5/3 | 8/5 | 8/3 | 5/3 | 8/5 |
| Fe ratio† | 2.6 | 2.9 | 0.91 | 5.6 | 4.2 | 1.32 | 4.9 | 3.9 | 1.28 |
| $E_i$†† | 0.14 | 0.13 | 0.15 | — | — | — | 1.26 | 0.99 | 1.15 |
| $T$††† | — | — | — | — | — | — | 0.99 | 0.85 | 0.82 |
| Cd ratio | 3.2 | 3.3 | 0.98 | 3.6 | 3.3 | 1.09 | 4.1 | 3.5 | 1.17 |
| $E_i$ | 0.33 | 0.32 | 0.35 | 0.63 | 0.56 | 0.70 | 0.85 | 0.77 | 0.92 |
| $T$ | 0.18 | 0.26 | 0.15 | 0.43 | 0.42 | 0.43 | 0.61 | 0.62 | 0.60 |
| Sn ratio | 4.3 | 4.1 | 1.05 | 4.1 | 3.5 | 1.18 | 4.2 | 3.6 | 1.15 |
| $E_i$ | — | — | — | 0.69 | 0.60 | 0.80 | 0.86 | 0.84 | 0.90 |
| $T$ | — | — | — | 0.48 | 0.45 | 0.52 | 0.62 | 0.69 | 0.58 |
| Ta ratio | 2.6 | 3.0 | 0.87 | 3.0 | 3.1 | 0.97 | 3.5 | 3.3 | 1.05 |
| $E_i$ | 0.31 | 0.31 | 0.31 | 0.52 | 0.49 | 0.55 | 0.67 | 0.65 | 0.70 |
| $T$ | 0.15 | 0.22 | 0.13 | 0.33 | 0.36 | 0.32 | 0.45 | 0.50 | 0.42 |
| W ratio | 3.2 | 3.2 | 1.02 | 3.3 | 3.2 | 1.02 | 3.02 | 3.4 | 1.10 |
| $E_i$ | 0.57 | 0.44 | 0.70 | 0.53 | 0.49 | 0.57 | 0.74 | 0.70 | 0.78 |
| $T$ | 0.38 | 0.33 | 0.42 | 0.33 | 0.36 | 0.33 | 0.51 | 0.55 | 0.48 |

† The ratios listed are the experimental ratios of the counting rates in the 8, 5, and 3 inch spherical counters due to both elastically-scattered and inelastically-scattered neutrons. The statistical probable errors in the ratios ar 10%, 8% and 6% on the 1.00, 2.44, and 5.0 MeV data respectively.

†† $E_i$ is the indicated energy of the inelastically scattered neutrons in MeV.

††† $T$ is the evaporation temperature in MeV.

scatterer in place. Data were obtained with spherical counters with diameters of 8 inches, 5 inches, and 3 inches.

Since the sample scatters neutrons into the detector by both elastic and inelastic processes, analysis was necessary to separate the counts due to the two processes. The energy of the elastically scattered neutrons is known and the cross sections for elastic scattering at 90° and for inelastic scattering are also known. The indicated energy, $E_i$, of the inelastically scattered neutrons was obtained for each of the counting rate ratios: 8 to 3, 5 to 3, and 8 to 5. If the inelastically scattered neutrons all had the same energy, as would be the case for scattering by a single level, then the indicated energies would all have the same value. However, if the neutrons have a continuous evaporation spectrum, then the indicated energies from each of the ratios should differ. The nuclear temperature, $T$, which corresponds to the most probable neutron energy in an evaporation spectrum, was determined from each of the ratios. When the three calculated values of $T$ agree within the experimental error, the spectrum agrees with the theoretical evaporation spectrum.

The results of these experiments are summarized in table 6. The experiment with 1.00 MeV neutrons scattered from Sn serves as a check on the method, since there are no inelastically scattered neutrons. The observed counting ratios are those expected for elastically scattered neutrons. The inelastic scattering from Fe is from a single level at 0.845 MeV, and the calculated energy of the single group of inelastically scattered neutrons is 0.14 MeV. The experimental results with 1.00 MeV neutrons on Cd and Ta are similar in that a nearly constant indicated energy, $E_i$, is obtained. This shows that a large fraction of the neutrons are of the indicated

energies and the distribution does not approximate an evaporation spectrum. The results with W at this energy are consistent with an approximate evaporation spectrum with a nuclear temperature of 0.38 MeV.

The results at 2.44 MeV and 5.0 MeV for Cd, Sn, Ta, and W show that the distributions are close to evaporation spectra. In all of these cases the nuclear temperature increases with the bombarding energy of the neutrons as predicted by theory. The results with Fe at 5.0 MeV agree within the experimental error with an evaporation spectrum and a nuclear temperature of $0.91 \pm 0.10$ MeV.

### 3.4. PENETRATION OF 15 MeV NEUTRONS THROUGH A SHIELD

The energy spectrum of neutrons resulting from penetration of 15 MeV neutrons through a shield of concrete blocks has been determined. Neutrons were produced by the $T(d,n)He^4$ reaction, using the Texas Nuclear Corporation 2 MeV Van de Graaff accelerator. A wall, 40 cm thick, which was made of concrete blocks, served as a neutron shield. The counter was positioned 6.41 m from the target and 30 cm behind the concrete wall. The other walls of the target room were also about 6 m from the target, which was 3.5 m above a concrete floor. The counting rates of the 12, 8, 5, 3, and 2 inch counters were obtained. The results of these measurements were analyzed to determine the neutron spectrum. Agreement with the experimental data was obtained with a neutron intensity inversely proportional to the neutron energy from about 0.5 eV to 2.5 MeV. In this energy range there are 90 neutrons/cm$^2$-sec. Below 0.5 eV, there are 50 neutrons/cm$^2$-sec. From 2.5 to 15 MeV neutron energy there are 32 neutrons/cm$^2$-sec. The distribution of the 32 neutrons/cm$^2$-sec over the latter energy range is not accurately determined by this experiment. Both a spike of 14–15 MeV neutrons and a flat distribution from 2.5 to 15 MeV fit the data. The actual spectrum probably lies between these two extremes.

The absolute yield of 15 MeV neutrons from the primary source was about $1.0 \times 10^9$ neutrons/sec. Without a shield, the flux of 15 MeV neutrons at the counter would be 194 neutrons/cm$^2$-sec. The number of neutrons above 2.5 MeV was reduced by the concrete wall to $\frac{1}{6}$ of this value, but comparison with the total flux of neutrons behind the shield shows that nearly all of the 15 MeV neutrons penetrate the shield, although at a much reduced energy.

### 3.5. BACKGROUND NEUTRONS FROM A NUCLEAR REACTOR

Measurements were made on the background neutrons in a working area of the Materials Testing Reactor at Idaho Falls, Idaho. The counting rates of the 8, 5, 3, and 2 inch counters were obtained under normal operating conditions of the reactor, and at a power level of 25 megawatts. The results of this experiment indicated that the number of neutrons per unit energy internal is inversely proportional to the neutron energy from about 0.5 eV to 0.9 MeV and the intensity above 0.9 MeV decreases rapidly. The neutron flux below 0.5 eV was 15 neutron/cm$^2$-sec as compared with 20 neutrons/cm$^2$-sec in the neutron energy range from 0.5 eV to 0.9 MeV. An independent measurement of the number of thermal neutrons was made by covering the counters with cadmium about 1 mm thick. This latter determination of the number of thermal neutrons agreed with the determination made with the counting ratios to within the experimental error of about 20%.

### 3.6. BACKGROUND NEUTRONS IN A VAN DE GRAAFF TARGET AREA

The neutron spectrum resulting from scattering of fast neutrons by the floor and walls surrounding the Rice Van de Graaff accelerator has been determined using the polyethylene moderated neutron detector. The primary source of neutrons was from the break-up of deuterium by proton bombardment at an energy of 4.5 MeV. The primary neutron spectrum at this bombarding energy ranges from 0 to 2.0 MeV with an average energy of about 0.7 MeV. The yield of neutrons from this reaction decreases very rapidly with angle; at 90° to the

incident beam of protons, the yield is less than 2% of that at 0°. The absolute yield from the primary source was $1.4 \times 10^8$ neutrons/sec. The counting rate of each spherical counter due to background neutrons was determined from the counting rates at two distances from the target at 90° to the beam of bombarding protons. That portion of the count not decreasing proportional to the solid angle subtended by the counter from the source was due to background neutrons. At a distance of 100 cm, over 75% of the counts in each sphere was due to background neutrons. Data was obtained with the 2, 3, 5, 8, and 12 inch counters. The results indicate that the background neutron intensity is inversely proportional to the neutron energy from 0.5 eV to 0.1 MeV. In this energy interval there are 22 neutrons/cm²-sec. There are 7 neutrons/cm²-sec in the energy range below 0.5 eV. From 0.1 MeV to 0.7 MeV there are 11 neutrons/cm²-sec. The distribution of the 11 neutrons/cm²-sec over the latter energy range is not accurately determined by this experiment. Both a spike of 0.5 to 0.7 MeV neutrons and a uniform distribution from 0.1 to 0.7 MeV fit the data. The actual spectrum probably lies between these two extremes.

### 3.7. APPLICATION OF THE COUNTER TO NEUTRON DOSIMETRY

Since the neutron detector described herein is sensitive to all energies of neutrons, it might well be applied to problems in neutron dosimetry. For example, the previously discussed neutron spectrum in a working area at the Materials Testing Reactor can be converted into units of radiation exposure using the published data[11]) on the relative biological effectiveness of neutrons. Using this data, the radiation exposure to neutrons was found to be 0.54 millirem per hour, of which 0.06 was due to thermal neutrons.

For some purposes, a neutron counter whose response is the same as the sensitivity of the human body to neutrons would be very useful. Such a counter might be used to monitor neutron exposure without regard to the actual spectrum of neutrons. The 12 inch diameter counter has approximately the same response to neutrons as the human body from thermal neutron energy to 15 MeV. This is shown in table 7, which gives, as a function of neutron energy, the number of counts in the 12 inch counter per millirem of neutron exposure. The variations in the number of counts per millirem given in table 7 are not much greater than the uncertainty in the neutron flux equivalent to one millirem.

TABLE 7
Response of 12 inch counter to neutron dose

| Neutron energy (MeV) | Neutrons equivalent to 1 millirem† ($10^3$ neutrons/cm²) | Response of 12 inch counter ($3.2 \times 10^3$ counts/millirem) |
|---|---|---|
| $2.5 \times 10^{-8}$ | 965 | 0.80 |
| 0.0001 | 720 | 1.62 |
| 0.01 | 430 | 1.31 |
| 0.1 | 115 | 0.62 |
| 0.5 | 43 | 0.62 |
| 1.0 | 26 | 0.72 |
| 2.0 | 29 | 1.26 |
| 3.0 | 26 | 1.23 |
| 15.0 | 25 | 0.77 |

† Taken from ref.[11]).

**Acknowledgement**

The authors would like to express their appreciation to Messrs. F. St. Romain and J. Hanna for their help in performing the experiments, and to Dr. T. W. Leland for his help with the experiments with the Rice reactor.

[11]) U.S. National Bureau of Standards Handbook No. 63 (1957).

NUCLEAR INSTRUMENTS AND METHODS 9 (1960) 13–20; NORTH-HOLLAND PUBLISHING CO.

# NOTES ON A FAST TIME ANALYZER FOR SHORT LIFETIME MEASUREMENTS

M. BONITZ† and E. J. BERLOVICH

*Physico-Technical Institute of the USSR Academy of Sciences, Leningrad*

Received 27 June 1960

A critical comparison of the single- and multichannel method for short lifetime measurements of excited states in nuclei is given. A new time-to-height converting system based on the pulse overlap principle of a biased diode discriminator, has been constructed. The time resolution of the prompt $\gamma-\gamma$ coincidence curve from a $Co^{60}$ source is $5 \times 10^{-10}$ sec. The influence of the energy of the coinciding particles on the performance of the time analyzer, and a stability control method are discussed. Experimental results are given for the following excited levels: 145 keV in $Pr^{141}$, $T_{\frac{1}{2}} = (2.0 \pm 0.2) \times 10^{-9}$ sec; 279 keV in $Tl^{203}$, $T_{\frac{1}{2}} = (2.9 \pm 0.2) \times 10^{-10}$ sec and 411 keV in $Hg^{198}$, $T_{\frac{1}{2}} = (3.5 \pm 0.8) \times 10^{-11}$ sec.

## 1. Introduction

The classical method of Graham, Bell and Petch[1]) for measuring the lifetimes of excited nuclear states with the help of delayed coincidences is a single-channel method. Since measurements of the individual points of the coincidence curve must be carried out successively, they take up much time. Furthermore because of this high stability of the electronic equipment is indispensible and it is difficult to investigate short-living isotopes.

After Neilson and James[2]) introduced the principle of time-to-amplitude conversion into the neutron time-of-flight spectrometry, Jones and Warren[3]) first used this principle in short lifetime measurements. If we convert the time intervals to be measured into corresponding amplitudes of electrical pulses, we get a multichannel method, with the help of which one can read all the points of the coincidence curve simultaneously, using an ordinary kicksorter. This disminishes the requirements on the stability of the equipment, greatly speeds up the measuring procedure and makes the investigation of short-living isotopes easier.

The principle of time-to-amplitude conversion, which can be realized in diverse ways[2–7]), was later used in many papers both in neutron time-of-flight spectrometry[8–12]) and in measurements of the lifetime of excited nuclear states[3,13–16]). Besides the above mentioned advantages, the switch-over from the single-channel method to the multi-channel one for measuring of lifetimes, which we will concern ourselves below, involves a number of problems, which have little been discussed in literature. Because of this the first part of this paper will be devoted to a critical comparison of the two methods. In the second part we formulate the requirements raised to a multi-channel time analyzer and describe a new simple system which completely satisfies these requirements. The third part contains some results of lifetime measurements in the range $10^{-11}$–$10^{-9}$ sec to illustrate the measuring possibilities of the instrument.

† On leave from the Technische Hochschule Dresden, German Democratic Republic.

[1]) R. E. Bell, R. L. Graham and H. E. Petch, Can. Journ. Phys. **30** (1952) 35.

[2]) G. C. Neilson and D. B. James, Rev. Sci. Instr. **26** (1955) 1018.

[3]) G. Jones and J. B. Warren, Journ. Sci. Instr. **33** (1956) 429.

[4]) C. Cottini and E. Gatti, Nuovo Cimento **4** (1956) 1550.

[5]) H. W. Lefevre and J. T. Russell, Nucleonics **16** (1958) 57.

[6]) Par J. Samueli and A. Sarazin, Journ. Phys. Rad. **19** (1958) 109 A.

[7]) Par S. Gorodetzky, Th. Muller, M. Port, G. Bergdolt and J. Graff, Journ. Phys. Rad. **20** (1959) 49 A.

[8]) Par E. Rémy and K. Winter, Journ. Phys. Rad. **18** (1957) 112A.

[9]) G. C. Neilson, W. K. Dawson and F. A. Johnston, Rev. Sci. Instr. **30** (1959) 963.

## 2. The Differences between the Single-Channel and Multi-Channel Method

### 2.1. TIME RESOLUTION

The most important characteristic of a coincidence circuit is its time resolution. This time resolution is mainly determined by the time properties of the scintillators, by the time dispersion of light collecting, the photomultiplier transit time, etc.

Bay[17]) showed that the magnitude of the resolution is of the same order as the length of the coinciding pulses. In the single-channel method improvement of the resolution is limited by the fact that it is impossible to diminish the rise time of the photomultiplier output pulses infinitely. Because of this, shorter clipping of the coinciding pulses leads to a reduction of their amplitude and consequently, at a given discrimination level of the coincidence circuit, to a loss in efficiency of the coincidence counting.

In contrary to this, in the multi-channel method, the resolution does not depend on the length of the coinciding pulses: this length is often about a hundred times larger than the resolution. Hence we think that Sunyars[16]) opinion is wrong, when he states, that the resolution of his instrument is determined by the length of the coinciding pulses.

So the multi-channel method does not impose such rigid requirements on the rise time of the photomultiplier output pulses as the single-channel method does.

### 2.2. EFFICIENCY OF COINCIDENCE COUNTING

In the single-channel method it is possible to improve the time resolution only by increasing the level of discrimination. This means a loss in the efficiency of coincidence counting, since not every pair of correlated pulses will be registered because of their time dispersion (for a given energy range).

In contrary to this we always have full efficiency in the multi-channel method, since every pair of correllated pulses will be registered by the kicksorter in that channel, which corresponds to the relative time delay between the coinciding pulses.

The method of restricting the allowed region of amplitudes after the coincidence act, used in ref.[7]), does not really improve the resolution, since it is not possible to do practical experiments with such a system, because one cannot observe the shift of the curves or the exponential form of the coincidence curve. Further, as opposed to Veretennikov and Averchenkov[12]), we think that it makes sense to speak about efficiency of coincidence counting only for given energy ranges of the coinciding particles.

### 2.3. TIME SCALE

Time calibration in the single-channel method is determined by the electrical properties (phase velocity) of the delay line on which the coincidences take place. The position of the coincidence curve (for prompt coincidences) depends only on the front of the coinciding pulses. If one decreases (increases) the rise time of the coinciding pulses at the same time and to the same degree, the position of the curve (for instance, the maximum) will not change.

In the multi-channel method the time scale is not a constant value and depends, for instance, on the rise time of the coinciding pulses i.e., on the energy of the coinciding particles, on the properties of the time-to-amplitude converter and on the amplification of the converter output pulses. Even simultaneous decreasing (increasing) of the coinciding pulses rise time leads to a change in the position of the coincidence curve. Hence the time scale is a magnitude which needs a new determination in new experimental conditions, especially for measuring very short lifetimes.

[10]) J. B. Garg, Nucl. Instr. and Methods **6** (1959) 72.

[11]) R. L. Chase and W. A. Higinbotham, Rev. Sci. Instr. **28** (1957) 448.

[12]) A. I. Veretennikov and V. Ya. Averchenkov, PTE **3** (1958) 48 (In Russian).

[13]) J. B. Warren and G. Jones, Bull. Am. Phys. Soc. **5** (1958) 327.

[14]) R. E. Green and R. E. Bell, Nucl. Instr. **3** (1958) 127.

[15]) A. G. Khapakhpashev and E. M. Center, JETP **37** (1959) 991 (In Russian).

[16]) A. W. Sunyar, Proc. of the Second UNO-Conference of Peaceful Uses of Atomic Energy, Vol. **14** (1958) 347.

[17]) Z. Bay, IRE Transactions of Nuclear Science vol. NS-3 (1956) 12.

### 2.4. SINGLE-REJECTION RATIO

In the multi-channel method the single-rejection ratio is not a constant and depends on the time delay between the coinciding pulses. The larger this delay, the better will be the single-rejection ratio. We will turn attention to this circumstance once more below (see 3.2.). Our definition differs from the usual one (see, for instance, Bay[17])) since our coinciding pulses have constant amplitude. However our definition of the single-rejection ratio as a doubles: singles ratio, i.e. as the ratio of the converter output pulses for coinciding and single input pulses correspondingly, is also a good characteristic of the properties of the coincidence detecting element.

## 3. Notes on a New System for Measurements of Short Lifetimes

### 3.1. REQUIREMENTS TO A TIME ANALYZER

A fast time analyzer must satisfy the following requirements:

(3.1a) Linearity in the measuring range.

(3.1b) Increasing of the converter output pulses when the delay between the coinciding pulses increases.

(3.1c) A single-valued relation of the converter output pulses to the delay between the input pulses.

(3.1d) A handy way of determining the time scale.

(3.1e) High stability and a possibility to control this stability.

In the most commonly used time-to-amplitude conversion systems, pulses with standard length and amplitude pass to the grids of a gated beam tube[2]) or to a crystal diode[3]). In both cases the output signal from the converter element on a definite part of the calibration curve is linearly related to the time overlap of the input pulses. Thus the requirement (3.1a) is fulfilled. Out of these two systems we chose the diode, because using it, it is very easy to satisfy the other requirements. A further principal advantage of the diode will be discussed below.

One can satisfy the condition (3.1b) by introducing a certain constant delay between the coinciding pulses, as was done by Green and Bell[14]): the maximum amplitude of the converter output corresponds to the maximum delay between the input pulses. Furthermore, these authors introduced a supervisory coincidence circuit, which ensures the fulfilment of the requirement (3.1c) and at the same time reduces the number of the chance coincidences twice. In the Green and Bell system (supervisory coincidence circuit and converter) however, it is necessary to form four pulses of different length. We will show (see 3.2), that one can ensure that the converter and supervisory coincidence circuit will carry out their functions with the help of only two pulses of equal length, if one uses a crystal diode as the converting element, instead of a gated beam tube, as it did Green and Bell.

So as to satisfy requirement (3.1d) we will use a variable delay line, analogous to that, described by Graham, Bell and Petch[1]), with the difference, that the pulse clipping is not performed there where the coincidences take place, but before the pulses pass to the line.

We will discuss the fulfilment of the requirement (3.1e) in 3.3.4 and 3.3.5.

### 3.2. DESCRIPTION OF THE CONVERTER

On fig. 1 the pulses A and B, the time delay between which is to be measured pass to a delay line of the spiral type (the full delay is about $10^{-7}$ sec).

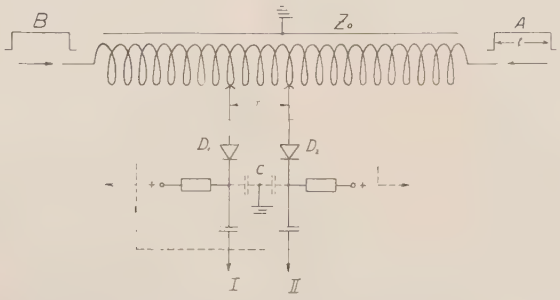


Fig. 1. Principal scheme of the time-to-amplitude converter and supervisory coincidence circuit. A,B-coinciding pulses of the length $l$; $Z_0$-characteristic impedance of the spiral type delay line; $D_1$-crystal diode of the time-to-amplitude converter; $D_2$-crystal diode of the supervisory coincidence circuit; $r$-time distance between the diodes $D_1$ and $D_2$; $C$-stray capacities; I,II-outputs to the cathode followers.

The diodes $D_1$ and $D_2$ of the type Д 2B perform the converter and supervisory coincidence circuit correspondingly. Their cathodes are biased by a positive voltage, so that single pulses do not pass. (In fact a part of the single pulses always does pass through the diode, because of its capacity and finite back resistance.) The diode $D_2$ is placed in the middle of the delay line,

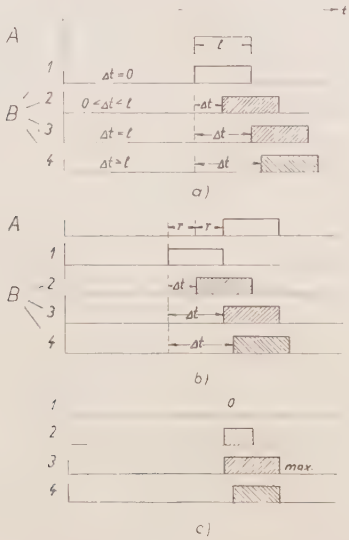


Fig. 2. Time sequence of the pulses A and B for different time delays $\Delta t$ between them, fig. 2a—at the converter, fig. 2b—at the supervisory coincidence circuit. Fig. 2c-overlap of the pulses A and B at the converter. $t$-time; $l$-length of the pulses A and B.

the diode $D_1$ is shifted by a time distance $r$. In our case $D_1$ lies to the left of $D_2$, because we want to investigate processes in which pulse A arises earlier than pulse B.

Such an arrangement of the diodes on the delay line ensures the most simple fulfilment of the conditions (3.1b) and (3.1c). This is illustrated by fig. 2: fig. 2a and fig. 2b show the time sequence of the pulses A and B at the supervisory coincidence circuit ($D_2$) and at the converter ($D_1$) correspondingly, fig. 2c shows the overlap at the converter for four delays $\Delta t$ between the pulses A and B: 1. $\Delta t = 0$; 2. $0 < \Delta t < l$; 3. $\Delta t = l$ and 4. $\Delta t > l$. $l$ is the length of the pulses A and B.

The coincidence circuit ($D_2$) gives its output pulses for delays $-l < \Delta t < l$ and the converter for $0 < \Delta t < 2l$. The requirement (3.1c) means that one must rule out the output pulses of the converter for $l < \Delta t < 2l$. This requirement is fulfilled, since the supervisory coincidence circuit does not give any output pulses for such delays and the outputs of $D_1$ and $D_2$ are subsequently connected in coincidence.

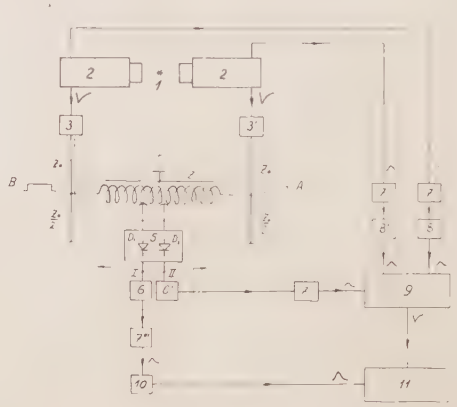


Fig. 3. Block-scheme of the time analyzer. 1-source under investigation; 2,2′-photomultipliers; 3,3′-valve limiter stages, which form a standard amplitude of the pulses A and B; 4-spiral type delay line with the characteristic impedance $Z_0$. Clipping of the pulses A and B to their length $l$ is carried out by short-circuited cables with the characteristic impedance $\frac{1}{2}Z_0$. 5-system converter—supervisory coincidence circuit with the diodes $D_1$ and $D_2$ (see fig. 1); 6,6′-cathode followers; 7,7′, 7″, 7‴-amplifiers; 8,8′-differential discriminators; 9-triple coincidence circuit, the output pulse of which gates the kicksorter; 10-constant delay, matching the time sequence of the gating pulse and the converter output pulse at the kicksorter (11).

The fact, that the supervisory coincidence circuit gives an output signal for delays $-l < \Delta t < 0$ (only chance coincidence pulses can have such delays) leads to the opening of the kicksorter (see block-scheme fig. 3) and the registration of single pulses, which are just passing through the converter diode $D_1$. In such experiments when it is necessary to work with a bad single-rejection ratio, these single pulses can distort the real coincidence curve. Thus it is necessary to carry in mind, that increasing $l$ in order to enlarge the linearity region of the converter, one increases the rate of chance coincidences, corresponding to the delay range $-l < \Delta t < 0$. This means that one should not take $l$ larger than is forced to by the concrete requirements of the given experiment. The value $r$ should be a little less than $\frac{1}{2}l$, so that the

converter output pulse for the delay $\Delta t = 0$ should already not be zero.

Fig. 2 shows the performance of the time-to-height converter in a much simplified aspect. The finite rise time of the pulses A and B is not taken into account. However it is necessary to allow for this finite rise time so as to understand the performance of the instrument correctly and we will return to this question in 3.3.3.

The described system is very handy for continuous introduction of delays from $10^{-11}$ sec to several nanoseconds within $10^{-11}$ sec. It is easier to satisfy the condition (3.1d) in this way than by introducing cable segments. To introduce a delay between the pulses A and B one has to move the system of diodes $D_1$ and $D_2$ along the delay line as far as necessary; this does not change the distance $r$ between the diodes.

The system "delay line-diodes" is the principal part of the instrument, the block-scheme of which is given in fig. 3. The block-scheme fig. 3 differs from the usual fast-slow coincidence systems only by the fact, that the pulse gating the kicksorter is formed by the joint action of two side channels (containing differential discriminators) and the supervisory coincidence circuit.

### 3.3. PERFORMANCE OF THE TIME ANALYZER

#### *3.3.1. Self-coincidences*

Fig. 4 shows the "self-coincidence" curve: output pulses from one photomultiplier pass to both limiters and consequently the pulses A and B always come to the inlet of the delay line simultaneously.

The pulse gating the kicksorter is delivered from the output of the corresponding differential discriminator, the window of which in our case was set at the hard part of the compton distribution in a stilben crystal, due to gamma quanta from a $Co^{60}$ source. The crystal occupied only the central part of the photocathode of the photomultiplier ФЭУ-33, the width of the crystal was 3 mm. The finite half-width of the self-coincidence curve is determined by:

a. The intrinsic electronic resolution of the instrument; b. The rise time dispersion of the photomultiplier output pulses, due to the time dispersion of the processes in the crystal and the transit time of the electrons in the photomultiplier.

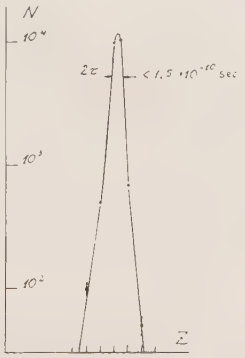


Fig. 4. Curve of self-coincidences in a half-logarithmic scale. $N$-number of coincidences; $Z$-kicksorter channel number; channel width: $2.11 \times 10^{-10}$ sec.

The half-width, which was less than $1.5 \times 10^{-10}$ sec, increased to $3.5 \times 10^{-10}$ sec, when we took a crystal of the size 30 × 30 mm.

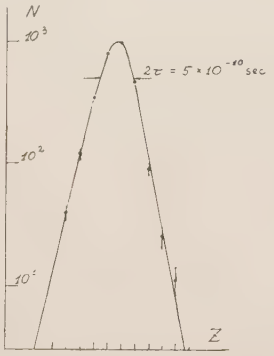


Fig. 5. Curve of prompt coincidences of $\gamma$-cascade quanta from a $Co^{60}$ source in a half-logarithmic scale. $N$-number of coincidences; $Z$-kicksorter channel number; channel width: $1.57 \times 10^{-10}$ sec.

#### *3.3.2. Prompt coincidences*

The prompt coincidence curve for cascade $\gamma$-quanta from a $Co^{60}$ source, obtained under the same conditions as the curve in fig. 4, is shown in fig. 5. One does not get such a good time resolution, if one uses greater crystals and passes on to smaller particle energies.

When measuring the lifetimes of excited states of nuclei, the energies are given and the size of the crystals depends on that loss of radiation measuring efficiency, which is still compatible with a reasonable duration of the experiment.

*3.3.3. Influence of the finite rise time of the photomultiplier output pulses*

When passing to smaller energies of the ionizing radiation the rise and fall-off time of the pulses A and B increase, because the amplitude of the photomultiplier output pulses decreases. Besides this the time dispersion of these pulses increases. These circumstances lead to the following effects:

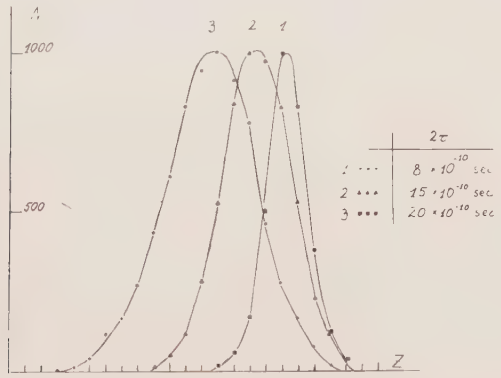


Fig. 6. Dependence of position and width of prompt coincidence curves on the energy of the coinciding particles. $N$-number of coincidences; $Z$-kicksorter channel number; channel width about $2.6 \times 10^{-10}$ sec. Energy intervals of the coinciding particles: $>$ 1 MeV (curve 1), 300–500 keV (curve 2) and 150–300 keV (curve 3). Length of the pulses A and B: $10^{-8}$ sec.

a. The overlap of the pulses A and B and hence the amplitude of the converter output pulses decreases. In the consequence we get a shift of the coincidence curve "to the left".

b. The coincidence curves become broader, the resolution of the instrument decreases.

All this is illustrated in fig. 6. Each of the curves 1, 2, 3 has a somewhat different time scale.

With the increasing of the length $l$ of the pulses A and B this effect of a "shift to the left" decreases, because the relative portion of the frontal part of the pulses A and B diminishes. However, the increasing of $l$ is accompanied by an increasing of the chance coincidence rate.

It follows from the stated above, that the resolution and time scale of the instrument are not constant values and should be determined separately for every experimental combination of the energies of coinciding particles.

*3.3.4. Stability*

All the time analyzer elements should be well stabilized. Special attention should be payed to the constancy of the temperature of the diode converter and the amplitudes of the pulses A and B.

If one stabilizes the temperature of the diode converter within $\pm \frac{1}{2}$°C, the time instability during 24 hours will be less than $(2\text{–}5) \times 10^{-11}$ sec. The time instability, due to changes of the current in the limiter stages (containing pentodes 6Ж 9*П*), which determine the amplitudes of the pulses A and B, is of the same order. The current (about 17 mA) can be well stabilized by applying negative feedback.

*3.3.5. Control of the performance stability. Method of singles control*

Even if the temperature of the diode and the current in the limiter stages are well stabilized, there can be additional instability due to alterations of the quality of the contact on the delay line, of the performance of the converter diode and of the kicksorter itself. Hence it is desirable to have a method by which one could simply and quickly control the performance stability of all the elements of the time analyzer, including the kicksorter.

We use the following method, based on the fact, that because of the finite capacity and back resistance of the converter diode, single pulses do pass to the input of the kicksorter, but their amplitude is of course much smaller than that of the coincidence output pulses. In order to analyze the amplitude distribution of the single pulses too, we amplify them a little and gate the kicksorter by the output pulses from the differential discriminator in that side channel, the single pulses of which are to be controlled. We have proved experimentally, that if the single pulses curves on the kicksorter show a stable position the coincidence curve will stay in an unchanged position too. Factors essentially affecting shape and position of the single pulses curves are: intensity differences between comparison source and source under investigation (see 4.2.), and differences in the form of their spectra within the

windows set in the side channels. To exclude possible instrumental time delays due to these factors, it is practically sufficient to take equal over-all intensities and to choose such window positions (equal for both sources), that shape and position of the single pulses curves corresponding to the same side channel window were the same for both sources.

One can add the following notes to this method, which was used in the measurements described in 4.2:

a. The single pulses curve can be checked in a few seconds. The method is especially handy, if the kicksorter gives its indications on an oscilloscope screen, as in the analyzer A *И*-100, which we used.

b. The method gives the simplest possibility to satisfy a condition which has been repeatedly expressed[16,18]: the spectra within the windows of the side channels should be kept identical during lifetime measurements. In general, one can satisfy this condition only approximately, since the forms of the spectra are given and cannot be changed. Usually one takes narrow energy intervals (otherwise the coincidence of the centroids of these intervals is not ensured). Using the method described above, one can use broader energy intervals. The only condition which one has to satisfy, is to bring to congruity both shape and position of the single pulses curves.

c. Using this method it is easy to estimate the time qualities of photomultipliers. As is generally known, the rise time of the output pulses is an essential parameter, characterizing the time qualities of a photomultiplier. The diode converter is just such an element that responds to changes in the rise time of pulses, passing on to it, by changing the amplitude of its output pulses. A photomultiplier that has a shorter rise time and better time dispersion properties, gives a narrower single pulses curve.

## 4. Lifetime Measurements

### 4.1. EXPONENT METHOD

Fig. 7 illustrates the determination of the mean lifetime of the 145 keV state of the $Pr^{141}$ nucleus by measuring $\beta\gamma$-coincidences with a $Ce^{141}$ source. The length of the pulses A and B in this measurement was $2 \times 10^{-8}$ sec. The time scale was determined by shifting the curve of prompt $\beta\gamma$-coincidences from a $Co^{60}$ source, introducing a definite time delay between the coinciding pulses. The energy intervals for the source $Co^{60}$ and the investigated cource $Ce^{141}$ were chosen the same for both sources. The exponent method is the simplest one, because one can obtain the halflife of the investigated state directly from the curve obtained by the

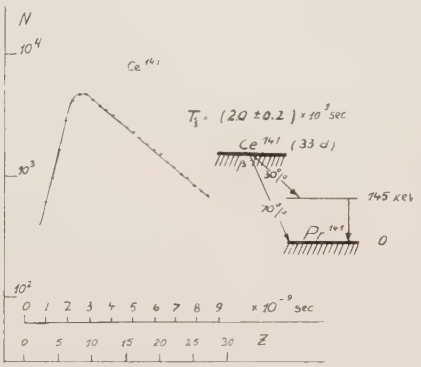


Fig. 7. Lifetime determination from exponential decay of the coincidence curve. $Ce^{141}$ source, $\beta\gamma$-coincidences. $N$-number of coincidences in a logarithmic scale; $Z$-kicksorter channel number; length $l$ of the pulses A and B: $2 \times 10^{-8}$ sec.

analyzer. The result for the halflife $T_{\frac{1}{2}} = (2.0 \pm 0.2) \times 10^{-9}$ sec is in agreement with published results: $T_{\frac{1}{2}} = 2.0 \times 10^{-9}$ sec[18]), $T_{\frac{1}{2}}\} = (1.9 \pm 0.2) \times 10^{-9}$ sec[19]) and $T_{\frac{1}{2}} = (2.0 \pm 0.3) \times 10^{-9}$ sec[20]).

### 4.2. CENTROID SHIFT ANALYSIS

Determining the lifetime of the 279 keV excited state of the $Tl^{203}$ nucleus (fig. 8), which in view of its shortness can be only done by comparison with a prompt source (in our case $Co^{60}$), we payed attention to the following conditions:

a. Both sources had the same intensity, $10^4$ pulses/sec in the $\gamma$-channel, $2 \times 10^4$ pulses/sec in the $\beta$-channel. This measure was necessary, because different intensities can lead to different

[18]) E. J. Berlovich, Izvestia ANSSSR, Phys. Ser. **21** (1956) 1438 (In Russian).
[19]) H. de Waard and T. Gerholm, Nucl. Phys. **1** (1956) 281.
[20]) F. Metzger, Phys. Rev. **99** (1955) 613.

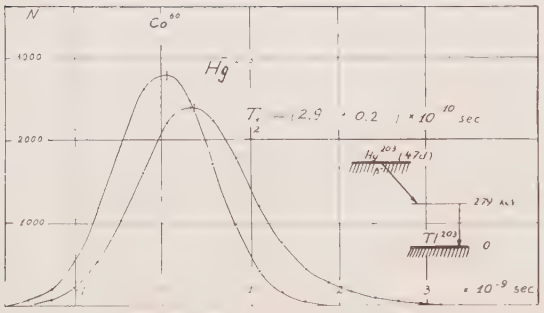


Fig. 8. Lifetime determination from centroid shift. Prompt source: $Co^{60}$, source under investigation: $Hg^{203}$, $\beta\gamma$-coincidences. $N$-number of coincidences. Length $l$ of the pulses A and B: $10^{-8}$ sec.

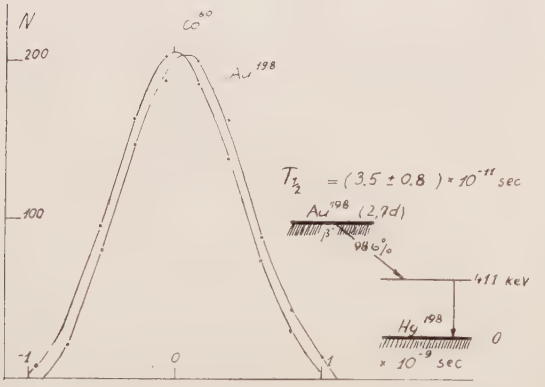


Fig. 9. Lifetime determination from centroid shift. Prompt source: $Co^{60}$, source under investigation: $Au^{198}$, $\beta\gamma$-coincidences. $N$-number of coincidences. Length of the pulses A and B: $10^{-8}$ sec.

transit times and different amplification of the photomultipliers.

b. The stability of the position of the single pulses curves was ensured (see 3.3.5). So as to check up this stability the measuring curves were read off in many series, between which the control was included. The separate curves obtained with each of the two sources were summarized and the centroid shift of the two curves was determined[17]).

Our result for the halflife $T_{\frac{1}{2}} = (2.9 \pm 0.2) \times 10^{-10}$ sec is in agreement with results of previous measurements: $T_{\frac{1}{2}} = (2.9 \pm 0.3) \times 10^{-10}$ sec[21]) and $T_{\frac{1}{2}} = (3 \pm 1) \times 10^{-10}$ sec[22]).

[21]) E. J. Berlovich and G. V. Dubinkin, JETP **32** (1957) 23 (In Russian).

[22]) R. E. Azuma and G. M. Lewis, Phil. Mag. **46** (1955) 1034.

[23]) D. Schiff and F. Metzger, Phys. Rev. **90** (1953) 849.

[24]) F. Metzger, Phys. Rev. **103** (1956) 983.

[25]) Z. Bay, V. Nouri and F. McLernon, Phys. Rev. **97** (1955) 561.

Note that the curve of the $Hg^{203}$ source shows a quite distinct asymmetry in spite of the small value of the lifetime of the excited state. There is no such asymmetry in measurements of lifetime of the order $10^{-11}$ sec. In fig. 9 is shown the result of the lifetime measurement of the 411 keV state in $Hg^{198}$, obtained by the same method ($\beta\gamma$-coincidences). The result $T_{\frac{1}{2}} = (3.5 \pm 0.8) \times 10^{-11}$ sec is in agreement with the results of other authors: $T_{\frac{1}{2}} = (3 \pm 1) \times 10^{-11}$ sec[16]) and $T_{\frac{1}{2}} = 3 \times 10^{-11}$ sec[23]).

### 4.3. SELFCOMPARISON METHOD

The selfcomparison method[18]) doubles the measured effect. However, the conditions which must be observed when using this method, namely equality of the energy intervals, cannot be fulfilled in all cases.

Our additional condition of equal intensities (see 4.2) can not be fulfilled principally (when measuring $\beta\gamma$-processes). For instance we found an "apparatus time" connected with the fact, that this condition was not fulfilled, when measuring $\beta\gamma$- and $\gamma\beta$-coincidences from a $Co^{60}$ source. As is generally known, the states of nucleus $Ni^{60}$ have a very small lifetime: $T_{\frac{1}{2}}$ (1332 keV) $= 1.1 \times 10^{-12}$ sec[24]) and $T_{\frac{1}{2}}$ (2502 keV) $< 1 \times 10^{-11}$ sec[25]). Because of this we prefer the method described in 4.2 together with the singles control for measuring short lifetimes, since it excludes any apparatus effect.

## 5. Conclusion

We think that it is possible to improve the properties of the instrument by using photomultipliers of the ФЭУ-36 type with an inner curved photocathode and mixer diodes with a better single-rejection ratio. Besides this it may be possible to devise a limiter with a lower limitation level than the usual valve limiters have. In that case the advantages of a diode converter in comparison with a valve converter will show up fully, since it can in principle work with pulses, the magnitudes of which are just a portion of a volt.

The authors express their gratitude to V. V. Nikitin for his help in tuning up the instrument and in carrying out the experiments.

NUCLEAR INSTRUMENTS AND METHODS 9 (1960) 21–28; NORTH-HOLLAND PUBLISHING CO.

# AUTOMATIC MASS NUMBER DETERMINATION FOR ISOTOPE SEPARATORS AND MASS SPECTROMETERS

L. WÅHLIN

*Nuclear Physics Division, National Physical Research Laboratory. C.S.I.R., Pretoria South Africa*

Received 11 July 1960

Automatic mass number determinations for isotope separators and mass spectrometers are possible by means of an electronic computer system. A detailed description of this method, as applied to the isotope separator in Pretoria[1]), is given below.

## 1. Basic Description

The following problems are often encountered with the isotope separator:

(i) *Accurate mass number determination of a line at the collector.*

It is important to know the origin of a given mass line especially when multi-charged and molecular ions are present in the mass spectrum.

(ii) *Control settings for a given mass number at the collector.*

This is important where radio-active isotopes with short half-lives are being separated, since the line intensity is usually too weak to be registered on the fluorescent screen, or by the ion current measuring device.

For a given mass line at the collector of the isotope separator the following relation between mass number $M$, acceleration voltage $V$ and magnetic field $H$ applies,

$$\frac{M}{e} = \frac{k^2 H^2}{V}, \qquad (1)$$

where $e$ = the charge of an ion and $k^2$ = the constant of proportionality for the apparatus in question. In practice $H$ and $V$ must be accurately determined because

$$\frac{\Delta M}{M} = 2\frac{\Delta H}{H} - \frac{\Delta V}{V}. \qquad (2)$$

This means that if $M = 250$ and $\Delta M = \frac{1}{4}$, then $H$ and $V$ must be measured within 0.05% and 0.1% respectively. This is complicated by slow fluctuations of $V$ and $H$ caused by drifts in the power supplies. These difficulties have been overcome with the aid of an electronic computer system employing drift compensated DC amplifiers. The required mass number can be selected on a potentiometer dial, irrespective of the value of the acceleration voltage.

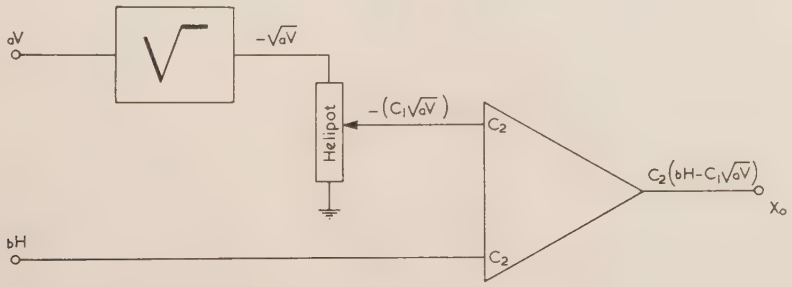


Fig. 1. Block diagram of the computer.

A block diagram of the computer is shown in fig. 1. Two voltages $aV$ and $bH$, proportional to

[1]) W. E. Frahn, W. L. Rautenbach and L. Wåhlin, Nuclear Instruments and Methods 7 (1960) 253.

the acceleration voltage $V$ and the magnetic field $H$ are fed into the network. The square root of $aV$ is obtained and is multiplied by a constant $C_1$ $(0 \leq C_1 \leq 1)$, by means of a Helipot, to give $-(C_1\sqrt{aV})$. (The negative sign is due to the selected by the Helipot and kept in position on the collector despite slow fluctuations in $V$ and $H$.

Fig. 2 shows how the computer is connected to the isotope separator. A high resistance connects the acceleration voltage $V$ to the square root

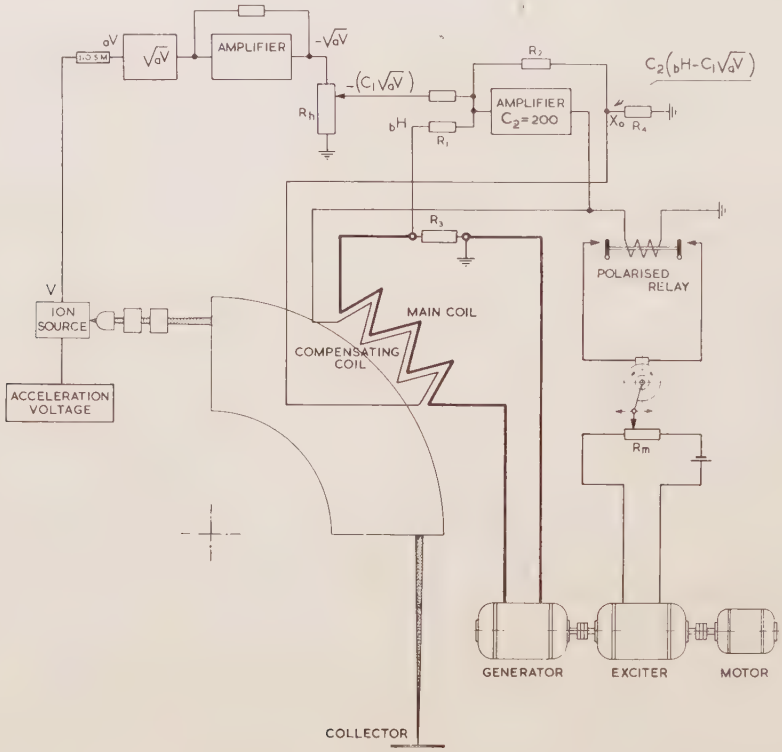


Fig. 2. The computer connected to the isotope separator.

180° phase shift in the square root generator.) In the summing amplifier stage $C_1\sqrt{aV}$ is algebraically added to $bH$ and multiplied by a factor $C_2$ to give an output $X_0 = C_2(bH - C_1\sqrt{aV})$. This output signal is used to change the magnetic field $H$ so that at equilibrium the output of the amplifier $C_2(bH - C_1\sqrt{aV})$ becomes zero. Hence, we get

$$C_1 = bH/\sqrt{aV}\,. \tag{3}$$

Substituting (1) in formula (3) gives

$$\sqrt{\frac{M}{e}} = kC_1\frac{\sqrt{a}}{b} = KC_1$$

where $K = k\sqrt{a}/b$ is a constant. $C_1$ is read on the dial of the Helipot and can be calibrated in mass numbers. Any mass number up to 250 can be

generator, which consists of a biased diode device. "$aV$" is determined by the ratio between the high resistance and the input resistance of the square root generator. $bH$ is the voltage drop over $R_3$ and is proportional to the magnetic field $H$. $R_3$ is a shunt resistance in series with the field coil of the magnet. The output of the computer, $X_0$, is connected to a polarised relay. (The compensating coil is for the moment regarded as being short circuited.) This actuates the motor rheostat, $R_m$, to change the current in the field coils of the magnet until the computer output, $C_2(bH - C_1\sqrt{aV})$ becomes zero. $C_2$ is the gain of the summing amplifier and acts as a constant before addition takes place. In this feed-back system the amplification factor $C_2$ must be $= \infty$ in order to obtain the output $X_0 = 0$. For a

permissible error of 0.05% ( c.f. eq. (2)) an amplification of $> 10^5$ is required to operate the polarised relay. The high time constant of the magnet compared with the relatively low time constant of the amplifier and the motor generator, makes it impossible to obtain a greater amplification than 300 before self oscillation occurs.

To overcome the above difficulty a new type of compensation was developed. The gain $C_2$ at the output $X_0$ of the summing amplifier is set to 200 by means of the input and feed-back resistances $R_1$ and $R_2$. An amplification of 200, which is well below the critical value, can by means of the compensating coil in fig. 2, be made to correct for an error of up to 1A in the current through the field coil in the following manner. Suppose the error current is 1A in the shunt resistance $R_3 = 0.1\Omega$; 0.1 volts will then be amplified by a factor of 200, 20 volts being obtained at $X_0$ over the loading resistance $R_4 = 20\Omega$; a current of 1A will thus flow through $R_4$.

The compensating coil is made of thin wire and is wound round the main field coil connecting the last stage of the summing amplifier to the output point $X_0$. This means that the current of 1A flowing through the loading resistance $R_4$ must also flow through the compensating coil. If the compensating coil has the same number of turns as the main field coil and is correctly polarised, then the total magnetic field will be the same as if $bH - C_1\sqrt{aV} = 0$.

The accuracy of this compensation will evidently depend on the accuracy of the relationship $C_2R_3 = R_4$, on the constancy of the resistances $R_3$ and $R_4$; and the gain $C_2$ over the working range. ($C_2$ is determined by the resistances $R_1$ and $R_2$ and will be dealt with later under the section on the high gain DC amplifiers.) Manganin is used for the shunt and load resistances $R_3$ and $R_4$ respectively to avoid changes in ohmic value with changes in temperature. Temperature variations in the compensating coil have no effect as the amplification is always 200 at $X_0$.

Since the time constant of the compensating coil is much lower than that of the main field coil, (due to the difference in internal resistances) stabilisation will occur almost immediately. The polarised relay, which is now connected across the compensating coil with $R_4$ in series, will in conjunction with the main coil, act as an error integrating device and eventually transfer accumulated corrections from the compensating coil to the main coil. This ensures that the range over which the compensating coil and its associated amplifier has to work, remains relatively small.

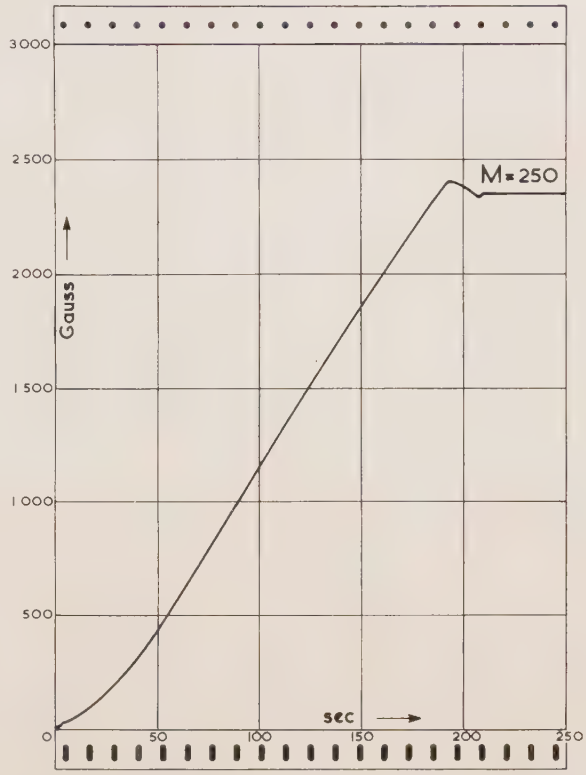


Fig. 3. Recorded diagram showing the time for the magnet to reach the required field for mass number 250 at 40 kV acceleration voltage.

The curve in fig. 3 shows the time the motor driven exciter rheostat takes to reach the required field for mass number 250 at 40 kV acceleration voltage.

## 2. The Square Root Generator and the Factor $C_1$

As mentioned previously, the square root function generator is a biased diode device[2]); the circuit is shown in figs. 4(a) and 4(b). Nine

[2]) Wass, Electronic Analoge Computers (Pergamon Press, 1955).

crystal diodes each with an adjustable loading resistance and a fixed bias voltage, are connected in parallel. The input voltage $V_1$ will cause a current $I$ to flow through the resistances $R_1$ and $R_2$, and the voltage drop over $R_2$ represents the output voltage $V_0$. If $V_0$ is plotted against $V_1$ as in fig. 5, a straight line is obtained until $V_0$ reaches the same value as the bias voltage of the first diode. At this instant the first diode starts conducting and causes an extra load across $V_0$, which makes the straight line follow a new slope. The procedure is repeated in the following diodes, so that a number of straight-line segments forming a series of chords or tangents are obtained. By adjusting the length and slope of these segments, by means of the bias voltages and the resistances in series with the diodes, a given curve can be approximated. The curve in fig. 5 represents the positive half of the parabola $V_0 = \sqrt{V_1}$.

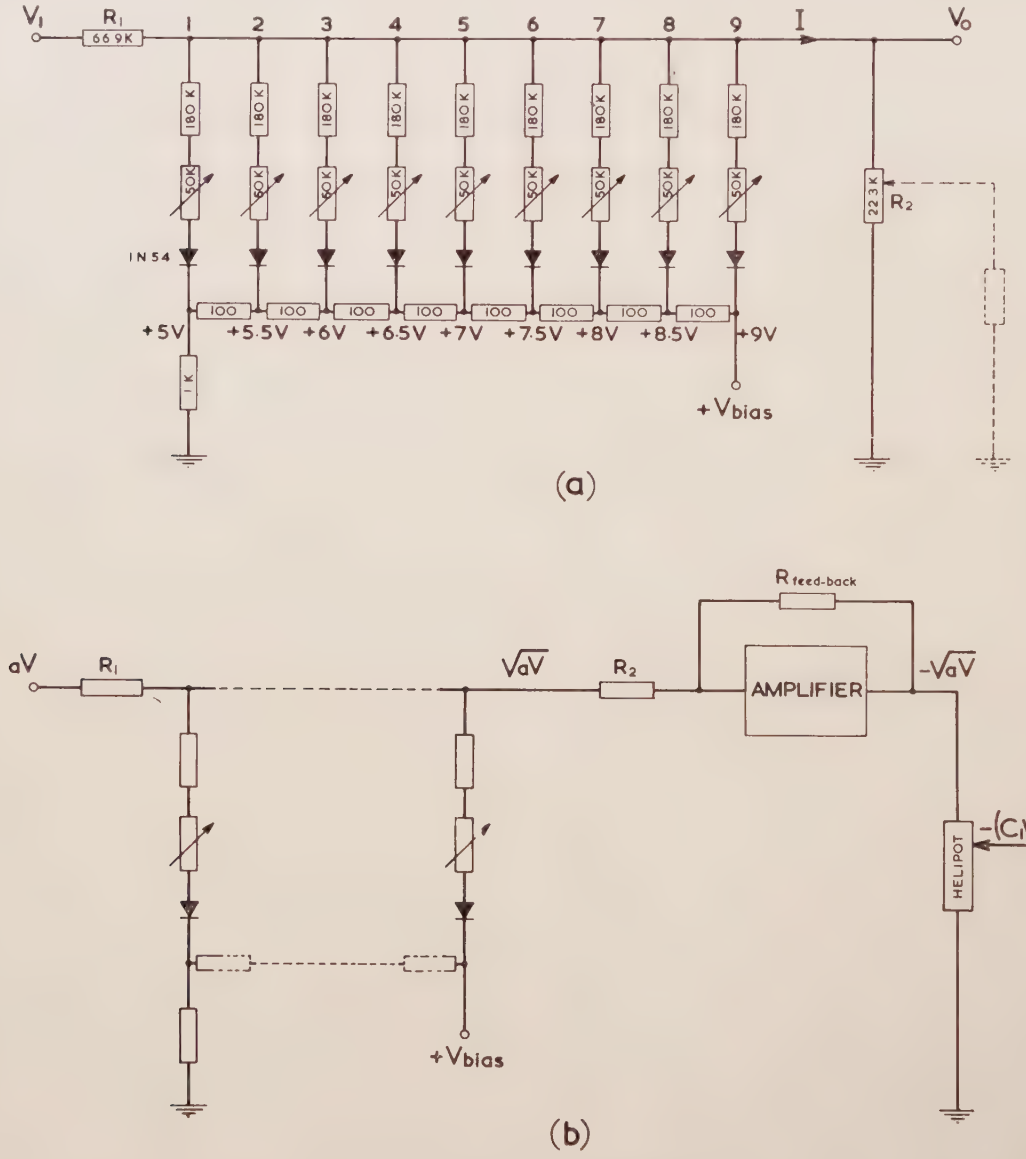


Fig. 4. The square root function generator.

If $R_2$ is replaced by a Helipot connected as a potentiometer, the output voltage $V_0$ can be

multiplied by the factor $C_1$ $(0 \leq C_1 \leq 1)$. In practice, however, the load impedance imposed at the output of the potentiometer is relatively low compared with the output impedance of the

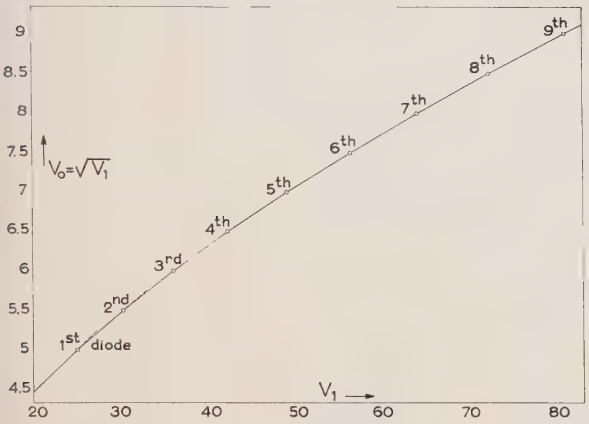


Fig. 5. The approximated parabola $V_0 = \sqrt{V_1}$.

square root generator, which means an error of $V_0$ at different settings of the potentiometer. By connecting a DC amplifier, with input and feed-back resistances, between the square root generator and the potentiometer, this effect can be eliminated (see fig. 4(b)). The input impedance of the amplifier is set to $R_2$ and the output impedance is kept very low because of the high-gain feed-back. (A more detailed description of the amplifier is given later.) If $V_1 = aV$, the gain of the amplifier is set to $= 1$ and the Helipot represents the factor $C_1$; then the output of the computing elements described will be $-(C_1\sqrt{aV})$, the negative sign being due to the 180° phase shift in the amplifier.

### 3. The High Gain DC Amplifiers

The high gain DC amplifiers are of the automatic balancing type first developed by Goldberg in 1950[3]). The DC amplifiers used in the computer (see fig. 6(a)) have a net gain of about 50 million and an equivalent input drift of consistently less than 50 $\mu$V. When connected as an operational amplifier (fig. 6(b)) the gain $V_0/V_1$ can be set by means of the input and feed-back resistances $R_1$ and $R_2$, $V_0/V_1 = -R_2/R_1$. Since it can be assumed that the input impedance of the amplifier is practically infinite; the sum of all currents flowing to grid must be zero according to Kirchhoff's law. This means that,

$$\frac{V_0/A - V_0}{R_2} + \frac{V_0/A - V_1}{R_1} = 0$$

or

$$V_0 = V_1 \frac{A}{(1-A)\dfrac{R_1}{R_2} + 1}.$$

If $A$, the net gain of the amplifier, is very large,

$$\frac{V_0}{V_1} \approx -\frac{R_2}{R_1}.$$

The negative sign is due to the phase reversal through the amplifier.

If a voltage $V_2$ is introduced to the amplifier by a second resistance $R_3$, application of Kirchhoff's law and the assumptional high value of $A$ gives,

$$V_0 = -\left(V_1\frac{R_2}{R_1} + V_2\frac{R_2}{R_3}\right).$$

Thus $V_1$ and $V_2$ are algebraically added after multiplication by the constants $R_2/R_1$ and $R_2/R_3$ respectively.

In the last stage of the computer a summing network as described is used with $R_2/R_1 = R_2/R_3 = 200 = C_2$. As previously mentioned, the equivalent input drift of the amplifier is less than 50 $\mu$V. At a gain of 200 the offset voltage at the output of the summing amplifier will not exceed 20 mV. This error will cause a current of 1 mA to flow through the compensating coil of the magnet, which at mass number 250 and 40 kV acceleration voltage corresponds to a change of about 0.003% in the magnetic field (see formula (2)).

An additional power stage is connected to the output of the summing amplifier in order to give sufficient output current for the compensating coil (fig. 7). The power stage acts as a bridge-balanced low-impedance driver circuit and can supply a current of 1A at maximum rating. It will be noted that the feed-back resistance is

[3]) R. L. Koningsberg, Advances in Electronic and Electron Physics, Vol. 11 (1959); Korn and Korn, Electronic Analog Computers (McGraw-Hill, 1952).

now connected to $X_0$ at the loading resistance $R_4$ and that $X_0$ becomes the actual output of the summing amplifier.

certain resistances and components used in the computer. The input and feed-back resistances of the amplifiers should be wire-wound, and the

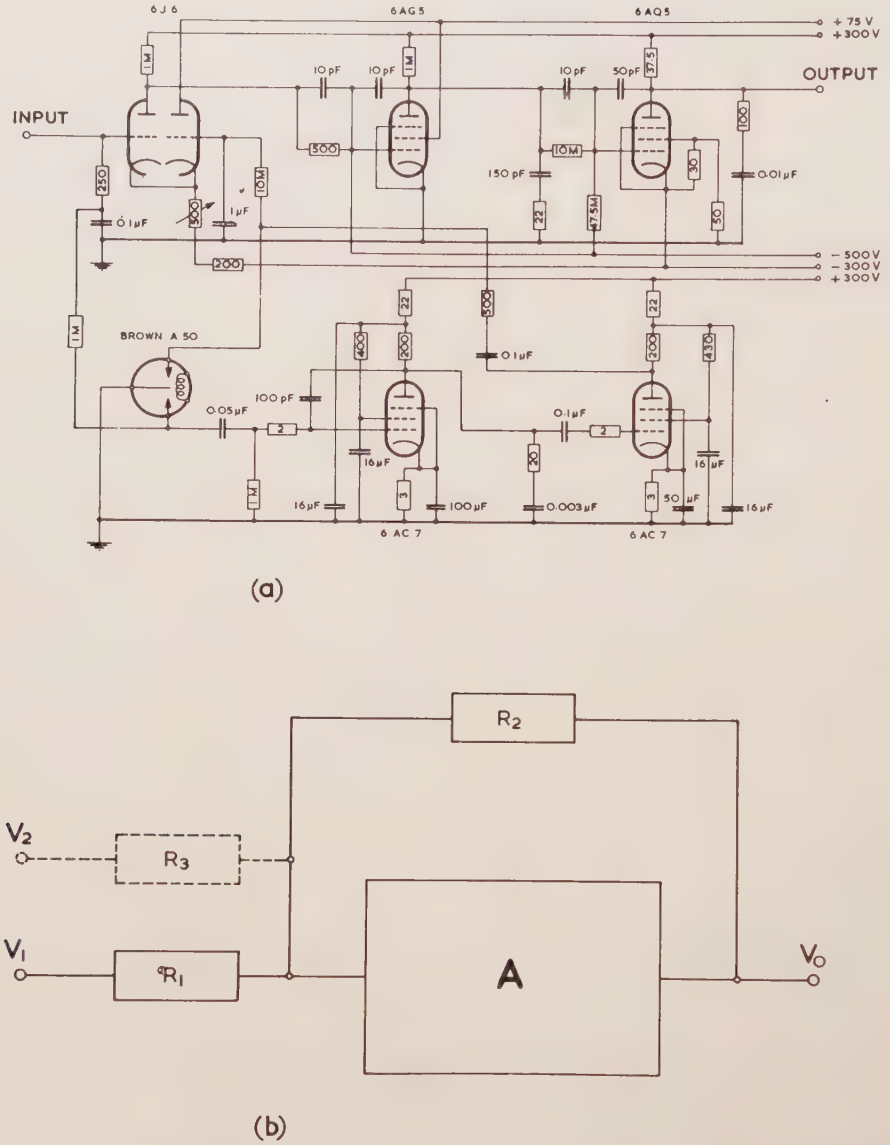


Fig. 6(a). The drift compensated high gain DC amplifier and (b) connected as an operational amplifier.

## 4. Discussion

As mentioned in the basic description, the acceleration voltage and the magnetic field must be measured more accurately than 0.1% and 0.05% respectively. This is to allow a maximum displacement of mass line 250 corresponding to a resolving power = 1000 of the isotope separator. Great care must therefore be taken in selecting high resistance connecting the acceleration voltage to the square root generator, should preferably be mounted in a recirculating oil bath. By using high quality resistances and carefully selected bias voltages in the square root generator, errors of less than 0.1% are possible. The power supplies for the two amplifiers and the bias voltage for the square root generator must

be stabilised, but it is not necessary to stabilise the separate power supply for the bridge-balanced driver circuit.

and the curve obtained shows a straight line up to 2350 gauss before saturation effects become noticeable. This means that at fields above 2350

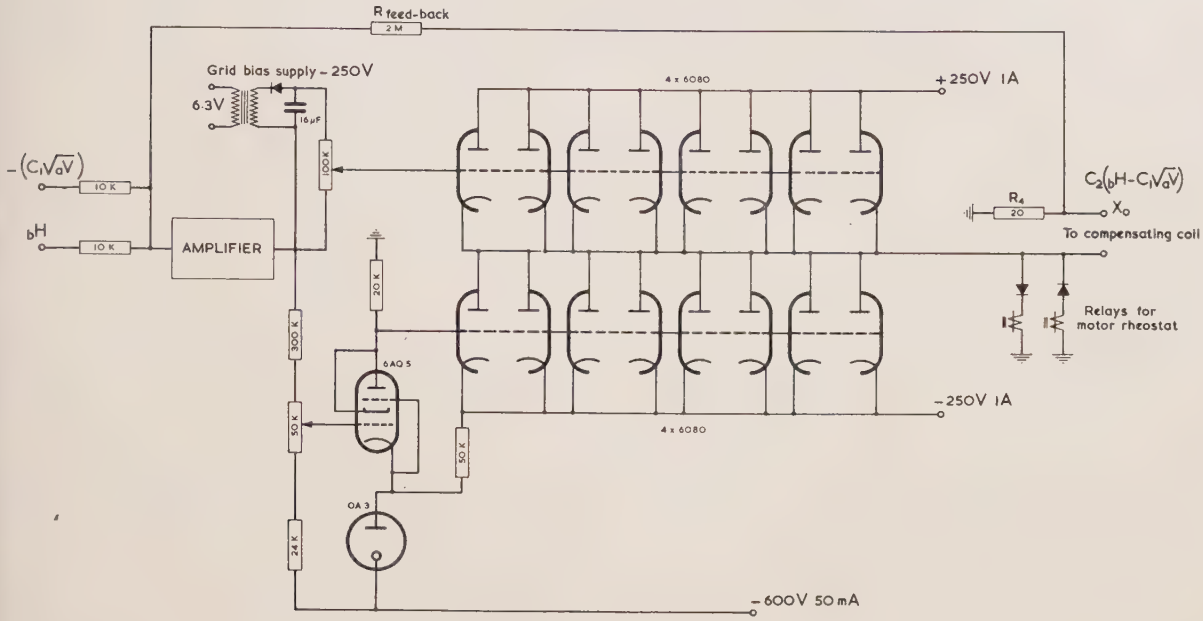


Fig. 7. The bridge-balanced low-impedance driver circuit.

Another important factor is the proportionality between $bH$ and the magnetic field $H$. This is shown in fig. 8, where the magnetic field of the isotope separator in Pretoria is plotted against $bH$, the voltage drop over the shunt in series with the field coils of the magnet. The magnetic field is measured by the proton resonance method

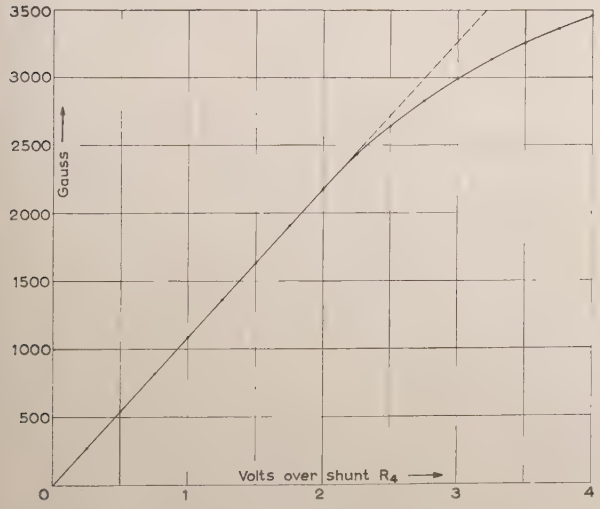


Fig. 8. The magnetic field and $bH$, the voltage drop over $R_4$.

gauss, $bH$ is no longer proportional to $H$, and accurate mass number determinations with the computer are therefore impossible. Thus at acceleration voltages of 80 kV and 40 kV, mass numbers ranging from 1 to 126 and from 1 to 250 respectively can be determined.

Before a mass number is determined or selected, the magnet must be demagnetised to avoid error caused by the remanence field. This can easily be done by taking the magnetic field up to maximum strength and then reversing it to a predetermined value. This remanence effect becomes noticeable also when selecting a low mass number after a high mass number. Therefore accurate mass number determinations are achieved by selecting the mass numbers in increasing order.

## 5. Conclusions

The system described above has proved satisfactory on the isotope separator in Pretoria and has considerably speeded up and simplified mass number determinations.

On mass spectrometers a more simplified computing system can be used. There is no need for a square root generator, as most of the spectrometers operate at a fixed acceleration voltage. A third winding on the analysing magnet could perhaps be used for scanning mass spectras from a determined mass number.

**Acknowledgement**

The author wishes to express his gratitude to Prof. Dr. W. E. Frahn and to Dr. W. L. Rautenbach for valuable discussions and criticism. Appreciation is also felt for the enthusiastic assistance of Messrs E. P. Blignaut, J. J. Selier and of the workshop staff.

NUCLEAR INSTRUMENTS AND METHODS 9 (1960) 29–36; NORTH-HOLLAND PUBLISHING CO.

# MESURES DE TEMPS DANS LE DOMAINE DE LA NANOSECONDE: CONVERTISSEUR DE TEMPS EN AMPLITUDES ET CIRCUITS DE COINCIDENCES

R. BALLINI et E. POMELAS

*C.E.N., Saclay, Gif-sur-Yvette (S & O)*

Reçu le 2 Juin 1960

A time-to-pulse height converter, associated to a pulsed accelerator was improved by using an electron beam switching tube and a convenient shaping of photomultiplier pulses. Such pulses were applied to a transistorized millimicrosecond coincidence circuit.

## 1. Enregistrement de temps de vol de neutron par conversion de temps en amplitudes

Le faisceau du Van de Graaff de 5 MeV de Saclay a été pulsé à une fréquence de quelques megahertz par déflexion électrostatique après accélération et découpage par un diaphragme[1,2]). Pendant une période de la tension de déflexion, le faisceau tombe deux fois sur la cible: on obtient ainsi deux impulsions de quelques nanosecondes, tandis qu'un circuit de chronométrage[2]) produit un seul signal bref dont le déphasage par rapport à une impulsion du faisceau peut avoir deux valeurs distinctes (fig. 1) dépendant de la géométrie jusqu'à la cible, de l'énergie des particules du faisceau et de la longueur du câble qui relie le circuit de chronométrage au convertisseur de temps en amplitudes: l'intervalle de temps enregistré est celui qui sépare une impulsion du détecteur et le signal de chronométrage qui la suit immédiatement. Pour un même temps de vol, il peut prendre deux valeurs différant de la demi-période de la tension de déflexion du faisceau. Il est à rappeler que le faisceau ne tombe pas au même endroit de la cible à une demi-période d'intervalle.

La fig. 2 représente le schéma en bloc de l'appareillage électronique: déjà assurée par la répartition des circuits de masse et des blindages[3]), l'élimination des parasites à l'entrée des deux amplificateurs a été améliorée en séparant le plus complètement possible les masses du circuit de chronométrage et du convertisseur de

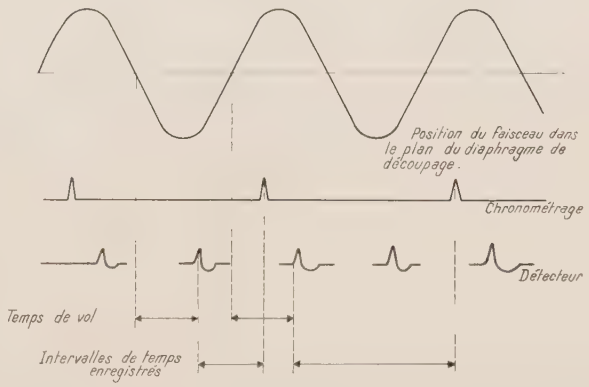


Fig. 1. Déphasage entre les débuts de temps de vol et les signaux de chronométrage: intervalle de temps enregistré.

temps en amplitudes par un transformateur d'impulsions. Ce dernier est constitué par deux enroulements de quelques spires. bobinées en deux régions diamétralement opposées d'un tore de ferrite. Le convertisseur de temps en amplitudes (fig. 3) et les versions qui l'ont précédé[3,4,5]),

[1]) R. Ballini et L. G. Kuo, J. Phys. **20** (1959) 47A.

[2]) R. Ballini, R. Moreau et B. Pierre, Rapport S.R.N.B.E. no. 1, C.E.N., Saclay (1959).

[3]) R. Ballini et L. G. Kuo, Rapport S.R.N.B.E., no. 2, C.E.N., Saclay (1959).

[4]) G. Philippe, Rapport S.R.N.B.E., no. 3, C.E.N., Saclay (1959).

[5]) R. Ballini et S. M. Shafroth, Nucl. Instr. **6** (1960) 331

dont une est représentée par la fig. 4, sont dérivés d'un appareil du à J. M. Neiler[6]). Son principe consiste à produire en B un signal carré positif pendant lequel un courant donné est établi dans le circuit de plaque de $V_2$ et intégré sur la capacité C. Le signal carré est obtenu en chargeant la capacité parasite du point B par le courant de $V_1$ qui débite à la montée du signal positif appliqué à sa grille et se coupe à la descente de ce signal; cette capacité parasite est déchargée par le courant de $V_3$ (impulsion de $10^{-10}$ coulomb environ) à l'instant du sommet du signal positif de chronométrage. Un circuit d'aiguillage oriente ces impulsions vers $V_4$ et la masse si une impulsion du photomultiplicateur n'a pas eu lieu depuis un délai de quelques $10^{-7}$ s.

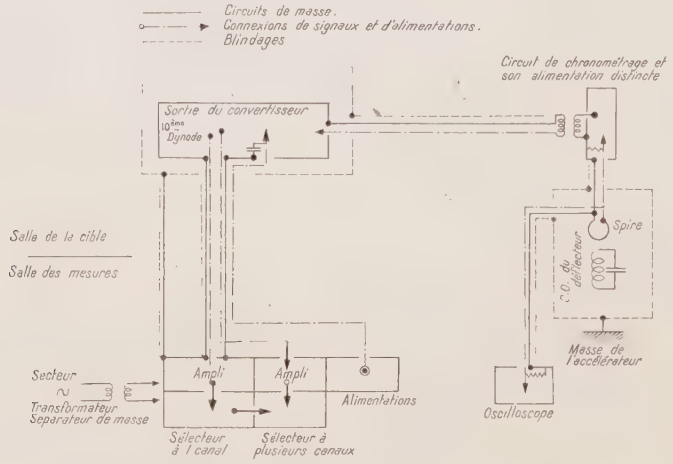


Fig. 2. Schéma en bloc de l'appareillage électronique.

[6]) L. E. Beghian, G. H. R. Kegel et R. P. Scharenberg, Rev. Sci. Instr. **29** (1958) 753.

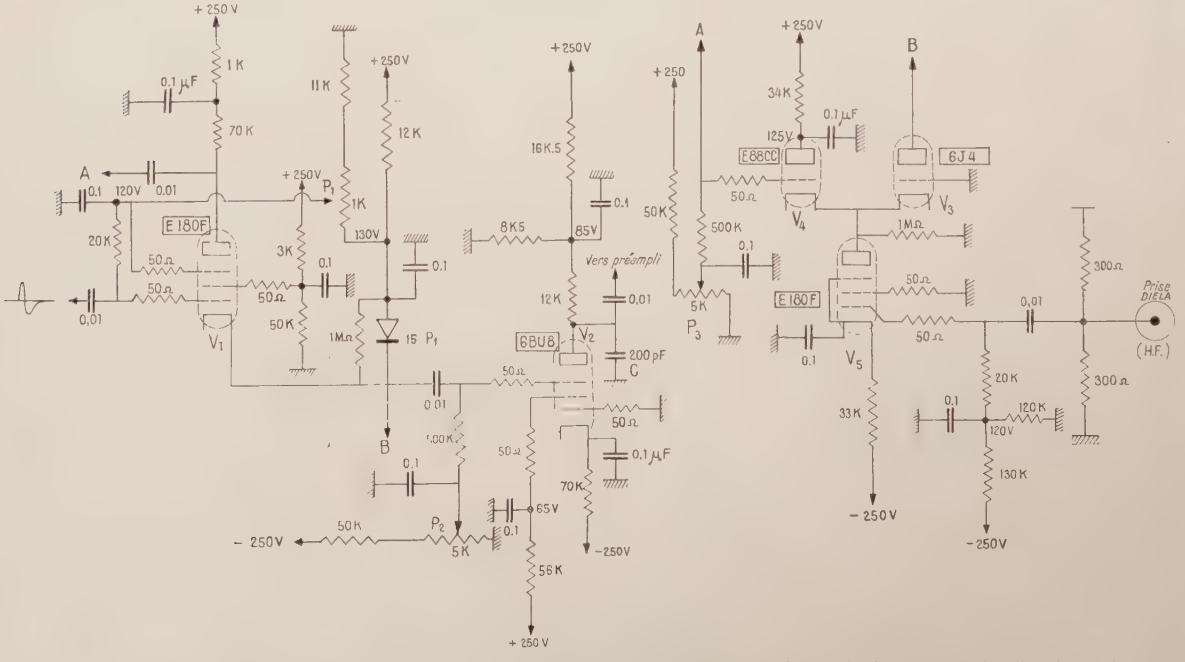


Fig. 3. *Convertisseur de temps en amplitudes.* Les filaments sont découplés et alimentés à travers des bobines de choc. Dans le montage d'étude, $V_3$ et $V_4$ étaient les deux éléments d'une double triode E88 CC.

Il est à noter que nous avons utilisé un circuit de chronométrage déjà existant, mais qu'il pourrait sans doute être remplacé par un circuit délivrant un signal sinusoïdal d'une trentaine de volts.

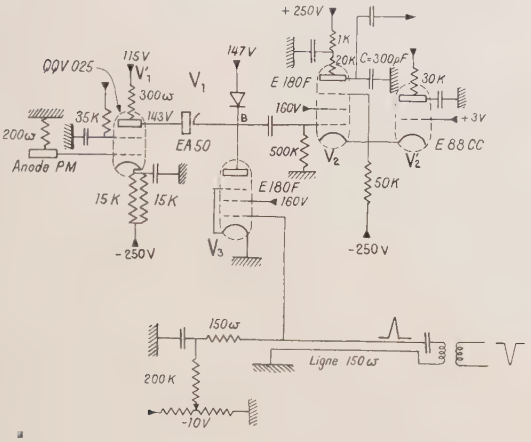


Fig. 4. Un exemple de réalisation antérieure du convertisseur de temps en amplitudes.

Des mesures de contrôle (appareil représenté fig. 3) ont été effectuées avec des neutrons de 2.9 MeV, produits par la réaction T(p,n). Les figs. 5 et 6 résument quelques résultats obtenus. Le seuil de sensibilité de l'appareil correspond à la détection de protons d'un peu moins de 200 keV dans le scintillateur plastique utilisé (préparé par le Service de Physique Corpusculaire à Haute Energie du C.E.N. de Saclay). L'instabilité n'excède pas 1 nanoseconde pendant un temps de l'ordre de l'heure.

## 2. Modifications par rapport aux réalisations antérieures du convertisseur de temps en amplitudes

Elles ont d'abord porté sur l'utilisation du signal de chronométrage, puis sur celle du signal du détecteur et sur le circuit d'integration.

Dans les appareils déjà publiés[3,4,5]), le signal de chronométrage (négatif) était transmis en O par l'intermédiaire d'un circuit de coïncidences à plaques couplées: l'instabilité qui en resultait sur la position des pics a conduit (fig. 4) à supprimer cette fonction "porte" et à polariser $V_3$ par courant moyen de grille, de façon à utiliser le sommet du signal de chronométrage (positif). La stabilité a ainsi été améliorée mais divers accidents sont apparus, notamment des oscillations sur le spectre de "coïncidences fortuites" entre une source radioactive quelconque et les signaux de chronométrage[7]).

Ce défaut a été atténué par le rétablissement de la fonction "porte" sous forme d'un circuit d'aiguillage et par la possibilité de régler le courant moyen qui traverse ce circuit (fig. 3). Mais l'amélioration décisive a été obtenue en remplaçant le circuit intégrateur à cathodes couplées ($V_2V_2'$ sur la fig. 4) par un tube (6BU8) dans lequel une impulsion appliquée au suppresseur commute vers la plaque une fraction donnée du courant d'écran: ce tube, dont les deux suppressors et les deux plaques sont montés en parallèle (fig. 3) est réglé en continu de façon que la commutation soit réalisée pour une variation de

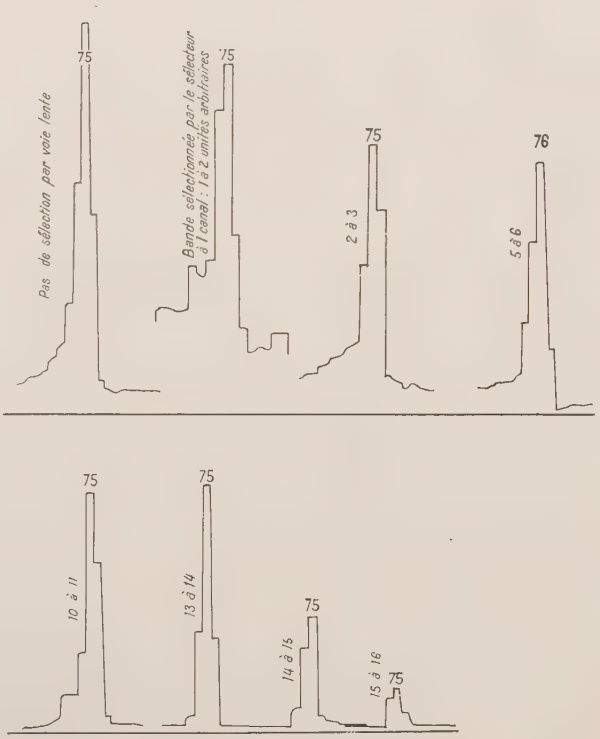


Fig. 5. *Pics produits par des neutrons de 2.9 MeV.* 1 canal $\simeq$ 1.2 ns. Impulsions du faisceau $\simeq$ 1.7 ns. Un des canaux est numéroté pour chaque pic. Photomultiplicateur RCA 7046 (voir fig. 9); $KT_1$ = 1000 V; $T_1A$ = 2300 V; $R = 700\,\omega$; $r = 2000\,\omega$ (voir fig. 8); Scintillateur plastique: diamètre 7 cm; épaisseur 2.5 cm ($\simeq$ 1 ns).

[7]) J. Duclos, J. Phys. **21** (1960) 19A.

4 à 5 volts de la tension du suppressor; une variation d'une dizaine de volts est nécessaire en régime d'impulsions pour obtenir un "spectre de fortuites" à peu près monotone.

pentode dont le courant remplace ainsi celui du phototube pour charger la capacité parasite du point O.

Cet ensemble de modifications a augmenté la

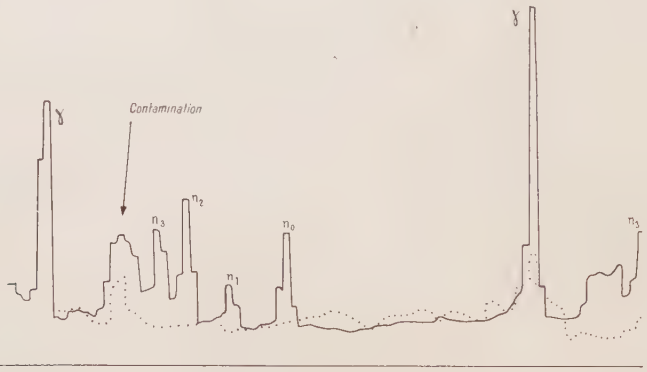


Fig. 6. Temps de vol des $\gamma$ et des neutrons émis sous un angle de 30° par rapport à un faisceau de protons de 4 MeV incident sur une cible de vanadium déposée sur or par évaporation thermique. Le pointillé représente le "fond" (cible retournée). Détecteur: voir fig. 5. Bande d'amplitudes sélectionnée sur la voie lente: 2 à 3 (voir fig. 5). 1 canal $\simeq$ 1.8 ns.

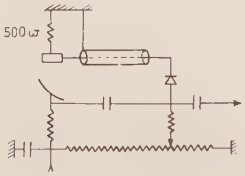


Fig. 7.
Essai d'écrêtage de l'impulsion sur la dernière dynode.

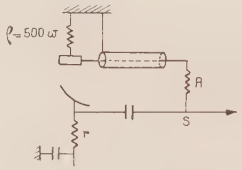


Fig. 8. Mise en forme par opposition des impulsions de courant sur la dernière dynode et l'anode.

Enfin, dans le cas de la fig. 4 par exemple, le front positif du signal en O est obtenu en faisant passer par la diode $V_1$, choisie thermique pour des motifs exposés par ailleurs[3]), une partie de la transition de courant plaque du tube $V_1$ que le signal d'anode du photomultiplicateur coupe pendant un temps très court.

Un essai (fig. 7) a eu pour but d'utiliser directement l'impulsion de courant dans le photomultiplicateur et d'écrêter l'impulsion de tension qu'elle produit sur la dernière dynode. Il s'est révélé qu'une amplitude à peu près constante n'était obtenue qu'en portant à la masse le point milieu du potentiomètre, ce qui a conduit au circuit que représente la fig. 8.

Le montage représenté par la fig. 3 remplace la diode EA50 par l'espace grille-cathode d'une

stabilité, abaissé l'énergie minimum des neutrons qui peuvent être enregistrés et diminué le déplacement des pics sur le spectre de temps de vol, en fonction des amplitudes sur la 10 ème dynode du phototube (peu saturée).

### 3. Etude sommaire de la mise en forme par opposition des impulsions d'anode et de dernière dynode

Les impulsions en S (fig. 8) ont été observées avec un oscilloscope Tektronix 517 A ou 543.

Avec des photomultiplicateurs RCA 6810 ou 7046 et un scintillateur plastique, les impulsions dues aux gamma de 0.5 et 1.3 MeV du sodium-22 apparaissent pratiquement superposées sur la partie positive de l'impulsion pour une tension de 2100 volts appliquée soit au phototube 6810,

soit entre la grille G2 et l'anode du phototube 7046. L'amplitude ainsi atteinte varie peu lorsqu'on augmente ces tensions de 300 volts.

Sur la fig. 10, correspondant à un cas où

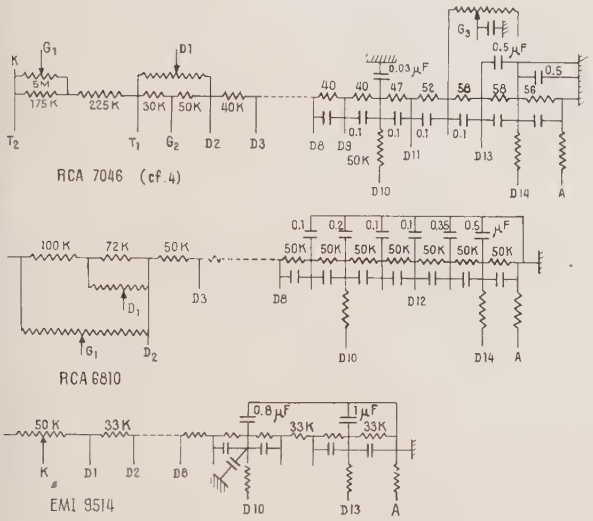


Fig. 9. *Câblages de photomultiplicateurs.* Les condensateurs sans indications de valeur sont des "céramique" de 0.01 ou 0.1 $\mu$F montés au plus près du support.

pour les essais précédents, mais de longueur moitié. Les résultats des deux procédés de mise en forme ont été comparés pour des rapports grossièrement égaux des impulsions mises en opposition.

En aucun cas une bonne saturation n'a été observée sur l'anode avec mise en forme par ligne à retard en court-circuit. Avec plusieurs des compteurs à scintillations ainsi essayés, la saturation était plus nette sur la dynode que sur l'anode (il n'a pas été établi si cette différence entre ces deux électrodes était due principalement à une diminution du gain du dernier étage multiplicateur). Toutefois, elle ne permettait pas

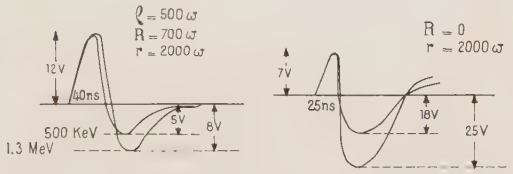


Fig. 10. Formes d'impulsions obtenues avec le montage de la fig. 8. Photomultiplicateur RCA 7046, scintillateur plastique, $\gamma$ du sodium-22.

l'effet de saturation n'est pas très accentué, on voit comment la durée et la forme des deux parties de l'impulsion dépendent de la résistance R (voir fig. 8).

Un effet analogue de saturation a été obtenu avec le phototube 6810 et un cristal de NaI(Tl). Avec un photomultiplicateur EMI 9514 (13 étages) essayé avec un scintillateur plastique et un cristal de NaI(Tl), la saturation est moins nette pour la tension maximum que peut supporter ce phototube sans bruit de fond prohibitif.

Soient $I_A(t)$ et $I_D(t)$ les courants d'anode et de dynode et $T$ le retard apporté par la ligne: l'amplitude du signal en S est voisine de:

$$r \frac{R+\rho}{r+R+\rho} \left[ I_D(t) + \frac{\rho}{R+\rho} I_A(t-T) \right].$$

Avec la mise en forme classique par ligne à retard en court-circuit, le signal en S est $I_D(t) - I_D(t-T)$ ou $I_A(t) - I_A(t-T)$.

Des essais ont été effectués avec une ligne à retard en court-circuit, de même modèle que

toujours d'expliquer les résultats obtenus avec la mise en forme par opposition des courants de dernière dynode et d'anode (fig. 8): c'est notamment le cas avec le photomultiplicateur RCA 7046 associé à un scintillateur plastique; la saturation est alors aussi peu visible sur la

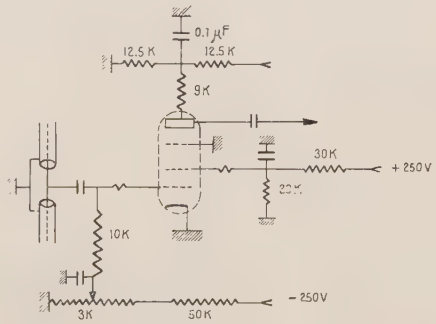


Fig. 11. Circuit de coïncidences par somme d'impulsions mises en forme (fig. 8) sur la grille d'un tube E180F bloqué.

dynode que sur l'anode avec mise en forme par ligne à retard en court-circuit, alors qu'elle est très nette dans les mêmes conditions de tension avec le montage de la fig. 8, même réglé en sorte

que les impulsions mises en opposition en S transportent à peu près la même charge.

Ce circuit offre donc des possibilités particulières pour utiliser les phénomènes complexes de saturation qui se manifestent dans les derniers étages d'un photomultiplicateur. L'impulsion obtenue dépend fortement des rapports des résistances $R$, $r$ et $\rho$ et du retard apporté par la ligne: une étude détaillée ne peut en être faite commodément qu'avec une ligne à réglage continu, mais un contrôle en a été effectué en l'utilisant dans des circuits de coïncidences qui exigent une mise en forme aussi parfaite que possible†.

Le principle du circuit représenté par la fig. 11 repose sur l'addition d'impulsions parfaitement mises en forme sur la grille du tube E180F, polarisée de façon à ne pas débiter avec l'impulsion d'un seul photomultiplicateur. Pour un retard donné entre les deux impulsions, une légère variation d'amplitude ou de durée de l'une d'elles se traduit par une variation importante de la charge collectée par la plaque du tube et de l'amplitude de l'impulsion de tension qui en résulte, dont la durée est de quelques dixièmes de microseconde.

Les impulsions de photomultiplicateurs sont transmises au tube E180F par des lignes à retard d'impédance caractéristique $Z = 75$ ohms dont chacune doit être adaptée au départ: l'expérience montre que, en dépit de divers eléments parasites, l'adaptation est acceptable en adoptant simplement

$$\frac{r\,(R + \rho)}{r + R + \rho} = Z\,.$$

La durée et l'amplitude de chaque signal peuvent être réglées par l'intermédiaire de $R$ et de la longueur de la ligne de mise en forme (voir fig. 10).

† Il a été noté que les impulsions étaient transmises avec une très faible intégration par un transformateur constitué de deux enroulements de quelques spires, bien séparés sur un tore de ferrite FN–104–2003 (LTT). Il est ainsi possible d'amplifier légèrement, d'inverser le signal, de le transmettre en séparant les masses. Les oscillations peuvent être coupées par un cristal.

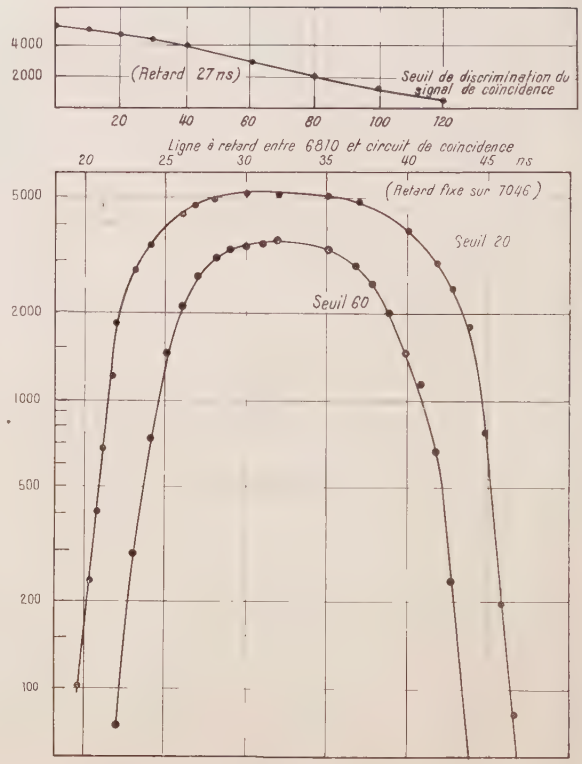


Fig. 12. Coïncidences produites par $^{22}$Na dans deux compteurs à scintillateur plastique: photomultiplicateurs RCA 6810 et 7046, circuit de la fig. 11.

Les figs. 12 et 13 représentent des résultats préliminaires ainsi obtenus, sans sélection d'énergie, avec une source de sodium-22. La discrimination des signaux de coïncidences, transmis par cathode suiveuse, était effectuée soit par un circuit d'entrée d'échelle de 1000 dit "tiroir universel TU2" (fig. 12), soit par un amplificateur proportionnel et un discriminateur d'amplitudes stable et précis (fig. 13). L'une des mesures (fig. 12) est effectuée avec des scintillateurs plastiques et des photomultiplicateurs RCA 6810 (avec $R = 0$: voir fig. 8) et 7046 (avec $R = 700$ ohms). L'autre (fig. 13) est effectuée avec des cristaux de NaI(Tl), le même photomultiplicateur RCA 6810 (2300 V) et un EMI 9514 (1900 V). $R = 0$ pour chacun. La polarisation de grille nécessaire pour empêcher les impulsions d'un seul détecteur de faire débiter le tube est — 4 volts à — 5 volts.

Les résultats (absence de plateau de discrimination) montrent qu'une partie appréciable des coïncidences, dues à des impulsions qui ne sont

pas correctement mises en forme à la sortie des photomultiplicateurs, est éliminée par le discriminateur.

Les figures 15 et 16 représentent quelques uns des résultats obtenus avec une source de sodium-22 et deux cristaux de NaI(Tl) associés à des

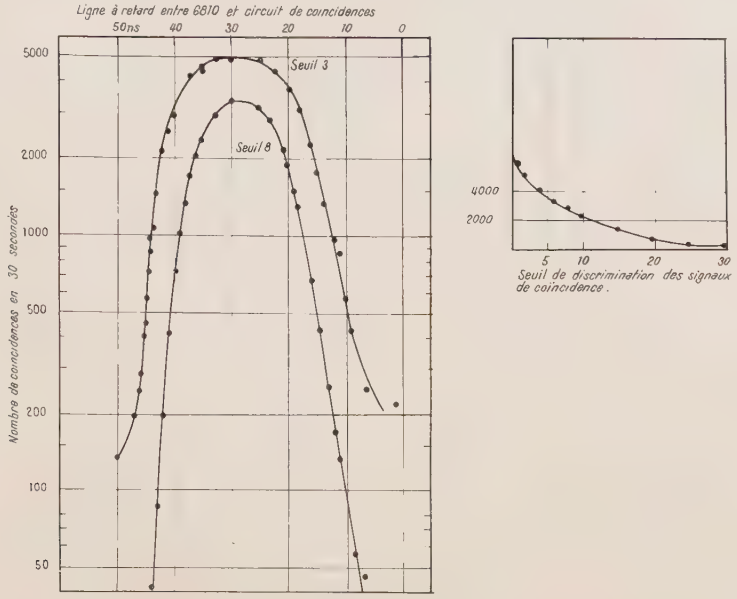


Fig. 13. Coïncidences produites par $^{22}$Na dans deux compteurs à NaI(Tl): photomultiplicateurs RCA 6810 et EMI 9514; circuit de la fig. 11.

Des mesures avec sélection d'énergie ont été effectuées avec le circuit de la fig. 14, dont le principe est le même mais qui utilise un transistor pnp, dont la jonction émetteur-base joue un rôle analogue à celui du cristal d'un circuit classique[8]). Sans sélection d'énergie, les circuits des figs. 11 et 14 donnent le même genre de résultats.

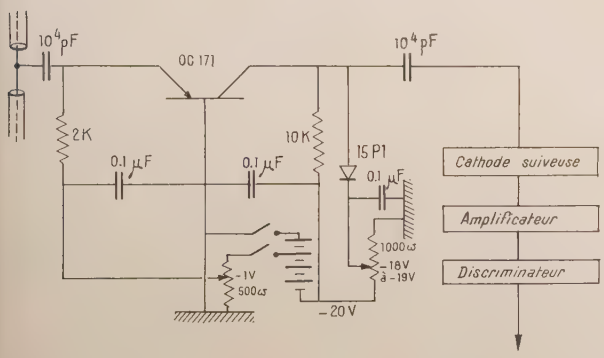


Fig. 14. *Circuit de coïncidences par addition de deux impulsions positives sur l'émetteur d'un transistor pnp.* Le cristal est destiné à éviter la saturation de l'amplificateur. Le seuil du discriminateur correspond à des impulsions de l'ordre du dixième de volt sur le collecteur.

photomultiplicateurs RCA 6810 et EMI 9514 dont les impulsions de 10 ème dynode sont analysées par un sélecteur à un canal et un sélecteur à dix canaux: l'enregistrement par ce dernier est conditionné par l'existence d'impulsions à la sortie du sélecteur à un canal et du discriminateur de signaux de coïncidences (fig. 14) dont la fig. 15 représente la courbe de discrimination (l'unité d'amplitude, non évaluée avec précision, est de l'ordre de quelques centièmes de volt sur le collecteur du transistor).

Pour les fig. 16a et 16b, le sélecteur à un canal,

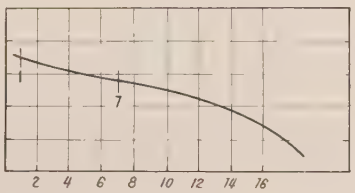


Fig. 15. Courbe de discrimination des coïncidences (seuil en unités arbitraires).

[8]) R. E. Bell, R. L. Graham et H. E. Petch, Can. J. Phys. **30** (1952) 35.

réglé aux environs de 500 keV, est associé au photomultiplicateur RCA 6810 et le sélecteur à dix canaux à l'EMI 9514. Les courbes représentées sont relevées pour deux canaux de ce dernier, aux environs de 500 et de 300 keV. Au-dessus de 300 keV, les courbes sont pratiquement confondues avec celle correspondant à 500 keV. Pour les énergies inférieures (jusqu'au-dessous de 100keV), elles ne présentent pas de plateau : toutes les coïncidences ne sont donc pas enregistrées.

Destinées surtout à contrôler la mise en forme réalisée par le montage de la fig. 8, ces mesures montrent qu'elle permet, si l'énergie abandonnée au scintillateur est assez élevée, de réaliser un circuit de coïncidences par addition (fig. 11 et 14) malgré l'exigence de ce type de circuit vis-à-vis de la standardisation des impulsions qui lui sont adressées.

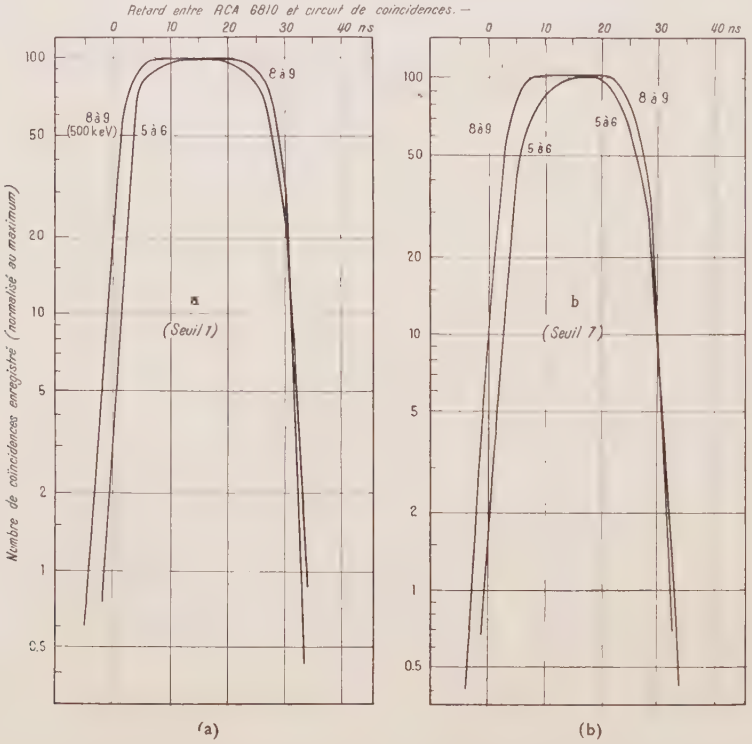


Fig. 16. Coïncidences entre deux compteurs à NaI (Tl) pour deux canaux d'amplitude (5–6 et 8–9) du photomultiplicateur EMI et pour deux valeurs (1 et 7 en unités arbitraires) du seuil de discrimination des signaux de coïncidence. Pour chacun des deux canaux (5–6 et 8–9) des courbes 16a et 16b, l'ordonnée 100 correspond au même nombre de coïncidences.

NUCLEAR INSTRUMENTS AND METHODS 9 (1960) 37–48; NORTH-HOLLAND PUBLISHING CO.

# SEDIMENTARY ROCK ANALYSIS BY CHARGED PARTICLE BOMBARDMENT

ROBERT F. SIPPEL and EVERETT D. GLOVER

*Socony Mobil Oil Company, Inc., Field Research Laboratory, Dallas, Texas*

Received 22 June 1960

Rapid analytic techniques are urgently needed in geochemical investigations where hundreds of analyses are often required. Methods based on nuclear reactions in the light elements are described for the analysis of Li, Be, B, C, O, F, Na, Mg, Al, and P. The reactions are induced by proton, deuteron, and alpha particle beams from a 2-MeV Van de Graaff machine. The methods are evaluated for sensitivity and accuracy by analysis of synthetic specimens of known composition and of National Bureau of Standards analyzed rocks samples. Errors arising from stopping power variations are shown to be small, in general not more than $\pm 2\%$. These methods exactly compliment the X-ray fluorescence technique, filling in the region inaccessible to the X-ray method. Used together, the methods can provide rapid instrumental analysis for virtually all elements in the periodic table to moderate sensitivity. Although sedimentary rocks receive the major emphasis in this paper, the methods are applicable (with due consideration for stopping power) to many other types of materials.

## 1. Introduction

Quantitative chemical analysis by neutron activation has been widely used in the past and is rapidly growing in importance today. A very extensive literature exists on the subject. In contrast, papers on quantitative chemical analysis by charged particle bombardment are very rare. These are limited to a few papers on the analysis of carbon and a few other elements in simple systems[1–5]). The use of charged particle reactions for the analysis of more complex systems seems to have been largely ignored. This paper shows that with proper consideration for stopping power effects charged particle reactions can be successfully used for analysis of light elements in sedimentary rocks or other complex systems. The rather recent application of the X-ray fluorescence methods of analysis[6]), provides an excellent analytic method for most elements. However, it has been impossible to extend the method into the very low end of the periodic table. Elements as light as aluminum and magnesium can be measured only with difficulty and with poor accuracy in samples with variable matrices.

In contrast, nuclear reactions induced by particles of a few MeV energy are most intense in the light end of the periodic table and decrease rapidly in intensity with increasing atomic number due to the Coulomb barrier effect, becoming negligible for elements much heavier than calcium. It, therefore, seems natural to inquire whether accurate and rapid nuclear methods of analysis can be devised for the light end of the periodic table. The question is given added importance, since several of the most important light elements are not amenable to neutron activation analysis or emission spectrography.

## 2. General Outline of Method and Experimental Details

First of all the problem is to find in the mass of nuclear data on the light elements a reaction for each element of interest which will produce some

[1]) J. J. Point, "Microdetermination of Carbon in Iron Irradiated by Protons", Radioisotopes Sci. Research Proc., Inter. Conf. Paris, **2** (1957) 180–9.

[2]) P. Süe and P. Albert, "Microdetermination of Sulphur by the $S^{32}$ (d,$\alpha$)$P^{30}$ Nuclear Reactions", Comptes Rendus Hebdomodaires des Séances de L'Academie des Sciences **242** (1956) 2461–62.

[3]) P. Süe, "Analytical Use of (d,n) and (d,p) Nuclear Reactions for Certain Light Elements", Comptes Rendus Hebdomodaires des Séances de L'Academie des Sciences **242** (1956) 770.

[4]) G. T. Seaborg and J. J. Livingood, J. Am. Chem. Soc. **60** (1938) 1784.

[5]) R. A. Gill, "Proton Activation Analysis in Determination of Submicrogram Amounts of Boron in Silicon", United Kingdom Atomic Energy Authority Rept., A.E.R.E. C/R 2758 1–50 (1958).

[6]) H. A. Liebhafsky, "X-ray Absorption and Emission", Analytic Chemistry **32** (1960) 240R–48R.

measurable type of radiation characteristic of the element in question. This identifying radiation can be prompt or delayed, consisting of particles or gamma-ray quanta. However, the methods will be most useful if they do not require chemical separations. For this reason, an additional qualification exists that each identifying radiation for an element be free of interferences from radiations arising from other elements commonly present in rocks. Charged particle analysis has a certain advantage in this respect, in that barrier penetration limits the production of radiation to elements in the light end of the periodic table. For elements heavier than calcium, the radiation yields are very small, becoming entirely negligible for elements heavier than iron. In contrast, neutron activation methods must contend with interferences arising from elements of all atomic weights, modified only by the highly variable cross sections. To minimize interferences we have at our disposal such factors as energy discrimination in counting of the radiations produced, half life of induced activities, range of beta rays, coincidence counting, and the use of thresholds for endothermic reactions. Reactions which are found useful for the light elements include (d,p) (d,n) (p,n) (p,$\alpha$) (p,p′) and ($\alpha$,n).

Experiments were performed to survey the light element reactions to select the best method of analysis for elements through phosphorus. Then using the best reaction for each element, the sensitivity and accuracy were evaluated with synthetic rocks of known composition and National Bureau of Standards analyzed rock samples. The synthetic rock samples were composed largely of $CaCO_3$ (simulated limestone) with addition of about 10 weight per cent of a binder. Suitable binders are KBr, KCl, and 325 mesh graphite. These materials not only served as binders but also imparted sufficient conductivity to the synthetic rock to allow the current integrator (measuring total beam to the target) to function. Various weighed quantities of "unknown" elements were added to the carbonate and binder matrix. The synthetic rock materials and National Bureau of Standards samples were thoroughly ground and mixed with the binder in a Spex Industries mixer mill using a stainless steel ball and vial. These mixtures were then pressed in a pellet die into consolidated disks $\frac{5}{8}$″ in diameter by $\approx 0.070$″ thick. The total weight of each specimen was 830 mg. It was found after considerable experimentation that the pellets could be pressed in a hardened stainless steel die without galding if the punch had greater than 0.003″ clearance in the die. Pressures on the order of 30 000 to 40 000 lbs/in.$^2$ applied for approximately 1 minute produced well-consolidated specimens. In routine operation, the same methods of specimen preparation can be used, or in the case of fine grained rocks it may prove feasible to simply bombard a cut surface of the rock. This would accelerate the specimen preparation phase considerably.

The specimens are introduced into the target chamber through a vacuum lock for rapid insertion and removal. Methods employing prompt radiation require the bombardment of one target at a time, and therefore it is imperative that the current integrator be working properly. To test the system, 9 specimens of highly purified Hanford graphite were bombarded by approximately 4 microcoulombs of 2-MeV deuterons. One specimen was bombarded every six minutes. Beginning 74 minutes after the first bombardment, the 10-minute $N^{13}$ activity was measured with an end window Geiger counter which afforded reproducible geometry. The results for the 9 different samples follow:

| *Counts/5 min* |
|---|
| 54 861 |
| 55 994 |
| 56 026 |
| 55 372 |
| 56 636 |
| 56 649 |
| 55 426 |
| 58 248 |
| 56 764 |
| Average 56 220 |
| rms deviation 1.67% |

Sources of error included in these results are energy shift in the Van de Graaff accelerator,

analyzing magnet current drift, counting geometry, and counter drift in addition to integrator instability. The results show adequate stability for all these factors, at least for highly conducting targets. We have found by experience that inaccurate results can arise from insufficient conductivity in the targets. This can be remedied by using a 10 or 15% addition of 325 mesh graphite.

For analysis involving delayed activities, we found the simultaneous bombardment of four or eight samples in a rotating target holder to be by far the best method of procedure. By including a standard target with the unknowns, one eliminates errors caused by the current integrator and in addition, the requirement on constant or even known bombarding energy is removed. The rotating target mechanism permits rapid introduction and removal of targets and measurement of target current at 288 rpm rotation. Counting was accomplished by a number of standard instruments which will not be reviewed here. Detectors used were NaI crystals, $Li^6I$ crystals, Geiger counters, and $BF_3$ proportional counters.

Applications of equipment which are in any way unique will be discussed further under the specific element.

### 3. Matrix Effects

Every analytic method has its matrix effects, in that the methods are somewhat sensitive to the chemical environment in which the unknown element is found. Such matrix effects can lead to large errors, i.e., several hundred per cent in the case of emission spectrography, or only second order errors as is the case in thermal neutron activation. In the charged particle methods the matrix effect arises from the variability of stopping power with changing specimen composition. The influence of stopping power may be understood from the following discussion. Although the arguments are presented for sedimentary rocks (the system of greatest interest to the authors), they are quite general and may be applied to any system whatever to evaluate the effects of stopping power.

If one can find a suitable radiation characteristic of a given element ($E_j$) and free from important interferences, then this reaction will be useful for analytic purposes if the yield of radiation $Y_j$ is proportional to the weight fraction of the element present in the specimen. Now the yield is given by

$$Y_j = \int_{E_0}^{0} \frac{N_j \sigma j(E)}{(1/\rho)\dfrac{\mathrm{d}E}{\mathrm{d}x}(E)} \mathrm{d}E \tag{1}$$

where $N_j$ = number of disintegrable atoms/g, $\sigma_j(E)$ = cross section for production of desired radiation or activity. $\rho$ and $\mathrm{d}E/\mathrm{d}X(E)$ are the density and stopping power of the rock matrix, respectively. $\sigma_j(E)$ and $\mathrm{d}E/\mathrm{d}X(E)$ are functions of energy. In fact the cross section may be a rapidly changing function as is the case where resonances occur. Now our conditions required for accurate analysis by charged particle reactions is that the radiation yield $Y_j$ be proportional to $N_j$. In other words the radiation yield must be invariant to changing rock matrix composition. In order for this to obtain, it is sufficient that for any two rocks

$$\frac{1}{\rho} \times \frac{\mathrm{d}E}{\mathrm{d}X}\bigg|_{\text{Rock 1}} = \frac{1}{\rho} \times \frac{\mathrm{d}E}{\mathrm{d}X}\bigg|_{\text{Rock 2}}$$

and that this equality hold for all energies. Now the stopping power for one element may be written as

$$-\frac{\mathrm{d}E}{\mathrm{d}X} = \varepsilon N \tag{2}$$

where $\varepsilon$ is the stopping cross section[7]), and $N$ the number of stopping atoms per $cm^3$. If one has a homogeneous mixture of elements, the stopping power of this material may be found by the prescription

$$-\frac{\mathrm{d}E}{\mathrm{d}X} = \sum_i \varepsilon_i N_i \tag{3}$$

where $\varepsilon_i$ and $N_i$ are the stopping cross sections and number of atoms of each element per $cm^3$ in the sample. Eq. (3) may be recast into more useful form by introducing the idea of a partial density

$$\rho_i = \frac{N_i}{N_0} A_i \,. \tag{4}$$

The partial density $\rho_i$ is the weight of the $i^{\text{th}}$ element per cm$^3$, $N_0$ Avagadro's number and $A_i$ the atomic weight. Introducing this into eq. (3) and dividing by macroscopic density one obtains the expression

$$-\frac{1}{\rho}\frac{dE}{dX} = \sum_i \Omega_i \frac{\rho_i}{\rho} \tag{5}$$

where

$$\Omega_i = \varepsilon_i \times \frac{N_0}{A_i}.$$

Whereas the quantities $\varepsilon_i N_i$ are formally analogous to partial linear absorption coefficients, the quantities $\Omega_i \rho_i/\rho$ are analogous to partial mass absorption coefficients. Notice that $\rho_i/\rho$ is just the weight fraction of element $i$ in the sample.

A theoretical expression for $\varepsilon$ has been given by Bethe[7]) as follows:

$$\varepsilon = \frac{4\pi e^4 z^2}{mv^2} Z \log\left(\frac{2mv^2}{I}\right) \tag{6}$$

where $ez$ is the charge of the incident particle, $v$ its velocity, $Z$ is the nuclear charge, and $m$ the mass of the electron. $I$ is the mean ionization potential of the atom. This equation has been derived by application of the Born approximation, and applies strictly to high energies. At low energy, corrections must be applied for binding effects in the atom and for pickup and loss of electrons. However, the expression is valid to first order down to 0.1 MeV for protons. The quantity $I$ increases with increasing $Z$, rising from 15.6 eV for hydrogen to 276 eV for copper.

It is clear then from 5 and 6 that the condition on nonvariability of the mass stopping power is not satisfied exactly. However, closer examination shows that the situation is not by any means hopeless. First of all, oxygen makes up about 50% of all sedimentary rocks. Furthermore, the major elements remaining are distributed over a rather narrow range of atomic numbers. The simplest way of evaluating the effects of stopping power is to calculate the stopping power of different rocks at various energies. Table 1 shows the results of such calculations for the typical sandstone, limestone, and shale[8]). The calculations are based on application of eq. (5), using fig. 1 for the determination of the $\Omega_i$. The data points are from the compilation of Fuchs and Whaling[9]). The individual $\Omega_i$ were taken from the smooth curves. As seen from the table, the stopping powers are essentially equal within $\pm$ 0.8% at all energies. This would be the correct estimate of errors which stopping power could cause, if

Table 1
Mass stopping power for homogeneous sandstone, limestone, and shale of average composition given by Mason[6])

| | $\frac{1}{\rho}\frac{dE}{dX}$ keV cm$^2$/mg | | |
|---|---|---|---|
| Proton energy (MeV) | Typical shale | Typical limestone | Typical sandstone |
| 2.0 | 120.69 | 118.72 | 120.64 |
| 1.5 | 147.9 | 145.3 | 147.7 |
| 1.0 | 184.6 | 182.0 | 184.4 |

one could completely homogenize a rock sample on the microscopic scale before bombardment. This, however, is not the case since the size of the rock particles is of the order of the range of the bombarding particles. For this reason one must consider stopping power effects in individual mineral grains. Table 2 shows the stopping power of the common minerals in sedimentary rocks[10]), for 2, 1, and 0.75-MeV protons. The results are surprising uniform both in value and in energy dependence. The maximum deviations are $\pm$ 5% from the average at all energies. However, since an unknown element will in general be distributed over a number of mineral types, and since the true state of affairs lies between the results of table 1 and table 2, we conclude that the accuracy limitations imposed by stopping power effects will be of the order of 2% for sedimentary rock analysis. Since this order of accuracy is adequate for almost all purposes, the effects of

[7]) M. S. Livingston and H. A. Bethe, Rev. Mod. Phys. **9**, No. 3 (1937) 271.

[8]) Brian Mason, Principles of Geochemistry (John Wiley & Sons 1958) p. 147.

[9]) R. Fuchs and W. Whaling, "Stopping Cross Sections", Kellogg Radiation Laboratory, California Institute of Technology, Pasadena, California.

[10]) F. J. Pettijohn, Sedimentary Rocks (Harper & Bros., N.Y., 1957).

TABLE 2

Mass stopping power for the principal minerals found in sedimentary rocks[8])

| Mineral | Chemical composition | % in sedimentary rock | $\frac{1}{\rho}\frac{dE}{dX}$ keV cm²/mg | | |
|---|---|---|---|---|---|
| | | | Bombarding energy | | |
| | | | 2 MeV | 1 MeV | 0.75 MeV |
| Quartz | $SiO_2$ | 34.8 | 121 | 184 | 218 |
| Orthoclase | $KAlSi_3O_8$ | 11.02 | 118 | 179 | 211 |
| Albite | $NaAlSi_3O_8$ | 4.55 | 121 | 185 | 218 |
| Sericite | $KAl_2(Si_3Al)O_{10}(OH)_2$ | 15.11 | 121 | 184 | 218 |
| Kaolin | $Al_2Si_2O_5(OH)_4$ | 9.22 | 126 | 195 | 231 |
| Calcite | $CaCO_3$ | 4.25 | 117 | 179 | 211 |
| Dolomite | $CaMg(CO_3)_2$ | 9.07 | 121 | 185 | 220 |
| Limonite | $FeO(OH)\cdot H_2O$ | 4.00 | 115 | 174 | 207 |
| Gypsum | $CaSO_4\cdot 2H_2O$ | 0.97 | 124 | 190 | 226 |
| Chlorite | $Mg_5Al(AlSi_3O_{10})(OH)_8$ | 5.29 | 126 | 185 | 230 |
| | | | 120.9 av | 185.1 av | 219 av |

stopping power need not be considered further in connection with sedimentary rock analysis. The only remaining question concerning stopping power involves the small volume of the specimen actually sampled, since the range of the bombarding particles is so small. This point, however, turns out to be unimportant so long as macroscopic homogeneity can be attained, since in a target made from 325 mesh rock material something in excess of $10^4$ individual grains will be sampled. That it is possible to achieve homogeneity on the required scale will be seen from the results which follow.

## 4. The Major Elements (C, O, Na, Mg, Al, Si, P)

### 4.1. CARBON

The choice of a reaction for the analysis of carbon is not difficult. The $C^{12}(d,n)N^{13}$ reaction has all the desirable attributes: convenient half life (10 min), large cross section over a large energy interval, and small possibilities of interferences. For detection of the $N^{13}$ produced, and for other $\beta^+$ emitters as well, a coincidence counting technique was used. Since the annihilation quanta are emitted in strictly opposite directions, coincidence counting can be employed without great losses in counting rate. Two $2\frac{1}{2}'' \times 2\frac{1}{2}''$ sodium iodide crystals were rigidly mounted so that specimens could be reproducibly inserted between them. The separate channels were fed to an R.I.D.L. coincidence circuit, having a measured resolving time of 0.37 microseconds. In addition to the coincidence requirement, each channel accepted only pulses falling in the interval 375–625 keV. This technique eliminates all $\beta^-$ emitting interferences. Carbon is in general abundant enough in sedimentary rocks to completely dominate the possible $\beta^+$ emitting interferences, mainly those arising from $N^{14}$, $B^{10}$, and $O^{17}$. The method was tested using a KCl matrix with various known additions of carbon in the form of calcium carbonate. Since calcium carbonate is only 12% carbon, a large weight fraction of carbonate had to be introduced for high carbon percentages. This causes a considerable change in stopping power for which correction must be made. These specimens were bombarded with 1.75 MeV deuterons in the eight target rotator for a total of approximately 2 microcoulombs per target. This energy was selected to eliminate the 66 sec $\beta^+$ activity from $O^{16}(d,n)F^{17}$. The specimens were counted on a 75-second module, counting for one minute, with 15-second intervals to change

TABLE 3

Results obtained from the bombardment of synthetic rocks of known composition

| Element | Reaction | Particle detected | $T_{\frac{1}{2}}$ | Concentration range studied (in weight %) | Number of Specimens in range | Total bombardment $\mu$ coulomb/target | Counting time (minutes) | Counts from 1 wt % of element | Intercept in % of unknown | rms deviation from straight line in % † | Estimated limit of detection in % †† |
|---|---|---|---|---|---|---|---|---|---|---|---|
| Lithium | $Li^7(p,n)Be^7$ | Neutron | Prompt | 0.02–0.9 | 7 | 100 | Prompt | 27 940 | 0.005 | 2.5 | 0.01 |
| Beryllium | $Be^9(\alpha,n)C^{12}$ | (4.3 MeV)$\gamma$ | Prompt | 100 | 1 | 20 | Prompt | 10 000 | — | — | 0.01 |
| Boron | $B^{10}(\alpha,n)N^{13}$ | (0.5 MeV)$\gamma$ | 10 min | 1 | 1 | 200 | 2 | 1 357 | — | — | 0.1 |
| Carbon | $C^{12}(d,n)N^{13}$ | (0.5 MeV)$\gamma$ | 10 min | 0.02–9.0 | 9 | 4 | 1 | 11 500 | 0.012 | 3.7 | 0.005 |
| Fluorine | $F^{19}(p,\alpha)O^{16}$ | (6 & 7 MeV)$\gamma$ | Prompt | 0.02–2.5 | 8 | 40 | Prompt | 225 000 | 0.005 | 5.0 | 0.01 |
| Sodium | $Na^{23}(d,p)Na^{24}$ | (1.4 & 2.8 MeV)$\gamma$ | 15 h | 0.05–2.0 | 6 | 400 | 5 | 19 000 | 0.01 | 1.0 | 0.01 |
| Magnesium | $Mg^{26}(d,p)Mg^{27}$ | (0.84 & 1.01 MeV)$\gamma$ | 9.5 min | 0.1–4.0 | 7 | 200 | 2 | 6 500 | 0.02 | 3.5 | 0.05 |
| Aluminum | $Al^{27}(d,p)Al^{28}$ | (1.78 MeV)$\gamma$ | 2.3 min | 00.1–3.0 | 6 | 25 | $\frac{1}{2}$ | 6 500 | 0.005 | 4.5 | 0.02 |
| Phosphorus | $P^{31}(d,p)P^{32}$ | (1.7 MeV)$\beta^-$ | 14.3 d | 0.1–3.0 | 6 | 400 | 5 | 1 100 | 0 | 4.2 | 0.01 |

† Includes specimen preparation errors. †† Estimated for average sedimentary rock distribution of interferences, under present experimental conditions. Not to be interpreted as the absolute limit of detectability.

targets. The eight targets were counted in sequence and as a check on the presence of activities other than 10 minute $N^{13}$ two complete counting sequences were made. Results corrected




Fig. 1. Mass stopping power for protons of various energies. Data points from compilation of Fuchs and Whaling[9]).

for stopping power effects and for radioactive decay for samples containing 0.1, 0.3, 0.5, 1.0, 3.0, 5.0, 7.0, and 9.0%† carbon are shown in fig. 2. The rms deviation of the points from a straight line is 3.7%. The intercept indicates the presence of about 125 ppm carbon in the KCl. The above and other information on the carbon analysis of synthetic specimens is shown in table 3 with similar information for the other elements. Two of the Bureau of Standards analyzed samples were run as a check on the method using reagent grade $CaCO_3$ as a standard. The results are given in table 4 along with similar results for the other elements.

Although there were no other analyzed specimens at hand for an accurate check of the method, we did run repeatability experiments on several clay minerals. The results showed rms deviations of the order of 3% for carbon analyses of samples containing 0.1% carbon or more. However, a metabentonite sample having a large percentage of quartz (74%) showed an 18% rms deviation. We believe this arises from the difficulty in grinding quartz to minute grain size. The presence of large quartz grains leads to macroscopic segregation, which is shown by the

† All percentages in this paper pertaining to element concentrations are percentages by weight.

TABLE 4

Results from bombardment of National Bureau of Standards analyzed rock samples

| Element | Argillaceous limestone # 1A | | Dolomite # 88A | | Plastic clay # 98 | | Flint clay # 97 | |
|---|---|---|---|---|---|---|---|---|
| | (Wt %) N.B.S. | (Wt %) This investigation | (Wt %) N.B.S. | (Wt %) This investigation | (Wt %) N.B.S. | (Wt %) This investigation | (Wt %) N.B.S. | (Wt %) This investigation |
| Carbon | 12.97 | 12.77 | 9.76 | 9.64 | | | | |
| Sodium | 0.29 | 0.30 | 0.060 | 0.062 | | | | |
| Magnesium | 1.31 | 1.22 | 12.89 | 12.46 | 0.43 | 0.38 | 0.16 | 0.16 |
| Aluminum | 2.24 | 2.26 | 0.036 | 0.059 | | | | |
| Phosphorus | 0.065 | 0.063 | 0.0013 | — | | | | |

large rms deviation in this case. These ideas are substantiated by the fact that on increasing the grinding time to 5 minutes and treating the

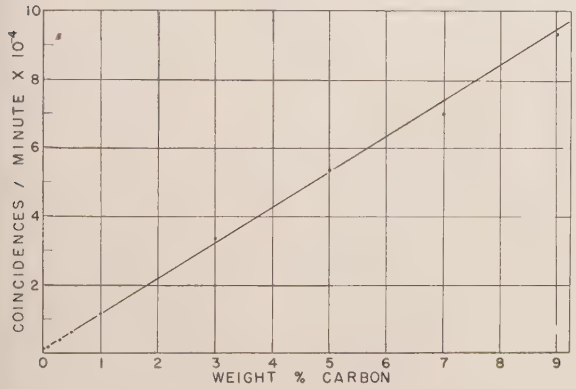


Fig. 2. Deuteron activation analysis of carbon in synthetic rocks of known carbon composition.

samples gently to avoid segregation, the rms deviation dropped to about 6%. To reduce this figure further for samples of high quartz content, it may be necessary to sieve such samples to assure that all particles are 325 mesh or smaller.

### 4.2. OXYGEN

There are numerous possibilities for the analysis of oxygen. All sediments contain approximately 50% oxygen. Of the common minerals in sediments, all have oxygen contents falling between 45 and 55%. In conventional analysis techniques, oxygen is determined by difference. A direct measurement of oxygen can be made using the $O^{16}(d,p)O^{17}$ reaction, giving a very intense prompt 875-keV gamma ray or by the $O^{16}(d,n)F^{17}$ reaction yielding 66 second $\beta^+$ radiation. In addition to the charged particle methods, oxygen can be measured by activation with 14-MeV neutrons by the $O^{16}(n,p)N^{16}$ reaction yielding the 7.6 second $\beta^-$ emitter $N^{16}$. No experiments on oxygen were performed.

### 4.3. SODIUM

There are three possibilities for the analysis of sodium which were all investigated. These are:

1. $Na^{23}(p,p')Na^{23*}$ $\quad Na^{23*} \rightarrow Na^{23} + \gamma$ (0.439 MeV)
2. $Na^{23}(p,\alpha)Ne^{20*}$ $\quad Ne^{20*} \rightarrow Ne^{20} + \gamma$ (1.63 MeV)
3. $Na^{23}(d,p)Na^{24}$ $\quad T\frac{1}{2} = 15$ h, $\gamma = 1.37$, 2.75 MeV.

The first of these reactions has a large yield; however, interferences from annihilation radiation caused by proton capture and from the 478-keV radiation caused by inelastic scattering excitation of the first excited state of lithium, in addition to general background in this region due to the production of higher energy radiations, rule out the reaction as a practical analytic technique.

The second reaction, although much weaker than the first, suffers much less from interference effects and can in fact be used for sodium analysis in the range of a few tenths of a per cent sodium or more. The principal interference is from fluorine which produces background radiation in the 1.63-MeV region. Bureau of Standards analyzed argillaceous limestone 1A was analyzed by this means, using a 0.5% known

target for standard. Both targets were bombarded for 400 microcoulombs and the prompt radiation detected with a sodium iodide crystal the pulses, being fed to a Penco 100-channel analyzer. Analysis involves integration of the total absorption peak at 1.63 MeV and subtracting the background by smooth extrapolation of the background spectrum across the 1.63-MeV peak. By this means we obtained:

National Bureau of Standards 0.29%
(p,$\alpha$) reaction 0.26%.

The main reason for discarding method 2 was simply that the third method turned out to be so much superior. The deuteron activation technique is more sensitive, faster in operation, and interferences are negligible. In practice eight targets are bombarded simultaneously in the rotating target holder for a total of 400 microcoulombs/target. The targets are set aside and counted the next day in a well scintillator crystal fed to a scaler. An integral bias was used at 1.5 MeV. The resulting data from bombardment of six known mixtures from 0.05 to 2% sodium is shown in fig. 3. Numerical data from this curve are shown in table 3, and results from analysis of National Bureau of Standards samples are shown in table 4.

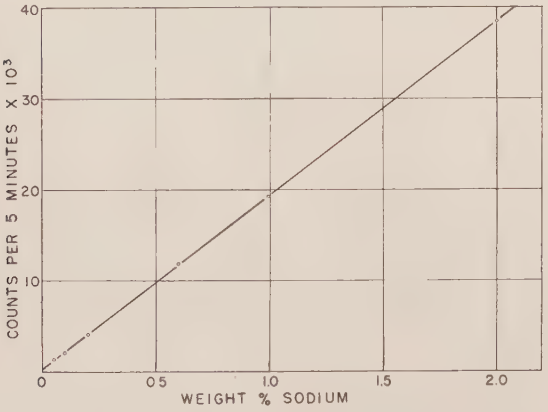


Fig. 3. Deuteron activation analysis of sodium in synthetic rocks of known sodium composition, counting 44 hours after bombardment.

4.4. MAGNESIUM

Only two reactions appear to be at all feasible for the analysis of magnesium. These are:

1. $Mg^{24}(p,p')Mg^{24*}$ $\quad Mg^{24*} \rightarrow Mg^{24} + \gamma$ (1.3 MeV)
2. $Mg^{26}(d,p)Mg^{27}$ $\quad T\frac{1}{2} = 9.5$ min, $\gamma = (0.84, 1.01$ MeV).

The first reaction is useful for specimens rich in Mg (> 2%) and providing the contents of sodium and fluorine are low. The Bureau of Standards dolomite 88 A was analyzed in this way, integrating over the 1.37-MeV full energy peak. Our result, 12.46% Mg, agrees within 3½% of the Bureau value of 12.89%. However, analysis of the argillaceous limestone 1A by this method was impossible because of the low magnesium content (1.31%), and interference from sodium (present at 0.3%). The method should be useful for magnesium analysis of dolomitic limestone, but not for general sedimentary rock analysis.

The second method of magnesium analysis produces strong radiation even though it uses the 11% abundant isotope. However, for general rock analysis, carbon is a serious interference. Even though the carbon produces radiation of only 511-keV energy (annihilation radiation), the carbon (d,n) cross section is so enormous that a pulse distribution is produced extending above 1-MeV energy. As a result the 0.84 and 1.01-MeV gamma-ray lines from small amounts of magnesium become lost. The only other serious interference is from $Al^{27}(d,p)Al^{28}$, which can be eliminated by half life considerations. In counting the specimens, it is important not to use greater than $2\pi$ geometry since then a sum peak from the annihilation quanta from $N^{13}$ will be superimposed on the 1.01-MeV line from magnesium. Since magnesium is a very important element from many viewpoints, it was decided to attempt the removal of the interfering $N^{13}$ activity, so as to obtain a general method of analysis in sedimentary rocks. After considerable experimentation it was found that the following procedure successfully removed all but a trace of the $N^{13}$ activity. Specimens were bombarded in the four target rotator to a total of $\approx$ 200 microcoulombs/target. The specimens were removed and digested in concentrated phosphoric acid. Upon complete dissolution, concentrated nitric acid was added and the specimens reheated until the mixture stopped bubbling or fuming, at which time the specimens were cooled to room temperature and made up to a standard volume using concentrated phosphoric acid. It

was found that neither treating with nitric or phosphoric acids alone, nor using both in the reverse order effected sufficient removal of $N^{13}$ activity. The specimens were counted by placing the beakers on a 3″ × 3″ sodium iodide crystal

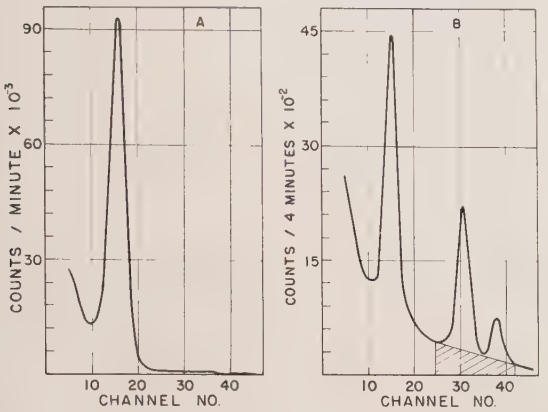


Fig. 4. a. Spectrum from synthetic limestone containing 1% Mg untreated; b. Spectrum from synthetic limestone containing 1% Mg treated for removal of $N^{13}$.

in reproducible geometry. The specimens were counted for two minutes each, recording the spectra on a 100-channel analyzer. About 20 minutes is required for the chemical separation. Fig. 4 shows the effect of chemical separation by comparing the spectra obtained from a target containing 1% Mg in a carbonate matrix counted without separation and from an identical target treated first to remove $N^{13}$ activity. The measure of magnesium content is obtained by adding counts in the channels covering the 0.84 and 1.01-MeV peaks, and subtracting the shaded area of fig. 6. Two sets of four targets were analyzed containing 0.1, 0.3, 0.5, 1.0, 2.0, 3.0, and 4.0% magnesium by weight. Each group contained a 1% target which was used for standardization. Corrections were applied for block time on the 100-channel analyzer (1% or less) and for decay. Results for synthetic specimens are shown in table 3 and for National Bureau of Standards analyzed samples in table 4.

### 4.5. ALUMINUM

Although a rather attractive method for aluminum analysis by thermal neutron activation has previously been developed[11]), it was decided to investigate the possibilities of charged particle analysis in the belief that, in some cases, the charged particle techniques might show unique advantages. The only real possibility for analysis is the $Al^{27}(d,p)Al^{28}$ reaction forming the 2.3 min $Al^{28}\beta^-$ emitter accompanied by a 1.78 MeV $\gamma$ ray. This is the same isotope as that formed by thermal neutron capture. However, deuteron bombardment induces considerably greater activity. Six known samples ranging from 0.1 to 3% aluminum were bombarded along with specimens of dolomite 88A and argillaceous limestone 1A in the 8-target rotator. Bombardment was for 2 minutes, giving about 25 microcoulombs/target of 2.1-MeV deuterons. The specimens were counted, starting at $1\frac{1}{2}$ minutes after the end of bombardment, for 30 seconds each with a total counting module of 47 seconds. Counting was done with a 3″ × 3″ NaI crystal, using an integral bias set at 1.4 MeV. A half-inch lead absorber was used to reduce the annihilation radiation from $N^{13}$ to a tolerable level. Under these conditions, the only interference of any importance is from $Na^{24}$. By recounting the specimens an hour later, the interference from sodium was evaluated. It turns out to be quite small. Of 14 454 counts coming from 2.3% aluminum in the argillaceous limestone 1A, 58 came from the 0.3% sodium content. It, therefore, appears that no correction need be made for rocks containing small sodium content. For larger sodium contents, a small correction may have to be applied, in no case greater than 5%. Results are shown in tables 3 and 4. Measurement of three different samples of dolomite 88a agreed within two per cent.

### 4.6. SILICON

Fortunately, an attractive neutron method for silicon analysis has previously been developed[11]), for no charged particle method has proven practicable. The $Si^{29}(d,n)p^{30}$ reaction is ruled out by interferences, and the $Si^{30}(d,p)Si^{31}$ reaction producing 1.48-MeV $\beta^-$ particles and a very weak

[11]) R. L. Caldwell and W. R. Mills, Jr., Nucl. Instr. and Meth. **5**, No. 5 (1959) 312.

gamma ray can only be separated from other $\beta^-$ emitters by half-life measurements. Such a procedure is impractical and would also be inaccurate.

### 4.7. PHOSPHORUS

The only possibility for phosphorus analysis seemed to lie in the $P^{31}(d,p)P^{32}$, $T_{\frac{1}{2}} = 14.5$ days, $\beta^- = 1.71$ MeV. Even though phosphorus is far up the periodic table for 2-MeV deuterons and the half life is so long, this reaction produces sufficient radiation to form the basis of a very sensitive method for phosphorus analysis. In practice, eight targets are bombarded in the rotating target holder for a total of 400 microcoulombs/target, then are set aside for a period of one week to 10 days, then counted in an end window Geiger counter, using a 68.3 mg/cm$^2$ aluminum absorber to remove any contribution from 87-day $S^{35}$. Results for synthetic samples and the National Bureau of Standards samples are shown in tables 3 and 4.

## 5. The Minor Elements Li, Be, B, N, F

Excellent methods of analysis for all these elements with the exception of nitrogen have been found. However, the practicality of the methods for general sedimentary rock analysis is still somewhat in question. The reason for this is that most of the above elements are present in the average sediment in very small amount. There was no readily available source of rock samples accurately analyzed for the minor elements, so evaluation is more difficult. Radiation yields for the Li, Be, and F reactions can be considerably enhanced by improvements now being incorporated into the target chamber arrangement, which will permit much closer spacing between the target and counters.

### 5.1. LITHIUM

Possible reactions for the analysis of lithium are:

1. $Li^7(p,n)Be^7$ $E_{\text{threshold}} = 1.88$ MeV
2. $Li^7(p,\gamma)Be^8$ + 17-MeV $\gamma$ rays
3. $Li^7(p,p')Li^{7*}$, $Li^{7*} \rightarrow Li^7 + \gamma(0.478\ \text{MeV})$.

Of these, the proton capture reaction turned out to be too weak for use and the inelastic scattering reaction, though possessing a very large cross section, was discarded because of interferences.

The (p,n) reaction in $Li^7$ is unique in that it is the only light element which can produce neutrons under 2-MeV proton bombardment. Going up the periodic table, no nuclide below $Cl^{37}$ ($Q = -1.5999$ MeV) can interfere. The next important nuclude from an interference standpoint is $K^{41}$ ($Q = -1.221$ MeV), which although abundant to only 6.8% can interfere by virtue of its high content in rocks and its low $Q$. $Ca^{48}$ ($Q = -0.513$ MeV) abundance 0.18% is another possibility as is $Mn^{55}$ ($Q = -1.012$ MeV) because of its high abundance (100%) and low $Q$. However, the cross sections of all these interferences should be very small compared to lithium, and above manganese, interferences should be entirely negligible.

The method was tested using known quantities of $LiCO_3$ dispersed in a matrix of $CaCO_3$ using graphite for a binder to eliminate interference from K. The specimens were bombarded with 2-MeV protons for a total of 100 microcoulombs each. The neutrons were measured by a $BF_3$ proportional counter on axis with the beam, and covered by a ring of lucite 4″ in diameter by 2″ thick. Specimens ranging from 0.02 to 0.9 per cent lithium were analyzed. The results are shown in fig. 5 and in table 3.

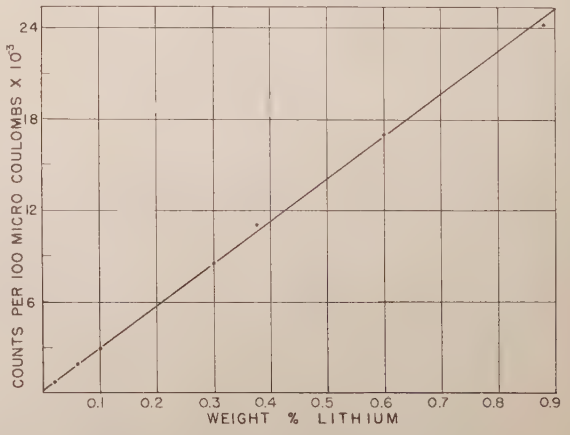


Fig. 5. Lithium analysis by the $Li^7(p,n)Be^7$ reaction in synthetic rocks of known lithium content.

To evaluate interference effects, targets of K, Cl, and $MnSO_4$ were also bombarded. Yields for 1% of lithium and the principal interfering elements are:

| Element | Neutron counts per 100 $\mu$ coulombs per % element |
|---|---|
| Lithium | 27 940 |
| Calcium | 2 |
| Potassium and/or chlorine | 100 |
| Manganese | 64 |

The present setup will permit analysis of Li down to $\approx 0.01\%$, if corrections are applied for K and Cl content. Proposed changes in target chamber design and use of a $He^3$ neutron proportional counter will raise the total counting rates at least a factor of 25, and may improve the sensitivity considerably.

### 5.2. BERYLLIUM

Beryllium is present to only a few ppm in most sedimentary rocks. It is absolutely unique in that it is the only element in the periodic table which can produce photoneutrons using gamma rays of 1.8-MeV energy. An attempt was made to observe photoneutrons from a beryllium disk placed in the target holder behind an aluminum disk which was bombarded with deuterons to produce a strong source of 1.78-MeV gamma rays. The effect was found to be much too weak to serve as an analytic technique using aluminum-28 produced with our 2-MeV accelerator.

The $Be^9(\alpha,n)C^{12}$ reaction producing 4.43-MeV gamma rays is apparently free from important interferences and from our experiments we conclude that it could be used to analyze for beryllium to about 0.01%. This, however, is not sufficiently sensitive for sedimentary rocks in general.

### 5.3. BORON

The two principal possibilities for boron analysis are:

1. $B^{10}(\alpha,n)N^{13}$ $\quad T_{\frac{1}{2}} = 10$ min $\beta^+$
2. $B^{10}(d,n)C^{11}$ $\quad T_{\frac{1}{2}} = 20.5$ min $\beta^+$ .

The $(\alpha,n)$ reaction is excellent for analyses to 0.1% boron, but lacks sensitivity to get into the range of boron contents encountered in the average sedimentary rock. In applying the method, we found that molecular deuteron contamination of the alpha particle beam produced a considerable interference from deuteron activation of carbon in the target. Extended running of the machine on helium would be required to eliminate the deuteron contamination, although the effect can be reduced by lowering the bombarding energy to 1.6 MeV. Very little loss occurs from the alpha particle reaction since the principal yield is from a narrow resonance at 1.52 MeV. At the same time, the deuterons are reduced to 800 keV where the (d,n) yield is considerably lower.

Reaction 2 is capable of producing very intense $\beta^+$ radiation which would permit analysis to a few parts per million, but for the interference from other elements, notably $N^{13}$ from the carbon (d,n) reaction. There is still the possibility of separating the $C^{11}$ after bombardment. This was tried by digesting the target in acid, trapping the $CO_2$ evolved in an ascarite filter, then counting the ascarite filter in a 3″ well crystal. Separation of $C^{11}$ from the $N^{13}$ was not sufficiently complete by this simple technique. Any proposed method of separation, either before or after bombardment, will depend on the chemical form of boron in sediments, which is is probably variable and presently unknown. Any proposed separation process should, therefore, be evaluated using natural rock materials. The possibilities will be investigated further using naturally occurring rocks, and in conjunction with spectrographic methods.

### 5.4. NITROGEN

No experiments were performed on nitrogen. A possible reaction is $N^{14}(d,n)O^{15}$, $T_{\frac{1}{2}} = 2.1$ min, $\beta^+(1.7$ MeV). However, again separation of the activity after bombardment is necessary to eliminate interferences.

### 5.5. FLUORINE

Certainly the most promising method for fluorine analysis is in observation of the 6 and

7-MeV gamma radiation produced by the $F^{19}(p,\alpha)O^{16*}$, $O^{16*} \rightarrow O^{16} + \gamma$ reaction. The gamma-ray spectrum produced is shown in

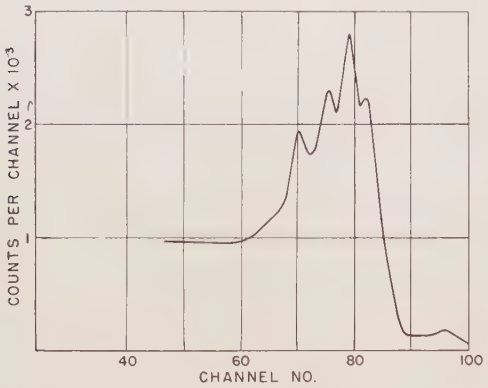


Fig. 6. Gamma-ray spectrum from 200 microcoulomb proton bombardment of a target containing 0.1% fluorine.

fig. 6. This is the spectrum obtain from a 200 microcoulomb bombardment at 2 MeV of a 0.1% fluorine target. To test the method specimens containing from 0.02% to 2.5% fluorine were bombarded for 40 microcoulombs each, counting the gamma rays with a scintillation counter, using an integral bias of 4 MeV. The targets were $CaCO_3$ with a graphite binder, to assure proper functioning of the integrator. Results are given in table 3. The previously mentioned changes in the target chamber will increase the counting rate from fluorine by a factor of at least 25. Interferences will be mainly from proton capture and should be small. They will be more thoroughly investigated with the new target chamber arrangement. It is already certain, however, that the method will extend into the useful region for sedimentary rock analysis.

**Acknowledgements**

The authors wish to express their appreciation to Professor T. W. Bonner for helpful discussions, to C. M. Wall and B. E. Stallings for assistance in data taking and specimen preparation, and to the management of Socony Mobil Oil Company, Inc. for permission to publish this work.

NUCLEAR INSTRUMENTS AND METHODS 9 (1960) 49–54; NORTH-HOLLAND PUBLISHING CO.

# IMPROVED FOCUSSING NEAR THE CYCLOTRON SOURCE

W. I. B. SMITH

*Research School of Physical Sciences, The Australian National University, Canberra*

Received 11 July 1960

The vertical focussing of a cyclotron beam near the ion source has been experimentally investigated as a function of the phase of the beam relative to the dee voltage. Considerable improvement in the vertical focussing of the beam has been obtained by offsetting the ion source and puller by 20° to the dee edge, and thus retarding by 20° the phase of the first turn.

## 1. Introduction

In a conventional cyclotron with the usual ion source geometry the useful beam crosses the dee gaps on the early turns slightly before the peak dee voltage is reached. Since the magnetic field must decrease with radius to provide vertical focussing on the outer turns, and because of the relativistic decrease of the orbital frequency of the ions with increasing energy, the beam near the ion source rotates faster than the radio frequency accelerating voltage. The beam shifts phase in this region such that subsequent dee crossings occur at phases successively earlier than the peak dee voltage, and where the accelerating voltage is increasing as the beam crosses the gap. The net vertical electrical forces on the beam under these conditions are defocussing[1]) and much beam is lost. The similar time variation of the electric field defocussing in the linear accelerator has been overcome by the insertion of grids on the exit sides of the accelerating gaps. In the cyclotron the same method has been applied to give vertical focussing by programming the early turns through a series of vertical bars on the down beam side of the dee gaps[2,3]). While providing good (possibly excessive) vertical focussing this system of grids

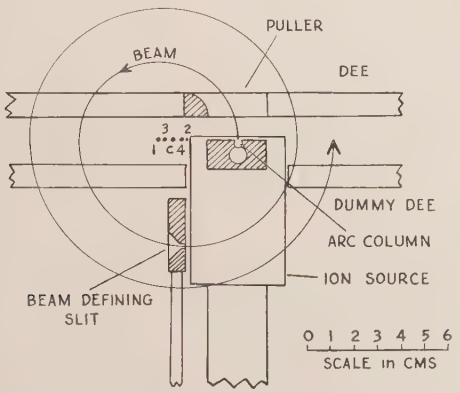


Fig. 1. The 0° offset ion source and puller sectioned in the median plane.

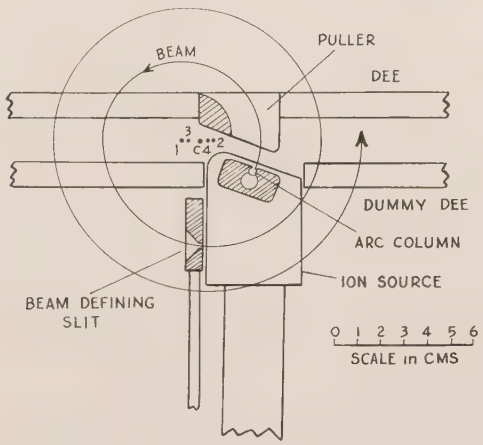


Fig. 2. The 20° offset ion source and puller sectioned in the median plane. 1, 2, 3, 4 refer to orbit centres of the main beam bunch on the corresponding half turns. C is the cyclotron centre.

[1]) M. E. Rose, Phys. Rev. **53** (1938) 392.

[2]) H. G. Blosser and F. Irwin, Bull. Amer. Phys. Soc., Series II, **3** (1958) 180.

[3]) A. H. Morton and W. I. B. Smith, Nucl. Instr. **4** (1959) 36.

introduces some horizontal defocussing or radial debunching of the beam. Some beam appears to be lost at the sudden transition from grid focussing to no grids after 5 or 6 turns.

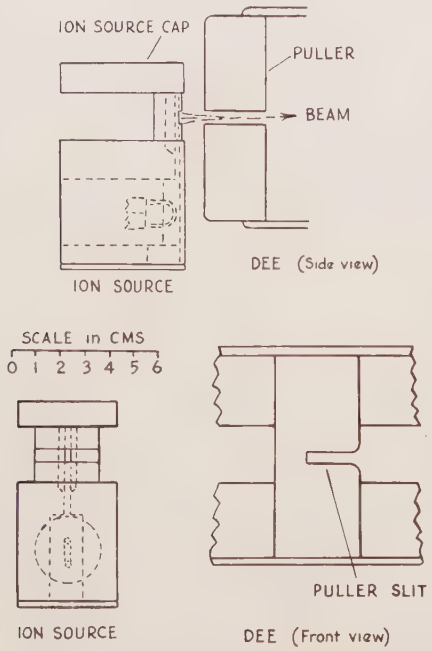


Fig. 3. Front and side views of the puller and ion source.

Recently excellent and adequate vertical focussing of the early beam near the ion source has been obtained in the Canberra 8 MeV proton cyclotron by offsetting the ion source and puller by 20° from the dee edge so that the first half turn is lengthened from the usual 180° to 200° as shown in figs. 1 and 2 respectively. The phase of the main beam is then changed at the second dee crossing from between 0° and 20° before to between 0° and 20° after dee voltage maximum, where the time variation electrical effect is focussing. Two subsidiary effects are also advantageous. Firstly, the possible phase excursion during acceleration is increased by 20° resulting in a lower dee voltage requirement. Secondly, the beam on the early turns crosses the accelerating gaps closer to peak dee voltage which results in a smaller spreading of the orbit centres and energy of the beam, that is in improved radial and energy bunching. Fig. 3 is a vertical view of the ion source. Apart from the ion-source puller region the dee and dummy dee aperture were each 2 cm, and the dee to dummy dee spacing was also 2 cm.

## 2. Theory

The vertical focussing in a cyclotron is governed by the equations given by Rose[1]). These can be combined into the following equation:

$$\frac{\mathrm{d}^2 z}{\mathrm{d}\phi^2} + (n_1 + n_2 + n_3)\, z = 0 \,.$$

where $z$ is the displacement from the median plane and

$\phi$ is the azimuth angle of the ion.

$n_1$ is $+ ve$ and is the usual radial fall off index of the magnetic field and equals d log $H$/d log $R$.

$n_2$ is $+ ve$ or $- ve$ and measures the focussing force resulting from the time variation of the electrical field.

$$n_2 = \frac{eV \sin\theta}{\pi E} = \frac{\tan\theta}{\pi(2m-1)} \,.$$

$2eV \cos\theta$ is the energy gain on crossing the dee gap at phase $\theta$ and $E = (2m-1)eV\cos\theta$ is the energy of the ion at the mid-point of the $m$th dee crossing in a single dee machine [for two dees $E = (2m-2)eV\cos\theta$].

$n_3$ is $+ ve$ and measures the electrical focussing force resulting from energy variation of the particle as it crosses the dee gap.

$$n_3 = b\left(\frac{eV}{E}\right)^{\frac{3}{2}} \frac{\cos^2\theta}{\pi} = \frac{\mathrm{b}\cos^{\frac{1}{2}}\theta}{\pi(2m-1)^{\frac{3}{2}}} \,.$$

where $b$ is a geometric factor close to 1.0, which for the following calculations is taken precisely as 1.0.

In typical cyclotron design, near the ion source the rotational frequency of the ions is about 1% greater, and at the final orbit about 1% slower than the radio-frequency accelerating voltage. Thus for these calculations a phase velocity of 2° per dee crossing has been assumed near the ion source towards negative phases. The corresponding magnetic field for this condition is the normal operating field for the cyclotron and will be referred to as the resonant magnetic field. In figs. 4(a) and 4(b) the total calculated electrical vertical focussing force $n_2 + n_3$ is plotted against $m$, the number of dee crossings, for the resonant

magnetic field and for the magnetic field 1.1% below this resonant value. The separate curves refer to ions which cross the dee gap ($m = 2$) subsequent to the ion source puller crossing with phases ranging from $-30°$ (before) to $+20°$ (after) relative to 0°, the phase of peak dee voltage. The effect of the $-2°$ per half turn phase velocity with the higher (that is resonant) is centred about a phase of $-10°$, that is 10° before the dee voltage maximum.

The ions in this group are the most desirable ones to accelerate to full energy if high beam quality is required, and these ions are readily selected by a beam defining slit on the first turn as shown in figs. 1 and 2. The focussing calculations shown in Figs. 4(a) and 4(b) indicate that

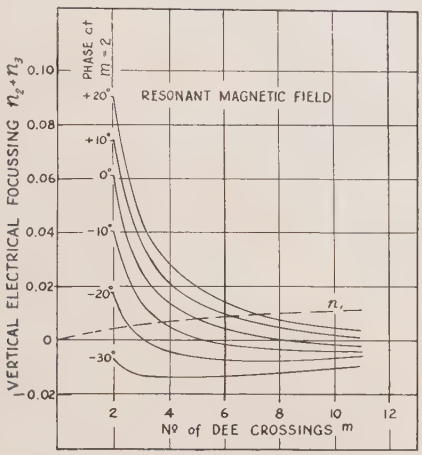


Fig. 4(a)

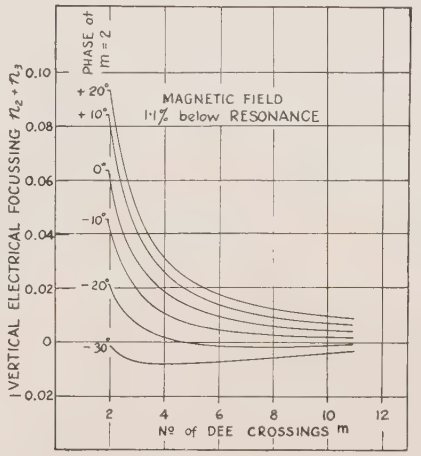


Fig. 4(b)

Fig. 4. Calculated total vertical electrical focussing index $n_2 + n_3$ plotted against the number of dee crossings $m$ with the cyclotron field on resonance (a), and 1.1% below resonance (b). The dotted line is the magnetic focussing index $n_1$.

magnetic field brings the ions of $-10°$ to $-20°$ phase at $m = 2$ into a defocussing region for $m$ greater than 6, whereas these are focussed with the lower magnetic field at the ion source. The detail but not the general conclusion of these calculations would be effected if the value of the geometrical factor $b$ differed a little from the assumed value 1.0.

Experimental evidence confirming these calculations is shown in figs. 5, 6, 7, 8 and 9. The motion of the ions in the median plane is essentially independent of the vertical motion and is discussed by Morton and Smith[3]). If the ion source-puller design is such that the electric field is perpendicular to the dee edge in the region of the beam, and if the transit time of the beam from ion source to puller is reasonably short (less than 70° of the R.F. cycle), a group of ions is well bunched in energy and in orbit centres, but not in phase[4,5,6]). This bunch of ions on its next crossing of the dee to dee gap after a half revolution, with the usual ion source puller geometry this desirable group of ions is marginal for vertical focussing, and half or more of these ions are lost through vertical defocussing on the early turns near the ion source. These results also explain why attempts to maintain magnetic focussing by peaking the magnetic field in the vicinity of the ion source have not been successful. The increased magnetic field near the ion source increases the phase velocity of the ions towards the region of electrical defocussing and more than compensates for the increase in magnetic focussing. On the other hand an ion source offset of 20° moves the ions from the $\theta = -10°$ to the $\theta = +10°$ curve of fig. 4(a), where they are adequately focussed. This theory and the experimental results indicate that an offset of as low as

[4]) N. D. Federov, J. of Nuc. Energy 6 (1957-58) 255.

[5]) V. S. Panasyuk, J. of Nuc. Energy 8 (1958–59) 256.

[6]) Sector focussed Cyclotrons. Publication 656, U.S. National Academy of Sciences, National Research Council (1959).

10° may be sufficient for greatly improved focussing over the usual parallel ion source.

### 3. Measurements

The 0° and 20° offset ion source-puller arrangements are shown in Figs. 1, 2, and 3. It should be particularly noted that an attempt has been made to keep the electrical accelerating fields on the first and subsequent turns as perpendicular as practicable to the dee edge in the beam vicinity. This condition is necessary for the orbit centre locus to be on the mid line

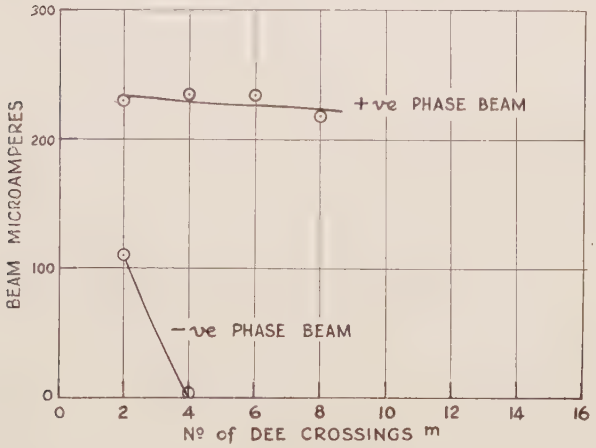


Fig. 5. The survival of the positive and negative phase components of the double beam accelerated after passing through the 1 millimetre defining slit set radially in by 2 mm from the main first turn beam. 0° offset ion source magnetic field on resonance.

between the dees. A moveable beam defining slit 1 mm wide can be inserted on the second half turn of the ion beam. A beam defining slit on the dee edge[7]) or in the electrical field region will usually distort the electric field away from the perpendicular to the dee edge, and can thus introduce some radial debunching. The vertical focussing as a function of the phase of the beam was determined by comparison of the 0° with the 20° offset ion source, and also by raising and lowering the magnetic field 1½% from the resonant magnetic field, and by inserting the beam defining slit in different regions of the second half turn beam. The beam was measured by inserting an insulated copper probe wired to a milliameter, and also checking the power dissipation on the target probe by a thermocouple in the cooling water. Alternatively a target of graphite fingers was inserted to allow visual observation of the vertical focussing by means of the red or white hot areas.

[7]) W. B. Powell, Nature **177** (1956) 1045.

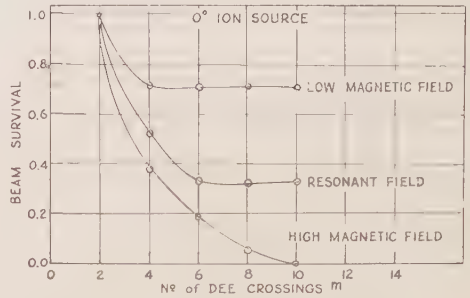


Fig. 6. The beam survival ratio for the 0° offset ion source with the 1 mm defining slit set on the main bunched first turn beam, with the magnetic field on and 1.5% above and below the resonant value.

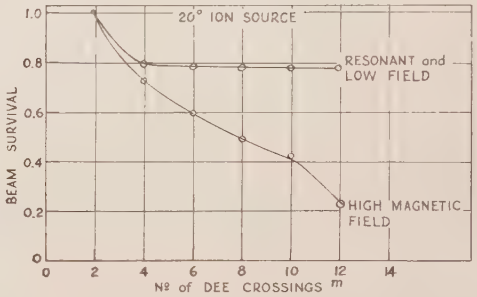


Fig. 7. The beam survival ratio for the 20° offset ion source with the 1 mm defining slit set on the main bunched first turn beam, with the magnetic field on and 1.5% above and below the resonant value.

Two separate beams could be observed visually on the latter part of the first turn with the defining slit set 2 millimetres radially in from the outer limits of the first turn beam. With the 0° ion source and resonant magnetic field the inner of these beams has large negative phase and is lost before the second turn, and the outer has large positive phase and is well focussed as is shown in fig. 5. With the 20° offset ion source and the magnetic field 1.5% below the resonant value to give increased focussing both beams were accelerated to the limit of observation of six turns. On the sixth turn these two beams

although both coming through the one defining slit were radially separated by 5 mm. With the beam defining slit set on the outer limits of the first turn the beam passed is that bunched in energy and orbit centres. Figs. 6 and 7 show the survival

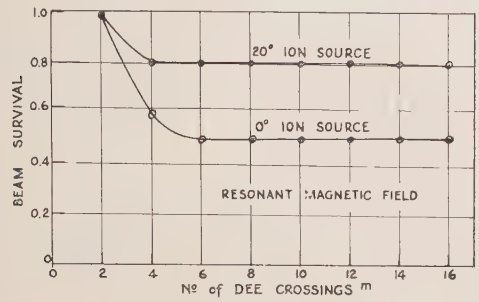


Fig. 8. Beam survival of the total beam without the defining slit with the 20° and 0° offset ion sources, and the magnetic field on resonance.

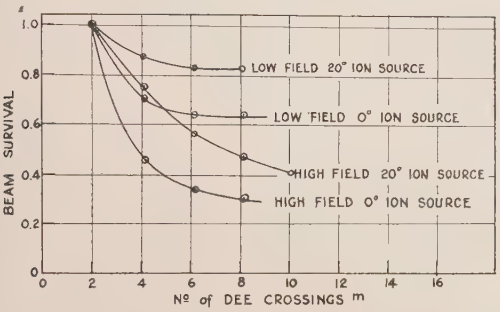


Fig. 9. Beam survival of the total beam without the defining slit with 20° and 0° ion sources and the magnetic field 1.5% above and below the resonance value.

of this beam against the number of dee crossings with the 0° and 20° ion source and with low, resonance and high magnetic fields. The beam survival at resonant magnetic field is increased from 30% to 80% in going from the 0° to the 20° offset ion source. The critical dependence of beam survival on magnetic field with the 0° ion source indicates the marginal vertical focussing which is present with this arrangement. Figs. 8 and 9 show the total beam survival with the defining slit withdrawn. With the 0° offset ion source (fig. 8) only half of the first turn beam is present after six dee crossings, whereas the 20° offset increases this to 80%. Fig. 9 shows the further effects of raising and lowering the magnetic field. Comparison of the full beam survival fig. 8, with the slit defined bunched beam survival in fig. 6, indicates that with the 0° offset ion source the loss of good beam is greater than the beam loss as a whole.

## 4. Ion Source-Puller Optics

Of particular importance is the ion source puller arrangement to give a well focussed beam injected into the first half turn. The curved plasma boundary of the arc column provides strong vertical focussing as the beam leaves the ion source[3,6]). Some defocussing occurs as the beam enters the puller. A balanced combination of these effects can produce an essentially parallel beam injected into the first turn. With an ion source slit height of 5 mm and width 1.5 mm, and an ion source to puller separation of 10 mm, a puller slit height of 5 mm offers the best compromise for vertical focussing on the first half turn. If the arc column is not sufficiently intense, the main ion beam comes from the filament end of the arc column and the plasma boundary is distorted so that the beam does not emerge parallel to the median plane. Some compensation for this effect can be made by lowering the centre of the ion source slit below the median plane. If the height of the puller slit relative to the ion source slit is changed by 0.2 mm from its optimum position the beam on the first turn is thrown appreciably off the median plane. It was also found that lack of electrical symmetry of the ion source about the median plane adversely affected the beam during its passage through the dummy dee region on the first and second turns. The top cap of the ion source was enlarged to the same dimensions as the base to provide vertical electrical symmetry as shown in fig. 3. With symmetry of the stray electric field about the median plane in the region behind the ion source as well as between the dees, the beam remained on the median plane on the early turns. With this ion source puller arrangement, an arc current of 1 ampere, arc voltage of 140 V and dee voltage of 70 kV peak, the first turn beam was 3 mA, of which 800 $\mu$A was passed through a millimetre wide by 15 mm high defining slit on the first turn. With the 20° offset

ion source the beam was confined near the median plane. As observed visually using the graphite fingered probe target, the full height of the focussed beam varied between 5 and 10 mm. The beam came to a vertical focus less than 5 mm high after 3 turns and again on the 8th turn.

**Acknowledgements**

The author wishes to thank Mr. R. W. Parkes for his assistance in these experiments, Dr. A. H. Morton for his interest and discussions and Professor M. L. Oliphant, Director of the Research School of Physical Sciences, for his encouragement of the project.

NUCLEAR INSTRUMENTS AND METHODS 9 (1960) 55–66; NORTH-HOLLAND PUBLISHING CO.

# A NEW TYPE OF ČERENKOV DETECTOR FOR THE ACCURATE MEASUREMENT OF PARTICLE VELOCITY AND DIRECTION†

ARTHUR ROBERTS

*Department of Physics††, University of Rochester*

Received 22 June 1960

A new type of Čerenkov radiation detector is proposed, in which the light emitted by a single particle traversing a radiator is imaged, by means of a lens or mirror focused at infinity, on the cathode of an image-intensifier tube. The image is a ring, whose diameter measures accurately the Čerenkov cone angle, and thus the particle velocity. In addition the coordinates of the center of the circular image accurately indicate the orientation of the particle trajectory (though not its position). The sensitivity of presently available systems of cascaded image-intensifier tubes allows the photographic recording of the image produced by a single particle. The system is inherently insensitive to background noise. It can observe simultaneously several incident particles whose directions span a wide angle. It may be gated with microsecond coincidence resolving times. It can use condensed of gaseous radiators; with the former, chromatic dispersion is likely to limit the accuracy. For gas radiators, the attainable accuracy of velocity determination is estimated as $\Delta\beta = \pm 0.0002$ or better; the accuracy of track orientation $\pm 0.001$ radians. The range of velocity and orientation simultaneously observable depends on the angular field of view of the objective. Sources of error, the precision attainable, the design of practical systems and some possible applications are discussed.

## 1. Introduction

The Čerenkov light emitted by a fast-moving particle consists of rays parallel to the elements of a right circular cone. As observed by a detector, it seems to originate from a ring source at infinity, whose angular diameter is that of the cone (see fig. 1). It has justly been likened to the light from a ring of faint stars. If such light is collected by a telescope objective, an image of the ring is formed in the focal plane with a diameter $d$, given by

$$d = 2f \tan\theta \qquad (1)$$

where $f$ is the focal length of the objective, and $\theta$ is the half-angle of the cone of light.

Precisely such an arrangement may be used to collect the Čerenkov radiation from a fast particle, as shown in fig. 2. The light emitted by the particle may all be collected in a ring image. In principle, a photographic plate could then record the particle's passage; but the light emitted is of course far too weak to allow the photography of single particles. However, existing image-intensifier tubes, as now used in cascade for scintillation track-imaging, can record such ring images. Fig. 3 shows such a cascade system.

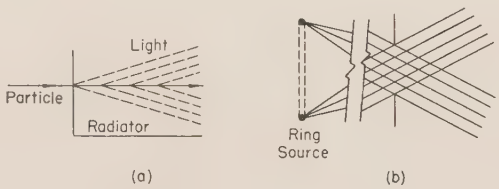


Fig. 1. a. The Čerenkov radiation emitted by a fast particle traversing a radiator lies in a circular cone of parallel light coaxial with the particle path; b. The light from a narrow ring source at infinity, after passing through an aperture, also lies in a cone of parallel light, which may be focused to a ring image by a lens or mirror objective.

One can construct in this way a Čerenkov detector that measures accurately both the particle velocity,—even at very high speeds ($\beta \geq 0.99$),—and the direction of motion of the particle. Furthermore, these measurements may be made on particles entering a large radiator at

† Supported in part by the U.S. Atomic Energy Commission.

†† Now at Argonne National Laboratory, Argonne, Illinois.

[1]) A short preliminary description of this device has been given by A. Roberts, Rev. Sci. Instr. **31** (1960) 579; Bull. Amer. Phys. Soc., Ser. 2, **5** (1960) 263.

any point within a given area, moving in any direction within an appreciable angular range, and falling within an appreciable velocity range.

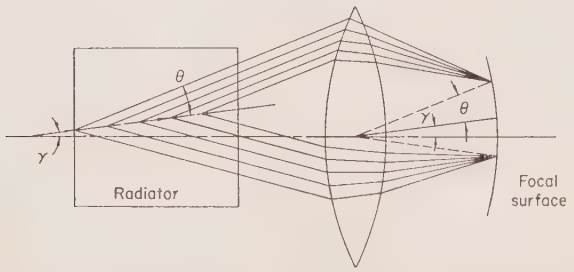


Fig. 2. The Čerenkov light cone, of half-angle $\theta$, will be imaged by the lens or mirror objective as a ring in the focal surface, with the same angular radius $\theta$. A line, joining the point where the objective axis crosses the principal plane with the center of the ring image, will make the same angle with the lens axis as the original particle path, or its projection in the case of a skew path. N.B. The refraction of the light cone leaving the radiator has been omitted; this is discussed in Sec. 9.

Together with an auxiliary momentum measurement, the attainable accuracy in velocity appears sufficient, as we shall see, to identify particles up to very high energies,—even for distinguishing pions from muons at energies up to 5 GeV and above, and to measure energies in the relativistic range with high precision.

Čerenkov detectors have previously been constructed that measure velocity accurately, but they have required, the incident particle direction to lie within a very narrow cone[2–5]). They have therefore been useful mainly for identifying particles in a well-collimated beam.

## 2. Intensity of Radiation Required

Since the peak absolute efficiency of good photocathodes ranges from ten to twenty percent, the particle must produce in the radiator a few hundred photons, within the sensitive spectral range of the photocathode, to form the image on the first cathode. This number is probably somewhat larger than that (60–100) needed by a photomultiplier for efficient particle detection.

### 2.1. RADIATOR LENGTH AND CATHODE SENSITIVITY

To determine the thickness of radiator necessary to produce an adequate image on the photocathode, we must fold together the spectrum of the primary Čerenkov radiation, and the absolute-sensitivity spectral characteristic of the photocathode. In addition, any losses of radiation between the light source and the photocathode must be taken into account: these arise in the radiating medium itself, the optical system, and the front face of the first image intensifier.

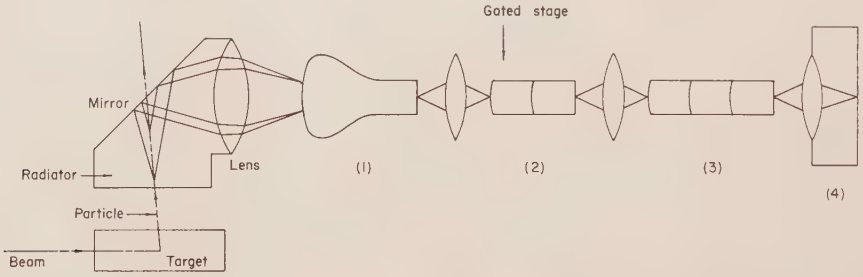


Fig. 3. A cascaded image-intensifier system capable of registering photographically ring images of Čerenkov light. 1. is a Westinghouse WX-4171 single-stage tube, with a 5″ cathode, 1″ image; 2. is an RCA C-73459 two-stage tube; 3. an RCA C-73491 three-stage tube, and 4. a camera. Wide-aperture lenses provide interstage coupling. An overall quantum gain of $10^5$ or more allows the photography of images produced by single photoelectrons from the first photocathode. If a short-period phosphor like P-15 is used in (1), the system may be gated by applying a one- or two-microsecond pulse to the first stage of (2).

The folding together of the Čerenkov spectrum

[2]) R. L. Mather, Phys. Rev. **84** (1951) 181.

[3]) D. E. Baldwin, C. Burrowes, D. O. Caldwell, S. G. Hamilton, D. Hill, L. S. Osborne and D. M. Ritson, IRE Trans. on Nuclear Science, NS-5, (1958) 177.

[4]) J. H. Atkinson and V. Perez-Mendez, Rev. Sci. Instr. **30** (1959) 864.

[5]) von Dardel *et al.*, CERN (unpublished); See. M. Deutsch. Proc. Intern. Conf. on High-Energy Accel. and Instrumentation. CERN, Geneva (1959) p. 593.

with the spectral sensitivity curve of an S-11 photocathode has been performed by Jelley[6]). For a typical cathode of this type one can write an equation for the number of photoelectrons emitted, per cm path of the particle, in the form

$$\frac{dN}{dl} = 1.13\, TS \sin^2\theta\,. \qquad (2)$$

Here $T$ is the optical transmission efficiency of the system between the particle path and the photocathode, including all transmission, absorption, and reflection losses, suitably weighted over the Čerenkov spectrum. $S$ is the photocathode sensitivity in microamperes/lumen (at 2848°K). A typical cathode of this sort, in commercial tubes, will have $S \geqq 40\ \mu$A/lumen (9% peak efficiency). If the optical transmission factor $T$ is about 0.7, a reasonable value for a mirror system, we get 32 $\sin^2\theta$ photoelectrons per cm; thus for an 18° cone, corresponding to $\sin\theta = 0.3$, we find 3 electrons/cm path.

Since the S-20 multi-alkali cathode is more sensitive than the S-11, the number of photoelectrons should be higher than for the S-11; but it will not be as much higher as might be suggested by the luminous sensitivity figures, for two reasons. First, the increased sensitivity lies mainly toward the red, where the Čerenkov spectrum is weak; and second, the peak sensitivity is a at shorter wavelength, 4200 Å, so that a greater fraction (more than half) of the weighted sensitivity lies below 4000 Å, where the transmission is likely to be poor.

Contrary to practice in some unfocused Čerenkov detectors, the use of wavelength shifters in the radiating medium to improve the photocathode efficiency is not permissible; they destroy the imaging properties of the system, unless they are optically coincident with the first photocathode. Wavelength shifters might conceivably be used with a first-stage image-intensifier tube with a glass-fiber face-plate.

### 2.2. RADIATOR LENGTH AND CONE ANGLE

Fig. 4 shows a plot of the cone angle $\theta$ as a function of $n\beta$, as determined from the well-known Čerenkov relation

$$\cos\theta = 1/n\beta\,. \qquad (3)$$

It also shows, as a function of $n\beta$, the length of radiator required to produce 32 photoelectrons from the S-11 cathode of an image-intensifier of sensitivity 40 $\mu$A/lumen, for an optical system of overall transmission 0.7; i.e., we plot $L = 1.0/\sin^2\theta$.

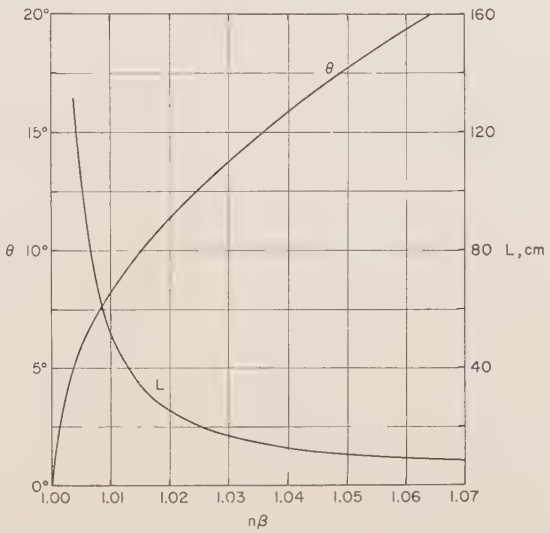


Fig. 4. The angle $\theta$ of the Čerenkov cone as a function of $n\beta$; and the length $L$ of radiator path required, as a function of $n\beta$, to liberate 32 electrons from an S-11 photocathode of sensitivity 40 microamperes/lumen, assuming an optical system transmitting 70 percent of the Čerenkov light to the first photocathode.

### 2.3. CONE ANGLE AND APERTURE REQUIRED

From eq. (2), the total number of photoelectrons obtained from a radiator of length $L$ is

$$N = 1.13\, TSL \sin^2\theta\,.$$

The exit radius of the cone is $a = L\tan\theta$. For small angles, assuming $\theta = \sin\theta = \tan\theta$, we get

$$N = 1.13\, TSa\,\theta\,. \qquad (2a)$$

If, as before, we take $T \approx 0.7$ and $S \approx 40\ \mu$A/lumen, we find that the required value of $a\theta$ to give $N \approx 30$ is just

$$a\theta = 1 \quad (a \text{ in cm}, \theta \text{ in radians}) \qquad (4)$$

which may be taken as a rule-of-thumb requirement for the aperture required for a given cone angle.

[6]) J. V. Jelley, Čerenkov Radiation and Its Applications (Pergamon Press, New York, 1958) p. 112ff.

### 3. Definition of the Circular Image

In presently available high-gain cascaded image-intensifier systems, the overall resolution is in the neighborhood of 10 line-pairs per mm at the output. Each primary photoelectron from the first photocathode will produce an image 0.1 to 0.2 mm in diameter[7]) at the output, bright enough to photograph. The precision with which the diameter of the circular image can be determined depends upon several factors; the diameter of the individual electron images, their number, and the overall system demagnification.

A ring image that produces, say, 20–30 or more primary photoelectrons should produce a readily recognizable circular image, well-enough defined to permit good accuracy in determining the diameter and position of the circle. The accuracy will at first improve as the number of primary electrons increases; eventually a stage will be reached at which an increase in the number of image points no longer materially improves the accuracy.

The definition of the image of the primary photoelectron depends on the resolution of the stages following the first one: defocusing the first stage will not change the image size, though it will move the images off the circle. Thus the error in determining the diameter of the primary image on the first photocathode will be proportional to the demagnification of the first stage. Clearly the highest possible overall resolution is desirable, as well as the largest practical final images.

### 4. Sources of Error in Velocity Measurement

The precision attainable in $\beta$ is limited by the image intensifier resolution and by angular spread in the Čerenkov light. Sources contributing to poor resolution include particle energy loss in the radiator; chromatic aberration, or dispersion, due to the variation of $n$ with wavelength; and multiple scattering and diffraction effects. We consider these in turn.

[7]) L. W. Jones, K. Lai, R. Newsome and M. L. Perl, Univ. of Michigan Res. Inst. Report No. 2, 1960 (unpublished); Proc. of Seventh Scintillation Counter Symposium, 1960, to be published in IRE Trans. of Prof. Group on Nuclear Science.

#### 4.1. LIMITATION DUE TO OPTICAL RESOLUTION

Let us suppose the diameter $d$ of a ring image can be determined with an error $\Delta d$. If the focal length of the objective is $f$, then from (1) and (3)

$$\Delta d = 2f \sec^2\theta \, \Delta\theta$$
$$= 2f \, \Delta\theta \, n^2 \beta^2 .$$

The error in $\beta$ corresponding to an error in $\theta$ is found by differentiating (3);

$$\frac{\Delta\beta}{n\beta^2} = \sin\theta \, \Delta\theta . \tag{5}$$

Combining these we find

$$\Delta\beta = \Delta d \sin\theta / 2fn . \tag{6}$$

The corresponding error in the determination of the total energy $\gamma$ is obtained by differentiating the relation $\gamma = (1 - \beta^2)^{-\frac{1}{2}}$ to get

$$\Delta\gamma = \beta\gamma^3 \, \Delta\beta . \tag{7}$$

The cascade image-intensifier systems now available have specifications that should permit distinguishing 2 line-pairs per mm on the 5″ cathode of a Westinghouse WX-4171 tube, which has the largest photocathode presently available. The exact relation among the overall system resolution, the number of photoelectrons in the circular image, the image diameter, and the accuracy with which the diameter can be measured is not yet known, and its elucidation must await experience with actual systems; it seems reasonable to suppose that an accuracy of $\pm$ 0.05 cm will be possible.

As an example of the precision to be expected, if $f$ is 20 cm, $\theta = 11.4°$, $\sin\theta = 0.197$, $n\beta = 1.02$, $\beta \sim 1$, then we find, for $\Delta d = \pm$ 0.05 cm, $\Delta\beta = \pm$ 0.000 25. The corresponding error in energy determination is given by eq. (7). Reducing $\theta$ and increasing $f$ will improve the precision; however, these steps run into difficulty with decreasing amount of light per unit radiator path, and the larger and larger area of photocathode surface required.

From eq. (2a), the total number of photoelectrons is proportional to $a\theta$, where $a$ is the radius of the cone at the exit from the radiator.

From (6), the velocity error $\Delta\beta$ is proportional to $\theta$; thus for a given number of photoelectrons in the image it will be inversely proportional to $a$.

Thus large-diameter, long focal-length objectives are desirable for high precision in $\beta$. The disadvantage to such objectives is the large area occupied by the image, and the current unavailability of image tubes with sufficiently large cathodes.

It may be noted that cascade magnetically-focused image intensifiers are now in development which should materially improve the possible overall resolution,—by a factor of four or more. However, it appears that in many practical cases other errors, like scattering and dispersion, may limit the precision.

### 4.2. LOSS OF PARTICLE ENERGY IN THE RADIATOR

The cone is broadened by particle deceleration, which in practice is due to ionization losses, which are greatest for slow, light particles. If a minimum-ionizing particle loses 20 MeV, for protons this is a $\Delta\gamma$ of 0.02, but for muons 0.2. The resulting change of velocity is readily taken into account; it may even provide a measure of recognition of the identity of the particle.

### 4.3. DISPERSION IN THE RADIATOR

Since the cone angle depends only on $n\beta$, a variation of $n$ is indistinguishable from an equivalent variation in $\beta$. In ordinary crown glass, to take an example, $n$ changes 1% between 4000 and 6000 Å. No achromatization is possible in the subsequent optics†, since the light now appears to originate in a halo of rainbow-colored stars, of finite angular width.

Dispersion is obviously a serious source of error; to retain high accuracy in $\beta$, it must be sharply limited. In solids and liquids this is possible only by monochromatizing techniques of dubious applicability (since they are wasteful of light), or the use of a radiator—if one can be found,—whose index of refraction is essentially constant over the desired range. The situation is much more favorable for gases. The nearer the index of refraction to unity, the smaller the effective dispersion.

The width of the cone due to dispersion is readily calculated. Differentiating (3) with respect to $n$, we find:

$$\Delta\theta = \Delta n/(n^2 \beta \sin\theta) . \tag{8}$$

For gases at moderate pressures, the index of refraction is given by the Lorentz-Lorenz law:

$$\frac{n^2 - 1}{n^2 + 2} = \rho K \tag{9}$$

where $\rho$ is the density and $K$ is a constant characteristic of the gas. If $n$ is close to unity, this reduces to

$$\begin{aligned} n - 1 &= \tfrac{3}{2}\rho K \\ &= K' p \end{aligned} \tag{10}$$

where $p$ is the pressure and $K'$ another constant. It is the variation of $K'$ over the spectrum that results in dispersion.

For air, the variation of $n$ over the useful spectrum range (4000–6000 Å) is approximately

$$\Delta n = 6 \times 10^{-6} p \tag{11}$$

where $p$ is in atmospheres. The corresponding spread in velocity $\Delta\beta$ is of course just equal to $\Delta n$ (for $\beta \approx n \approx 1$).

The curve obtained by folding the S-11 sensitivity curve into the Čerenkov spectrum peaks at about 3700 Å, and its median is at 4300 Å. Selective absorption by the lens and radiator will both shift the median wavelength and narrow the range of wavelengths. A glass lens will reduce the dispersion by absorbing light below 4000 Å. Thus for a practical system these effects must be calculated in detail; for present purposes we approximate them by taking as $\Delta\beta$ $\frac{1}{3}$ the value corresponding to (11).

Unless special steps to reduce it are taken, dispersion will usually limit the velocity precision in condensed radiators, and often in gaseous radiators. Jelley[9]) gives extensive data on the dispersion of many common radiators.

† Achromatization is possible only for particles of one direction and velocity, not for a distribution in either quantity.

[8]) J. V. Jelley, (ref.[9])) p. 112.
[9]) *Ibid.*, p. 143 ff.

4.4. MULTIPLE SCATTERING AND DIFFRACTION

The angular width of the cone of Čerenkov light emitted by a particle undergoing multiple scattering, taking into account the diffraction effects produced by loss of coherence due to the scattering, has been calculated by Dedrick[10]). Slowing-down in the radiator is not taken into account, so that the calculation is valid only for sufficiently fast particles.

The result of the calculation is that the half-width of the emitted cone at half-intensity points is rather less than (about half) the mean scattering angle of the particle. The relevant results are contained in Dedrick's curves (fig. 5) which, together with the following equations:

$$K = [\, (6\pi/\sqrt{2})\, n \sin\theta_0 \cdot (L/\lambda) \cdot \bar{\theta}\, ]^{\frac{1}{3}}\,, \qquad (12)$$

$$\varkappa = \delta\, \bar{\theta}/\sqrt{2}\,, \qquad (13)$$

allow the calculation of $\varkappa$, the half-width of the cone at half-intensity, from $n$; $\theta_0$, the mean cone angle; $\bar{\theta}$, the mean multiple scattering angle; $L$, the path length in the radiator; and $\lambda$, the wavelength of the Čerenkov light. The procedure is to calculate $K$ from eq. (12); then to read off from fig. (5) the value of $\delta$ at which the intensity is half-maximum; and then to find $\varkappa$ from eq. (13).

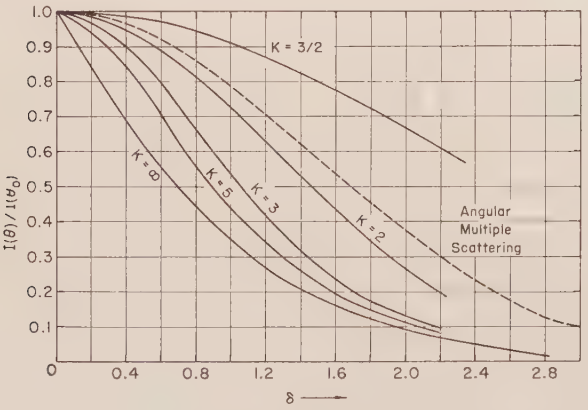


Fig. 5. The intensity distribution of the Čerenkov cone, taking into account multiple scattering and diffraction, as a function of the parameters $K$ and $\varkappa$ (from ref.[10]).

In principle, the final width of the Čerenkov cone should be found by a calculation similar to Dedrick's, which would however take into account the slowing down of the particle in the medium, and would also fold in the effects of dispersion, spectral sensitivity and transmission loss.

4.5. INTERFERING EFFECTS

Čerenkov threshold photomultiplier detectors suffer[3]) from vagueness of threshold, and from spread of the pulse height distribution as a result of the presence of knock-on electrons (Landau effect). In addition, certain of the media used as Čerenkov radiators scintillate to some extent, thus partially masking the Čerenkov radiation and destroying its directional properties.

None of these effects is likely to be of significance in the proposed detector. Thus, a knock-on electron will in general have a different direction from the primary particle, and will usually scatter considerably, except at the very highest energies. Its Čerenkov radiation will therefore not obscure the primary circle. Neither will the omnidirectional light due to scintillations, unless it is so intense as to blot out the entire picture.

In addition to the errors mentioned above, others, due to causes like misalignment, distortion and inaccurate calibration, will undoubtedly occur. Nonetheless, measurements of $\beta$ to $\pm$ 0.0002 or better, with existing equipment, do not appear overly optimistic[2–5]), as the following example indicates.

## 5. Sample Calculation of Precision in Velocity Determination

Consider an air detector for highly relativistic particles; let us take $n = 1.0060$, $\beta = 0.9990$, $n\beta = 1.0050$. Then $\theta = 5.7°$, $\sin\theta = 0.100$. To obtain enough light, we note from eq. (2) that 100 cm of path gives 30 photoelectrons. Since the cone angle is small, we can use a long focal length and still contain the image on the available area of the image tube. Let $f = 40$ cm; we now calculate the precision in $\beta$.

a. The resolution of the system, from eq. (6), gives $\Delta\beta = \pm$ 0.000 06 (half-width).

b. Energy loss: the radiator thickness is 100 cm, and the index $n = 1.0060$ requires a pressure of 22 atmospheres. The radiator thickness is then 3.0 g/cm², and the energy loss 5.5 MeV, which requires a negligible correction.

[10]) K. G. Dedrick, Phys. Rev. **87** (1952) 891.

TABLE 1

The velocity error due to scattering and diffraction, and the total velocity error, for the gas radiator of Sec. 5, calculated from the considerations of Sec. 4.3 and Sec. 5, for various assumptions about the identity of the incident particle. The mean scattering angle $\bar{\theta}$, given for comparison, is calculated from the familiar approximation $\bar{\theta} = 21\ t^{\frac{1}{2}}/p\beta$

| Particle | Momentum for $\beta = 0.9990$ (MeV/$c$) | Mean scattering angle, $\bar{\theta}$ (radians) | Half-width of Čerenkov cone (radians) | Half-width in $\beta$, due to multiple scattering | Total half-width of $\beta$ |
|---|---|---|---|---|---|
| Proton | 20 500 | $\pm$ 0.000 28 | $\pm$ 0.000 16 | $\pm$ 0.000 016 | $\pm$ 0.000 09 |
| K-meson | 10 800 | 0.000 54 | 0.000 28 | 0.000 028 | 0.000 09 |
| pion | 3 100 | 0.001 8 | 0.000 92 | 0.000 092 | 0.000 13 |
| muon | 2 400 | 0.002 4 | 0.001 23 | 0.000 123 | 0.000 15 |
| electron | 11 | 0.49 | — | — | — |

c. Dispersion: From eq. (11), $\Delta\beta = \pm 0.00006$ (half-width).

d. Multiple scattering and diffraction: Table 1 lists the momenta for various particles having $\beta = 0.9990$ (corresponding to $\gamma = 22$). For each of these, the full width at half-maximum of the cone is calculated from the considerations of Sec. 4.3 above; the corresponding half-width in the determination of $\beta$ is given, and the total error $\Delta\beta$, including all contributions.

The multiple scattering and diffraction contribution to the error for these very fast particles is appreciable for pions and muons, but negligible for heavier particles. Pions and muons can be distinguished up to $\gamma = 50$, if the minimum $\Delta\beta$ observable is $\pm$ 0.0002.

The particle cannot be an electron; electrons with enough momentum to reduce multiple scattering to the point where a ring image is formed always have $\beta$ indistinguishable from 1. Even a very rough momentum determination is enough to identify the particle.

## 6. Measurement of the Direction of the Track

The position of the center of the ring image determines the orientation, with respect to the objective axis, of the trajectory of the particles. The position of the track is not determined; it may be moved parallel to itself without moving the image. If a counter hodoscope or a visual detector is used in conjunction with the Čerenkov detector, the location of one point on the trajectory of the particle then fixes it in space.

If the orientation of the track makes an angle $\alpha$ with the camera axis, the angular error will be

$$\Delta(\tan\alpha) = \Delta x/f \tag{14}$$

where $x$ is the distance of the center of the circle from the camera axis.

Since the error $\Delta x$ in determining the position of the center of the circle is likely to be comparable to the error $\Delta d$ in determining its diameter, let us take them to be the same. Then the error in $\alpha$ is given by

$$\Delta(\tan\alpha) = \Delta d/f$$

and

$$\Delta\alpha = \Delta d \cos^2\alpha/f\ . \tag{15}$$

For the parameters assumed in Sec. 5; namely $f = 40$ cm, $\Delta d = \pm 0.05$ cm, we find $\Delta\alpha = \pm 0.001$, i.e., one milliradian.

## 7. Mass Determination

The high accuracy of velocity determination possible suggests the possibility not merely of mass identification, but also of mass measurement. If both the momentum and velocity of a particle are known, the mass is determined by the relation

$$p/c = m_0\beta\gamma\ .$$

The fractional error in mass is readily seen to be, using eq. (7)

$$\Delta m_0/m_0 = [\ (\Delta p/p)^2 + (\gamma^2\,\Delta\beta/\beta)^2\ ]^{\frac{1}{2}}\ . \tag{16}$$

A precise momentum measurement, at not too high a total energy, should thus allow measurements of mass with accuracies of the order $10^{-3}$ without much difficulty.

## 8. Angular Acceptance and Field of View

In order to allow the measurement of velocity over a wide range, it is desirable to use a moderately high index of refraction, and to be able to measure a wide spread of cone angles: $(n\beta - 1)$ is proportional to $\theta^2$ for small angles. However, the range of cone angle visible to the objective is limited by its angular field of view. Thus there is a direct connection between the optical design of the objective and the velocity range that may be covered at one time.

### 8.1. USE OF PLANE MIRRORS

The use of plane mirrors can extend the angular range at the expense giving images broken into several angular sectors. Fig. 6 shows the design of a tetrahedral pyramidal mirror with an axial angle of 10°. Such a mirror will change the direction of a 20° ray to make it zero, and of a 30° ray to — 10°. It thus has the property of tripling the effective angular range for axial particles. The circle is broken into four arcs (or more, for rays reflected more than once) as shown in fig. 7. The radius of each arc is unaffected by reflection.

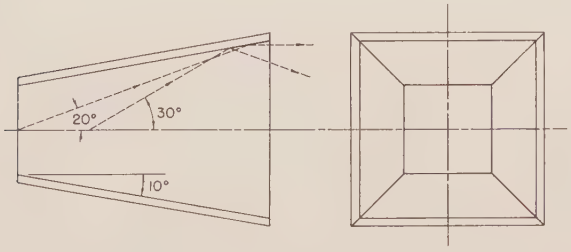


Fig. 6. The angular field of view may be increased with the aid of a mirror system. The tetrahedral mirror above is in the shape of a truncated pyramid, each side making a 10° angle with the axis. Rays making angles between 10° and 30° with the axis will be reflected into angles between + 10° and — 10°.

While this image dissection will clearly impair the accuracy of determination of the diameter and center of the original circle, it is difficult to say without experience just how much impairment will result. The procedure for finding the original particle direction is implicit from fig. 7.

[11]) R. J. Potter and R. E. Hopkins, NYO-9027, Univ. of Rochester report (unpublished); also Proc. of Seventh Scintillation Counter Symposium, 1960, IRE Transactions on Nuclear Science (to be published).

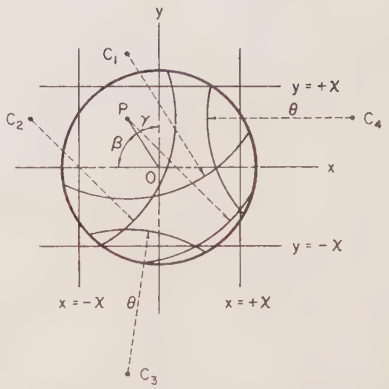


Fig. 7. The geometry of the image produced by a pyramidal mirror. The heavy circle represents the field of view. The radial polar coordinate of the image represents the angle $\alpha$ made by the particle trajectory with the $z$-axis, which is the optic axis. The angular coordinate represents its azimuthal orientation. P represents a particle making an angle $\alpha$ with the $z$-axis, with the radius OP $= \alpha$. Let $\beta$ and $\gamma$ represent the angle made by the projection of the particle path on the $xy$-plane with the $x$- and $y$-axis, respectively. The mirror planes may be represented by the lines $x = \pm\chi$, and $y = \pm\chi$, where $\chi$ is the angle made by the optic axis with the respective mirror planes. The points $C_1$—$C_4$, representing the images of the particle trajectory in the four mirrors (and thus the apparent centers of the reflected circles) are now found by reflecting P in the mirror lines. The image may now be found by drawing circular arcs, of radius corresponding to the Čerenkov cone angle $\theta$, with P and $C_1$ to $C_4$ as centers, as permitted by the field of view.

## 9. Design Characteristics for Practical Systems

### 9.1. OPTICAL SYSTEM

The primary requirements for the optical system are high transmission over a wide spectral range, and wide angular field of view. Long focal length is desirable for high precision in velocity measurement.

Other things being equal, mirror objectives are preferable to lenses because of their superior spectral transmission characteristics. However, the use of mirror objectives entails the obstruction of part of the field of view by the detecting equipment. Also, since it is desirable not to allow intense particle beams to traverse the first image-intensifier cathode, it is preferable that the first tube not be in line with the particle beam. Both of the objections may be met, at least in part, by using a glass fiber bundle to transmit light from the objective focal surface to the first stage image intensifier. This is possible at the cost of some light[11]) (especially in the

ultraviolet); it also requires that the first image-intensifier stage be equipped with a fiber-optics face-plate.

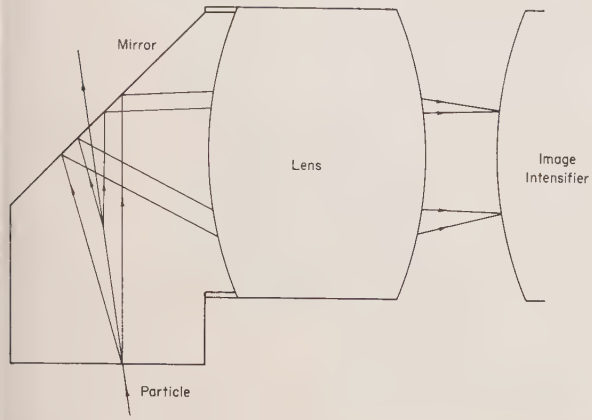


Fig. 8. Design for 5″ field, f/1.5 lens system and a liquid radiator. The angular acceptance without a pyramidal mirror is $\pm$ 12°; with a 12° tetrahedral mirror this becomes $\pm$ 36°. The velocity range measurable would then be from $n\beta$ = 1.005 to 1.157 (from fig. 9); without a mirror it is 1.005 to 1.02.

Fig. 8 shows a tentative design for a small detector using a liquid radiator and a lens[11] with a 5″ diameter field and $f/1.5$ aperture.

### 9.2. MINIMUM DIAMETER OF OBJECTIVE AND MINIMUM MEASURABLE ANGLE

We have seen (eq. (4)) that to obtain an adequate amount of light the aperture-angle product $a\theta$ should equal about 1 cm-radian. This implies a minimum diameter for any objective, depending on the smallest angle $\theta_{\min}$ accepted. Thus, allowing a factor of 1.25 for the use of a 45° mirror (as in fig. 8), which moves the lens back from the radiator exit aperture, the diameter of the lens should be at least

$$d = 2.5/\theta_{\min} \text{ cm},$$

or

$$d = 1/\theta_{\min} \text{ inches} \qquad (17)$$

where $\theta_{\min}$ is in radians.

### 9.3. EFFECT OF REFRACTION ON THE LENS ANGULAR FIELD

If the index of refraction of the radiator is $n_2$, and the radiator is separated by a medium (usually air) of index $n_1$ from the lens, the outgoing cone will be refracted according to Snell's law. If $n_2 > n_1$, the apparent vertex of the cone is moved nearer to the interface in the ratio $n_2/n_1$.

Since the acceptance angle of the lens is ordinarily given for use in air, the effective acceptance angle $\theta_2$ within a radiator of index $n_2$ is given by

$$n_2 \sin\theta_2 = n_1 \sin\theta_1$$

or

$$\sin\theta_2 = \frac{n_1}{n_2}\sin\theta_1 \qquad (18)$$

where $n_1 \approx 1$, and $\theta_1$ is the cone angle at the lens.

The use of high-index radiators thus appreciably constricts the angular field of view; and immersion does not circumvent the difficulty with lens objectives. With mirror objectives, on the other hand, immersion of the objective in the radiating medium is beneficial; this constitutes an advantage for mirror objectives. Fig. 9 shows the maximum index of refraction that can be accommodated for a lens (curve A) and an immersion mirror (curve B), given the angular acceptance of the objective; this assumes no pyramidal reflectors are used.

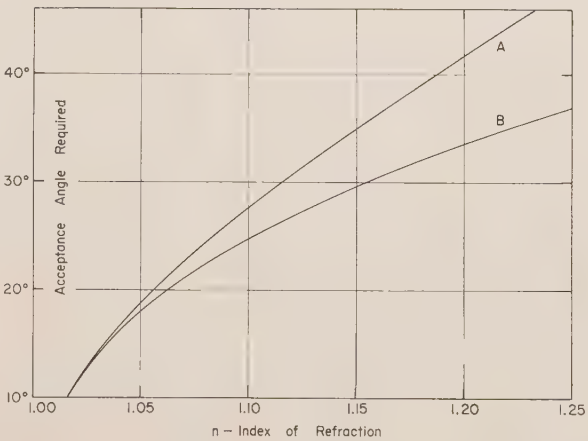


Fig. 9. Refraction increases the angular acceptance needed to accommodate a given velocity range. Curve B shows the acceptance angle required of an immersion mirror objective to accommodate the widest-angle cones obtained with a stated index of refraction $n$. Curve A shows how this angle is increased for a lens objective; it can also be used to show how the measurable velocity range is narrowed for a given angular acceptance. The use of a pyramidal reflector is thus more effective in increasing the angular aperture for a lens than for a mirror.

TABLE 2

Image-intensifier tubes presently available in the U.S. (not an exhaustive list). These tubes are not standard production items, and are available only on special order. All are electrostatically focused. The cathodes are S-11 or S-20, (tri-alkali), and the phosphors P-11 unless otherwise specified by the user.

| Tube type No. | No. of stages | Cathode diam. (in.) | Central magnification | Resolution, line pairs/mm (at cathode) | Nominal gain with P-11 phosphors |
|---|---|---|---|---|---|
| RCA C-73459 | 2 | 1 | 0.82 | 18 | 500 |
| RCA C-73491 | 3 | 1 | 0.82 | 15 | 5000 |
| Westinghouse WX-4171 | 1 | 5 | 0.2 | 1.5–2.5 | (50) |

### 9.4. IMAGE INTENSIFIER SYSTEM

Although the image intensifier tube dates back to 1934, high-gain, low noise, image-intensifier tubes are at present in a relatively early stage of development. The few samples with which scintillation-chamber track-imaging experiments have been carried out are mostly laboratory pilot models. Cascaded image-intensifier systems also find applications in astronomy and in military use; but none of these uses has resulted in volume production of tubes for viewing the visible spectrum. Table 2 shows some image-intensifier tubes presently available in the United States, that have been useful in scintillation-chamber track imaging.

Magnetically-focused multi-stage tubes are being developed; and multistage transmission secondary-electron-multiplier image intensifiers are under development at Westinghouse and in England. Also under development are experimental image-intensifier orthicons, containing one or two stages of image intensification ahead of an image orthicon. Such tubes, which give a television-type output signal, are currently within a factor of 10 or so of being sensitive enough to give direct images of single photoelectrons.

### 9.5. DESIGN OF PLANE MIRROR SYSTEMS TO INCREASE ANGULAR ACCEPTANCE

The tetrahedral mirror systems mentioned in Sec. 8 will improve the effective acceptance angle of the system by decreasing the angular spread of the light, at the expense of increased displacement from the axis. This necessary consequence of Lagrange's law (or phase space conservation) has the effect of decreasing the allowable initial displacement of the trajectory from the axis, as indicated in fig. 6. In addition, it has the effect of severely limiting the location of particle trajectories from which light will be collected, since for large angles the light must be reflected by the mirror to be useful, and the mirror may subtend only a small solid angle at the axis; this is especially true for axial particles at cone angles just greater than the mirror angle. If the particle path is inclined to the axis, however, a fraction of the primary circle may fall within the field of view even for circles larger than the maximum acceptance angle. (as in fig. 7).

## 10. Experimental Test of Image Quality

While no complete test of the proposed sytem has yet been made, a preliminary check on the optical system has been possible. Fig. 10 shows

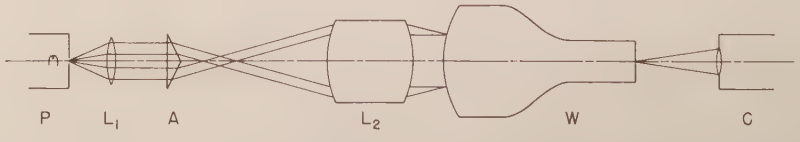


Fig. 10. Experimental system for testing the optics of circular image formation. P is a point source, $L_1$ a lens giving a parallel beam of light. A is an axicon,—a glass cone that converts the incidental parallel light into a cone. $L_2$ is the lens objective that gives a circular image of the simulated Čerenkov cone on the cathode of the WX-4171 image intensifier W, and C a camera photographing the output image of W.

a diagram of an experimental system for producing a simulated Čerenkov cone of light, and fig. 11 is a photograph of the circular image obtained with the special $f/1.5$ relay lens[11]) and a WX-4171 single-stage image intensifier. This is

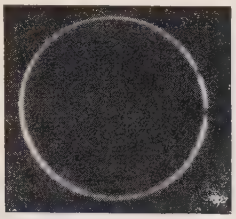

Fig. 11. A photograph of the circular image produced by the system of fig. 10. The diameter of the image can be measured to an accuracy of $\pm$ 0.5%, corresponding to an angular accuracy better than $\pm$ 0.001 radian.

not a weak light image, of course; nevertheless the definition of the image is such that its diameter can readily be determined to better than $\pm$ 0.5%. This corresponds to an angular accuracy considerably better than $\pm$ 0.001 radian. The equivalent velocity error is given by eq. (5).

## 11. Data Handling

Current cascade image-intensifier systems present the output data as light from a phosphor screen (usually P-11) or a kinescope, for recording by a camera using fast 35-mm film. Conventionally the system has a fast (P-15) phosphor in the first stage to allow gating with a coincidence resolving time of about a microsecond. There is a dead time of many milliseconds while the image is recorded and the film is advanced. The rate of collecting data is correspondingly restricted.

Much faster systems than the present one are in principle possible, even using phosphor-photocathode cascades; and secondary-electron multiplication systems are inherently as fast as photomultipliers. Systems of image intensifiers with microsecond or shorter overall dead times are quite possible, and aspects of them are already under development. Such systems will store data at a very rapid rate, and will doubtless require faster automatic or semi-automatic reading and analyzing devices. The type of display available—namely, the ring or multiple-arc image,—appears well-suited to such automatic treatment. The eventual on-line automatic analysis of the output data of Čerenkov image detectors appears to be within the capacity of present automatic data-handling systems, even without further developments in the intensifier systems.

## 12. Possible Methods of Using the Proposed Detector

A detector of wide angular acceptance, capable of measuring relativistic velocities with high precision, and track orientation in space as well, offers some interesting possibilities in high-energy physics. A measurement of momentum, combined with velocity, identifies all but the most highly relativistic particles. Thus the detector might profitably be used in conjunction with a visual detector like a bubble chamber, for the analysis of complex events in the relativistic range, since it can readily accomodate several simultaneous particles. If the visual device determines their momentum with a magnetic field, most of the particles may be identifiable. In such use, the major problem may be that of obtaining a suitably large field of view.

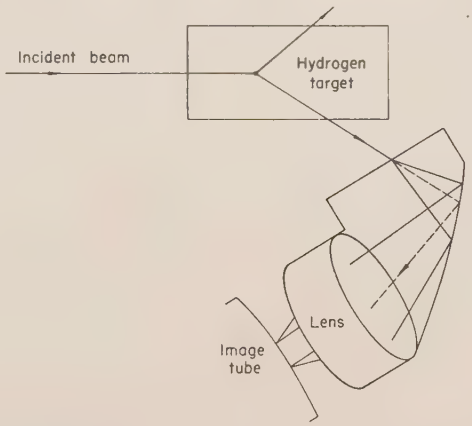


Fig. 12. One possible way of using the detector to measure the direction and velocity of scattered particles over a considerable angular range.

In the lower relativistic reaches, rather precise measurements of velocity may be feasible. Thus, for scattering or two-body reactions, a detector measuring the velocity and direction of secondary

particles over a considerable angular range (and thus readily distinguishing elastic from inelastic events) should find useful applications; see e.g., fig. 12.

It seems likely that detectors can be designed to observe the tracks of particles that do not traverse the entire radiator, but decay or scatter within it. Thus, in an elastic scattering within the radiator, (which might be liquid hydrogen) the centers of the ring images produced by the three particles will be collinear, if the particles are coplanar. Small-angle scattering might be observed in this way.

**Acknowledgements**

I am indebted to Professor Robert E. Hopkins of the University of Rochester Institute of Optics for useful conversations and comments.

NUCLEAR INSTRUMENTS AND METHODS 9 (1960) 67–77; NORTH-HOLLAND PUBLISHING CO.

# APPARATUS AND ANALYSIS FOR SUM-COINCIDENCE (n, γ) SPECTROMETER

J. E. DRAPER and A. A. FLEISCHER *†

*Yale University, New Haven, Connecticut* ††

Received 1 July 1960

Apparatus is described for analyzing two-step cascades of neutron capture gamma rays by the sum-coincidence method and consideration is given to the types of results which can be obtained. A detailed analysis is given of detection efficiency and peak shapes and their dependence on the characteristics of the sum discriminator. Several background effects are analyzed quantitatively such as back-scattering between scintillators, annihilation photon transfer between scintillators, cascades which terminate only near to the ground state, three-photon cascades and uncertainties caused by unknown angular correlations.

## 1. Introduction

Much valuable information about nuclear energy levels and transition probabilities has been obtained by measuring the energies and intensities of gamma rays following neutron capture. Such singles spectra may contain 30 (or more for heavy elements) resolved lines, and the interpretation is often difficult without coincidence data. The low detection efficiency in coincidence experiments and the small source strength often associated with neutron experiments, particularly for resonance capture, necessitate special techniques. The sum-coincidence technique, described by Hoogenboom[1]) is particularly well suited to an investigation of processes consisting of two photon cascades from the capturing state to the ground state. For this technique two conditions are set: (1) The pulses from the two scintillators must be in coincidence. (2) The sum of these two pulse heights must be equivalent in energy to the neutron binding energy of the nucleus. This requires that the energy of both photons has been expended completely in the detectors so that each pulse contributes to a peak at the full energy of the photon.

* Present address: Ramo-Woolridge Corporation, Canoga Park, California.

† Based in part on a Ph. D. thesis submitted by A.A.F. to Yale University.

†† Supported in part by the U.S. Atomic Energy Commission.

## 2. Experimental Method

The experimental geometry[2]) is shown in fig. 1. The NaI(Tl) scintillators were 5 in. diam by 4 in. thick and were mounted on 3 in. photomultipliers. The resolution for 660-keV photons was 9%. The gamma-ray source of photoneutrons was the electron linear accelerator operated at 6 MeV, 200 mA during the burst, 112 pulses per sec. The electron beam was piped to within 3 ft of the end of a hole in the 8 ft concrete shielding wall. In fig. 1 the beam would strike the gold target from the left. The intense forward photon flash from the electron beam burst necessitated careful shielding of the scintillators and made it necessary to gate off the current in the photomultipliers during the burst to minimize gain shifts. The capacitative coupling of this gate to the collector of the photomultiplier produced a slow ringing in the amplifiers (DD2). This feedthrough was cancelled by coupling a mirror image of the gate to the collector through a small capacitor. These efforts greatly reduced the gain shift produced by the beam flash, but there remained a shift of $\sim 1\%$ in 5 hours which was monitored and manually compensated.

The pulses from the two detectors shown in fig. 1 were added and a gate was opened whenever:

[1]) A. M. Hoogenboom, Nucl. Instr. **3** (1958) 57.

[2]) Experimental results to be published. Preliminary report by J. E. Draper and A. A. Fleischer, proceedings of Los Alamos Conference on Neutron Capture Reactions, October, 1959.

(1) their sum corresponded to the binding energy of the neutron in the product nucleus and (2) there were coincident pulses from each of the detectors. Ideally these conditions indicate that: (1) a two-photon cascade has occurred between the capturing state and the ground state *via* any intervening state (2) that one of the photons has been detected in each of the scintillators and (3) that the full energy of each photon has been deposited in its scintillator. When the conditions were fulfilled, the pulse from one of the scintillators was passed to the pulse height analyzer. The resulting spectrum contained no pulses due to events in which part of the photon energy escaped from the scintillator. Departures from these ideal circumstances will be discussed later.

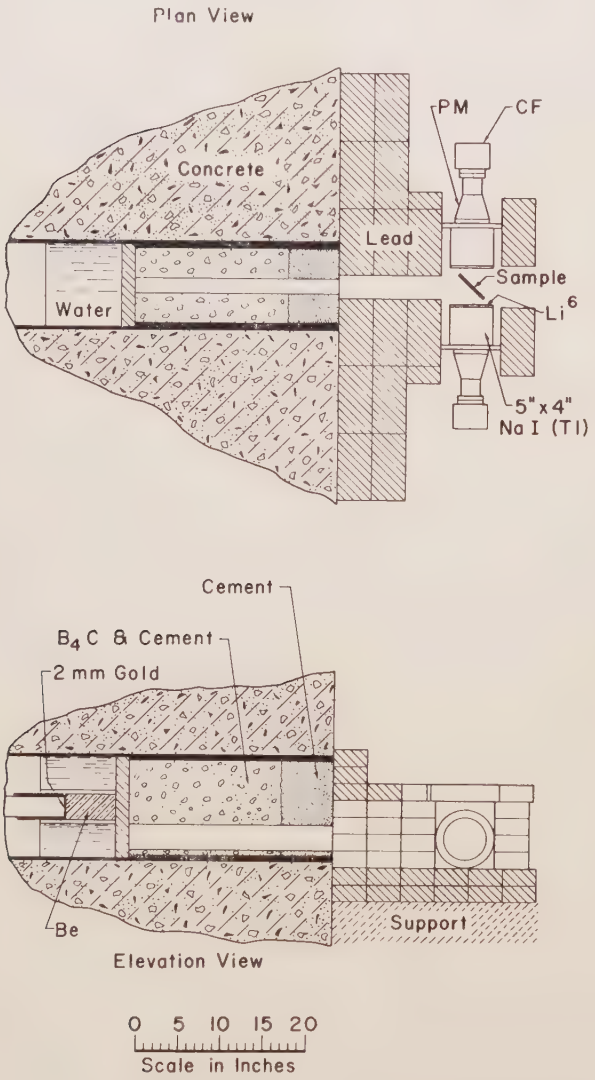


Fig. 1. Experimental geometry. The 5-in. diam × 4-in. NaI scintillators are separated by 4.5 in. between faces.

The block diagram of fig. 2 illustrates schematically the functions of various elements of the spectrometer. In normal operation switches S1 and S2 were closed. The gate circuit was opened by occurrence of all the following circumstances: (1) The time after the accelerator pulse was between 400 $\mu$sec and 800 $\mu$sec as set by the time gate generator. The choice of this interval was dictated by a compromise between recovery from the accelerator flash effects and the rate of arrival of thermal neutrons at the sample. (2) Coincident pulses occurred in detectors A and B. (3) The mixed pulse from detectors A and B was of proper height to correspond to the neutron binding energy of the sample so that the sum discriminator had triggered the sum gate generator. Under these conditions the gate circuit delivered undistorted the pulse from detector A to the multichannel pulse height analyzer. The switches S1 and S2 were used in calibrating gains under operating conditions, and the 180-ohm potentiometer before C.F.2a was used to equalize gains in the two legs feeding the sum amplifier. The units labeled C.F. were White cathode followers[3]). The cables between the detectors and the C.F. units were each approximately 150 ft of RG 114/U.

The fast coincidence circuit has already been described in detail[4]). Essentially it permits resolving times much shorter than the rise time of the data pulses by adjusting the bias of a trigger circuit appropriately to match the height of each input pulse. The pulses delivered to it reached full amplitude in 300 m$\mu$sec, and it gave undistorted spectra at a resolving time $2\tau =$ 12 m$\mu$sec. It is particularly important in this work that real coincidences between pulses in the A and B legs of all combinations of heights

[3]) Moody, Howell and Jarker, Rev. Sci. Instr. **22** (1951) 557.

[4]) J. E. Draper and A. A. Fleischer, Rev. Sci. Instr. **31** (1960) 49.

be accepted with unvarying efficiency. The required range of the ratio of A height to B height was approximately from 1/13 to 13/1 or a combined factor ~ 170. While the performance

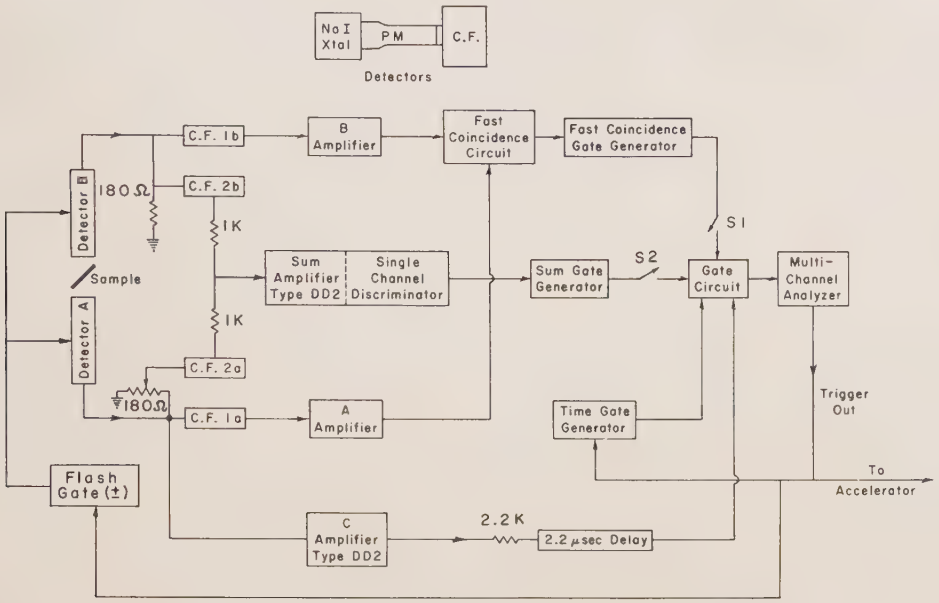


Fig. 2. Block diagram of electronic circuits.

was satisfactory at $2\tau = 12$ m$\mu$sec, the accidental rate was sufficiently low that $2\tau =$ 48 m$\mu$sec was used in the interest of conservatism. The real coincidence rate was then measured as essentially independent of inserted delay over a range of 36 m$\mu$sec and was independent (within $\pm$ 0.5%) of pulse height over the pulse height range specified above.

In fig. 3 is shown a sum-coincidence spectrum produced by thermal neutron capture in chlorine. The full spectrum up to the binding energy is shown here to illustrate the features. Note that symmetry is required about a line at one-half the binding energy. This symmetry is in peak centers and peak areas—not in peak shapes which are energy dependent. There is no peak at the binding energy since coincidences are required. All the peaks indicated here are members of fairly strong two-step cascades in $Cl^{36}$ except that at 8.06 MeV (matched by a peak at 0.51 MeV which was here below the threshold of the pulse height analyzer). The 0.51- and 8.06-MeV peaks are caused by annihilation quantum transfer as analyzed later. Since the information in the upper half of the spectrum is duplicated with better resolution in the lower half, the lower half is usually spread over the entire pulse height analyzer which increases the resolution somewhat and reduces the low energy cut-off.

The problem of balancing the A and B gains and setting the sum discriminator channel should be considered since these adjustments are crucial. The accurate gain balancing must be done in the sum channel of fig. 2 and must be done with the accelerator operating and a sample in place. This was effected by routing the output of the sum amplifier through the gate circuit with S1 open and S2 closed, and then to the pulse height analyzer. The sample of interest was used if its singles spectrum showed sufficient detail, or else the 7.64-MeV line of an iron sample was used. The single channel sum discriminator was set to view all pulses above ~ 4 MeV. The A and B pulses were analyzed separately (without altering matching impedances), and the 180 ohm potentiometer in the input of C.F.2a was used to obtain a balance. Then mixed A and B pulses were viewed to check that the sum

resolution was substantially like the singles resolution. This was repeated at the end of a run.

Next, in order to set the sum channel the sample under investigation was put into place,

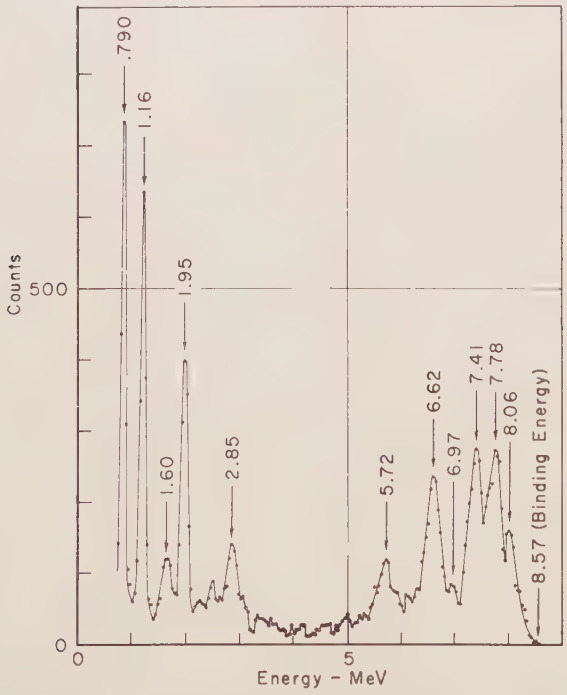


Fig. 3. Sum-coincidence spectrum of $Cl^{35}(n,\gamma)$ $Cl^{36}$.

S1 was closed, and the spectrum from the sum amplifier was analyzed. This sum spectrum usually showed a well defined cut-off corresponding to the binding energy, and its position (taking resolution into account) agreed with that predicted from a 7.64MeV Fe calibration within one analyzer channel (0.7% or about 60 keV). The sum discriminator channel width was then reduced until the narrow rectangular sum spectrum on the monitor of the pulse height analyzer had the required position and width.

Although the gains of the system with the accelerator turned off were stable to within 1% per day, there was a slow drift upwards of photomultiplier gain in both legs with the beam on. This drift was about 0.3% per hour. In order to compensate this drift during a 10 hour run, the monitor corrected sum discriminator counting rate was checked periodically, and series trimmer resistors at the outputs of detectors A and B were adjusted (each by the same amount) to stabilize the count rate. Checks of the gains at the end of a run always verified that the pulse heights were proper.

### 3. Properties of the Sum-Coincidence Method

There are several relevant properties of the sum-coincidence arrangement, some of which have been summarized by Hoogenboom[1]). Consider the photopeaks of the singles spectrum of the two members of a cascade as gaussian curves centered at $E_1$ and $E_2$ with half widths at 1/e of $\Gamma_1$ and $\Gamma_2$, respectively. Define these gaussian shapes as functions $f_1(e_1)$ and $f_2(e_2)$ having unit area. The variables $e_1$ and $e_2$ denote the departure from the centers $E_1$ and $E_2$ respectively. These are shown in fig. 4. The output of the sum amplifier is expressed by the function $f_s(e_s)$, of half width at 1/e of $\Gamma_s$ and centered at $E_s = E_1 + E_2$. The gains in the two legs A and B in fig. 2 contributing to the summed output must be well equalized. This is necessary because the energies of members of various cascades pair together to give the same sum each time, viz., the neutron binding energy. If the gains were not equal the corresponding sum pulse height would not be invariant and the efficiency of detection of cascades would have a false energy dependence.

It can be shown that the shape of the summation peak $f_s(e_s)$ is a gaussian curve of unit area centered at $E_s = E_1 + E_2$ and of width

$$\Gamma_s = (\Gamma_1^2 + \Gamma_2^2)^{\frac{1}{2}}. \qquad (1)$$

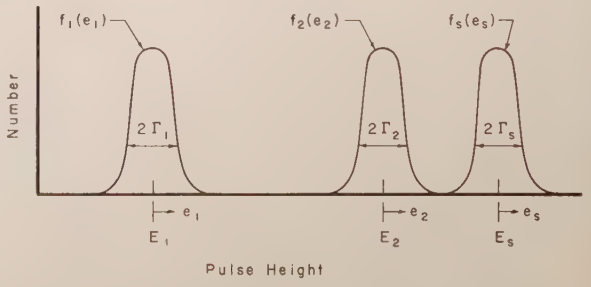


Fig. 4. Schematic illustration of sum-coincidence pulses and notation.

In general the singles photopeak widths can be expressed as

$$\Gamma_1^2 = \alpha_1 E_1 + \beta_1 \qquad (2)$$

$$\Gamma_2^2 = \alpha_2 E_2 + \beta_2$$

where $\alpha$ and $\beta$ are constants of the scintillators and electronic circuits. Then if $\alpha_1 = \alpha_2$, *i.e.*, if the energy dependent part of the resolution of each scintillator has the same coefficient, then $\Gamma_s$ is a constant for a given neutron binding energy. This condition simplifies the expression for the efficiency of detection of cascades.

Given a two-photon cascade with one photon at energy $E_1$, denote the probability of obtaining a count in the peak at $E_1$ in a sum-coincidence spectrum as $\varepsilon(E_1)$. We designate the shape of the transmission function of the sum discriminator as $f_d(e_s)$. Then

$$\varepsilon(E_1) = \Omega_1\Omega_2\, p_A(E_1) p_B(E_2) \int_{-\infty}^{\infty} f_s(e_s)\, f_d(e_s) de_s \qquad (3)$$

where $4\pi\Omega$ is the solid angle subtended by the scintillator and $p_A(E_1)$ is the intrinsic peak efficiency of scintillator A at photon energy $E_1$. When the discriminator transmission function $f_d(e_s)$ has a gaussian shape centered at $(E_s + \delta)$ — viz.,

$$f_d = e^{-(e_s - \delta)^2/\Gamma_d^2}, \qquad (4)$$

then eq. (3) gives

$$\varepsilon(E_1) = \Omega_1\Omega_2\, p_A(E_1) p_B(E_2)$$

$$\frac{\Gamma_d}{(\Gamma_1^2 + \Gamma_2^2 + \Gamma_d^2)^{\frac{1}{2}}} e^{-\delta^2/(\Gamma_1^2 + \Gamma_2^2 + \Gamma_d^2)} \qquad (5)$$

Consequently, the relative areas of various peaks in a given sum-coincidence spectrum are energy dependent only through the photopeak efficiencies even if the discriminator channel should be improperly off center by the amount $\delta$. Note that $\varepsilon(E_1) \equiv \varepsilon(E_2)$.

The gaussian discriminator transmission function is mathematically convenient but unrealistic. Consider instead a rectangular discriminator transmission function

$$f_d = \begin{cases} 1 \mid e_s - \delta \mid \leqslant \Gamma_d \\ 0 \mid e_s - \delta \mid > \Gamma_d \end{cases} \qquad (6)$$

which is centered at $(E_s + \delta)$. Then the efficiency is given by

$$\varepsilon(E_1) = \frac{\Omega_1\Omega_2\, p_A(E_1) p_B(E_2)}{\sqrt{\pi}\,(\Gamma_1^2 + \Gamma_2^2)^{\frac{1}{2}}} \int_{\delta - \Gamma_d}^{\delta + \Gamma_d} e^{-e_s^2/(\Gamma_1^2 + \Gamma_2^2)}\, de_s \qquad (7)$$

which again is energy dependent only through the photopeak efficiencies. For the particular case (used in the present experiments) where the rectangular discriminator function is properly centered (*i.e.*, $\delta = 0$), and its width is set equal to the full width at half maximum of the sum peak *i.e.*, $[\Gamma_d = (\Gamma_1^2 + \Gamma_2^2)^{\frac{1}{2}} \ln 2]$ then

$$\varepsilon(E_1) = 0.67\, \Omega_1\Omega_2\, p_A(E_1)\, p_B(E_2)\,. \qquad (8)$$

It is also of interest to consider the shape of the component peaks in a sum coincidence spectrum. These are the peaks recorded by the multichannel pulse height analyzer of fig. 2. With the gaussian discriminator transmission function of eq. (4) the peak shape for energy $E_1$ is gaussian with width

$$\Gamma_{SCI} = \Gamma_1\, (\Gamma_2^2 + \Gamma_d^2)^{\frac{1}{2}} / (\Gamma_1^2 + \Gamma_2^2 + \Gamma_d^2)^{\frac{1}{2}} \qquad (9)$$

which is always less than the width $\Gamma_1$ of the peak in the singles spectrum and is independent of $\delta$, the sum channel center. If $\delta \neq 0$ the center of the peak is shifted to $E_1 + \sigma_\delta$ where the shift is

$$\sigma_\delta = \frac{\delta}{(\Gamma_1^2 + \Gamma_2^2 + \Gamma_d^2)^{\frac{1}{2}}} \frac{\Gamma_1}{(\Gamma_2^2 + \Gamma_d^2)^{\frac{1}{2}}} \Gamma_{SCI}\,. \qquad (10)$$

This indicates that the discriminator channel must be set with care. However, in the extreme case where $\delta = \Gamma_d = (\Gamma_1^2 + \Gamma_2^2)^{\frac{1}{2}}$ and $E_1 = E_2$ then $\sigma_\delta / \Gamma_{SCI} = 1/\sqrt{6}$. The estimate for the present experiments is that

$$\sigma_\delta / \Gamma_{SCI} \leqslant 0.13\, (E_1/E_2)^{\frac{1}{2}}\,. \qquad (11)$$

When the rectangular discriminator transmission function is used the sum coincidence peak is not generally of gaussian shape as it was for eq. (9). However it is gaussian in the limit $\Gamma_d \ll \Gamma_2$ in which case it has the properties described in eqs. (9) and (10). It is also gaussian in the limit $\Gamma_d \gg \Gamma_1$, $\Gamma_d \gg \Gamma_2$ in which case it has the shape of $f_1$. The general shape for the sum

coincidence peak with the rectangular discriminator transmission function is $f_1(e_1)\, g(e_1)$ where

$$g(e_1) = \frac{1}{\sqrt{\pi}\, \Gamma_2} \int_{-(e_1-\delta)-\Gamma_d}^{-(e_1-\delta)+\Gamma_d} e^{-e_2^2/\Gamma_2^2}\, de_2 \quad (12)$$

and $f_1(e_1)$ is the gaussian of width $\Gamma_1$ as defined earlier. The function $g(e_1)$ is a difference of error functions and is evidently a bell shaped curve centered at $e_1 = \delta$, with width $\sim \Gamma_2 + \Gamma_d$.

In selecting the discriminator channel width for these experiments a compromise was required between loss of efficiency and gain of resolution as the channel width is decreased. The greatest gain in useful resolution occurs at $E_1 = E_2$. For this condition eq. (9) shows that if $\Gamma_d \to 0$ then $\Gamma_{SCI}/\Gamma_1 = 0.71$ while if $\Gamma_d = (\Gamma_1^2 + \Gamma_2^2)^{\frac{1}{2}} \ln 2$ then $\Gamma_{SCI}/\Gamma_1 = 0.81$. The latter value of $\Gamma_d$ was used for the experiments in view of the great difference in efficiency and the small difference in resolution. Several tests of the width of sum-coincidence peaks using radioactive sources and (n,$\gamma$) sources confirmed the expected widths.

## 4. Detection Efficiency

Eqs. (5) or (7) indicate that the only energy dependence of efficiency is in the intrinsic peak efficiencies. These were measured for the specific experimental geometry with $Cs^{137}$, $Zn^{65}$ and RaD-Be sources giving 0.662, 1.11 and 4.43 MeV photons. First the source strengths were measured in a parallel beam geometry for which the total efficiencies could be calculated accurately. Then those sources were used in the specific experimental geometry to obtain the $p(E)$ of eqs. (5) or (7). The intrinsic peak efficiency is here defined in the usual manner as the number of counts in the full energy peak divided by the number of photons which traversed any of the scintillator. Correspondingly, $4\pi\Omega$ is the solid angle, in steradians, included within the most divergent rays from the source center which touch the scintillator. In order to check these measurements, the same sources were used to obtain photopeak efficiencies of a 3-in. by 3-in. NaI(Tl) scintillator at 9.3 cm. the conditions used in extensive investigations by Heath[5]).

Fig. 5 shows the composite results of these measurements and the upper solid line represents the photopeak efficiencies used in analyzing the present (n,$\gamma$) experiments, A greater variety of

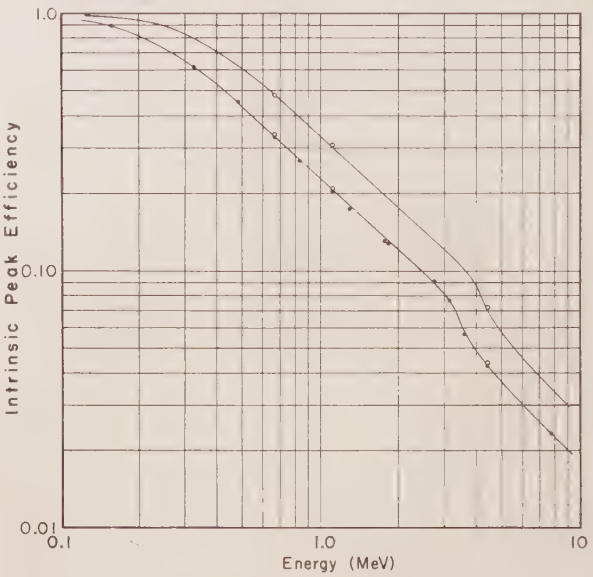


Fig. 5. Intrinsic peak efficiency. The bottom curve is for a 3-in. × 3-in. NaI(Tl) scintillator at 9.3 cm. The top curve is for the present scintillator geometry of fig. 1.

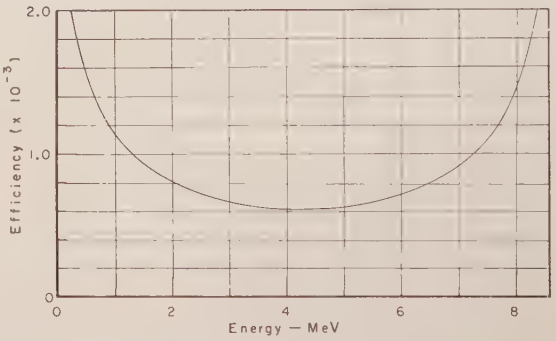


Fig. 6. Sum-coincidence efficiency for the conditions of fig. 1.

source energies would have been useful, but they were not available. Fig. 6 shows the resulting curve of the quantity $\Omega_1\Omega_2\, p_A(E_1)p_B(E_2)$ against $E_1$ for $E_1 + E_2 = 8.57$ MeV and the experimental geometry of fig. 1—viz. 5-in. diam by 4-in. crystals separated by 11.4 cm. Hence the curve in fig. 6 would be the probability of detecting a two-photon cascade of unit intensity in the limit of a very large sum discriminator channel width.

[5]) R. L. Heath, A.E.C. Research and Development Report IDO-16408 (1957).

## 5. Types of Results

Let us consider the detection of a two-photon cascade following neutron capture. Denote the intensity of a particular transition from the neutron capturing state as $I_1$ photons per captured neutron. Such a transition populates a level which has a branching probability, denoted $b_2$, of depopulating directly to the ground state. Note that $b_2 \equiv 1$ for the first excited state. Then the counting rate of pulses in the sum-coincidence peak at energy $E_1$ will be denoted by $R_{12}(E_1)$. Consequently

$$R_{12}(E_1) = R_{12}(E_2) = I_1\, b_2\, \varepsilon(E_1) C\, \tau(E_1\,, E_2)\alpha \quad (13)$$

where $C$ denotes the rate of capture of neutrons in the sample, $\tau$ is a photon absorption factor to be discussed later, and $\alpha$ is an angular correlation factor to be discussed later.

In these experiments the energy dependence of $\varepsilon(E_1)$ on $E_1$ is considered as known from eqs. (5) or (7), and $\varepsilon(E_1)C$ is calibrated for each sample by a cascade for which $I_1 b_2$ is known. Such a cascade would preferably be through first excited state for which $b_2 = 1$ and $I_1$ is the obtained from previously available data on the singles spectrum.

Consider what results could be obtained from an *ideal* sum-coincidence experiment with line widths small compared to level separations, with great sensitivity above background, and with $\varepsilon(E_1)C$ already known: (1) Identification of the energies of all levels for which $I_1 b_2$ is not vanishingly small under the assumption that the lower energy member of the cascade is the second transition. (2) When values of $I_1$ are available from singles spectra, then $b_2$ is obtained which may give information related to the angular momentum and parity of the level. (3) When information about $b_2$ is available (*e.g.* from radioactivity studies) then $I_1$ is obtained under the usual assumption that $b_2$ is independent of the method of population of the level. (4) When $I_1$ is already available from a singles spectrum and $b_2$ is available from radioactivity studies then the question of whether $b_2$ is independent of the method of formation of the level can be studied. Presumably, the answer would be in the affirmative. (5) By varying the angle between the scintillators an angular correlation study of all these levels can be made at once.

Results of type (1) are already available in a large number of cases from singles spectra insofar as their interpretation does not require coincidence data. Consequently for the nucleides studied here the results of type (2) are obtained Combinations of results of types (2) and (5) would be extremely useful for evaluating the parameters of excited states, but the neutron flux obtainable during the present experiments was too small† to allow a suitable geometry for this type of work.

There is a possibility that the sum-coincidence method can be used to investigate resonance neutron capture when larger fluxes are obtainable. Then the thermal neutron experiments would be combined with thermal values of $I_1$ to obtain $b_2$. Under the assumption that the same values of $b_2$ apply for resonance capture the sum-coincidence results would provide values of $I_1$ for capture in various resonances. Furthermore, a particular initial transition would be identified and selected with an energy uncertainty appropriate to that of the lower energy photon in the cascade—*e.g.*, $\sim 1\%$ for a 1 MeV-7 MeV cascade. The efficiency indicated in fig. 6 would be significantly larger than that of other devices of comparable resolution, a feature of great importance in resonance capture.

## 6. Perturbing Effects

There are several perturbing effects which might influence the results. They include two-photon cascades which do not terminate in the ground state, photons which originate in one scintillator and deposit their energy, in the other, and three-photon cascades.

Consider the effect of the sum peak width $\Gamma_s$, eq. (1), on the results. When the width is not small compared to the energy of the first excited

† The flux of thermal neutrons at the sample in fig. 1 averaged over one second was $\sim 40\ \mathrm{cm^{-2}\,sec^{-1}}$ while external thermal neutron beams of more than $10^5\ \mathrm{cm^{-2}\,sec^{-1}}$ have been available from reactors.

state, then two-photon cascades to the first excited state will be included in the spectrum with reduced probability. Let us define the rejection ratio $R_R$ as (probability of detecting a two-photon cascade to the ground state) $\div$ (probability of detecting a two-photon cascade to the first excited state at energy $E_x$). Then for a gaussian sum discriminator transmission function eq. (5) indicates that the rejection ratio is

$$R_R = e^{E_x^2/(\Gamma_s^2+\Gamma_d^2)} \qquad E \ll E_s . \tag{14}$$

For a rectangular sum discriminator transmission function, eq. (7) indicates that

$$R_R = \int_{-\Gamma_d}^{\Gamma_d} e^{-e_s^2/\Gamma_s^2}\, de_s \Big/ \int_{-\Gamma_d+E_x}^{+\Gamma_d+E_x} e^{-e_s^2/\Gamma_s^2}\, de_s$$

$$E_x \ll E_s . \tag{15}$$

Eq. (15) is plotted in fig. 7 for $E_s = 8$ MeV, $2\Gamma_s = 2\Gamma_d/\ln 2 = 0.46$ MeV. Thus, fig. 7 represents the factor of rejection of twophoton cascades terminating at a level of energy $E_x$ rather than at the ground state.

Another important consideration involves events in which the full energy $E_s$ is shared between the two scintillators, but a Compton

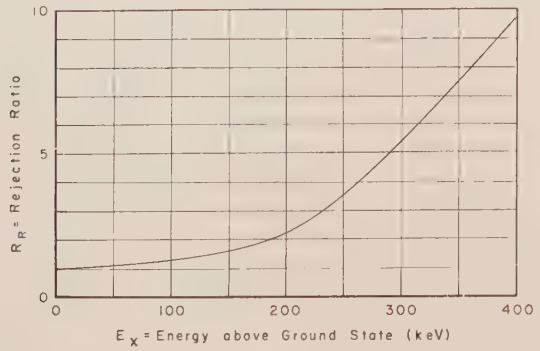


Fig. 7. Rejection ratio for two-fold cascades terminating at a level of energy $E_x$. See eq. (15).

recoil photon or annihilation photon has its origin in one crystal and deposits its energy in the other crystal. In this way false peaks can be generated at points 511 or $\sim$ 255 keV on either side of a proper peak, zero energy or $E_s$.

It is evident that the geometry of fig. 1 could be improved in terms of this cross-talk between scintillators by increasing dimensions and inserting lead shielding. However, the neutron flux limitation precluded this solution of the problem since the counting rate would have been reduced by a factor $\gtrsim 10$ in a geometry with appreciable shielding between crystals. Consequently it was decided to: (1) calculate the magnitude of the effect to determine under what conditions it was important and (2) make one run for each sample with the geometry of fig. 1 and a second run for each sample with a 2.1 g cm$^{-2}$ lead sheet absorber over the face of each scintillator.

To estimate the magnitude of these effects, consider the following processes in which the full energy $E_2$ is deposited in one of the scintillators and:

(1) The full energy $E_1$ is deposited in the other scintillator.

(2) The full energy $E_1$ is deposited in a scintillator except for a Compton recoil photon in the backward direction which deposits all of its energy in the $E_2$ crystal. The energy of the Compton recoil photon will generally be about 255 keV in the present experiments.

(3) The full energy $E_1$ is deposited in a scintillator except for a 510-keV annihilation photon which deposits all of its energy in the $E_2$ crystal.

In each of the above cases the proper sum energy is obtained. In processes (2) and (3) false peaks could be obtained in one of the crystals at 255 keV, 510 keV, $E_s$-255 keV, $E_s$-510 keV, and ($E_1$ or $E_2$) $\pm$ (255 or 510 keV). Let $f_{255}(E_1)$ be the probability of process (2) divided by the probability of process (1). Let $f_{510}(E_1)$ be the probability of process (3) divided by the probability of process (1).

The quantity $f_{255}(E_1)$ is evaluated by approximating that the path lengths for photons are those of trajectories parallel to the NaI-NaI axis. However, the correct three-dimensional solid angles are used. Then

$$f_{255}(E_1) = \frac{p(255)}{p(E_1)} \cdot$$

$$\cdot \int_0^D e^{-\mu(E_1)x}\, \frac{\mu_C(E_1)}{\mu(E_1)}\, f_\Omega(E_1)\, e^{-\mu(255)x}\, \mu(E_1)\, dx \tag{16}$$

where $D$ is the NaI thickness; $\mu(E)$ is the total linear attenuation coefficient at the energy $E$ for

NaI; $\mu_C(E_1)/\mu(E_1)$ is the probability that the first interaction is a Compton collision; $f_\Omega(E_1)$ is the probability that the direction of the scattered photon is in the cone subtended by the other NaI crystal from the site of collision; and $p(E)$ is the intrinsic peak efficiency at energy $E$. Since plots of the Compton recoil electron energy distribution, $\sigma(\varepsilon)d\varepsilon$ were available[6]), the magnitude of $f_\Omega$ was evaluated as

$$f_\Omega(E_1) = \int_{\varepsilon_0}^{E_1} \sigma(\varepsilon)\,d\varepsilon \Big/ \int_0^{E_1} \sigma(\varepsilon)\,d\varepsilon \qquad (17)$$

where $\varepsilon_0$ (a function of $E_1$) is the recoil electron energy at the angle defined by the half-angle of the cone which one crystal subtends from a point 1.3 cm into the other crystal along the axis. The result is

$$f_{255}(E_1) = \frac{\mu_C(E_1)}{\mu(E_1) + \mu(255)}\, f_\Omega(E_1)\, \frac{p(255)}{p(E_1)}. \qquad (18)$$

This was evaluated for the geometry of fig. 1, using $p(E)$ from fig. 5. The result is given in fig. 8 with a constant factor $X^2(255) = 0.11$ which takes into account the effectiveness of the lead absorbers as explained below.

Although this estimate of $f_{255}(E_1)$ is approximate, fig. 8 shows that the effect is so small that the approximations are unimportant. Furthermore, eq. (18) was tested experimentally with $Co^{60}$ at $E_1 \cong 1.2$ MeV, and the results differed from those predicted by less than 15%.

Evaluation of $f_{510}(E_1)$ with the same type of approximations as above gives

$$f_{510}(E_1) = \int_0^D e^{-\mu(E_1)x} \cdot \frac{\mu_p(E_1)}{\mu(E_1)}\, 2\Omega\, e^{-\mu(510)[R_+ + x]}\, \mu(E_1)\, dx\, \frac{p(510)p'(510)}{p(E_1)}. \qquad (19)$$

In this notation $\mu_p(E_1)/\mu(E_1)$ is the probability that a given first interaction is pair production. The $\Omega$ is the solid angle subtended by either crystal from the interaction site in the other crystal. Since the $E_1$ flux at the center of the crystal is nearly half that at the entering face, for $E_1 = 2$–10 MeV, the $\Omega$ is approximated to be constant and is evaluated from the point at the center of the body of the crystal. The factor 2 before $\Omega$ takes into account the duplicity of

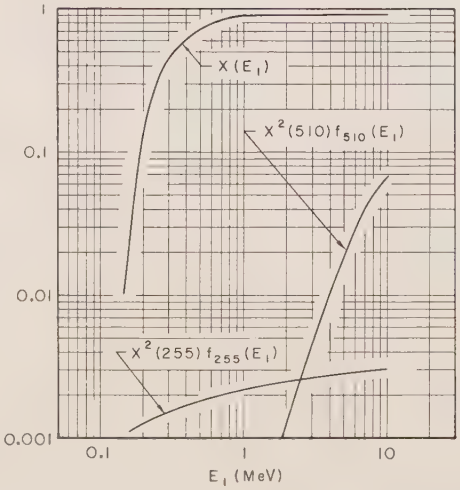


Fig. 8. Correction factors relevant to photon transfer between scintillators. See eqs. (18) and (20) and table 1.

annihilation photons. The $R_+$ is the mean penetration of a positron of energy $\frac{1}{2}(E_1 - 1.02$ MeV) so the annihilating positron is treated approximately as going in the forward direction with half the available energy. This approximation is unimportant since $f_{510}$ is increased only 8% at 10 MeV and 5% at 6 MeV if the other extreme is taken that the annihilation site is the same as the pair production site. The symbols $p'(510)$ and $p(510)$ represent, respectively, the intrinsic peak efficiency for the annihilation photon in the crystal of initial interaction and in the other crystal.

The result is

$$f_{510}(E_1) = \frac{p(510)\,p'(510)}{p(E_1)}\, \frac{\mu_p(E_1)}{\mu(E_1) + \mu(510)}\, 2\Omega\, e^{-R_+\mu(510)}. \qquad (20)$$

This is shown in fig. 8 after being multiplied by $X^2(510) = 0.58$ as explained below.

In order to reduce the perturbing effects represented by $f_{255}(E_1)$ and $f_{510}(E_1)$ the two lead absorbers were used as mentioned above. Each slab was 2.1 g cm$^{-2}$ in thickness and one was placed in contact with the front face of each

[6]) U.S. National Bureau of Standards Circular NBS 542 (1953).

crystal. These background processes in which photons originate in one crystal and are absorbed in the other crystal are reduced relative to foreground by the attenuation of the two slabs of lead. The foreground processes are not so attenuated since a low energy photon in one crystal must be accompanied by a high energy photon in the other crystal.

The transmission of one slab of lead is shown in fig. 8 as $X(E_1)$. The circumstance of poor geometry is approximately taken into account by using only removal cross sections, *i.e.*, the full pair cross section and photoelectric cross section, but only that fraction of the Compton cross section for which the recoil photon energy is not within the NaI resolution half-width from the incident energy $E_1$. Experimental checks of $X(E_1)$ through 3 MeV with this geometry gave satisfactory results.

When the neutron capture sample is of appreciable thickness its absorption has an effect like that of the lead. So we denote the effective transmission of the sample for its (n,$\gamma$) photons as $Y(E_1)$. To first approximation $Y(E_1)$ is the transmission of half the sample. This would be strictly true if the absorption coefficients for $E_1$ and $E_2$ were the same since $e^{-x}\, e^{-(2D-x)} = e^{-2D}$. When the sample shadows one crystal from the other, then the attenuation of the 255- or 511-keV background is $Y^2(255)$ or $Y^2(511)$ if $Y$ is the transmission of half the sample.

The factor $\tau(E_1, E_2)$ in eq. (13) is now

$$\tau(E_1, E_2) = X(E_1)\, X(E_2)\, Y(E_1)\, Y(E_2)\,. \qquad (21)$$

TABLE 1
Background peak areas

| Energy | Peak area |
|---|---|
| $E_1$ or $E_2$ | 1 |
| $E_1 + 255$ or $E_2 - 255$ | $f_{255}(E_2)\, X^2(255)\, Y^2(255)$ |
| $E_1 - 255$ or $E_2 + 255$ | $f_{255}(E_1)\, X^2(255)\, Y^2(255)$ |
| $E_1 + 510$ or $E_2 - 510$ | $f_{510}(E_2)\, X^2(510)\, Y^2(510)$ |
| $E_1 - 510$ or $E_2 + 510$ | $f_{510}(E_1)\, X^2(510)\, Y^2(510)$ |
| $255$ or $E_s - 255$ | $[f_{255}(E_1) + f_{255}(E_2)]\, X^2(255)\, Y^2(255)$ |
| $510$ or $E_s - 510$ | $[f_{510}(E_1) + f_{510}(E_2)]\, X^2(510)\, Y^2(510)$ |

Table 1 lists the intensities of a foreground peak at $E_1$ and the various possible background peaks described above. These are plotted in fig. 9 for the case that the sample transmissions $Y(255) \to 1$, $Y(510) \to 1$ and $E_1 = 2$ MeV, $E_s = 7$ MeV.

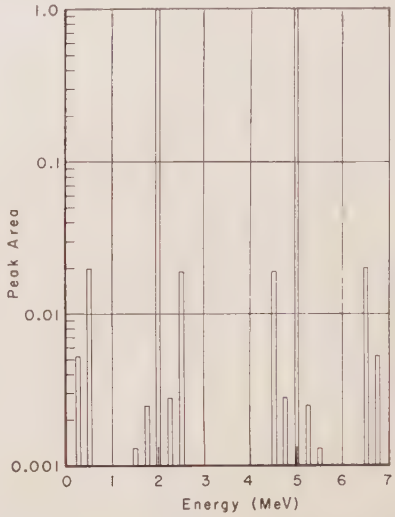


Fig. 9. Example of the low intensities of false peaks from table 1 for $E_1 = 2$ MeV and $E_s = 7$ MeV.

For this example there is no background peak greater than $\frac{1}{50}$ of foreground. The worst case is for large $E_2$. For example if, $E_2 = 9$ MeV then the peak at $E_1 + 510$ would have an area 0.07 that of the $E_1$ peak. This is still small enough that fig. 8 can be used to evaluate the correction.

Triple coincidences will contribute another kind of background. In this case a triple cascade of energies $E_3$, $E_4$ and $E_5$ whose sum is $E_s$ can be detected by total absorption of two of the photons in one crystal and total absorption of the third photon in the other crystal. Let $f_3$ be the ratio, probability of a count at $E_3$ from such triple cascades divided by the probability of a proper count at $E_2$ from a double cascade of photons of energies $E_1$ and $E_2$ whose sum is also $E_s$. Then

$$f_3 = \frac{I_3}{I_2} \frac{p(E_3)p(E_4)p(E_5)}{p(E_1)p(E_2)} \frac{\Omega}{2} \qquad (22)$$

where $I_3/I_2$ is the ratio of the frequency of occurrence of the triple cascade to that of the double cascade, $p(E)$ is the intrinsic peak efficiency as in fig. 4, and $\Omega$ is the fractional solid angle of one of the crystals. The $\Omega$ is the

same for either crystal at any energy. The sum-coincidence spectrum from triple cascades alone would have equal numbers of counts at pulse heights corresponding to $E_3$, $E_4$ and $E_5$. Thus only half the triple cascade events produce a count in the A crystal at any particular energy, *e.g.*, $E_3$, while every double cascade event produces a count in the A crystal at $E_1$. This accounts for the factor $\frac{1}{2}$ in eq. (22).

Consider $E_3 \approx E_1$. Then the worst case is $E_4 \ll E_5$, whereupon $p(E_4) \to 1$, $p(E_5) \to p(E_2)$ and $f_3 \to (I_3/I_2)(\Omega/2)$. Note that for $E_4 \ll E_5$ the effect of the rejection ratio of eqs. (14) and (15) must also be included. For the geometry of fig. 1 we have $\Omega/2 = 0.08$ which would represent the relative probability of a count in the region $E_3 \approx E_1$ from a triple cascade and from a double cascade of equal intensity ($I_3 = I_2$) in the worst case that one of the other members of the triple cascade is of energy $\lesssim 300$ keV. For the same conditions except that this latter energy is $\geqslant 650$ keV then $f_3 < 0.04$. This effect must be neglected unless auxiliary information about triple cascades can be obtained for use in eq. (22). It is fortunate that the effect is small. When counting rate permits, the effect can be investigated experimentally by measurements at two values of crystal separation *i.e.*, by a change of $\Omega$ in eq. (22).

The effect of angular correlation of successive transitions in a two-step cascade can be considered as follows. The correlation coefficient is generally

$$W(\theta)\,\mathrm{d}\Omega = (1 + a_2 \cos^2\theta + a_4 \cos^4\theta)\,\mathrm{d}\Omega\,. \quad (23)$$

The usual condition is that the initial transition is dipole so that $a_4 = 0$ [8]). For the geometry of fig. 1 the average value of $\theta$ is $\pi$, and it is approximated that the photopeak efficiency is independent of $\theta$ until a limiting angle where it goes to zero. Then the angular correlation factor $\alpha$ of eq. (13) is

$$\alpha = \frac{1 + f_2 a_2 + f_4 a_4}{1 + \frac{1}{3}a_2 + \frac{1}{5}a_4}\,. \quad (24)$$

The quantities $f_2$ and $f_4$ take into account the $\theta$ extent of the detectors, and they are approximately 0.87/3 and 0.96/5 respectively. For an extreme example of $a_2 = 1$, $a_4 = 0$ then $\alpha = 0.97$.

Consequently, angular correlation is not usually an important perturbation for the close-up geometry of fig. 1. When the level spins and transition multipolarities are separately known then $\alpha$ can be evaluated exactly. Also, it is possible to measure $W(\theta)$ directly with the sum-coincidence method by varying the angle between detectors in relatively good geometry.

[8]) C. N. Yang, Phys. Rev. **74** (1948) 764.

NUCLEAR INSTRUMENTS AND METHODS 9 (1960) 78–86; NORTH-HOLLAND PUBLISHING CO.

# SYNCHROTRON MAGNET POWER CIRCUIT WITH A DISTRIBUTED CAPACITOR BANK†

SIGURD WAABEN

*Princeton - Pennsylvania Accelerator, Princeton University*

Received 5 May 1960

This paper deals with a synchrotron magnet ring circuit suitable for exciting the bending magnets with exactly equal DC biased sinusoidal currents. A distributed series resonance excitation is made practicable by the introduction of network constraints on the capacitor potentials. The central network component is a transformer choke. The practicable arrangements of the choke topology may take various forms determined essentially by economic considerations. Model tests and analysis are given.

## 1. Introduction

There are several well known ways to produce the periodic magnet field variation in a synchrotron. A basic problem in any scheme suitable for a big accelerator is simply where to store energy when it is not stored as magnetic energy in the airgaps of the bending magnets. Energy storage in flywheels, as well as energy storage in capacitors, has been used.

A simple *L-C* resonance network for achieving a DC biased sinusoidal excitation of accelerator bending magnets has been used in some accelerators[1]). Simple series coupling of the magnets has been used in cases involving several magnets for securing equal current through all the magnets. However, the inevitable stray capacities to ground of the magnet coils act in such a way that the series coupled magnet string has the character of a low frequency pass filter. Exact current equivalence in all magnets is, therefore, not possible in this simple series connection. Furthermore, this scheme becomes impractical for accelerators having many magnets because of the necessary high driving potential across the series coupled magnets. If a low magnet impedance is chosen, it results in impracticably large currents for giving the necessary magnet ampere turns. To overcome this dilemma a distributed resonance scheme was originally proposed by M. G. White for the Princeton-Pensylvania Accelerator. It consisted of 16 magnet semioctants in series with 16 equal capacitors each shunted by separate choke coils to provide the DC path. In order to minimize the size of the choke cores E. M. Purcell suggested winding the choke coils on a common ring core as shown in fig. 1. This circuit originally was adopted by the Princeton group and in a modified form

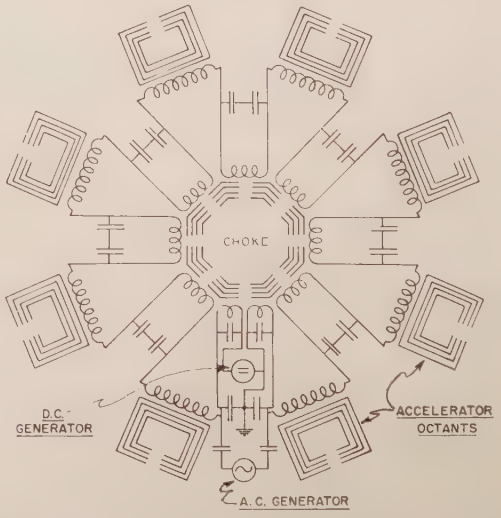


Fig. 1. Proposed magnet power circuit with distributed capacitor bank, from ref.[2]).

† This work was supported by the A.E.C. and the Higgins Fund.

[1]) W. F. Westendorp, J. app. Phys. **16** (1945) 657.

by the Cambridge Electron Accelerator group[2,3]).

The philosophy of the network shown in fig. 1 is as follows: In a multi $L$-$C$ series resonance circuit the AC potential across each inductance is in phase opposition to the potential across each capacitor. The sum of the potentials across the magnets, with respect to ground potential, therefore, does not accumulate around the magnet ring. The parallel resonance tuned choke coils provide a DC path around the capacitors and act, together with the capacitors, as a temporary storage for the energy fluctuating in and out of the accelerator magnet airgaps.

There can be a substantial saving in choke size if it is possible to operate the circuit by using one common choke core where the same magnetic flux lines pass through several or all choke coils. The energetically advantageous scheme has a rather involved circuit performance.

## 2. Ferrite Model

The behavior of networks is determined by the simultaneous solutions of circuit loop equations of the well known type:

$$e = Ri + L\frac{\mathrm{d}i}{\mathrm{d}t} + \frac{1}{c}\int i\mathrm{d}t + \sum_k M_k \frac{\mathrm{d}i_k}{\mathrm{d}t}\,. \qquad (1)$$

or the equivalent in an operational calculus notation. For a low loss circuit the $Ri$ term is small in relation to the other individual terms.

The general network equation system may easily be set up on a loop basis or on a node basis. The subloop intercoupling terms in the equations depend on the geometry of the choke's magnetic circuit layout. This, taken together with the great number of interaction terms in the equations, makes necessary a computation aid for investigating the problem adequately. Preferably, this should be a system having a complete analogy with the magnetic flux pattern of the choke, as well as analogy with the system impedance. A scaled model run at high frequency constitutes such an analogue.

[2]) The Princeton-Pennsylvania Accelerator, CERN Symposium 1956 Proceedings. p. 525.

[3]) The Cambridge Electron Accelerator, CERN Symposium 1956 Proceedings. p. 439.

The impedance level will be the same in a scaled system if the model frequency is scaled by the same factor as the reactive parameters. A brief study of eq. (1) shows this is so.

Ferrite has small losses in the audiofrequency range. Therefore, by using ferrite as the magnetic material in a scaled core, it is possible to choose a high time-scale factor and, therefore, correspondingly small geometrical dimensions without getting excessive losses that would violate the condition that the resistive term in eq. (1) should be small.

A ferrite model has been built with a geometrical scale factor of 1:50 and, for ease of coil winding, with a scaling of the number of turns, resulting in a 15 kc/s table model of the planned full size multimegawatt 20 c/s system. The ferrite model choke core is a circular ring having 16 equal airgaps. The model has 16 identical ferrite inductances representing magnets, and the 16 capacitor banks are each 1.5 $\mu$F. The model network is thus electrically, as well as mechanically, symmetrical.

The photograph, fig. 2, shows the ferrite model. The model is easily powered by a standard 75 watt audioamplifier.

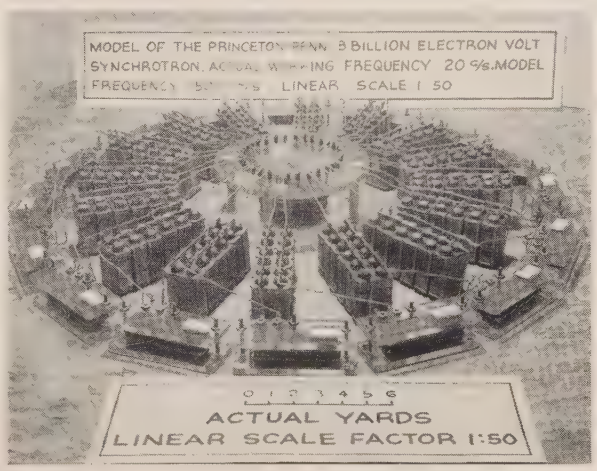


Fig. 2 Photograph showing the 15 kc/s ferrite analog model.

## 3. The Practicable Network

It is well known that a circuit scheme, as shown in fig. 1, with a common choke core, has a multiple resonance pattern. This is so because it

involves magnetically coupled resonance circuits. The presence of multiple resonances is, in itself, not an absolute argument against this network scheme, since exactly the same current flows in each magnet as demanded by Kirchoff's equation. However, model analysis showed that the capacitor potential distribution is so sensitive to small changes in the circuit parameters that it is difficult to achieve even a reasonably uniform capacitor potential distribution. It is, therefore, necessary to introduce network constraints on the capacitor potentials in order to avoid overstressing some capacitors while understressing others.

A capacitor potential constraint is the same as a choke coil constraint since in this circuit a capacitor and a choke coil are directly parallel coupled. A choke coil constraint may be achieved in the following way. Primary coils are added, each strongly coupled to a choke coil, as shown in fig. 3. A constraint on the primary coils gives a constraint on the choke coils, only limited by the finite amount of leakage flux between a primary and choke coil. Parallel connection of the primary coils gives a constraint on the potential across them and, therefore, gives the capacitor potential constraint sought.

The electromotive force induced in a coil is proportional to the time rate of change of the magnetic flux through the coil area. The magnetic flux through a given choke coil is a complicated function of the instantaneous current distribution throughout the choke and of the

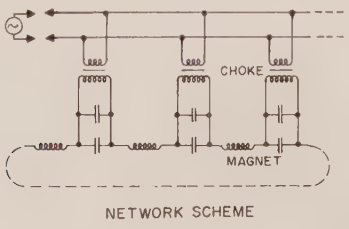


Fig. 3. Practicable magnet power circuit with distributed capacitor bank.

configuration of magnetic material present. Electrical network asymmetries will, therefore, result in self-adjusting equalizing currents flowing in such a way as to equalize the induced potentials in the parallel connected primaries.

For an ideal symmetrical system, the primary coils will have induced voltages equal in amplitude and phase and may, therefore, be parallel coupled without any equalizing current flowing between these parallel coils.

The effect of the parallel connected windings on the multiple resonance pattern mentioned above for the network (fig. 1) may be understood by the following simple argument. It is well known from elementary network analysis that an increase in the coupling between $L$-$C$ circuits separates the frequencies of the resonant modes. Since the parallel connected primary windings effectively couple together the whole choke by forcing the same flux through all choke coils, the effect on the multiple resonances must be an increased separation from the fundamental mode. From a practical point of view, the effect is a complete elimination of these modes of resonance. The measured ferrite model resonance patterns (fig. 4) show this increasing separation of the multiple resonances from the fundamental modes as the resistance in each primary equalizer winding is reduced.

Model analysis showed that it is a very good first order approximation to the general network to conceive it as a simple parallel connection of independently resonating sections. Feeding the AC power losses via the parallel connected equalizer coils suggests that the choke now can be visualized in a conventional way as a transformer, where the secondary winding is resonated with a capacitor. The flux equalizer coils will hereafter be called primary coils and the choke coils will be called secondary coils.

For an ideal resonance excitation, the primary current is, therefore, resistive in all the primary coils. For a resonance excitation of the ring-coupled magnets, the impedance loading of the choke secondary is purely resistive, since the magnet inductance and its series coupled capacity cancel, leaving the resistive component only. The choke secondary potentials may thus be imagined as equivalent to AC generators inserted in series with the magnet ring.

The general network problem is thus reduced

to separate minor problems of a more or less routine nature. Only two characteristic features will be brought to attention. For an ideal resonance excitation, the choke section input impedance is resistive, as mentioned above. The input resistance is equal to $R_P/N^2$, where $N$ is the turns ratio of the primary to the secondary coil and $R_P$ is a fictitious resistance placed in parallel with each choke secondary section representing the choke and magnet circuit section losses. The other feature to be pointed out is that for frequencies substantially higher than the main resonance frequency, the choke section input impedance is similar to a series resonance circuit, including the primary to secondary winding leakage inductance and the total section capacitor bank.

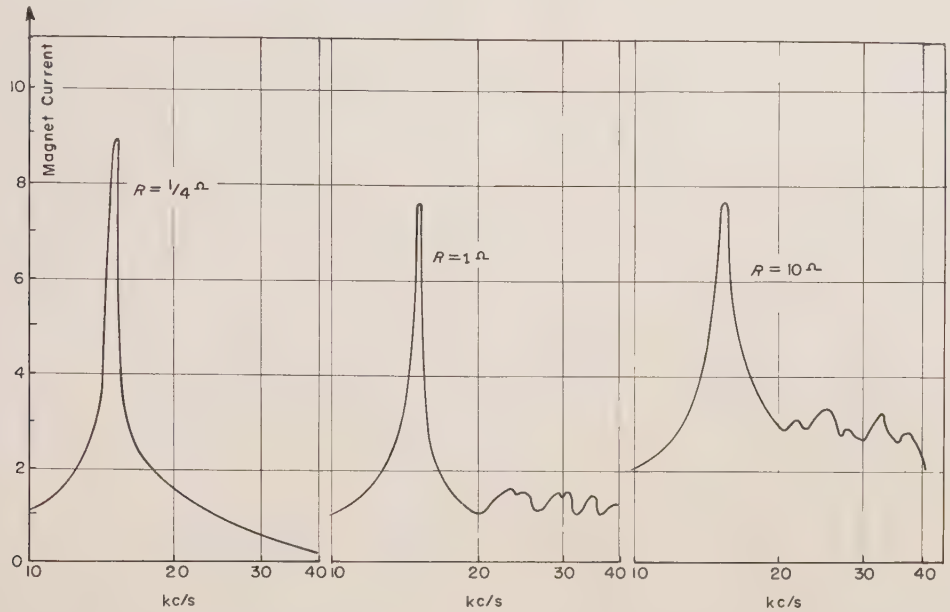


Fig. 4. Measured resonance patterns for the ferrite model magnet current. The choke flux lock is perturbed by inserting a resistor in series with each individual equalizer coil. The AC generator current is kept fixed for all frequencies.

## 4. Pertubations

A next order approximation incorporates the cross coupling between a particular choke section and its adjacent choke sections. The neighboring choke windings induce a net voltage of zero, in a particular choke coil, if the system is ideally symmetrical. The cross coupling terms only come into the picture when the effect of a local off-resonance detuning is considered. This local effect may be considered a perturbation on the ideal in-resonance network.

A perturbation may be evaluated as follows: The so-called network compensation theorem, which is a variant of Thevenin's rule states: Assume an impedance $Z$ in a branch of a linear network passes a current $I$. If the impedance $Z$ is modified by a small amount $\Delta Z$, then the currents in the whole network will be changed by amounts corresponding to the introduction of a series electromotive force $-\Delta Z I$ into the branch $Z + \Delta Z$. The equivalent rule holds for changes in mutual inductances. It therefore follows that since the coupling between a secondary and a primary choke coil is much stronger than the coupling to the other coils on the choke that the effect of the local secondary tuning deviation is mainly propagated into the network via the adjacent primary choke winding which, therefore, shows a peak in the primary current distribution. The peak is distributed into the neighboring primary coils (see fig. 8).

The primary currents in a practical case may have various amplitudes and phases. The sum of the resulting real components of the primary

currents, which are in phase with the AC generator voltage, is the loss feed current for the system. For a resonance excitation the sum of the positive imaginary current components in all the primary windings is equal to the sum of the negative imaginary current components. The imaginary current components are in quadrature with the AC generator voltage. These quadrature currents flow internally within the parallel coupled equalizer windings. These statements have, of course, merely pointed out that the law of charge conservation holds for the primary choke windings.

### 5. Possible Choke Configurations

The general quantitative expressions for the effects of the mechanical and electrical asymmetries of the choke are quite complicated. Results from the ferrite model showed in particular that the amount of additional losses introduced by the equalizing current set up by reasonable electrical asymmetries is small compared to the total losses of the network. Furthermore, the system may be tuned up relatively easily by modifying the capacitor banks. Monitoring the primary currents indicates where capacity should be added or subtracted. The system tuning converges rapidly to the ideal state where all primary currents are resistive.

The general principles outlined so far makes reasonable the assertion that, in general, almost any configuration of choke coil and core material, producing roughly the same magnetic flux through the effective choke coil area, is equivalent. A practicable choke having any of various topological configurations is feasible in the network, provided adequate trimming is performed. A satisfactory system, with a minimum amount of equalizer currents, may be obtained in different ways, such as by trimming capacitor banks, adjusting the number of coil turns on a secondary-primary coil unit, or adjusting the magnetic flux confining material, if any. All may equally well lead to a satisfactory system with a minimum of equalizer currents. This is a very important point since the cost of the choke for a large synchrotron is extremely high. Giving manufacturers some freedom in the choice of choke configuration can reduce the cost of the choke drastically.

Different "practicable" choke configurations have been investigated with the aid of 1:10 scale models operating at 200 c/s. A linear 1:50 scale model is too small to permit detailed evaluations of the influence of choke topological changes on the performance. The choice of a scale factor of 1:10 for the geometrical dimensions represents a compromise between reasonable detailed information obtainable and the size and cost of a model. The weight of a model scales with the linear dimensions to the third power. At 200 c/s, the magnetic core material used can be one of the better grades of transformers steel, without encountering excessive core losses.

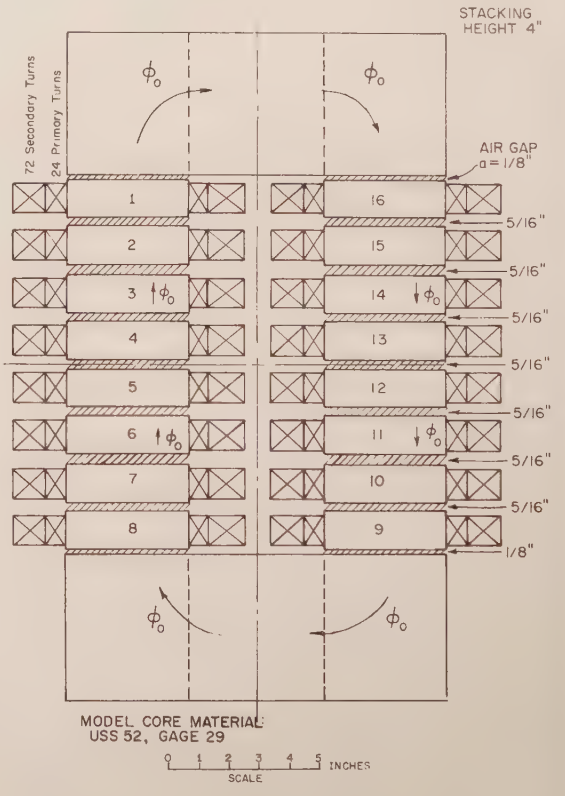


Fig. 5. A 1:10 scale model choke core configuration.

### 6. Practicable Models

Fig. 5 shows a sketch of the model choke under consideration now. This model, as mentioned above, is a 1:10 scale model working at 200 c/s

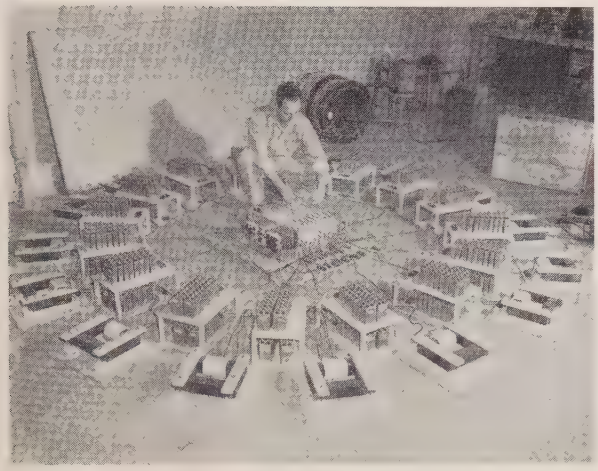

Fig. 6. Photograph showing the 200 c/s model.

for the main resonance. The 16 capacitor banks are each 144 $\mu$F unless otherwise indicated, and the 16 inductances simulating the magnets in the network are each tuned to resonance with 70 $\mu$F at 200 c/s. The overall model $Q$ is about 35. Fig. 6 is a photograph of the model.

The general pattern of the magnetic flux lines in the choke is as follows; the main flux through the iron, leakage at the airgaps, corner leakage, and stray flux around the coilheads.

The well-known approximate formula for calculating inductance of the choke for all the secondary coils coupled in series is the following:

$$L \cong \frac{\mu_0 N^2 A}{\delta} \text{ Henry} \qquad \begin{aligned} \mu_0 &= 4\pi \times 10^{-7} \text{ H/m} \\ N &= \text{number of turns} \\ A &= \text{core cross section (m}^2\text{)} \\ \delta &= \text{total air gap length (m).} \end{aligned} \qquad (2)$$

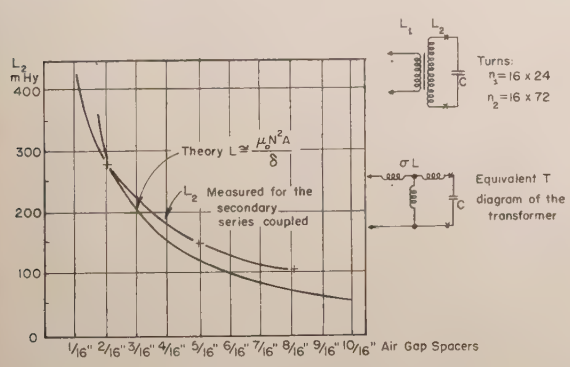


Fig. 7. For choke of fig. 5 the inductance for the secondary windings series coupled. The choke section inductance is $\frac{1}{16}$ thereof.

This formula does not include such factors as the core packing factor, the gap fringing flux factor, the finite iron $\mu$ and coil head fringing flux. Fig. 7 shows the measured series coupled inductance of the choke above for various airgap sizes. A reasonably good fit can be made by taking into account the factors mentioned above.

Figs. 8, 9, 10, 11 and 12 show some model measurements for this choke configuration placed in the network. All the measurements have been obtained for the AC generator frequency so adjusted that the AC generator current is resistive. The changes in the total system resonance frequency, defined by this criterion, are however, very small indeed when the local section amount of reactance is modified.

Fig. 8 shows the absolute value of the primary currents for two different lengths of the corner airgaps. The data shows that choosing $\frac{1}{8}$" cornergaps gives very close to an ideal flat primary current distribution. This choke configuration may thus work satisfactorily in the system without further adjustments.

Changing an airgap changes the local magnetic flux pattern of the choke. This is, therefore, equivalent to changing the local effective choke

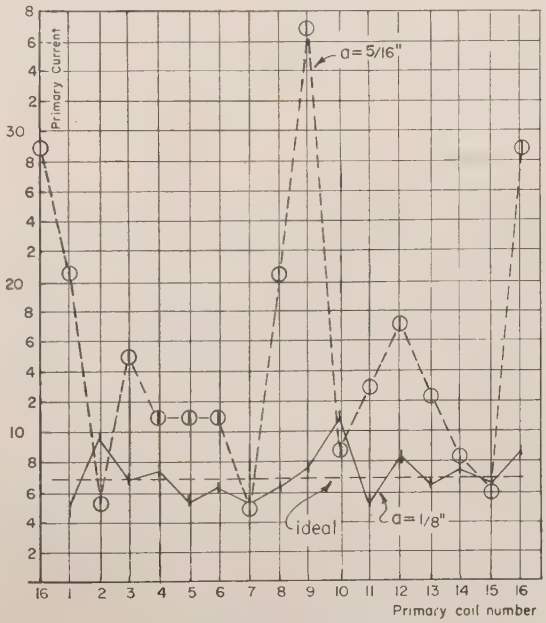


Fig. 8. For choke of fig. 5, the primary current distribution for all airgaps of length $\frac{5}{16}$", except the four corner gaps of length $a$.

tuning inductance. Fig. 9 shows the variation of primary current in a corner coil as the adjacent airgap is altered.

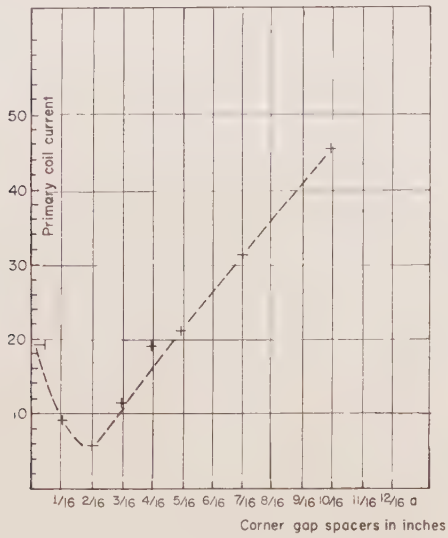


Fig. 9. For choke of fig. 5, dependence of primary coil current in corner coil No. 8 as function of the four corner gap spacings.

The coil sections on the choke adjacent to a deviating airgap may be brought into resonance by modifying the section capacitor-banks instead of correcting the airgap. Fig. 10 shows the variation of primary current in coil No. 5 as the associated capacitor-bank is varied.

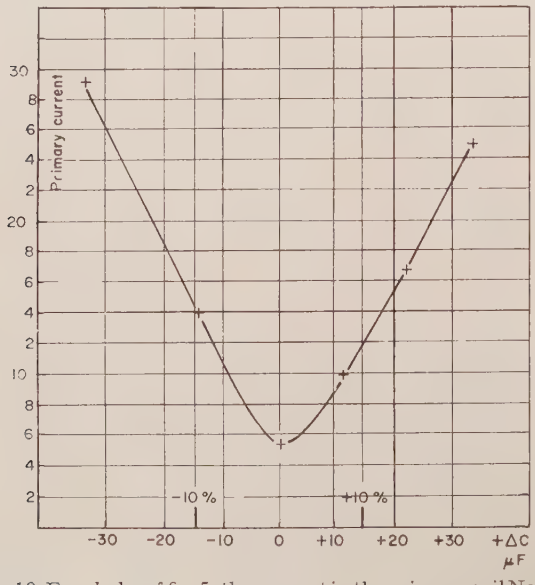


Fig. 10. For choke of fig. 5, the current in the primary coil No. 5 as function of capacity variation on bank No. 5. All capacitor banks 144$\mu$F, the 10% perturbation points are indicated.

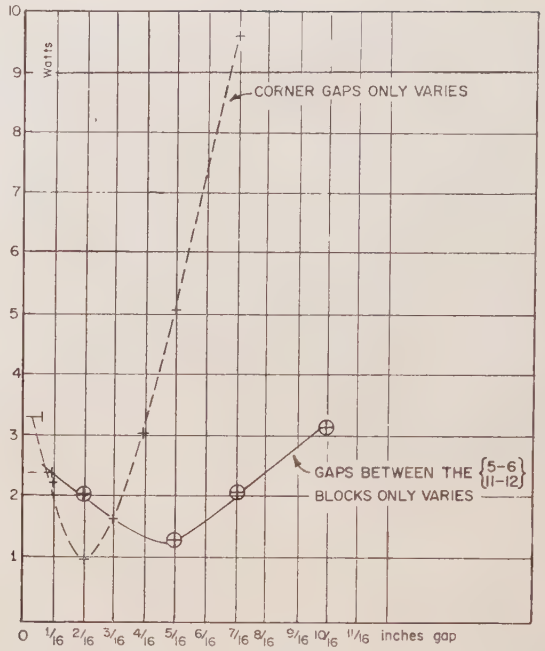


Fig. 11. For choke of fig. 5 the total copper losses in the primary windings versus different airgap spacers.

Fig. 11 shows the total primary coil loss for various airgaps in the choke core. As is well known, it is the square of absolute value of the current which produces losses in a coil winding. The primary coil losses are, for a reasonable amount of equalizer current, a small fraction of the total losses of the system.

All capacitor-bank potentials would be equal if the coupling between the primary windings and the adjacent secondary windings were perfect. A practical transformer with leakage flux between the primary and secondary winding may be visualized for this purpose in the well known equivalent T diagram. If all choke sections were identical, then the potential drop across the T of the equal resistive section feed current would all be equal, and, therefore the potentials across all the capacitor banks would be equal.

A local off-resonance results in local current deviations in the system. These additional currents superimposed on the in-resonance currents produce an additional potential drop across the T. A small deviation in the local section capacity potential is the resulting effect.

This potential deviation is, of course, minimized by increasing the magnetic coupling between the adjacent primary and secondary winding. Fig. 12 shows the measured capacitor potential distribution for two different corner airgaps, the effect is seen as being of no real practical importance.

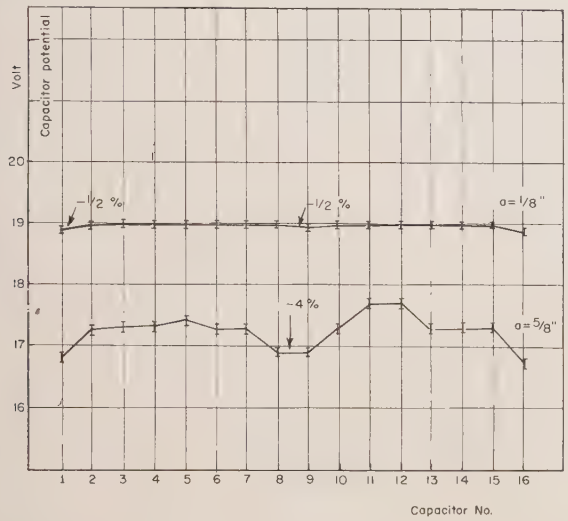


Fig. 12. For choke of fig. 5 the capacitor potential distribution for two different corner gaps of length $a$. The deviations in potential are reduced by interleaving the layers of turns of the primary and secondary coil, thereby increasing the coupling between the primary and the secondary. The measured leakage between the primary and the secondary coil here is $\approx 12\%$.

### 6.1. AIRCORE CHOKE

An aircore choke having no iron core for confining the magnetic flux lines, has been suggested by a manufacturer as being the cheapest possible choke configuration. Fig. 13 is a photograph of a simple model of the coil arrangement where the coils are the same as those in the choke pictured in fig. 5. This model choke is essentially a simple stack of equal, coils, only very roughly having the same flux through the effective coil area of each primary-secondary coil unit. However, experiments on the 1:10 scale model system showed, as expected from the general principles already outlined, that a satisfactory trimming of the network is easily performed by adding a suitable amount of "negative reactance" or capacity to the capacitor banks resonating the choke end-coils. End section trimming may equally well be performed by modifying the end coil number of turns, which amounts to modifying the local amount of "positive reactance" or inductance.

Fig. 14 shows the current in the primary winding in one of the choke end-coils, as a function of the end section capacitor-bank size. Qualitatively, the current distributions follow the same principles as for the choke of fig. 5.

The choke for the Princeton-Pennsylvania 3 BEV 20 c/s proton synchrotron will be an air core choke.

### 6.2. TRANSIENTS

As is well known, the transient network behavior, in the case of network faults, may often be evaluated by imagining capacitors as shorts and inductances as high impedances. Model experiments showed that this simple picture is sufficient for understanding the transient behavior. It should be remembered that just as for conventional transformers, very low leakage inductance between the choke secondary and primary winding will give extremely large fault transient currents for some types of network breakdown. Therefore, it is not advisable to design for minimum leakage flux between primary and secondary.

A multitude of simulated fault conditions indicated that the system is safe in so far as no

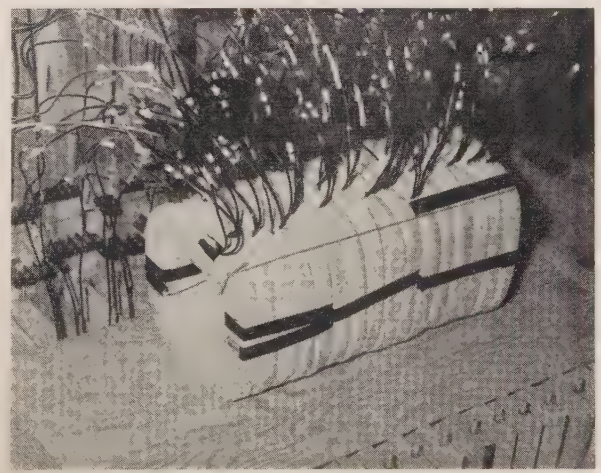

Fig. 13. Photograph showing a simple model of the solenoidal air core choke, the coil units of fig. 5 are used.

network fault chain reactions can take place. A protection system is, therefore, relatively easy to design for keeping damage localized.

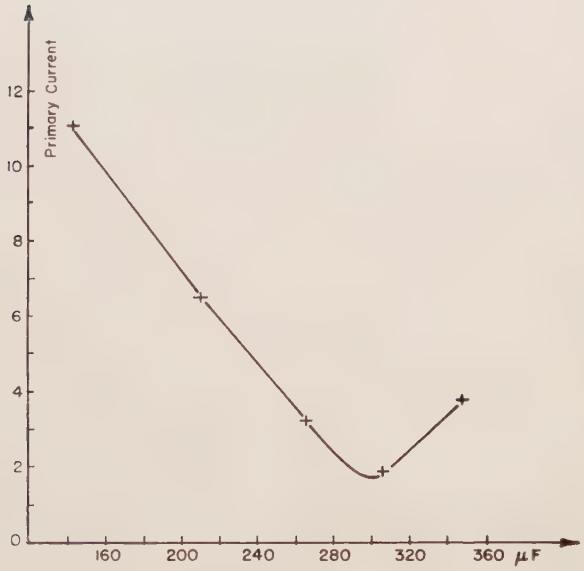


Fig. 14. For air core choke of fig. 13, the current in the primary winding of the choke end coil as a function of the end section capacitor bank. The other capacitor banks are each, 144$\mu$F.

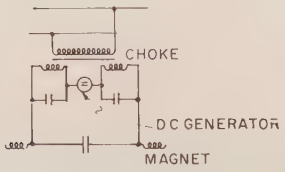


Fig. 15a

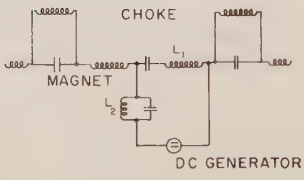


Fig. 15b

Fig. 15. Basic DC current feed networks.

6.3. DC FEED

The problem of feeding DC current into the magnet ring from a DC generator is essentially a problem of arranging the network in such a way that the full AC magnet current does not pass through the DC generator. This may be achieved by placing a high AC impedance, having a low DC impedance, in series with the DC generator; or by placing a low AC impedance, having a high DC impedance, in parallel with the DC generator. Fig. 15 shows practical network arrangements for achieving either of these two basic possibilities. Figure 15 b has a better rejection of the AC current through the DC generator than the scheme shown in fig. 15a. Which one of the two to select depends upon the characteristics of the DC generator, such as its internal impedance, the ripple current generated by the DC generator, and upon economic considerations.

The network fig. 15a will be used in the Princeton-Pennsylvania Accelerator.

## 7. Conclusion

Principles have been presented for a practicable network scheme for a high repetition rate accelerator magnet power system. Models have been used for obtaining solutions to network problems as well as for evaluating the parameters of practicable choke configurations. The general problem is separated into minor problems of a more or less routine nature.

A practicable choke for the network may have various topological configurations; which one to choose is essentially determined by economic considerations.

I wish to thank Professors M. G. White and F. C. Shoemaker as well as M. Scheibner, E. de Haas, T. Weisz, M. Isaila and E. P. Tomlinson for valuable discussions and much interest.

The model building and most of the measurements were done with much care by J. Agabati and R. Overholt.

NUCLEAR INSTRUMENTS AND METHODS 9 (1960) 87–91; NORTH-HOLLAND PUBLISHING CO.

# THE CORRECTION OF RESONANCE PEAKS FOR EXPERIMENTAL RESOLUTION†

R. O. LANE, N. F. MOREHOUSE, Jr., and D. L. PHILLIPS

*Argonne National Laboratory, Argonne, Illinois*

Received 22 June 1960

A technique is discussed for the determination of the true resonance shape from a measured resonance shape when the apparatus resolution shape is known, or, conversely, the determination of the resolution function if the true resonance shape is known. The problem is essentially that of the solution of an integral equation of the first kind and use is made of the relations among the Fourier coefficients to determine the unknown function. A successful application is made to the case of a resonance in the total neutron cross section of carbon where the widths of the resonance and resolution function are comparable. Some of the limitations of the technique are discussed.

## 1. Introduction

The problem of determining a true distribution function $f(x)$ from an observed distribution function $g(\lambda)$ arises in many fields. The function $f(x)$ is transformed into $g(\lambda)$ by an apparatus function or resolution function $k(x)$. Expressed mathematically, the problem is to solve the following integral equation of the first kind:

$$g(\lambda) = \int_{-\infty}^{\infty} k(x-\lambda)\, f(x)\, \mathrm{d}x = \int_{-\infty}^{\infty} k(x)\, f(x+\lambda)\, \mathrm{d}x, \quad (1)$$

where, for certain problems, $k(x-\lambda)$ in (1) is replaced by $k(\lambda - x)$. If $k(x)$ is known, then (1) may be solved for $f(x)$ directly. Otherwise, as in the case treated in this discussion, it may be necessary to use the symmetry of the integral to determine $k(x)$ from measurements with a known $f(x)$ first, and then in turn solve for an unknown $f'(x)$ with the same $k(x)$. Although literature dealing with integral equations of the first kind is scanty, several methods[1–9]) for solving them numerically have been proposed. For solving eq. (1), methods employing Fourier series have been considered but rejected in view of the time consumed in carrying out the computation for a large number of terms. With the aid of modern high-speed computers, the computation becomes quite easy and the Fourier method gives promise of being very useful for solving eq. (1) for certain cases.

† Work performed under the auspices of the U.S. Atomic Energy Commission.

## 2. The Problem

The particular problem considered here is the measurement of neutron cross sections near resonance peaks as a function of energy. The incident neutrons used are not monoenergetic but distributed about the desired energy with a distribution independent of this desired energy. This leads to the integral equation.

$$\bar{\sigma}(\lambda) = \int_{-\infty}^{\infty} w(E-\lambda)\, \sigma(E)\, \mathrm{d}E = \int_{-\infty}^{\infty} w(E)\, \sigma(E+\lambda)\, \mathrm{d}E\,, \quad (2)$$

where $\bar{\sigma}(\lambda)$ is the experimentally measured cross section, $\sigma(E)$ the true cross section, and $w(E-\lambda)$ the distribution of the incident neutrons about the desired energy $\lambda$.

For the type of problem considered here, $w(E-\lambda)$ and $\sigma(E)$ are smooth single-peaked distributions. In order to solve (2) numerically, the range of integration is made finite. The

[1]) P. D. Crout, J. Math. Phys. **19** (1940) 34.
[2]) P. D. Crout and F. B. Hildebrand, J. Math. Phys. **20** (1941) 310.
[3]) T. Fox and E. J. Goodwin, Phil. Trans. Roy. Soc. (London) A **245** (1953) 501.
[4]) G. Kreisel, Proc. Roy. Soc. (London) A **197** (1949).
[5]) E. J. Nystrom, Acta Math. **54** (1930) 185.
[6]) A. Reiz, Arkiv. Mat. Astro. Fysik **29**A no. 29 (1943).
[7]) H. C. Van de Hulst, Bull. Astro. Inst. Netherlands **10** (1946) 75.
[8]) Andrew Young, Proc. Roy. Soc. (London) A **224** (1954) 561.
[9]) R. Gold and N. E. Scofield, Bull. Am. Phys. Soc. **2** (1960) 276.

interval $(a,b)$ is chosen to be approximately that for which $\bar{\sigma}$ is nonzero. In the case that $\bar{\sigma}$ has "long tails", some cutoff assumption has to be made in order to preserve the accuracy around the peaks.

### 3. The Method

If $\bar{\sigma}$, $\sigma$, and $w$ are expanded in Fourier series† on the interval $(a,b)$, which we take as $(-T,T)$ for simplicity, we obtain the equations

$$\sigma(E) \approx A_0^{\sigma} + \sum_{k=1}^{N} \left( A_k^{\sigma} \cos\frac{k\pi E}{T} + B_k^{\sigma} \sin\frac{k\pi E}{T} \right) \quad (3)$$

$$\bar{\sigma}(\lambda) \approx A_0^{\bar{\sigma}} + \sum_{k=1}^{N} \left( A_k^{\bar{\sigma}} \cos\frac{k\pi\lambda}{T} + B_k^{\bar{\sigma}} \sin\frac{k\pi\lambda}{T} \right)$$

$$w(E-\lambda) = w(z)$$

$$\approx A_0^{w} + \sum_{k=1}^{N} \left( A_k^{w} \cos\frac{k\pi z}{T} + B_k^{w} \sin\frac{k\pi z}{T} \right)$$

where

$$A_0^{w} = \frac{1}{2T}\int_{-T}^{T} w(x)\,dx\,, \quad A_0^{\bar{\sigma}} = \frac{1}{2T}\int_{-T}^{T} \bar{\sigma}(x)\,dx \quad (4)$$

$$A_k^{w} = \frac{1}{T}\int_{-T}^{T} w(x)\cos\frac{k\pi x}{T}\,dx\,,$$

$$A_k^{\sigma} = \frac{1}{T}\int_{-T}^{T} \bar{\sigma}(x)\cos\frac{k\pi x}{T}\,dx$$

$$B_k^{w} = \frac{1}{T}\int_{-T}^{T} w(x)\sin\frac{k\pi x}{T}\,dx\,,$$

$$B_k^{\bar{\sigma}} = \frac{1}{T}\int_{-T}^{T} \bar{\sigma}(x)\sin\frac{k\pi x}{T}\,dx\,.$$

$$k = 1, \ldots, N\,.$$

Eq. (2) reduces to a simple set of algebraic equations among the Fourier coefficients of $\bar{\sigma}$, $\sigma$, and $w$, namely,

$$\begin{aligned} B_k^{\bar{\sigma}} &= T\,[\,B_k^{\sigma} A_k^{w} - A_k^{\sigma} B_k^{w}\,] \\ A_k^{\bar{\sigma}} &= T\,[\,B_k^{\sigma} B_k^{w} + A_k^{\sigma} A_k^{w}\,] \\ A_0^{\bar{\sigma}} &= 2T\,[\,A_0^{w} A_0^{\sigma}\,]\,. \end{aligned} \qquad k = 1, \ldots, N\,. \quad (5)$$

† Since it is assumed that the functions in eq. (2) are essentially zero at the end points $T$ and $-T$, it may be better to expand the functions in a modified Fourier series involving the orthogonal functions

$$\cos\frac{(2k-1)\pi x}{T}\,, \qquad \sin\frac{k\pi x}{T}$$

instead of the usual series.

Solving for the coefficients of $\sigma$, we find

$$B_k^{\sigma} = \frac{A_k^{\sigma} B_k^{w} + B_k^{\bar{\sigma}} A_k^{w}}{T\,[\,(B_k^{w})^2 + (A_k^{w})^2\,]}$$

$$k = 1, \ldots, N \quad (6)$$

$$A_k^{\sigma} = \frac{A_k^{w} A_k^{\bar{\sigma}} - B_k^{w} B_k^{\bar{\sigma}}}{T\,[\,(B_k^{w})^2 + (A_k^{w})^2\,]}$$

$$k = 1, \ldots, N$$

$$A_0^{\sigma} = \frac{A_0^{\sigma}}{2T\,A_0^{w}}\,.$$

In the following description it will be assumed that $w(E)$ is known and $\sigma(E)$ is unknown. However, equations similar to (6) for the converse situation may readily be obtained from eq. (5).

In practice $\bar{\sigma}$ and $w$ are often known only at a set of discrete, equally spaced points. For this case the coefficients are determined by evaluating the integrals by use of the trapezoidal rule. When this is done we obtain the equations

$$A_0^{w} = \frac{1}{2R} \sum_{r=-R+1}^{R} w\left(\frac{rT}{R}\right) \quad (7)$$

$$A_k^{w} = \frac{1}{R} \sum_{r=-R+1}^{R} w\left(\frac{rT}{R}\right)\cos\left(\frac{kr\pi}{R}\right) \qquad (k \neq 0, R)$$

$$A_R^{w} = \frac{1}{2R} \sum_{r=-R+1}^{R} w\left(\frac{rT}{R}\right)\cos(r\pi)$$

$$B_k^{w} = \frac{1}{R} \sum_{r=-R+1}^{R} w\left(\frac{rT}{R}\right)\sin\left(\frac{kr\pi}{R}\right),$$

where $2R+1$ $(R \geq N)$ is the number of points. Similar formulas hold for the coefficients of $\bar{\sigma}$.

### 4. Smoothing of the Solution

When one tries to solve eq. (2) [or (1)] accurately, spurious peaks and valleys appear irregularly in the solution $\sigma$. This is due to random errors of the measured function $\bar{\sigma}$. This phenomenon occurs regardless of the method used to solve the equation. It is inherent in the equation itself and is usually described by saying the equation is unstable. Small errors in the measured function $\bar{\sigma}$ tend to give amplified errors in $\sigma$. This can be seen by noting that if we

add a term like sin $(mE/T)$ to $\sigma$, where $m$ is large, the integral changes very little. Also notice that the accuracy of the solution, $\sigma$, depends on the smoothness of $w$. If $w$ is a very smooth and flat function the change in the integral arising from changes in $\sigma$ is small, but if $w$ is a function with a single very sharp peak the change may be appreciable. (If for example $w$ is the $\delta$-function, the solution is obvious.) Hence we conclude that the success in solving eq. (2) [or (1)] by any method depends to a large extent on the accuracy of $\bar{\sigma}$ and the shape of $w$.

Regardless of the method of solution, some device is needed to "stabilize" the solution, i.e., to reduce as far as possible the effects of random errors in $\bar{\sigma}$. For the method presented here, two devices are used. The first one is the obvious one of setting all Fourier coefficients of $\bar{\sigma}$ beyond the $N$th terms equal to zero. The second one is to smooth the resulting $\sigma$ by forming the integral

$$\sigma_s(x) = \int_{-T}^{T} h(y - x)\, \sigma(y)\, dy ,$$

where $h(y - x)$ is a "smoothing function". In order to carry out the integration we need only to determine the Fourier coefficients of $h(z)$ up to the terms of order $N$. The coefficients of $\sigma_s$ can then be obtained as linear combinations of products of the coefficients of $h$ and $\sigma$, i.e.,

$$A_0^{\sigma_s} = 2T\, A_0^h A_0^\sigma$$

$$A_k^{\sigma_s} = T\,[\, A_k^h A_k^\sigma + B_k^h B_k^\sigma \,]$$

$$B_k^{\sigma_s} = T\,[\, A_k^h B_k^\sigma - B_k^h A_k^\sigma \,] \qquad k = 1, 2, \ldots, N .$$

The amount of smoothing necessary will depend on the individual problem. It should be noted that the smoothing not only tends to eliminate "noise", but unfortunately at the same time tends to obscure any "fine" structure that $\sigma$ might have.

## 5. Application

In order to test the method, a mathematical case was constructed from an assumed $\sigma(E)$. This constructed case very closely approximated the experimental measurements[10]), made at this laboratory, of the total neutron scattering cross section of carbon in the region of the 2.08-MeV resonance. This case was so chosen that it would be representative of typical experimental situations, while still free from *systematic* experimental uncertainties (such as proper background determination, uncertainties in the exact values of the assumed member of the integral in eq. (2), and the like) which would not give a fair test of the technique.

This resonance has been shown[10,11]) to correspond to a $D_{\frac{5}{2}}$ state in $C^{13}$ and to have a width $\Gamma = 7$ keV. The single-level Breit-Wigner expression for the cross section can be written near the resonance in the simple form

$$\sigma(E) = \frac{\frac{1}{4}A\Gamma^2}{(E - E_r)^2 + \frac{1}{4}\Gamma^2} + \frac{\frac{1}{2}B(E - E_r)\Gamma}{(E - E_r)^2 + \frac{1}{4}\Gamma^2} + C , \quad (8)$$

where $E_r$ is the resonant energy and $C$, the background, is taken to be zero for purposes of these calculations since it contributes no information. The values of $A$ and $B$ appropriate here are $A = 4.36$ barns and $B = 0.52$ barns. The solid curve in fig. 1 is a plot of $\sigma(E)$ as a function of $(E - E_r)$.

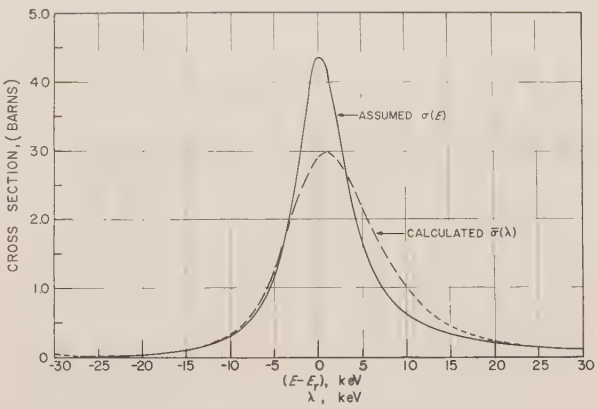


Fig. 1. Plots of the assumed theoretical cross section $\sigma(E)$, for the 2.08-MeV resonance in $C^{12}$ as a function of $(E - E_r)$, and the calculated "measured" cross section $\bar{\sigma}(\lambda)$ as a function of $\lambda$. The background cross section is not shown since it is not relevant to the present discussion.

[10]) R. O. Lane, A. S. Langsdorf Jr., J. E. Monahan and A. J. Elwyn, Ann. Phys. (to be published).

[11]) J. E. Wills, J. K. Bair, H. O. Cohn and H. B. Willard, Phys. Rev. **109** (1958) 891.

An experimental weight function $w(E-\lambda)$, shown in fig. 2 (solid curve), was chosen so as to closely resemble the shape of the weight function determined by other calculations[12]) under similar

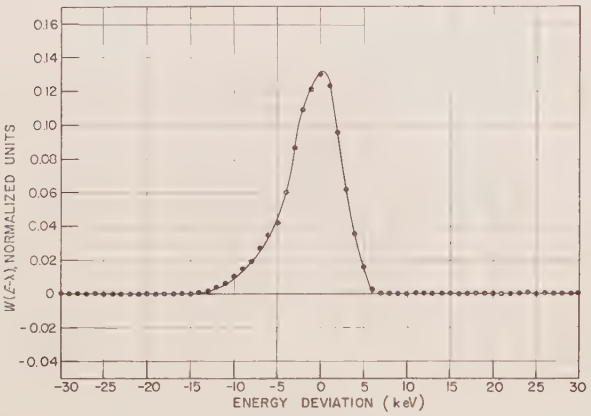


Fig. 2. Comparison of the assumed distribution function $w$ (solid curve) as a function of energy deviation from the value at the peak with the resulting calculations of $w$ (points) for the case in which the calculated $\bar{\sigma}(\lambda)$ was rounded off to 5 decimal places.

circumstances. With the aid of an IBM-704 computer, the integral in eq. (2) was then computed by use of the Fourier expansions of $w$ and $\sigma$. Each of the two functions were reproduced at every point to better than 1% of their peak heights by their respective Fourier series expansions. In all calculations described here, $R = 30$ and the interval $-30\ \text{keV} \leqslant E - E_r \leqslant +30\ \text{keV}$, was employed with 1 — keV subintervals. Fig. 1 shows the integral $\bar{\sigma}(\lambda)$ for this case, where $\lambda$ is the relative distance between the peak of $\sigma(E)$ and that of $w(E-\lambda)$. The asymmetry which existed about $E - E_r = 0$ for $\sigma(E)$ is now seen to be increased in $\bar{\sigma}(\lambda)$ as a result of the asymmetry in $w(E-\lambda)$.

This calculated mean cross-section curve $\sigma(\lambda)$ can now in turn be considered as an "experimental" cross-section curve for the purpose of testing the method. The values for $\bar{\sigma}(\lambda)$ obtained by integration were rounded off to 5 decimal places and fed back into the program as a simulation of an accurately measured experimental cross section. For this test case it was assumed that $\sigma(E)$ was known and $w(E-\lambda)$ unknown, however from the symmetry of the problem the results of the test apply equally well to the converse situation. Eq. (2) was then solved for $w(E-\lambda)$ as described in Section 3 on the assumption that $\sigma(E)$ is given by the same expression as was used in the integration. The points in fig. 2 show the resulting weight function. It agrees very well with the originally assumed curve for $w(E-\lambda)$. While this does show that the method operates successfully for this case, experimental data are seldom known to such high accuracy. To obtain an example more representative of practical conditions, the numerical values of $\bar{\sigma}(\lambda)$ obtained in the integration above were rounded off to two decimal places and these data were fed into the program simulating experimental cross section data. Again with the same expression for $\sigma(E)$, eq. (2) was solved for $w(E-\lambda)$. The resulting $w(E-\lambda)$, shown in fig. 3 as points, shows that a considerable amount of high-frequency harmonic structure was introduced by the random errors in $\bar{\sigma}(\lambda)$ (i.e., as a result of rounding off). This structure was largely smoothed out by integrating the $w(E-\lambda)$ just obtained over a symmetrical trapezoidal smoothing function of top

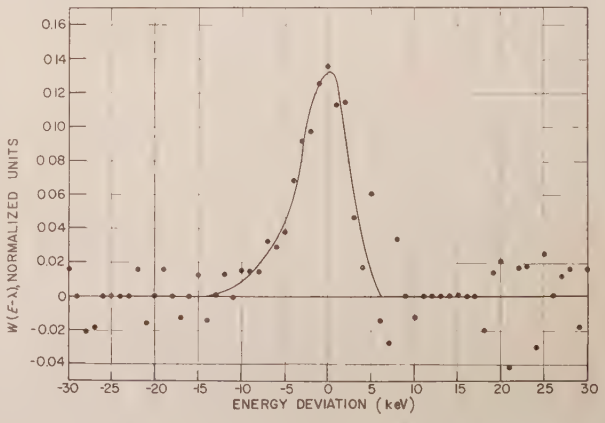


Fig. 3
Comparison of assumed $w$ (solid curve) with resulting calculations of $w$ (points for $\bar{\sigma}(\lambda)$ rounded off to 2 decimal places.

width 2 keV and base width 4 keV by use of the procedure described in Section 4. The resulting smoothed $w(E-\lambda)$ curve is shown in fig. 4. It is slightly more rounded than the true curve, but

[12]) J. E. Monahan and F. P. Mooring, Nucl. Instr. **6** (1960) 343.

the general shape is preserved. The degree of smoothing of the resulting weight function depends upon the amount of high-harmonic structure present in any individual case. Of course too much smoothing will appreciably reduce the amount of information in the gross structure of the weight function itself, so that the width of the smoothing function must be tailored to the individual situation.

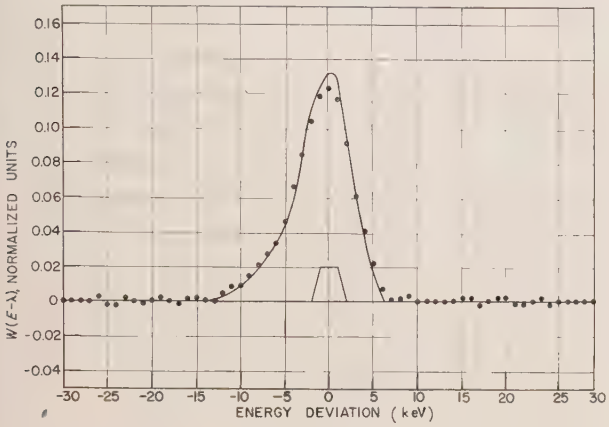


Fig. 4. Comparison of assumed $w$ (solid curve) with resulting points for $w$ shown in fig. 3 when averaged over trapezoidal smoothing function.

## 6. Discussion and Conclusions

The case described here is one in which the width of the weight function is comparable to that of the resonance peak so that if $\bar{\sigma}(\lambda)$ is known, information may be obtained about either $\sigma(E)$ or $w(E-\lambda)$ if the other is given. As the unknown function, say $w(E-\lambda)$, becomes very narrow compared to the known $\sigma(E)$, the problem becomes more unstable and the solution more difficult to find, regardless of the method used. Here small errors in the experimental $\bar{\sigma}(\lambda)$ introduce large harmonic terms into $w$, so that it is not well defined. This effect was beginning to occur in the case in which the $\bar{\sigma}(\lambda)$ data were rounded off to 2 decimal places.

When the width of $w$ is very large compared to that of $\sigma(E)$, random errors in $\bar{\sigma}(\lambda)$ present little if any problem, and $w$ can be well determined. However, $w(E-\lambda)$ is already rather well determined from $\bar{\sigma}(\lambda)$, so that there is little to be gained by solving for $w$ itself. For example, when $\sigma(E)$ is the $\delta$-function, $w = \bar{\sigma}$, and eq. (3) gives the correct coefficients of $w$ even though the Fourier series for the $\delta$-function does not converge. Notice that in this case the errors in $\bar{\sigma}(\lambda)$ are transmitted to $w$ without magnification. If the random errors on $\bar{\sigma}$ are large, then they may introduce so much noise into the solution that too much smoothing is needed. In this case it may prove more informative to take as data for $\bar{\sigma}$ the values from smooth curves drawn through the measured points, in which case limits can be placed upon the shape of the solution consistent with the errors in the measurements.

The case discussed here shows that the method can give a good description of the weight function $w$ for the case of comparable widths.

In attempting to apply this method to any given situation, the degree of success in solving the problem will depend not only upon the relative widths of the functions and the accuracy of the experimental data, but also upon such things as the shapes of the functions involved, the amount of truncation needed to make the intervals finite, and the accuracy needed in the results. A certain amount of trial and error is necessary to determine the usefulness of the method in any particular case.

### Acknowledgements

The authors wish to express their appreciation to G. Hawley, R. Bare, and Mary Fisherkeller for their invaluable assistance in programming and running calculations on the IBM–704 computer.

*Note added in proof*: Since this manuscript was prepared, one of the authors (D.L.P) has developed a method of "smoothing" the matrix solution of eq. (1) which gives similar results to those described here for kernels of the form $k\ (x-\lambda)$, but may also be used for kernels of the more general form, $k\ (x,\lambda)$ (to be published).

NUCLEAR INSTRUMENTS AND METHODS 9 (1960) 92–96; NORTH-HOLLAND PUBLISHING CO.

# A SEMI-AUTOMATIC ANALYSER FOR BUBBLE CHAMBER PHOTOGRAPHS

O. R. FRISCH and A. J. OXLEY

*Cavendish Laboratory, Cambridge,*

Received 6 Juni 1960

Photographs of nuclear particle tracks can be accumulated rapidly with fast-cycling bubble chambers. This article describes a machine for measuring the photographs quickly so that the subsequent computations can be done with an electronic computer.

The films are projected onto a ground glass screen bearing a reference mark, and moved by hand through a pantograph to bring interesting points onto the mark. The pantograph carries a plate with a fine square lattice of dots, and four photocells serve to digitise its $X$ and $Y$ coordinates. The two stereoscopic images of a point can be merged by moving one of the projection lenses; this motion also is digitised photoelectrically. After setting each point, the measured data are punched on tape, to be fed later to an electronic computer.

The design, operation, and performance of the machine are described in some detail, together with the principles of measurement and some proposed improvements.

## 1. Introduction

The Bubble Chamber (see e.g. Bugg[1])) represents an important advance on the cloud chamber. It contains matter of much greater density than a cloud chamber does even at high pressure; hence many more nuclear events will be found on a given number of pictures. In addition it requires very little recovery time, so many more pictures can be taken in a working day. As early as 1955 it was clear that fast measuring devices would be needed to deal with the expected glut of tracks reflecting nuclear events, and the design of this instrument was then begun by one of us (O.R.F.).

Some measuring machines were constructed elsewhere, at considerable cost, for maximum accuracy and convenience. This article describes a Track Analysing and Recording Apparatus (TARA) that was built with modest means and found adequate. Its features, we thought, may be of interest even though we can already see how the instrument should be improved.

The machine is designed to punch certain coordinates on tape for subsequent processing in an electronic computer. But it is not fully automatic; the operator decides which points on the pictures should be measured and does the setting. For this, the picture is projected from below onto a ground-glass screen, inclined at about 45° for convenient inspection by the sitting operator.

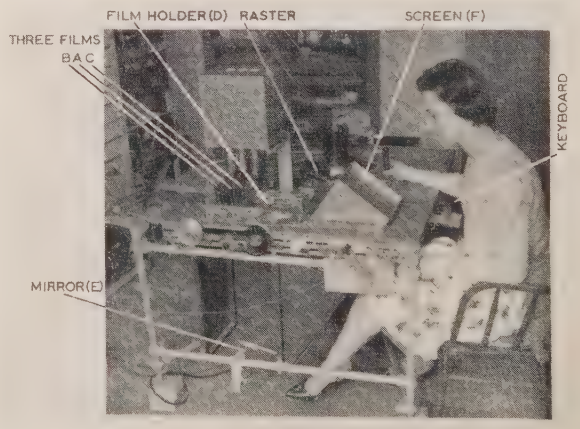


Fig. 1.

Setting could have been done by moving a hair-cross over the stationary picture; but then any distortion due to the projection lens would have caused errors. This is avoided by using a fixed mark on the screen and moving the film instead, in its own plane. The optical arrangement used (fig. 1) allows the film to be horizontal. The film holder is moved by hand

[1]) D. V. Bugg, Progress in Nuclear Physics 7 (1959).

(the cheapest and most convenient servo-mechanism obtainable) through a pantograph by which the motion of the hand is geared down by a factor of 8. A pen attached to the handle allows one to take tracings of the tracks if desired; however, we find this facility is seldom used.

It is common practice to take two or more pictures by separate cameras, for stereoscopic effect. One can then either measure the tracks independently on two or more of the views, or one can attempt to merge the two views of the same point on the screen. We have chosen the latter system, and we do it by moving one of the projection lenses in the appropriate direction.

Digitizers are used to convert the coordinates of both the pantograph and of the moveable projection lens into decimal form. After setting, the operator presses a button, whereupon the coordinates are punched on tape, to be processed later by EDSAC, the electronic computer of the Cambridge University Mathematical Laboratory.

## 2. Details of Measuring Procedure

Professor J. Steinberger (Columbia University) kindly lent us some films with bubble-chamber photographs and promised a further

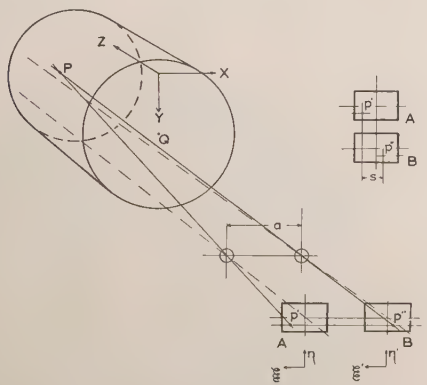


Fig. 2. Stereoscopic photography.
Distance of negatives behind lenses $= V$. Distance of bubble in front of lenses $= Z + C$. Then $Z = \mu av/s - c\mu$.

supply, so TARA was designed to fit his camera geometry. He uses three cameras with their lenses in an equilateral triangle and their film planes parallel to the window of the bubble chamber. There will be a stereoscopic displacement (parallax) between the images of a bubble in the chamber, as indicated in fig. 2. This displacement between corresponding images on two views is, to first order, always in a fixed direction (parallel to the plane containing the camera axes) and its magnitude is a measure of depth in the chamber ($Z$ coordinate). Even if one picture is in some way unfavourable or useless, the two others can be used as a stereoscopic pair to reconstruct the tracks in space. TARA does not make full use of this, but allows the choice of two stereo-pairs, namely AB and AC (see fig. 1). For this end, the two lenses which project B and C are moveable, in the appropriate directions.

The operator, using image A, moves the film holder until the point on the image which he wants to measure (end of track, branching point etc.) coincides with a mark on the screen. He then switches to image B or C and moves the appropriate projection lens until the point in question again falls on the mark; the movement required determines the depth of that point in the chamber. Actually—because of second order refraction effects and slight misalignments—one can often not achieve perfect coincidence. A correction for this is applied in the computer.

If, as is often the case, we cannot find identifiable points along a track, we arrange both images of the track to pass through the screen mark and assume that we are measuring the same point on both images. Again, the fact that the true stereo-shift is not accurately in the direction of lens motion causes small errors for which we can correct.

Together with each event we measure the images of certain fiducial marks scratched on the inside of the chamber windows; this permits us to place the event correctly in the chamber (for instance to know whether a track ends inside the chamber or by reaching a window) and to allow for misalignments during photography or projection.

## 3. Details of Construction of TARA

A general view of the machine is given in fig. 1. The three films are arranged parallel on

the film holder (D, fig. 1), which is supported above a flat brass plate by three free-rolling $\frac{1}{4}''$ steel balls. The brass plate is screwed to the wooden table top and carries three 4″ $f/3.5$ projection lenses underneath, as well as three rings

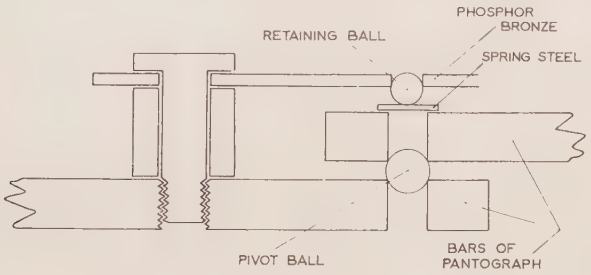


Fig. 3. Pantograph joint.

on top to prevent the balls from straying. Three 100-watt projector lamps (of which any one can be switched on at a time) illuminate the films, and the optical system is completed by a mirror (E) which projects the image onto the ground glass screen (F) in front of the operator. The three films are carried separately to allow fine longitudinal control by means of accessible adjusting screws, and appropriate spring guides and clamps ensure that the films are correctly aligned before measurement.

The film holder is moved by a pantograph, whose kinematic design makes backlash negligible and allows it to follow irregularities of the table surface without strain. The irregularities are in fact small, and produce only a second

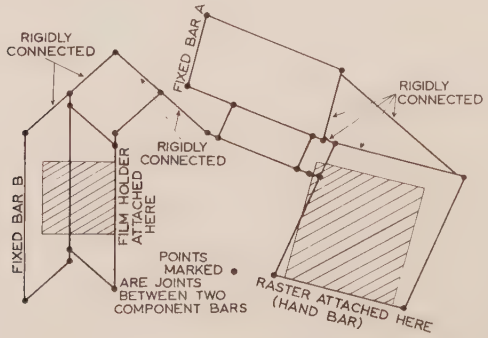


Fig. 4. Sketch of pantograph.

order (and in practice negligible) effect on the measuring accuracy. These properties of the pantograph joints may be deduced from fig. 3, and the complete linkage is sketched in fig. 4.

There is a 1 : 8 reduction between the operator's hand and the film holder, and a 13 : 1 magnification in the projection system. It is quite easy for the operator to set the film to its required position to an accuracy of about ten microns for a normal film.

The motion of the pantograph (and thus of the film holder) is digitised by use of a variant of the Moiré fringe method. Attached to it at the fast-moving end is a raster, a photographic plate carrying square transparent dots arranged in a square mesh on a black background. The raster is obtained by contact printing from a "master" negative, supplied by Messrs. Hunter Penrose Ltd. Both the dots themselves and the spaces between them are 0.08 mm across. The raster is attached as in fig. 4 to the hand bar of the pantograph, and it will be noticed that this bar remains perpendicular to the fixed bar A of fig. 4 as the pantograph is moved, and that the film holder remains parallel to the fixed bar B. Thus the raster and film holder preserve their orientations, and moreover both $X$ and $Y$ motions of the holder are one-eighth of those of the raster. Thus a displacement of the raster by one dot width corresponds to a motion of ten microns of the film.

Displacements of the raster are detected by

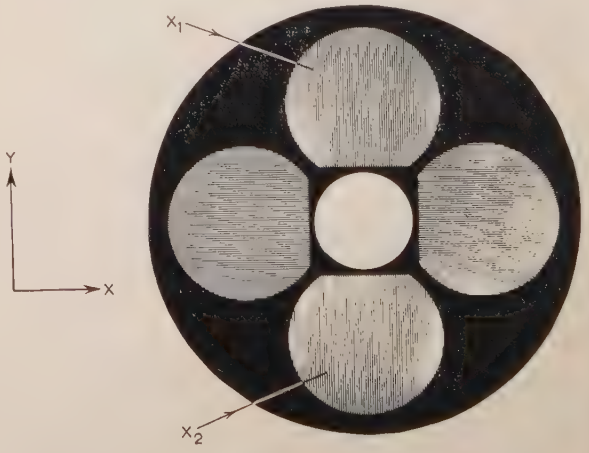


Fig. 5

phototransistors. A 1″ disc of photographic plate carrying the pattern of fig. 5 is pressed lightly against the raster from below, and is set so that

the lines of the disc are parallel to those of the raster. The raster is illuminated from above (see fig. 1) and four short perspex light pipes guide the light from the quadrants into four photocells. As the black and transparent stripes of the disc are each 0.08 mm wide, the raster can produce complete darkness at any one photocell, say that below $X_1$ quadrant, and subsequent movement by 0.08 mm in the $X$ direction will produce maximum illumination at this cell. If the raster is moved in the $Y$ direction this photocell will not be affected. By counting pulses from the $X$ and $Y$ photocells separately the two components of motion of the raster are thus obtained.

Two cells are needed for both $X$ and $Y$ because the forwards and backwards motion along each must be distinguished. Opposite quadrants of the disc are arranged with their lines staggered by 0.04 mm, so the outputs of the two photocells (on emergence from a squaring circuit) are as in fig. 6(a) if moving forwards, or as 6(b) if moving backwards. These are distinguished electronically in a coincidence circuit and pulses sent along "add" or "subtract" channels as appropriate to a reversible Dekatron counter, whose content therefore represents the position of the raster, measured from some arbitrary origin. The Dekatron circuit is similar to that described by Oxley[2]).

The parallax between the images of points on two views—the stereo shift—is measured by a digitised micrometer system. Initially both views have been set so that the two images of a fiducial mark fall on the screen mark. Then the

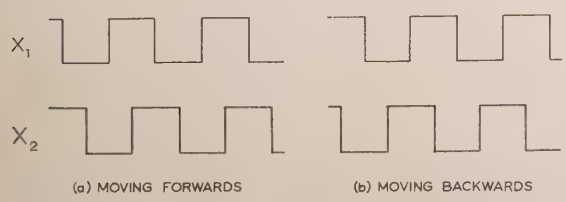


Fig. 6. Photocell outputs.

film holder is moved until the image of the desired point as seen on one view falls on the cross. When the other view is illuminated the corresponding image will appear displaced, in a fixed direction as pointed out in Section 2. By moving the projection lens in this direction it is possible to bring this image also onto the screen

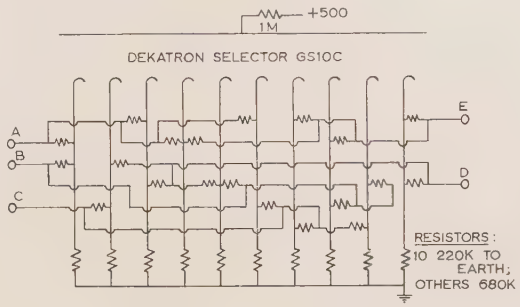


Fig. 7. Coding network.

cross. The lens is mounted kinematically in a ball and V-groove system and spring-loaded against a micrometer screw of 0.025″ pitch. The screw carries a large pulley (permitting fine control by a smaller hand-driven pulley to which it is coupled) and also a perspex wheel whose circumference is divided into black and clear strips of equal width. Movement is measured by two phototransistors separated 90° in phase, and recorded in a reversible Dekatron counter, in a very similar way to the system previously described. In fact two of the projection lenses are moveable in this way, to permit use of all three films.

If the Dekatron counters are set to zero after the initial lining-up, and both images of the desired point brought onto the screen mark, the three counters will contain numbers from which the cartesian coordinates of the point in space can be evaluated. These numbers are coded and punched onto paper tape for subsequent handling by an electronic computer.

The EDSAC computer uses standard five-hole paper tape. It was decided to follow the normal code for number input, in which each of the ten possible arrangements of two holes per row of tape represents a decimal digit. This is an error-detecting code, for any single error will cause a one- or a three-hole combination which cannot be mistaken for another digit, and causes the EDSAC to report the error.

Dekatron selector tubes, with ten separate

[2]) A. J. Oxley, Electronic Engineering (to be published).

cathode loads each, are used in the counters. Each tube has a resistance coding network as shown in fig. 7, so that raised potentials occur at those two of the output points A to E which correspond in EDSAC code to the digit represented by the Dekatron. The five output wires of each are connected to one row of a uniselector, successive decades being connected to successive rows. Thus as the uniselector wipers rotate, they pick up the coded voltage representation of the digits in successive decades, starting with the most significant $X$ digit and passing through to the least significant $Z$ digit. There are four decades in the $X$ and $Y$ counters and three in $Z$, which records stereo-shift.

Simple D.C. amplifiers are used to drive the tape punch from the signals picked up by the uniselector wipers. The punch and the uniselector are of course synchronised so that they keep in step. A few extra symbols are punched on the tape for each set of coordinates so that the computer can interpret the tape correctly, and a keyboard is available to the operator by which extra information can be punched, such as a frame number, a code number indicating the type of event being measured, etc.

The system described so far is liable to error if the raster moves slightly while the digits are being punched. If one counter reads 3999, for instance, and a small movement brings it to 4000 after the first digit has been punched, the tape will bear digits 3000, and thus be 999 counts in error. A simple buffer store has been provided to overcome this difficulty. Instead of making connections directly from the five output points of each Dekatron stage to the uniselector, they are made via normally-closed relay contacts, and 0.01 $\mu$F mica condensers are attached on the uniselector side of these contacts. The relays are energised simultaneously when the coordinates are to be punched, and the required voltages are held on the condensers long enough for the uniselector wipers to pick them off correctly, regardless of any alteration of the counter reading meanwhile.

## 4. Performance of the Machine

TARA has proved to be reasonably easy and quick in use, but many improvements are possible, and will be incorporated in a second version of the machine now being built.

The accuracy of measurement is normally about ten microns on the film, which is adequate for many purposes; but greater precision is often desirable. Continuous use of the machine has proved to be a strain on the operator, mainly through eye fatigue caused by the need for accurate visual settings of an often somewhat fuzzy image onto the mark on the screen. Brighter illumination (which will allow the use of a screen with less glitter), a screen more nearly vertical, and maybe a photoelectric setting indicator (such as a "sambatron" described by Goldsack[3]) should be provided.

The speed of operation is limited partly by the time taken in aligning the films before measuring, partly by the low speed of the Dekatron counters. The fastest ones available have a maximum speed of 20 kc/s, so the handle of the pantograph must not move faster than 80 cm/sec. This can be exceeded in short bursts, by jerking or knocking the pantograph; hence it is necessary to repeat the initial setting of the films after measuring an event and to discard the event if the counters do not return to their initial readings. To avoid exceeding the speed limit, and thus having to repeat a number of measurements, there is a natural tendency for the operator to work more slowly than is really necessary. The new TARA will have a fringe counting digitizer which operates after the setting is done, so there will be no speed limit to trouble the operator.

**Acknowledgements**

The work was made possible by the financial support of the United Kingdom Atomic Energy Authority. We also wish to acknowledge the help given to us by Mr. R. C. Marsh and Mr. K. E Turner in constructing the machine.

[3]) S. J. Goldsack, C.E.R.N. Report 58–24 (STS Division.) (October, 1958).

NUCLEAR INSTRUMENTS AND METHODS 9 (1960) 97–101; NORTH-HOLLAND PUBLISHING CO.

# AUTOMATIC LIVE-TIME MEASUREMENT AND BACKGROUND SUBTRACTION FOR THE HUTCHINSON-SCARROTT PULSE HEIGHT ANALYZER

K. F. ORTON † and K. WILKINS

*The English Electric Company Limited, Whetstone, Leicester*

Received 18 July 1960

A circuit is described which measures the live-time of the pulse height analyzer, presents this value on a Dekatron display and automatically performs background subtraction for preset periods of live-time.

## 1. Introduction

The Hutchinson-Scarrott pulse height analyzer[1]) suffers a drawback in that the time taken to sort an incoming pulse depends upon the height of the pulse and the state of the comparison waveform at the instant the pulse is received. This results in a variable dead time which depends not only upon the frequency of the comparison waveform but also on the shape of the pulse height spectrum. Moreover it is advantageous if the analyzer can be made to perform its own subtraction of background since this reduces the read-out time by one half and also reduces any errors in read-out of the binary code.

McCutchen[2]) has described circuits for subtraction of background and for the measurement of live-time. A method of background subtraction based on real time has also been described by Davey[3]) but this circuit does not eliminate the drawback of variable dead time mentioned above. It is shown here how the circuits described by McCutchen may be combined with circuits which provide for automatic subtraction of background at given intervals of live-time. The incorporation of such circuits enables the analyzer to be used with a double crystal spectrometer of the type described by Peirson[4]) and is necessary when using the technique described by Lee[5]) for the analysis of complex gamma emitters.

## 2. Circuit Operation

Live-time measurement is performed by switching a standard current to a standard current integrator during the live-time, so that,

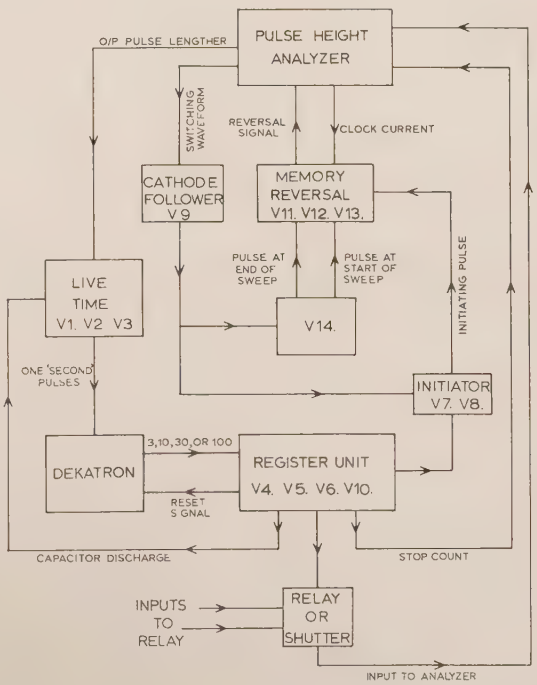


Fig. 1

† Now at C.E.G.B. Berkeley Nuclear Laboratories.

[1]) G. W. Hutchinson and G. G. Scarrott, Phil. Mag. **42** (1951) 792.
[2]) C. W. McCutchen, Phil. Mag. **2** (13) (1957) 113.
[3]) C. N. Davey, AERE EL/M 103.
[4]) D. H. Peirson, Atomics (Sept. 1956) p. 316.
[5]) W. Lee, Analytical Chemistry **31** (1959) 800.

while a pulse is being sorted, the current is switched off and only comes on again when a sorting operation has finished. The waveform necessary for switching is derived from the free anode of the double triode which controls the discharge of the pulse lengthener. Subtraction is made possible by being able to reverse the memory of the pulse height analyzer, an acoustic delay line, i.e. reversing the signal in the delay line so that each "0" is replaced by a "1" and vice versa. An extra valve in the adding gate controlled by a timing circuit performs the operation of memory reversal.

The live-time unit delivers pulses at the end of each second of live-time to a Dekatron display. Pulses are derived from the Dekatron unit at the ends of pre-selected intervals of live time and these pulses are used to drive a register circuit which initiates the process of memory reversal. Memory reversal is achieved by diverting the clock current pulses for one cycle of the sweep period. This requires pulses defining the beginning and the end of the sweep period and these pulses are obtained from V9 and V14. During the process of reversal the register unit resets the system and prepares for the next live-time interval.

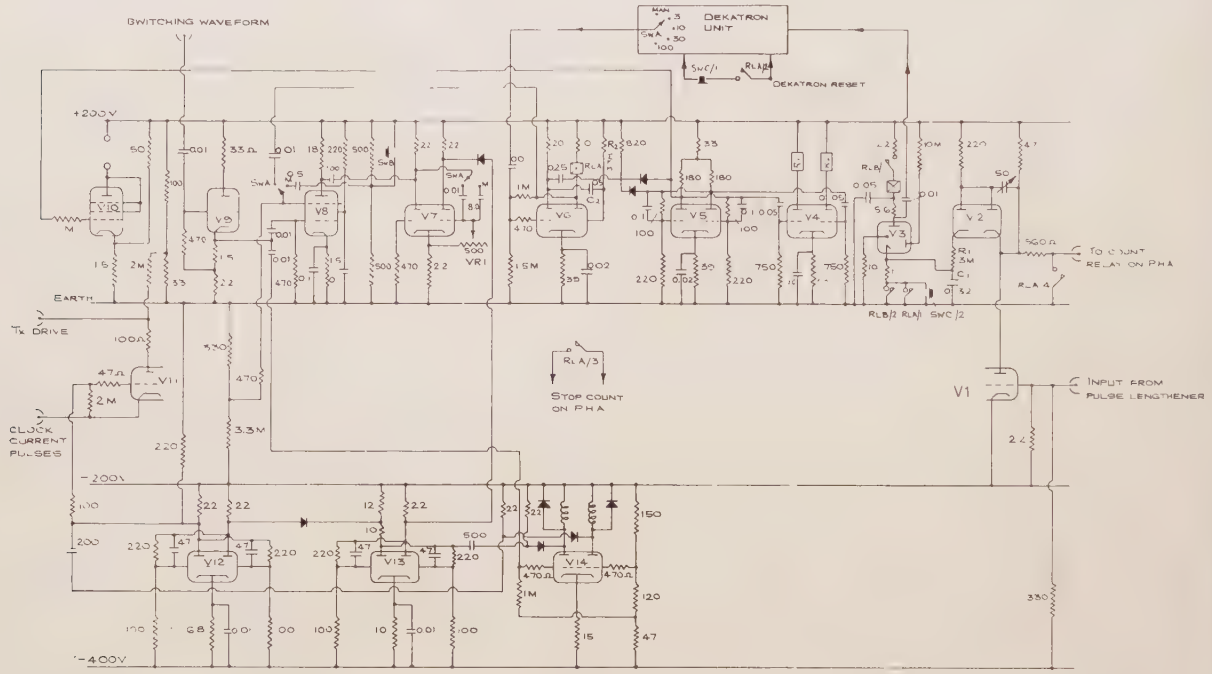


Fig. 2

| | | | |
|---|---|---|---|
| V1, V11 | ECC.81 | V10 | EF.91 |
| V2 | EB.91 | V5 | E88.CC |
| V3 | Z.803U | | |
| V4, V6 | ECC.82 | All diodes 0 A.70 | |
| V7, V12, V13, V14 | ECC. 91 | | |
| V8 | 6 F.33 | | |
| V9 | EC.70 | | |

Relays are 6000$\Omega$ P.O. type

Resistors in k$\Omega$ unless otherwise stated

Capacitors Values below 0.01$\mu$F stated in $\mu\mu$F
Values above 0.01 $\mu$F stated in $\mu$F

Inductances 14 mH

Registers are Stonebridge type ATCe Z4E Res. 10 000$\Omega$

The method of automatic operation can be followed from the block diagram (fig. 1) and the circuit diagram (fig. 2). The unit can conveniently be separated into sub-circuits which will aid the description.

### 3. Live-Time Unit

The live-time measurement unit consists of valves V1, V2 and V3. The waveform from the pulse lengthening circuit of the p.h.a. is used to switch V1 and thus controls the charging of the

integrating capacitor C1 through V2. The potential on C1 will be proportional to live-time and when this potential reaches a given amount V3 will trigger and the capacitor will discharge through relay contacts RLB/2, whilst contacts RLB/1 open the anode circuit and quench the discharge. The values of R1 and C1 are chosen so that triggering occurs at the end of every second of live-time. Pulses from the anode of V3 are used to operate a Dekatron scaling unit. Since it is necessary to reverse the memory at the end of equal periods of live-time the Dekatron unit is arranged so that it gives an output pulse at the end of either three, ten, thirty, or one hundred seconds of live-time, the output pulse being used to initiate the process of memory reversal.

**4. Register Unit**

At the end of a counting period the p.h.a. input and live-time measuring circuit must be made inoperative until reversal of the memory is complete. The Dekatron scaling unit must be reset and the changeover made from sample to background, or vice versa, as the case may be. This latter change may involve change of input from one detector to another, if a second detector is used to measure the background, or the movement of a shutter or source, if a single detector only is being used. Finally one of two registers is operated. These services are performed by the Register unit, comprising valves V4, V5, V6, the relay RLA, and the two registers R1, R2.

The positive pulse from the Dekatron unit causes the Kipp relay, V6, to change its state for a time determined by the values of R2, and C2, de-energising RLA. This relay has four sets of contacts which reset the Dekatron unit, by opening RLA/2, maintain the discharge of the integrating capacitor by closing RLA/1, render the live-time measurement unit inoperative by closing RLA/4, and stop the analyzer counting by opening RLA/3. This last set of contacts is in series with the contacts of the "count" relay of the analyzer. The negative-going edge of the negative pulse on the left hand anode of V6 changes the state of the bistable V5. The rise in anode potential associated with V5 causes V4, which normally has both halves non-conducting, to conduct in one half and operate a register before returning to its stable state. The change in potential on the left hand anode of V5 is transmitted to the grid of V10 causing the valve either to conduct or to cease conducting as the case may be. The anode of V10 has a change-over relay as its anode load and it is this which changes the input to the analyzer from sample to background. The valve V5 will remain in each state for a period determined by the output selected from the Dekatron unit.

**5. Memory Reversal Unit**

A valve in the pulse height analyzer, which provides the switching waveform for the channel and digit oscillators, produces a large positive pulse during the flyback and waiting period of the linear sweep. The edges of this pulse correspond to the beginning and end of the sweep period. This positive pulse is taken via the cathode follower V9 to the grid of V8.

While the left hand anode of V6 is providing a negative pulse, the positive pulse on the right hand anode is used to initiate the reversal by switching on V8 and allows just two of the positive pulses from the analyzer to appear at the anode of V8. The negative-going edge of the first of these triggers the Kipp relay V7. A positive pulse of duration greater than the waiting period, but less than the sweep period, appears on the right hand anode of V7; its negative-going edge triggers the timing circuit associated with the extra valve in the adding gate, V11.

In addition to requiring the initiating pulse, the timing circuit also needs negative pulses at the beginning and end of the sweep period. These pulses are derived from the positive pulse output of the cathode follower V9. This is taken to the grids of V14, which has inductive anode loads, giving a "ringing" output which is damped and clipped by crystal diodes to provide a negative pulse at each anode, one marking the beginning of the sweep and the other the end.

These pulses are taken to the left hand anodes of the bistables V13 and V12 respectively. The process of memory reversal is then as described by McCutchen. The initiating pulse from V7 triggers V13 which is reset by the negative pulse may be varied by means of the variable resistor VR1. It has been found that the most reliable operation is obtained when this negative edge occurs at the middle of the sweep period.

Briefly, then, live-time is measured, counted,

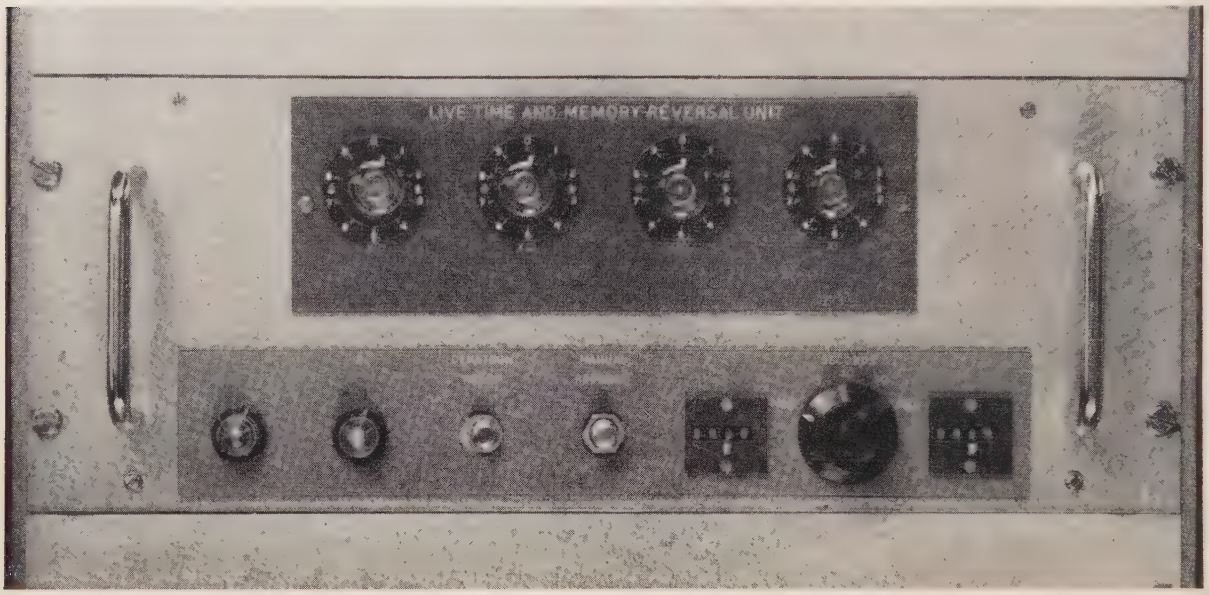


Fig. 3

at the beginning of the sweep. The negative going edge of the positive pulse which appears on the left hand anode of V13 therefore defines the beginning of the sweep and is used to trigger V12. This valve is reset by the negative pulse at the end of the sweep giving a positive pulse on the left hand anode of duration equal to one sweep period. Thus, during one cycle of the memory, the left hand side of V12 holds V11 conducting leading to the diversion of the clock pulses necessary for memory revesal.

One way in which the circuit differs from the original is in the nature of the pulse which triggers V13. In the system described it is no longer random in time since it was found that this could lead to failure of memory reversal. The valves V7 and V8 ensure that the negative edge of the pulse which triggers V13 has a definite relation to the beginning of the sweep period. Its position with respect to the start of the sweep and after a preselected time the memory reversed. Whilst reversal is taking place the analyzer is prevented from counting and the system reset before another period of live-time is measured for a different analyzer input.

Provision is made for manual operation of memory reversal by the switch SWA. The positive pulse necessary for gating V8 is obtained from a resistor chain and a push button switch SWB, and a longer time constant is employed on V7 to ensure that, after being triggered by the initial pulse, any spurious pulses that might occur with the use of such a switch have no effect. In the condition of manual operation live-time will be counted as long as the analyzer is counting; when the count switch of the analyzer is switched "off" a set of contacts on the count relay in the analyzer close and inhibit the action of the live-time measuring unit. The Dekatron unit may be reset and the integrating capacitor

discharged by the contacts of the push button switch SWC.

The units as described have been found to be extremely reliable, being able to perform several thousand operations at three second intervals with no failures.

**Acknowledgements**

We are grateful to Dr. C. W. McCutchen for a helpful discussion of his paper, to Mr. M. Kind, and Mr. M. Hitchman for their assistance in the course of the work, and to the English Electric Co. for permission to publish this paper.

NUCLEAR INSTRUMENTS AND METHODS 9 (1960) 102–106; NORTH-HOLLAND PUBLISHING CO.

# PULSE HEIGHT DISCRIMINATOR EMPLOYING DISTRIBUTED AMPLIFICATION

C. INFANTE

*C.N.R.N., Laboratori Nazionali di Frascati*

Received 8 July 1960

An integral pulse-height discriminator employing distributed amplification is proposed. The discriminator accepts 0.5–12 volts positive input pulses with a maximum repetition rate in excess of 20 mc. Dead time is less than 25 m$\mu$sec and threshold uncertainty is 30 mV. The circuit uses 20 vacuum-tubes in an arrangement believed to be new.

## 1. Introduction

The problem of fast integral discriminators has received considerable attention in recent literature[1,2,3]: this is due mainly to the inadequates of older discriminators (e.g. those employing secondary emission type tubes[4])) and to the increasing trend towards fast circuitry in conjunction with high-intensity pulsed accelerators. Instantaneous counting rates experienced with these machines may easily be as high as $10^7$ pps: in other words speed is at a premium. It often turns out that the resolving time of the discriminator is the limiting factor in the speed of an electronic counting system: the dead time of a typical fast coincidence circuit may be as low as 5 m$\mu$sec[5]), while the resolving time of the discriminator following it is more often in the 0.1 $\mu$sec range[2]).

With these facts in mind the design of the present discriminator was undertaken: the apparatus is bulky and expensive, difficult to align and to repair, but its performance is so superior to the abovementioned circuits that the effort was deemed worthwhile.

The principles and operation of distributed amplifiers have been known for some while[6,7]), their main advantage being in the very large gain-bandwidth products available: this would make them ideally suited for fast trigger cricuits, except that their large inherent delay makes them useless in regenerative-type circuits[8]). In the present application a distributed amplifier is employed to amplify the signals coming from a diode comparator: the amplified signal is sufficient to turn a vacuum tube off, thus producing a signal of constant amplitude. If the gain of the amplifier is large enough, the threshold uncertainty will be reduced to an acceptably low value (in the present case about 30 mV). The principle outlined above (i.e. that of straightforward amplification without positive feedback) while giving up the advantages of positive feedback, (e.g. that of very large gains with few tubes) provides one important advantage in that the delay of input-to-output is not a function of pulse height. It is a well-known fact[9]) that any positive feedback circuit with a threshold $V_S$, introduces a delay that depends on much the input exceeds $V_S$. Strictly speaking a regenerative triggered device may be thought of as an amplifier and a positive feedback loop containing a non-linear element such as a diode or a vacuum tube at or near cutoff. If one employs piece-wise linear approximation of the non-linear element by postulating that its

[1]) F. J. M. Farley, Rev. Sci. Instr. **29** (1958) 595.

[2]) J. Mey, Rev. Sci. Instr. **30** (1959) 282.

[3]) D. V. Swift and V. Perez-Mendez, Rev. Sci. Instr. **30** (1959) 1004.

[4]) N. F. Moody, G. J. R. McLusky and M. O. Deighton,— Electr. Eng. **24** (1952) 214.

[5]) U. Pellegrini, B. Rispoli and A. Serra, N. Cim. Ser. X, **9** (1959) 171.

[6]) E. L. Ginzton, W. R. Hewlett, J. H. Jasberg and J. D. Noe, Proc. I.R.E. **36** (1948) 956.

[7]) H. W. Horton, J. H. Jasberb and J. D. Noe, Proc. IRE **38** (1950) 748.

[8]) M. Brown, Rev. Sci. Instr. **30** (1959) 169.

[9]) J. Mey, L'onde Électrique **38** (1958) 622.

transfer function is zero for signals lying below the threshold and unity for signals lying above it, one can easily show that the time $T$ necessary for the output voltage to reach a specified value $V$ is given by

$$T = \frac{\theta}{\ln F} \ln \frac{V}{\varepsilon} + \theta$$

where $F$ and $\theta$ denote loop gain and delay respectively, while $\varepsilon$ is the portion of the unit pulse exceeding the threshold.

## 2. Circuit description

The discriminator consists of three parts: a comparator circuit, a distributed amplifier and an output or pulse-shaping circuit (fig. 1).

The comparator is of the differential-amplifier-derived type as proposed by J. Mey[2]) with a few modifications which consist essentially in the use of low-capacitance pentodes instead of triodes and in the use of limiting diodes $D_3$ and $D_4$. Use of pentodes instead of triodes brings the gain-bandwidth product between grid of $V_1$ and plate of $V_2$ from 24 for the Mey circuit to 40 Mc/sec for the present circuit. Use of high-speed diodes $D_3$ and $D_4$[10]) was made necessary to avoid overloading the following amplifier: limiting action is quite sharp and takes place at about 0.4 volts

[10]) Made by Qu-Tronic Semiconductor Corp.

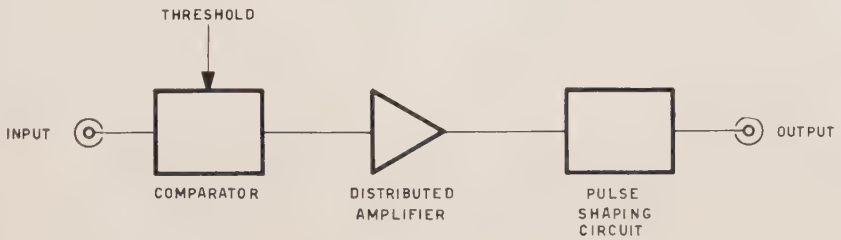


Fig. 1. Block diagram of discriminator.

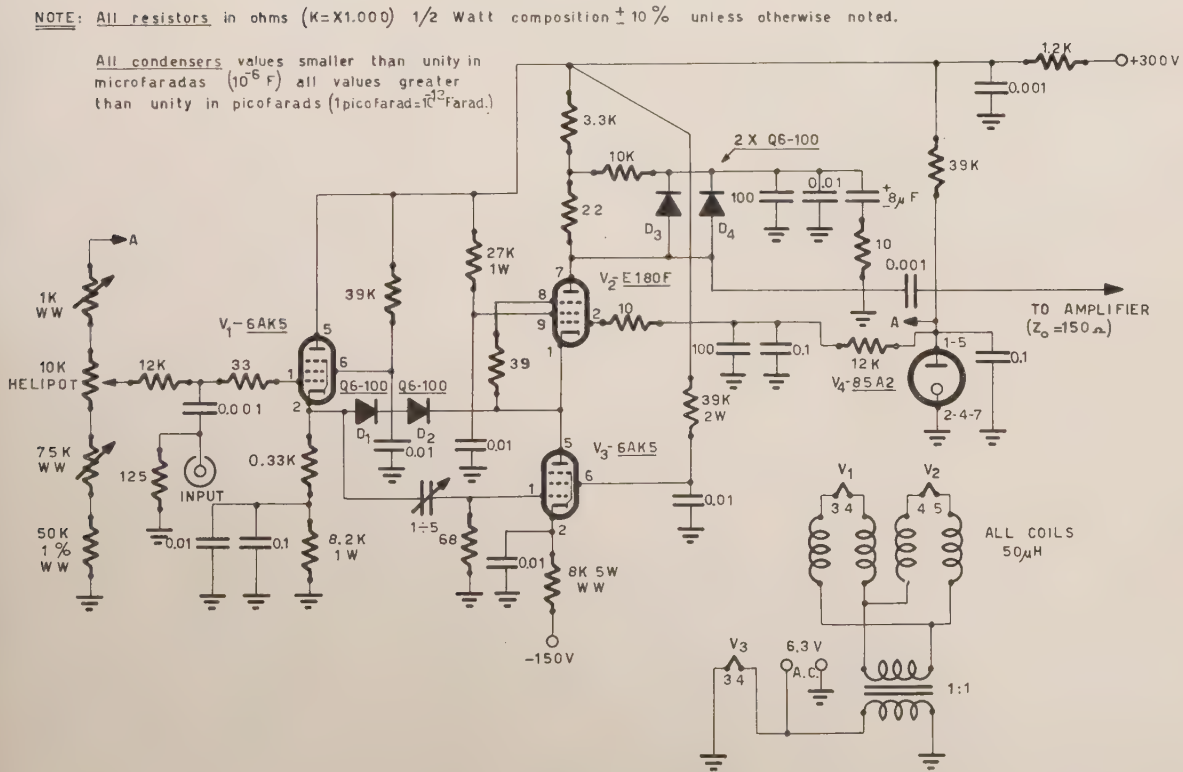


Fig. 2. Comparator circuit.

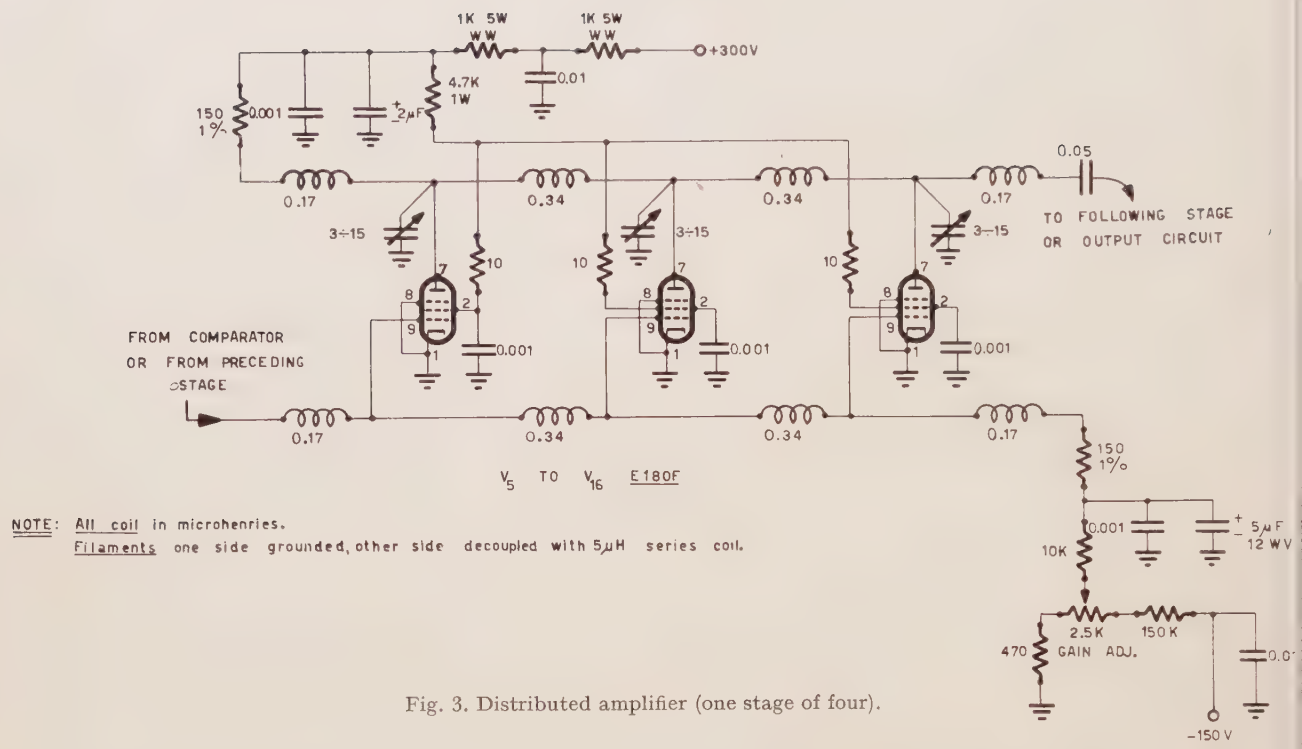


Fig. 3. Distributed amplifier (one stage of four).

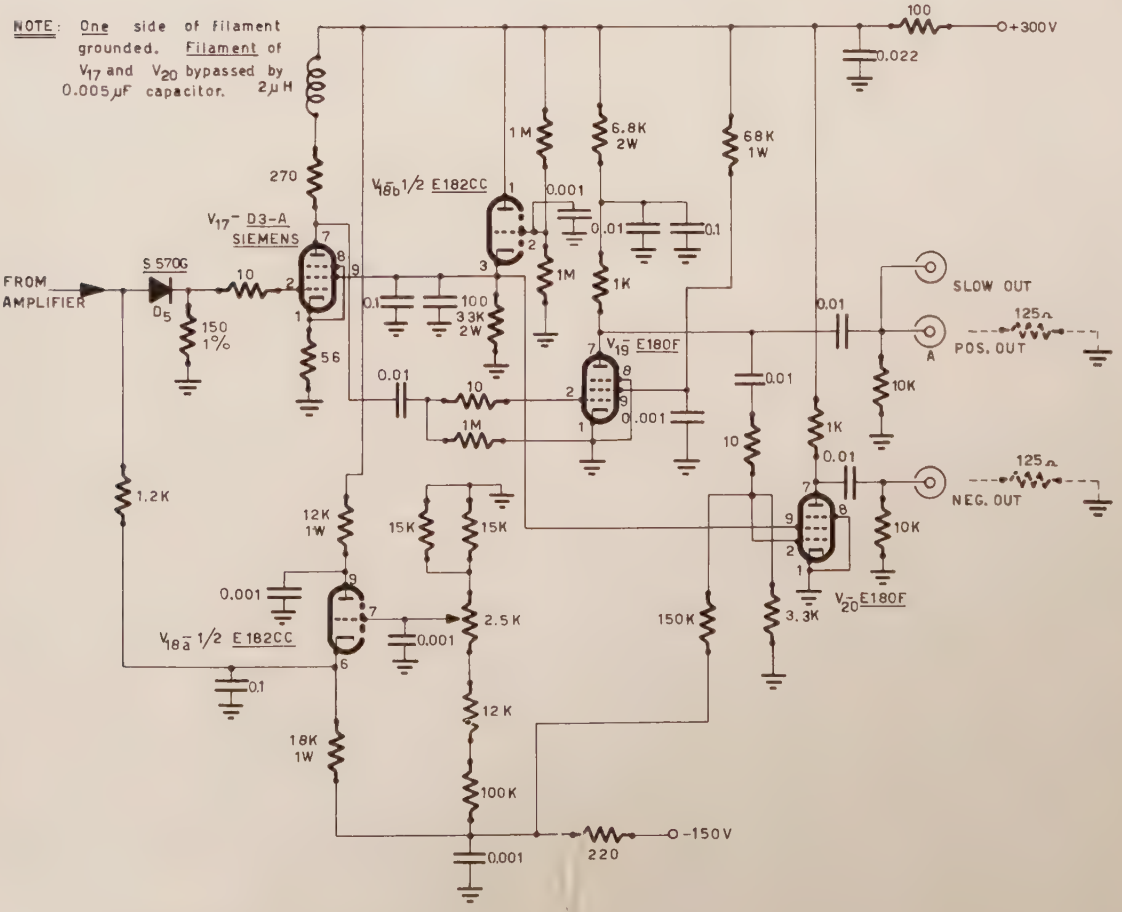


Fig. 4. Output circuit diagram.

amplitude. The circuit diagram of the comparator is given in fig. 2: it should be borne in mind that the effective plate impedance "seen" by $V_2$ is the grid-line impedance of the distributed amplifier, i.e. 150 ohms.

The distributed amplifier is made up of four identical stages one of which is shown in fig. 3; grid and plate-line impedances are 150 ohms, while total gain and rise time are $\times$ 150 (43 dB) and 5 m$\mu$sec respectively. Alignment had to be of course quite accurate to avoid double pulsing.

The diagram of the pulse-shaping circuit is given in fig. 4.

Diode $D_5$ [11]) eliminates small reflections and noise coming from the amplifier and is biased by cathode follower $V_{18a}$: the other half of $V_{18}$ provides a low impedance d.c. source for the screen grids of tubes $V_{17}$ and $V_{20}$. A positive pulse coming from the amplifier makes $V_{17}$ conduct strongly, thus turning $V_{19}$ off, and allowing a constant-amplitude positive pulse to reach output terminals. $V_{20}$ in turn is switched *on*, thereby producing a standard negative pulse. Both positive and negative output are 2 volts in amplitude when terminated in 125 ohms: e.g. the former for triggering fast scalers[12]), the latter for coincidence work. The output pulse duration is dependent mainly on the duration of the input signal: due to rise-time deterioration, minimum pulse-width at full amplitude is of the order of 10 m$\mu$sec. A larger slower output pulse is also available for triggering slow scalers when output A is unterminated.

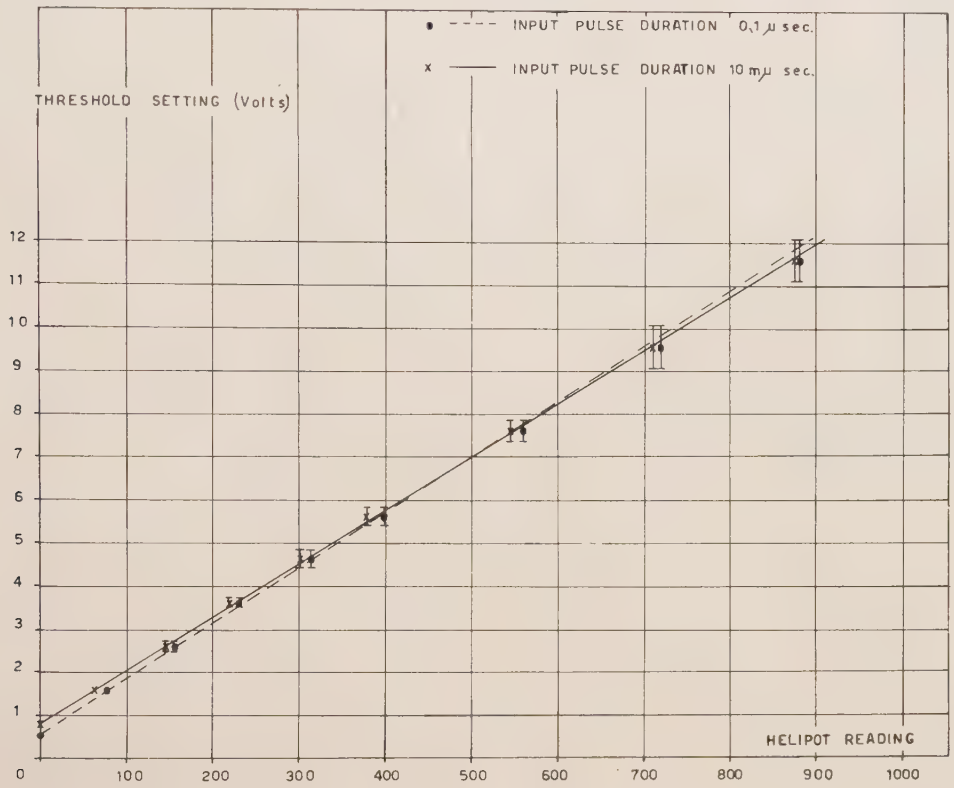


Fig. 5. Discriminator calibration.

### 3. Performance

The threshold linearity in the useful range of 0.5 to 12 volts in better than 3% for pulses whose duration lies between 10 and 100 m$\mu$ seconds as evidenced by fig. 5. The lower limit is

[11]) Made by Transitron Electronic Corp.

[12]) The 40 Mc/sec scaler described by M. Nakamura (Rev. Sci. Instr. **28** (1957) 1015) will trigger with a 2V pulse.

due to uncertainty in diode break-point, while the upper limit (due to diode break-down) is ample considering the dynamic range of present-day photo-multipliers and fast amplifiers. With 25 m$\mu$sec rectangular pulses the absolute value of the threshold increases by 15 mV, while with 10 m$\mu$sec pulses the absolute value increases by 0.3 volts maximum. The resolving time is less than 25 m$\mu$sec, in the sense that two 10 m$\mu$sec rectangular pulses, 25 m$\mu$sec apart are handled independently with no loss in accuracy or in threshold definition. The discriminator has been triggered at repetition rates as high as 20 Mc/s without threshold variations greater than 0.1 volts. 20 Mc/s is the limit of available pulse generators[13,14,15]), but probably still below the limit of the discriminator. The delay between input and output is of about 40 m$\mu$sec and does not change by more than 2 m$\mu$sec as the input exceeds the threshold by 0.03 to 10 volts. Long term (8 hrs) drift was found to be about 20 mV.

[13]) C. C. Cutler, Proc. IRE **43** (1955) 140.
[14]) U. Pellegrini, N. Cim. Ser. X, **9** (1958) 533.
[15]) M. Nakamura, Rev. Sci. Instr. **30** (1959) 778.
[16]) A. Alberigi-Quaranta, C. Bernardini and I. F. Quercia, Nucl. Instr. **3** (1958) 201.

## 4. Conclusion

The proposed circuit is novel in the sense that it employs distributed amplification and no positive feedback in an integral discriminator. Although it uses a large number of tubes (twenty), it is felt that instances may arise in which its superior performance as regards to speed may outweigh the disadvantages of added cost and complexity. An example of this could be a recently proposed multichannel analyzer[16]) employing only one discriminator and whose total dead time is equal to the discriminator dead time multiplied by the number of channels.

## Acknowledgements

The advice and support of Profs. A. Alberigi-Quanranta and I. F. Quercia are gratefully acknowledged. The Author wishes likewise to express his thanks to Mr. R. Rizzi who carried out most of the tests.

NUCLEAR INSTRUMENTS AND METHODS 9 (1960) 107–110; NORTH-HOLLAND PUBLISHING CO.

# CORRECTIONS FOR BACKSCATTERING AND ENERGY RESOLUTION IN BETA SPECTROSCOPY BY SCINTILLATION DETECTORS

G. BERTOLINI, F. CAPPELLANI and A. ROTA

*C.N.R.N., Ispra, Italy*

Received 7 June 1960

The correction for phosphor backscattering and energy resolution is applied to plastic detectors. The application of the correction terms to the beta spectra of $Tl^{204}$ and $Tm^{170}$ gives satisfactory results.

## 1. Introduction

Anthracene and plastic phosphors, due to the good linearity of the energy response to electrons, have been widely employed in the last years in beta spectroscopy.

Their use however requires a correction for the backscattering of the electrons on the phosphor and for the resolution in energy. These effects result in a distortion of the beta spectra markedly in the low energy region.

An attempt for eliminating the backscattering has been done with a certain success by Ketelle[1]) sandwiching the source between two anthracene crystals and placing a phototube viewing the two scintillators.

R. G. Johnson *et al.*[2]) obtained very good results mounting the source between two plastic phosphors viewed by two indipendent phototubes.

Unfortunately a $4\pi$ source-detector geometry cannot be used in all kinds of experiments, as in the case of angular correlations measurements in which our laboratory is interested. The only attempt we know to correct the experimental shape of beta spectra for backscattering and resolution using external geometry, has been performed by M. S. Freedman *et al.*[3]) following a general method outlined by G. E. Owen and M. Primakoff[4]). In our paper, following the method of Freedman *et al.* and using plastic phosphors instead of anthracene, we have obtained good results in correcting the beta spectra of $Tl^{204}$ and $Tm^{170}$, having experimental backscattering distributions quite different from those obtained by Freedman *et al.*

## 2. Method

The distortion, due to the backscattering and the resolution, which transforms a true spectrum $N(E)$ in an experimental one $M(E)$ is described by the following equation:

$$M(E) = \int_0^{E'\max} N(E')L(E\ ,\ E')\,\mathrm{d}E' \simeq \sum_i{}' N(E'_i)L(E\ ,\ E'_i)\ \Delta_i E' \qquad (1)$$

where $L(E, E')$ is the fraction of electrons of energy $E'$ which loose in the phosphor an energy from $E - \frac{1}{2}\Delta E$ to $E + \frac{1}{2}\Delta E$.

$L(E,E')$ is equal to:

$$\frac{S(E\ ,\ E')\ \Delta E}{\int_0^{\infty} S(E\ ,\ E')\mathrm{d}E'},$$

where $S(E, E')$ is the experimental spectrum of the electrons hitting the phosphor with energy $E'$.

$S(E, E')$ and then $L(E, E')$, is available from

[1]) B. H. Ketelle, Phys. Rev. **80** (1950) 758.

[2]) R. G. Johnson, O. E. Johnson and L. M. Langer, Phys. Rev. **102** (1956) 1142.

[3]) M. S. Freedman, T. B. Novey, F. T. Porter and F. Wagner Jr., Rev. Sci. Instr. **27** (1956) 716.

[4]) G. E. Owen and H. Primakoff, Phys. Rev. **74** (1948) 1406; Rev. Sci. Instr. **21** (1956) 447.

experimental data. The equation (1) is resolved by a method of successive approximations.

The experimental spectrum $M(E)$ is taken as zero order approximation $N_0$. Using this approximation a function $M_1$ is obtained from:

$$M_1(E) = \int_0^{E'_{\max}} N_0(E')L(E\,,\,E')\mathrm{d}E' \,.$$

Considering that $N(E) - M(E) \sim N_0(E) - M_1(E)$, the first approximation is obtained: $N_1(E) = N_0(E) + M(E) - M_1(E) = 2M(E) - M_1(E)$.

The successive approximations, performed by the same method, may be expressed as:

$$N_i(E) = N_{i-1}(E) + M(E) - M_i(E) \,.$$

The good reliability of the method is tested by the fast approach of $M_i(E)$ to $M(E)$.

The $S(E, E')$ functions were determined by a careful measurement of the pulse distribution of five internal conversion electron lines and by interpolation for the intermediate energy values.

## 3. Experimental Data

### 3.1. SOURCES

The calibration sources were evaporated on thin films of wins[5]) of about 10 $\mu$g/cm$^2$, metallized under vacuum. The characteristics of the single sources were:

$In^{114m}$: Specific activity 22.4 mc/g; source activity 0.3 $\mu$c source; diameter $\simeq$ 5 mm.

$Sn^{113}$: Specific activity 10 mc/g; source activity 0.25 $\mu$c; source diameter $\simeq$ 4 mm.

$Cs^{137}$: Source activity 0.6 $\mu$c; source diameter 4 mm.

$Bi^{207}$: Source activity 1 $\mu$c; source diameter $\simeq$ 4 mm.

### 3.2. ELECTRON LINES

$e_k$ = 163 keV ($In^{114m}$) observed in coincidence with KX rays of In.

$e_k$ = 364 keV ($In^{113m}$) observed in coincidence with KX rays of In.

$e_k$ = 624 keV ($Ba^{137m}$) observed in coincidence with KX rays of Ba.

$e_k$ = 482 and 976 keV ($Pb^{207}$) observed in coincidence with KX rays of Pb.

The gamma background was subtracted. The line of 976 keV was also observed in coincidence with the 570 keV gamma in order to test the flat pulse distribution of the backscattered area.

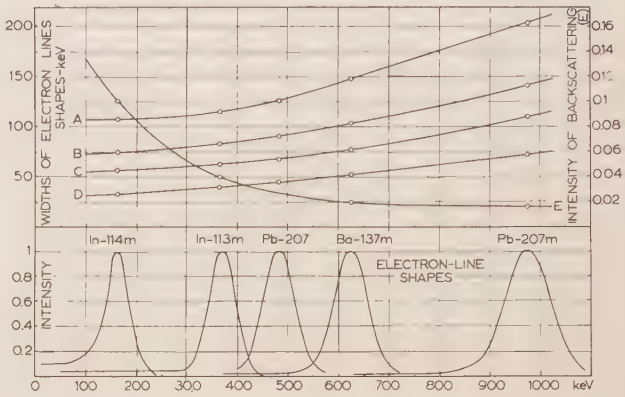


Fig. 1

Fig. 1 shows the results with the intensity on the peak normalized to the same value. In the upper part of the figure the points on the curves A, B, C and D correspond to the widths of the line shapes respectively at $\frac{1}{10}$, $\frac{3}{10}$, $\frac{1}{2}$ and $\frac{3}{4}$ from the base; the points on the curve E correspond to the height of the flat tail of backscattering. The ratio of the backscattered area to the total area for the 171, 364 and 976 keV electron lines was respectively: 18%, 13% and 10.5%. The line at 482 keV was taken in account only with regard to energy resolution and not for the backscattering distribution. The intensity on the peak was always not lower than 8000 counts.

The energy response is linear from 163 to 976 keV and the extrapolation of the obtained straight line to zero pulse height intersects the energy axis at 20 keV, according to the result found by Hopkins[6]).

### 3.3. DETECTORS

Plastic phosphors from National Radiac, Nuclear Enterprise and Pilot Chem. were tested. The latter exhibited the best resolution together with the highest light efficiency and was chosen for our measurements.

[5]) M. Bresesti, F. Girardi, G. J. Segre and O. Terracini, CNI 2 (1958).

[6]) J. I. Hopkins, Phys. Rev. **77** (1950) 406.

The phosphor 1″ × ½″, optically coupled to a phototube DuMont 6292, was covered with an aluminum sheet of 0.23 mg/cm² and the surface sensitive to beta particles was reduced to 2 cm² in order to avoid edge effects.

The X and gamma rays were detected with a NaI(Tl) crystal.

### 3.4. APPARATUS

All the measurements were carried out in vacuum. The source was viewed by the two phototubes aligned on the same axis. The pulses from the plastic scintillator and from NaI(Tl) crystal were sent to a standard coincidence spectrometer with a resolving time of 1 $\mu$sec.

In the NaI(Tl) channel, a single channel analyzer selected the X or the gamma rays.

The pulses from the plastic scintillator were finally sent to a 256 channels analyzer gated by the coincidence pulses.

### 3.5. BETA SPECTRA

$Tl^{204}$: The sources were obtained by electrospraying[7]) of $TlNO_3$ in acetone on a 0.23 mg/cm² aluminum sheet. $Tl^{204}$ decays with a first forbidden unique transition to the ground level of $Pb^{204}$.

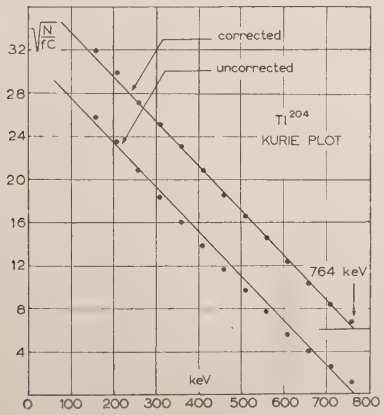


Fig. 2

Fig. 2 shows the Fermi-Kurie plot of the same spectrum corrected for resolution and backscattering with two steps of approximation.

$Tm^{170}$: The sources were obtained by electrospraying of a solution of $TmCl_3$ in alcohol on a 0.23 mg/cm² aluminum sheet. The $Tm^{170}$ decay is well known[8]). The conventional Fermi-Kurie plot of the total spectrum and of the spectrum in coincidence with the 85 keV gamma-rays of

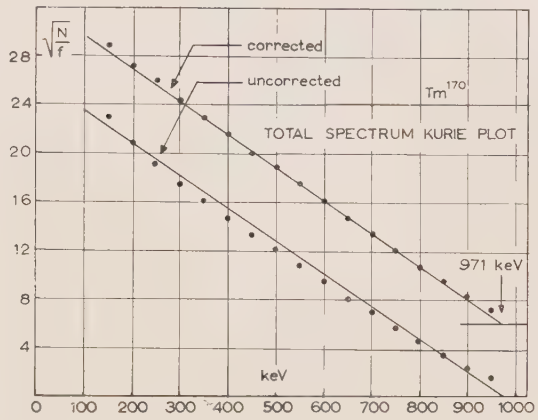


Fig. 3

$Yb^{170}$ are shown respectively in fig. 3 and in fig. 4 with and without backscattering corrections.

## 4. Conclusions

The plots 2, 3 and 4 show the reliability of the method. The limitation consists in the difficulty of the correction under 150 keV in the first place because in our case we had not experimental lines

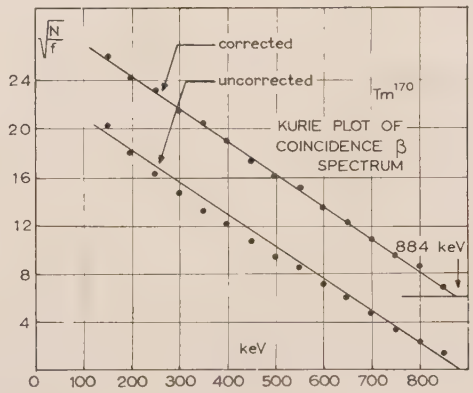


Fig. 4

shapes of energy lower than 100 keV, secondly for the difficulty of the background subtraction with a good accuracy.

[7]) D. J. Carswell and J. Milsted, Nuclear Energy **4** (1957) 51.
[8]) R. W. King, Rev. Mod. Phys. **26** (1954) 327.

In the plots the straight line drawed through the corrected points has been transferred on the uncorrected ones. In this way we put in evidence that it is not possible an exact determination of the true shape of beta apectrum, of its intensity and of its maximum energy without correcting for the backscattering.

The different values of the backscattering obtained by Freedman *et al.* can be due, at 163 keV, to a different criteria used in evaluating the backscattered area, but at higher energies it is not completely clear why they used a backscattering tail of equal intensity for all the electron lines.

Our experiments have been carried out taking very much care that the backscattering of electrons by the source support and by the walls of the vacuum chamber was negligible.

However good results are equally obtainable because the corrective method requires only that the determination of the shape of the monoenergetic electron lines is obtained in the same experimental conditions used in the determination of the beta spectra.

**Acknowledgements**

It is a pleasure to express our thanks to Dr. A. M. Del Turco for the preparation of the sources of $Tl^{204}$ and $Tm^{170}$ and to Mr. G. Melandrone for his helpful cooperation in the measurements.

NUCLEAR INSTRUMENTS AND METHODS 9 (1960) 111–112; NORTH-HOLLAND PUBLISHING CO.

# A DIFFERENTIAL BEAM COLLECTOR

W. T. H. VAN OERS

*Instituut voor Kernphysisch Onderzoek, Amsterdam*

Received 23 June 1960

A double faraday cup has been built, which can measure the energy of a beam of charged particles by determining their mean range, and which can simultaneously be used to integrate the current of the beam.

When a beam of charged particles stops in matter, there is a distribution in the position of endpoints due to straggling. For a monoenergetic beam the distribution of endpoints can be given by a symmetric function about the mean range of the particles. The same is true for a beam with a symmetric beamspread about the mean energy. Thus if the beam enters a plate of absorber, whose thickness equals the mean range of the particles, half the particles will be stopped in the plate, and half will emerge from the rear side. In consequence an equal current due to the collection of charge will be measured, if the emerging particles are stopped in a second beam collector.

An apparatus has been built consisting of a stopping plate followed by a faraday cup. Rather than cutting the first plate to be the mean range, its thickness was chosen somewhat smaller. The second plate was thick enough to stop the particles. An interchangeable set of thin foils of varying thickness was placed before the whole assembly. During operation these trimming foils, which reduce the energy of the particles incident on the two absorber system, were adjusted to obtain the condition of equal currents from both collectors. The mean range is thus given by the thickness of the first plate plus the thickness of the combination of trimming foils. As absorbing material aluminum was chosen, because 99.9% pure aluminum foils and plates were available, and because the range-energy relation of protons in aluminum is known very accurately[1]).

A diagram of the apparatus is shown in the figure. The first absorber is placed in the center of a cylindrical tube, while the second is at the end of a short faraday cup. These side walls on

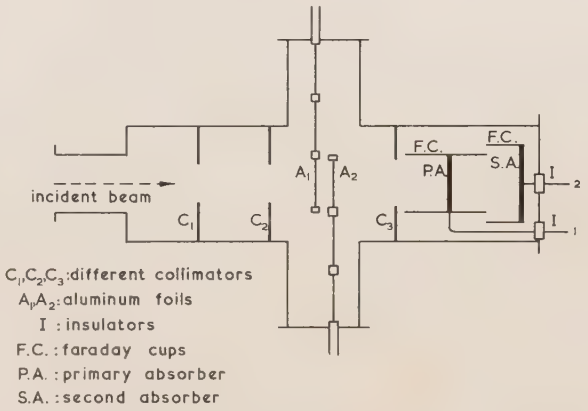


Fig. 1. Differential beam collector for monitoring the energy of the external beam.

the absorbers served the purpose of collecting secondary electrons, which might be emitted from the plates. The whole apparatus was placed in a magnetic field transverse to the axis of the assembly to suppress effects due to secondary emission. A field strength of 150 gauss proved to be most useful. A set of rather broad collimators before the assembly limited the incoming beam to the area of the plates. A collimator of the same size was also placed between the interchangeable set of foils and the first plate to catch secondary electrons from the foils.

The system may also be used to integrate the

[1]) H. Bichsel, Phys. Rev., **112** (1958) 1089.
[2]) R. Littauer, Rev. Sci. Instr. **25** (1954) 148.

beam current by adding the output of the two collectors. When current integration is applied, one must be sure, that the beam size is smaller than the collimators of the apparatus, so that the beam is only collected on the plates. The use of two integrators of the type that allows measurement of the current concurrently with the current integration[2]), would permit integration of the total current of the beam while monitoring the energy continuously. Alternatively, the output of a difference amplifier connected between the outputs of the two collectors could be used to stabilize the energy of a cyclotron following the procedure described by Schrank[3]).

[3]) G. Schrank, Rev. Sci. Instr. 26 (1955) 677.

The apparatus was used to measure the energy of the external beam of a 24 MeV deuteron synchrocyclotron. The results were in good agreement with the value of the energy measured by other methods. The instrumental error is in the order of 0.15%.

The author is grateful to Dr. K.W. Brockman jr. for interesting discussions.

This work was performed as part of the research program of the "Stichting voor Fundamenteel Onderzoek der Materie (F.O.M.)", which is financially supported by the "Nederlandse Organisatie voor Zuiver-Wetenschappelijk Onderzoek (Z.W.O.)".

NUCLEAR INSTRUMENTS AND METHODS 9 (1960) 113–114; NORTH-HOLLAND PUBLISHING CO.

# OPTIMALE LÄNGE DES BESCHLEUNIGUNGSSPALTES BEIM MIKROTRON

A. PAULIN

*J. Stefan Institut, Ljubljana, Jugoslavia*

Eingegagnen am 27. Juni 1960

The optimal length of the accelerating gap using field emission cathode was calculated. For the S-band mikroton this length should be 5 mm in the 511 keV mode ($a = 2$) and 4 mm in the 255 keV mode ($a = 3$).

Beim Mikrotron können die Elektronen mittels einer Elektronenkanone eingespritzt oder im Resonatorspalt selbst durch Feldemission gewonnen werden. Im letzten Falle hängt der Strom der beschleunigten Elektronen sehr von der Länge des Beschleunigungsspaltes ab. Scheinbar ist noch keine genaue Berechnung der optimalen Spaltlänge veröffentlicht worden.

Bei den Mikrotronen nach Redhead u.a.[1]) (Spaltlänge 13.8 mm) und Henderson u.a.[2]) (Spaltlänge 7.8 mm) wird nur etwa 1% des emittierten Stromes beschleunigt. Der Grund dürfte sein, daß wegen zu großer Spaltlänge nur die Elektronen, die etwas vor oder im Augenblick des Spannungsmaximum an der Kathode starten, in den phasenstabilen Bereich gelangen, während die etwas später startenden verloren gehen. Durch Senkung des Magnetfeldes wird erreicht, daß beim nächsten Durchgang die Verdichtung in die phasenstabile Fläche eingeschossen wird. Dabei findet für die erste Umlaufzeit eine kleine Abweichung vom ganzen Vielfachen der Hochfrequenzperiode $\tau$ statt[3]). Somit wird bei den nächsten Durchgängen das Elektronenmaximum etwas verschoben.

Im Folgenden soll die optimale Länge $L$ des Beschleunigungsspaltes berechnet werden unter der Bedingung, daß das Elektron, welches im Augenblick der größten Feldstärke an der Kathode startet, in die Resonanzphase $\varphi$ kommt und in derselben verbleibt. Die drei Unbekannten, die Spannungsamplitude $U$, die in Wellenlängen gemessene Spaltlänge $l = L/\lambda$ und die Phase $\omega t_2$, bei welcher die Elektronenverdichtung den Resonatorspalt verläßt, sind durch die drei Gleichungen bestimmt:

$$U = \frac{m_0 c^2}{e} \frac{1}{a \cos \varphi} \frac{\pi l}{\sin \pi l} (1 + A^2 \sin^2 \omega t_2)^{\frac{1}{2}} ,$$

$$A = \frac{e}{2\pi m_0 c^2} \frac{U}{l} , \qquad (1)$$

$$\cos \omega t_2 = \frac{(1 + A^2)^{\frac{1}{2}}}{A} \sin \left( \arcsin \frac{A}{(1 + A^2)^{\frac{1}{2}}} - 2\pi l \right) , \qquad (2)$$

$$p - \frac{\omega t_2}{2\pi} \quad \tfrac{1}{2} l - \frac{\varphi}{2\pi} - 0 . \qquad (3)$$

Die Gleichungen entstammen einem früheren Artikel[3]). Die ersten zwei sind soweit veralgemeinert, daß das Resonanzelektron den Spalt zur noch unbekannten Phase $\omega t_2$ und nicht $\pi/2$ verläßt. Um zu gewährleisten, daß die erste Umlaufzeit $T_1 = a\tau$ ist (wobei $a = 2, 3, \ldots$) und das Resonanzelektron immer in der Resonanzlage verbleibt, wurde für die Gleichung (3) die Beschränkung $p = 0$ einbezogen.

Aus den Gleichungen (1) bis (3) folgt

$$\left[ \frac{\cos 2 (\omega t_2 - \varphi) - \cos \omega t_2}{\sin 2 (\omega t_2 - \varphi)} \right]^2 + \sin^2 \omega t_2 = [\, 2a \cos \varphi \sin (\omega t_2 - \varphi) \,]^2 . \qquad (4)$$

In der Tabelle 1 sind die Werte für $\omega t_2$, $l$ und $U$, die aus den obigen Gleichungen resultieren, für die Resonanzphase $\varphi = 18°$ bzw. $\varphi = 24°$, jedesmal für $a = 2$ und $a = 3$, angegeben.

[1]) P. A. Redhead, H. LeCaine und W. J. Henderson, Can. J. Research A **28** (1950) 73.

[2]) C. Henderson, F. F. Heyman und R. E. Jennings, Proc. Phys. Soc. B **66** (1953) 654.

[3]) A. Paulin, Nucl. Instr. and Methods **5** (1959) 107.

Tabelle 1

| | $\varphi = 18^0$ | | | $\varphi = 24^0$ | | |
|---|---|---|---|---|---|---|
| $a$ | $\omega t_2$ (°) | $l$ $(-L/\lambda)$ | $U$ (kV) | $\omega t_2$ (°) | $l$ $(-L/\lambda)$ | $U$ (kV) |
| 2 | 25.56 | 0.0420 | 531 | 34.12 | 0.0563 | 578 |
| 3 | 23.32 | 0.0296 | 271 | 31.22 | 0.0401 | 283 |

Bei $\varphi = 24°$ und $\lambda = 10$ cm sollte demnach die Spaltlänge $L = 5.6$ mm bei $a = 2$ und 4 mm bei $a = 3$ betragen. Das hat eine bedeutende Senkung der Güte des Resonators sowie eine Steigerung der Durchschlagsgefahr zur Folge. Es scheint jedoch, daß diese Gefahr oft überschätzt wird. Als Beispiel mag erwähnt werden, daß ein X-Band Resonator mit einer Spaltlänge von 2.8 mm eine Spannungsamplitude von 180 bis 200 kV stundenlang tadellos aushielt und zwar selbst bei schlechtem Vakuum[4]) (etwa $10^{-4}$ mm Hg). Sedlaček und Wernholm[5]) berichten, daß das S-Band Mikroton in Stockholm (Spaltlänge 10.5 mm) eine Spannung über 1 MV aushielt.

Um die Feldemission zu lokalisieren, wäre es vielleicht am Platze, einen breiteren Spalt zu konstruieren und nur an einer Seite des Spaltes eine spitze Feldemissionskathode anzubringen um eine Länge gemäß der Tabelle 1 zu ermöglichen. Die Länge des Spaltes ist nämlich nur für den ersten Durchgang wichtig.

Professor I. Kuščer möchte ich herzlichst für die sorgfältige Durchlesung des Manuskriptes danken.

[4]) A. Paulin und F. Požar, wird in Elektroteh. vestnik **28** (1960) veröffentlicht.

[5]) M. Sedlaček and O. Wernholm, unveröffentlicht.

NUCLEAR INSTRUMENTS AND METHODS 9 (1960) 115–117; NORTH-HOLLAND PUBLISHING CO.

# ON THE PARTICLE LOSS AT A SYNCHROCYCLOTRON LIMIT RADIUS

V. P. DMITRIEVSKY, V. V. KOLGA and B. I. ZAMOLODCHIKOV

*Joint Institute for Nuclear Research, Laboratory of Nuclear Problems*

Received 15 May 1960

Resonance interaction of radial and vertical oscillations near $n = 0.25$ is considered. This resonance is shown to be more dangerous than a parametric excitation of vertical oscillations which is caused by the first harmonic in the magnetic field structure.

At the operating high energy synchrocyclotrons (400–700 MeV) the limit energy (up to which particles can be accelerated) corresponds to the radii where the index of the magnetic field lies between

$$0.25 > n > 0.2 \left(n = -\frac{r}{H}\frac{\mathrm{d}H}{\mathrm{d}r}\right).$$

Coupling oscillations in the range $n = 0.2$ are not able to cause the total beam loss[1]). This range is directly adjoined by the parametric excitation region of vertical oscillations by the first harmonic in the magnetic field structure at the frequency $Q_Z = 0.5$ ($n = 0.25$). As is known[2]) for such a resonance the amplitude of vertical oscillations increases "e" times depending on the value of the first harmonic ($\varepsilon_1$) per $(\frac{3}{2})^{\frac{1}{2}}\, 1/\varepsilon_1$ ion revolutions. At the operating synchrocyclotrons the value $\varepsilon_1$ does not exceed 0.001 and, consequently, the treated parametric excitation cannot cause a considerable increase of the amplitude since the width of the resonance range with such a value of $\varepsilon_1$ is usually less than a hundred revolutions.

Consider now by what effect the amplitude increase of the vertical oscillations can be caused, the azimuth inhomogeneity of the magnetic field being present.

In this case the equation for oscillations in the cylindrical coordinate system is described by the following equations†:

$$z'' + [n + \varepsilon_1 n \cos(\varphi + \varphi_0)]\, z - \\ - \frac{2}{R}(d - n)\, z\rho - \frac{z'\rho'}{R} = 0\,;$$

$$\rho'' + (1 - n)\rho + \frac{1 - 2n + d}{R}\rho^2 - \frac{\rho'^2}{2R} - \\ - \frac{2d - n}{2R} z^2 = \varepsilon_1 R \cos(\varphi + \varphi_0)\,, \quad (1)$$

where

$$n = -\frac{R}{H}\frac{\mathrm{d}H}{\mathrm{d}r}\bigg|_{r=R}, \quad d = \tfrac{1}{2}\frac{R^2}{H(R)}\frac{\mathrm{d}^2H}{\mathrm{d}r^2}\bigg|_{r=R}, \quad \rho = r - R$$

$$H_z = H(r)\,[1 + \varepsilon_1 \cos(\varphi + \varphi_0)], \qquad z' = \frac{\mathrm{d}z}{\mathrm{d}\varphi}.$$

Now consider coupling oscillations which are caused by the distortion of the closed orbit due to azimuth inhomogeneity in the magnetic field structure. In this case the equation for vertical oscillations can be written as follows:

$$z'' + \left\{n + \frac{\varepsilon_1^2 d}{n(1 - n)} + \right. \\ \left. + \varepsilon_1 n \left[1 + \frac{(2d - n)}{n^2}\right] \cos(\varphi + \varphi_0)\right\} z = 0\,. \quad (2)$$

For all the operating synchrocyclotrons the magnitude

$$\frac{2}{d} - \frac{n}{n^2} \gg 1 \text{ with } n = 0.25\,,$$

i.e. the beam loss at critical radii is caused by coupling of oscillations rather than by parametric

† In system (1) only resonance terms containing $\varepsilon_1$ are left.

[1]) D. R. Hamilton and H. I. Lipkin, Rev. Sci. Instr. 22 (1951) 783.

[2]) L. R. Henrich, D. C. Sewell and J. Vale, Rev. Sci. Instr. 20 (1949) 887.

excitation of vertical oscillations due to the first harmonic of the magnetic field. The deflection of the resonance band centre from $n = 0.25$ is negligibly small (the term $\varepsilon_1^2 d/n(1 - n)$. The maximum index of exponential growth at the resonance band from (2) equals:

$$\mu = \frac{\varepsilon_1 d - n}{n} \tag{3}$$

i.e. the oscillation amplitude increases "e" times in $\nu$ revolutions, where

$$\nu = \frac{n}{2\pi\varepsilon_1 |d - n|} . \tag{4}$$

Taking into account that $d \approx \frac{1}{2} r \, \mathrm{d}n/\mathrm{d}r$, it is easy to obtain the width of a resonance band

$$\Delta r = \frac{\varepsilon_1 R}{n} . \tag{5}$$

If the average energy gain per turn is equal to $eV$, the number of revolutions at the resonance band is

$$\nu = \varepsilon_1 \frac{1 - n}{n} \frac{E_k}{eV} \frac{2E_0 + E_k}{E_0 + E_k} . \tag{6}$$

Thus, in a quasistatic regime the ion amplitude increase can be evaluated from (3) and (6) in passing through the resonance

$$\ln \frac{a}{a_0} \approx 2\pi\varepsilon_1^2 d \frac{1 - n}{n^2} \frac{E_k}{eV} \frac{2E_0 + E_k}{E_0 + E_k} . \tag{7}$$

Using the method of averaging[3]), one can evaluate the amplitude increase in a dynamic regime:

$$\ln \frac{a}{a_0} \approx 4\sqrt{\pi} \frac{\varepsilon_1 d}{\sqrt{\chi}} \tag{8}$$

where $\chi$ (the rate of self-frequency change in the resonance range $n = 0.25$) is obtained from

$$\chi = \frac{4d}{3\pi} \frac{eV}{E_k} \frac{E_0 + E_k}{2E_0 + E_k} . \tag{9}$$

The test of these results have been performed with an electronic analog computer ЭМУ-8. This device made it possible to solve the problem of the dynamic passage of particles through the coupling resonance with the forced radial oscillations with $n = 0.25$ as it is known that even the shortened equations of this problem are not integrated in quadratures. With the help of the analog computer ЭМУ-8 eq. (2) has been integrated which can be written as a system of two equations

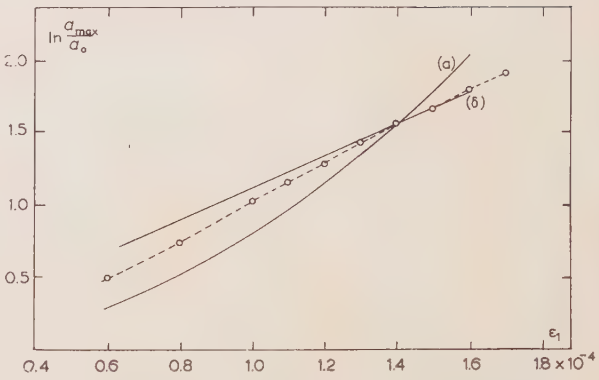


Fig. 1. Dependence of the maximum amplitude on the value of the first harmonic of the magnetic field for a synchrocyclotron $E_k = 680$ MeV.

$$z'' + n(\varphi) z + \frac{2\varepsilon_1 d}{n} uz = 0$$

$$u'' + u = 0 \tag{10}$$

where

$$n(\varphi) = n_0 + \chi\varphi , \qquad u(\varphi_*) = 1 , \qquad u'(\varphi_*) = 0 ,$$

$$z(\varphi_*) = a_0 , \qquad z'(\varphi_*) = 0 .$$

Since time serves as an argument, when system (10) is being solved with an electronic computer, a free choice of the initial phase $\varphi_0$ is possible.

While integrating, $\varphi_0$ was chosen in order to obtain the maximum amplitude growth of vertical oscillations during their passage through the coupling resonance with $n = 0.25$.

The maximum amplitude of oscillations have been observed directly in the indicator screen and determined by voltage on the integrator output. The accuracy of determination is 1%.

System of equations (10) have been solved for parameters of two operating synchrocyclotrons:

1. $E_k = 680$ MeV, $V = 10$ kV, $d = -10$ (Joint Institute for Nuclear Research, Dubna)[4]).

2. $E_k = 57$ MeV, $V = 7$ kV, $d = -7.5$ (Institute for Nuclear Study, Tokyo)[5]).

[3]) N. N. Bogolyubov and Yu. A. Mitropolsky, Asymptotic methods in non-linear oscillations theory, Physmatgiz (1958).

[4]) V. P. Dzhelepov *et al.*, "High-energy particle beams from the 6 metre synchrocyclotron and their utilization", Geneva, CERN Symposium, 1956.

[5]) A. Suzuki (private communication) Japan, Tokyo.

The dependences $\ln (a_{max}/a_0) = f(\varepsilon_1)$ after passing through the coupling resonance $n = 0.25$ are given in fig. 1 and fig. 2, respectively. In these diagrams there are curves (a) and (b) which have been calculated by means of a quasistatic method according to formula (7) and

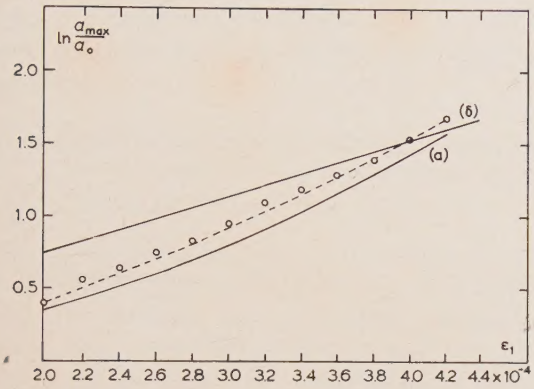


Fig. 2. Dependence of the maximum amplitude on the value of the first harmonic of the magnetic field for a synchrocyclotron $E_k = 57$ MeV.

by using a method of averaging according to formula (8), respectively.

In figs. 3 and 4 there are photographs taken from the indicator screen of the analog computer ЭМУ-8 which illustrate the process of swinging of vertical oscillations during the dynamic passage through the treated resonance of the synchrocyclotron with $E_F = 57$ MeV.

Theoretical treatment of oscillation excitation in the nonlinear resonance range of a higher order caused by the coupling with forced oscillations ($Q_z = \frac{1}{3}$, $Q_z = \frac{1}{4}$) has shown that the former does not occur with the mirror-symmetric structures of the magnetic field and resonances, beginning from $Q_z = \frac{1}{4}$, are not dangerous. Resonance excitation of vertical oscillations of the second and higher harmonics in the magnetic field structure is not practically dangerous.

## Conclusion

As is shown by numerical calculations and also by simulation of the process of passing through

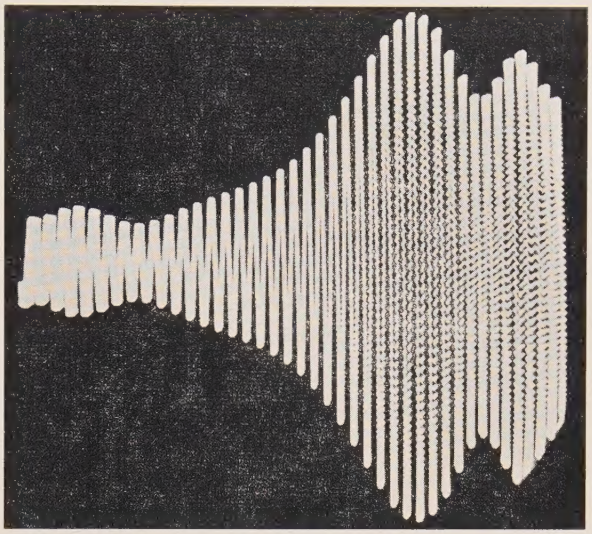

Fig. 4. Process of passing through the resonance range for a synchrocyclotron $E_k = 57$ MeV and $\varepsilon_1 = 2.6 \times 10^{-4}$.

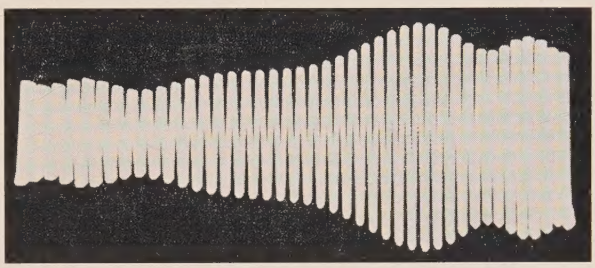

Fig. 3. Process of passing through the resonance range for a synchrocyclotron $E_k = 57$ MeV and $\varepsilon_1 = 4 \times 10^{-4}$.

the resonance of the oscillation coupling in the range $n \approx 0.25$, this resonance determines a limit radius up to which ions are accelerated with high energy synchrocyclotrons. At synchrocyclotrons of a smaller radius ($R < 100$ cm) the passing of particles through the area of this resonance is possible as the rate of changing of self-frequency near $n = 0.25$ at such synchrocyclotrons is considerably higher

The authors wish to express their gratitude to Prof. V. P. Dzhelepov for valuable discussions of the results.

NUCLEAR INSTRUMENTS AND METHODS **9** (1960) 118–119; NORTH-HOLLAND PUBLISHING CO.

LETTER TO THE EDITOR

# A NEW TYPE OF LIQUID ANODE GAMMA AND BETA HALOGEN COUNTER

S. C. PANCHOLI

*Department of Physics, University of Delhi, Delhi-8. India*

Received 27 July 1960

A new type of radiation counter is described which uses a thin glass tube filled with conducting water as the anode. This type of halogen counter is characterised by a fairly good plateau slope and a large plateau width. The preliminary findings are described.

Presently, halogen counters are being increasingly used in Nuclear Science applications. G. M. type of halogen counters utilize a thin platinum wire as an anode and a stainless steel cylinder as cathode. These counters have the advantage that they can operate at lower voltages than conventional argon and alcohol mixture counters. The plateau slopes obtained in halogen counters are generally steeper. We have developed a new type of halogen counter in which the central platinum wire anode is replaced by a thin pyrex glass tube which contained distilled water made conducting by adding one or two drops of conc. $H_2SO_4$ in 100 cc distilled water. An ordinary copper wire spiral wound over the outer glass cylinder replaces the stainless steel cathode. This type of construction has two distinct advantages:

(a) the platinum wire is not required, so this avoids the difficulty in making the glass to platinum joints which are sometimes the leak points for the counter, and

(b) this avoids the use of costly stainless steel, which is used because of the strong halogen action over cathode materials.

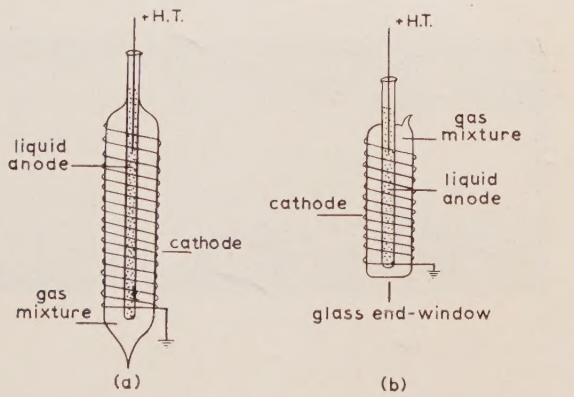


Fig. 1a. Gamma counter.

Fig. 1b. Glass end-window bottle type beta counter.

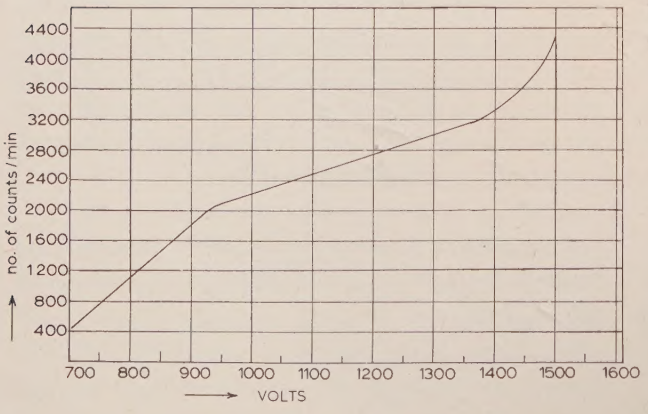


Fig. 2a. Characteristics of the gamma counter. The plateau slope is 10 percent/100 V and the plateau width is 400 V.

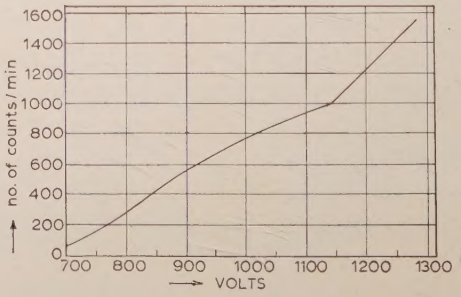


Fig. 2b. Characteristics of the end-window beta counter. The plateau slope is 30 per cent/100 V and the plateau width is 300 V.

The present paper describes the preliminary results obtained with the new type of counter which may prove to be of equal value to a G.M. counter on further adjustment in halogen and noble gas proportions and noble gas pressures. Further work will be published later.

Fig. 1(a) shows the construction details of the gamma counter. The counter has the following dimensions:

Length of the counter = 14 cm.
Diameter of the inner tube = 1.2 cm.
Diameter of the outer tube = 3 cm.

Fig. 1(b) shows the design of the blowed glass end-window bottle type beta counter. The length of the counter is 10 cm and rest of the dimensions are the same as for the gamma counter.

The gamma counter was filled with 6 cm of argon in the presence of traces of bromine vapours, probably adsorbed to the glass walls, and the beta counter with 0.2 mm of bromine vapour and 100 mm of argon. The characteristics of the two gamma and beta counters are shown in figs. 2(a) and 2(b) respectively. A weak $Co^{60}$ gamma-source placed outside near the centre of the gamma counter gave plateau slope 10%/100 V with plateau width of ~ 400 volts. When a similar counter was filled with higher pressures of the constituents (i.e., 0.2 mm bromine and 100 mm argon) it was found that the detection efficiency decreases considerably. This may be attributed to the negative ion formation in the counter due to the higher halogen proportion. So it is recommanded that a low argon pressure (< 6 cm) in presence of traces of halogen may be used.

The beta counter gave a slope of 30%/100 V and a plateau width of ~ 300 V with a $Cs^{137}$ beta source placed at a distance of ~ 34 cm from the flat glass window of the counter.

The counters are not found to be photosensitive.

The author is thankful to Prof. D. S. Kothari, Head of the Physics Department, University of Delhi for the facilities given for carrying out the work. I am also grateful to Shri H. S. Thaira, Aligarh University, Dr. N. K. Saha, Delhi University, and Dr. A. P. Saxena, M. L. B. College, Gwalior for their kind help and keen interest in the work.

# BOOK REVIEWS

GORDON FRANCIS, *Ionization Phenomena in Gases* (Butterworths Sci. Publ. vii + 300p.)

After an introductory review of some fundamental processes in gas discharges a major part of the book is devoted to alternating and high-frequency discharges. The remaining chapters treat ionization and excitation in the upper atmosphere, high-current discharges including thermonuclear research, and oscillations and waves in ionized gases. At the end of the book some useful numerical data on ionization potentials, etc. are collected.

Considering the extent of the subjects chosen, and the number of pages at disposal, there are no opportunities to exhaustive or mathematically rigorous treatments. Instead there are summarizing discussions of theories and experiments, supplemented by a large number of references to more detailed monographs and to the original works. Although intended as complementary to what can be found in other textbooks, the authors principles of selection and disposition of the material may be subject to some discussion. For example, the first chapter is devoted to elementary atomic theory, but it is assumed that the reader is rather familiar with thermodynamics and glow discharges among other things. There is also some question, whether plasma oscillations and waves should not be treated before discussing some of the phenomena in high-current and microwave discharges.

As a whole, however, the book reflects the author's thorough knowledge of all parts of his subject and his ability to give a proper background of classical gas discharge physics to the last few years' rapid expansion in the fields of plasma physics and thermonuclear research.

LARS HÖGBERG

*A Series in the Radiochemistry of the Elements.* Issued through the Office of Technical Services, Department of Commerce, Washington 25, D.C.

A series of monographs dealing with the radiochemistry of some eighty elements. The monographs have been compiled at various centres in both America and Europe and comprise extensive information relative to their subject. Titles so far in circulation are as follows:

NAS–NS 3001 Cadmium, by James R. DeVoe,
3002 Arsenic, by Harold C. Beard,
3003 Francium, by Earl K. Hyde,
3004 Not received by this reviewer,
3005 Fluorine, Chlorine, Bromine and Iodine, by J. Kleinberg and G. A. Cowan,
3006 Americium and Curium, by R. A. Penneman and T. K. Keenan,
3007 Chromium, by J. Pijpck,
3008 Rhodium, by G. R. Choppin,
3009 Molybdenum, by E. M. Scadden and N. E. Ballou,
3010 Barium, Calcium and Strontium, by D. N. Sunderman and C. W. Townley.

Each monograph begins with a general review of the inorganic and analytic chemistry of the element in question followed by a table of isotopes and the detailed chemistry of the element. In conclusion, counting techniques and a collection of detailed procedures are given. The monographs are paper bound, fully referenced and well illustrated where necessary. It is this reviewers opinion that these monographs will prove to be a much valued reference work to anyone concerned with work of this nature. Those monographs listed are available from the above address at a price of between $ 0.50 and $ 1.15. W. C. PARKER